

UNCLASSIFIED

AD NUMBER
ADB131204
NEW LIMITATION CHANGE
TO Approved for public release, distribution unlimited
FROM Distribution authorized to U.S. Gov't. agencies and their contractors; Critical Technology; Feb 88. Other requests shall be referred to WRDC/FIBR, Wright-Patterson AFB, OH 45433-6553. This document contains export- controlled technical data.
AUTHORITY
DFOISR/WHS/DOD ltr, 30 Nov 2001

THIS PAGE IS UNCLASSIFIED

AFWAL-TR-87-3096

2

# ACTIVE FLEXIBLE WING (AFW) TECHNOLOGY



AD-B-131 204

Gerald D. Miller

Rockwell International  
North American Aircraft Operations  
P.O. Box 92098  
Los Angeles, California 90009

DTIC  
ELECTE  
APR 06 1988  
S D & D

February 1988

Final Report for Period June 1985 - May 1987

Distribution <sup>Quota</sup> limited to U.S. Government agencies and their contractors; critical technology: February 1988. Other requests for this document must be referred to the Air Force Wright Aeronautical Laboratories (WRDC /FIBR) Wright-Patterson AFB, OH 45433-6553.

WARNING - This document contains technical data whose export is restricted by the Arms Export Control Act (Title 22, U.S.C., Sec 2751, et seq.) or the Export Administration Act of 1979, as amended, Title 50, U.S.C., App. 2401, et seq. Violations of these export laws are subject to severe criminal penalties. Disseminate in accordance with the provisions of AFR 80-34.

**DESTRUCTION NOTICE** Destroy by any method that will prevent disclosure of contents or reconstruction of the document.

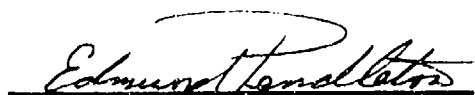
FLIGHT DYNAMICS LABORATORY  
AIR FORCE WRIGHT AERONAUTICAL LABORATORIES  
AIR FORCE SYSTEMS COMMAND  
WRIGHT-PATTERSON AIR FORCE BASE, OHIO 45433-6553

89 1 001

## NOTICE

WHEN GOVERNMENT DRAWINGS, SPECIFICATIONS, OR OTHER DATA ARE USED FOR ANY PURPOSE OTHER THAN IN CONNECTION WITH A DEFINITELY GOVERNMENT-RELATED PROCUREMENT, THE UNITED STATES GOVERNMENT INCURS NO RESPONSIBILITY OR ANY OBLIGATION WHATSOEVER. THE FACT THAT THE GOVERNMENT MAY HAVE FORMULATED OR IN ANY WAY SUPPLIED THE SAID DRAWINGS, SPECIFICATIONS, OR OTHER DATA, IS NOT TO BE REGARDED BY IMPLICATION, OR OTHERWISE IN ANY MANNER CONSTRUED, AS LICENSING THE HOLDER, OR ANY OTHER PERSON OR CORPORATION; OR AS CONVEYING ANY RIGHTS OR PERMISSION TO MANUFACTURE, USE, OR SELL ANY PATENTED INVENTION THAT MAY IN ANY WAY BE RELATED THERETO.

THIS TECHNICAL REPORT HAS BEEN REVIEWED AND IS APPROVED FOR PUBLICATION.



EDMUND PENDLETON  
Project Engineer  
Aeroelasticity Group  
FOR THE COMMANDER



TERRY HARRIS, Technical Manager  
Aeroelasticity Group  
Analysis & Optimization Branch  
Structures Division



JOHN T. ACH  
Acting Chief  
Analysis & Optimization Branch  
Structures Division

IF YOUR ADDRESS HAS CHANGED, IF YOU WISH TO BE REMOVED FROM OUR MAILING LIST, OR IF THE ADDRESSEE IS NO LONGER EMPLOYED BY YOUR ORGANIZATION PLEASE NOTIFY AFWAL/FIBRC, WRIGHT-PATTERSON AFB, OH 45433-6523 TO HELP MAINTAIN A CURRENT MAILING LIST.

COPIES OF THIS REPORT SHOULD NOT BE RETURNED UNLESS RETURN IS REQUIRED BY SECURITY CONSIDERATIONS, CONTRACTUAL OBLIGATIONS, OR NOTICE ON A SPECIFIC DOCUMENT.

The following notice applies to any unclassified (including originally classified and now declassified) technical reports released to "qualified U.S. contractors" under the provisions of DoD Directive 5230.25, Withholding of Unclassified Technical Data From Public Disclosure.

NOTICE TO ACCOMPANY THE DISSEMINATION OF EXPORT-CONTROLLED TECHNICAL DATA

1. Export of information contained herein, which includes, in some circumstances, release to foreign nationals within the United States, without first obtaining approval or license from the Department of State for items controlled by the International Traffic in Arms Regulations (ITAR), or the Department of Commerce for items controlled by the Export Administration Regulations (EAR), may constitute a violation of law.
2. Under 22 U.S.C. 2778 the penalty for unlawful export of items or information controlled under the ITAR is up to two years imprisonment, or a fine of \$100,000, or both. Under 50 U.S.C., Appendix 2410, the penalty for unlawful export of items or information controlled under the EAR is a fine of up to \$1,000,000, or five times the value of the exports, whichever is greater; or for an individual, imprisonment of up to 10 years, or a fine of up to \$250,000, or both.
3. In accordance with your certification that establishes you as a "qualified U.S. Contractor", unauthorized dissemination of this information is prohibited and may result in disqualification as a qualified U.S. contractor, and may be considered in determining your eligibility for future contracts with the Department of Defense.
4. The U.S. Government assumes no liability for direct patent infringement, or contributory patent infringement or misuse of technical data.
5. The U.S. Government does not warrant the adequacy, accuracy, currency, or completeness of the technical data.
6. The U.S. Government assumes no liability for loss, damage, or injury resulting from manufacture or use for any purpose of any product, article, system, or material involving reliance upon any or all technical data furnished in response to the request for technical data.
7. If the technical data furnished by the Government will be used for commercial manufacturing or other profit potential, a license for such use may be necessary. Any payments made in support of the request for data do not include or involve any license rights.
8. A copy of this notice shall be provided with any partial or complete reproduction of these data that are provided to qualified U.S. contractors.

D E S T R U C T I O N   N O T I C E

For classified documents, follow the procedures in DoD 5200.22-M, Industrial Security Manual, Section II-19 or DoD 5200.1-R, Information Security Program Regulation, Chapter IX. For unclassified, limited documents, destroy by any method that will prevent disclosure of contents or reconstruction of the document.

REPORT DOCUMENTATION PAGE

1a. REPORT SECURITY CLASSIFICATION <b>UNCLASSIFIED</b>		1b. RESTRICTIVE MARKINGS	
2a. SECURITY CLASSIFICATION AUTHORITY		3. DISTRIBUTION/AVAILABILITY OF REPORT Distribution <i>Out</i> to U.S. Government agencies and their contractors; critical technology. February 1988. Continued	
2b. DECLASSIFICATION/DOWNGRADING SCHEDULE		5. MONITORING ORGANIZATION REPORT NUMBER(S) AFWAL-TR-87-3096	
4. PERFORMING ORGANIZATION REPORT NUMBER(S) NA-87-1515L		7a. NAME OF MONITORING ORGANIZATION Flight Dynamics Laboratory	
6a. NAME OF PERFORMING ORGANIZATION Rockwell International	6b. OFFICE SYMBOL (If applicable)	7b. ADDRESS (City, State and ZIP Code) WRDC/FIBRC Wright-Patterson AFB, Ohio 4533-6553	
6c. ADDRESS (City, State and ZIP Code) P.O. Box 92098 Los Angeles, CA. 90009		9. PROCUREMENT INSTRUMENT IDENTIFICATION NUMBER F33615-85-C-3209	
8a. NAME OF FUNDING/SPONSORING ORGANIZATION AFWAL	8b. OFFICE SYMBOL (If applicable)	10. SOURCE OF FUNDING NOS.	
8c. ADDRESS (City, State and ZIP Code) Wright-Patterson AFB, Ohio 4533-6553		PROGRAM ELEMENT NO. 62201F/ 61101F	TASK NO. 2401 02
11. TITLE (Include Security Classification) Active Flexible Wing (AFW) Technology		WORK UNIT NO. 68	
12. PERSONAL AUTHOR(S) G./D. Miller			
13a. TYPE OF REPORT Final Report	13b. TIME COVERED FROM June 1985 to May 1987	14. DATE OF REPORT (Yr., Mo., Day) Feb 1988	15. PAGE COUNT 256
16. SUPPLEMENTARY NOTATION			
17. COSATI CODES		18. SUBJECT TERMS (Continue on reverse if necessary and identify by block number)	
FIELD	GROUP	SUB. GR.	Active flexible wing, controllability, wing roll control, wind tunnel testing, transonic aeroelastic control effectiveness, active control design and tests. (511)-4
19. ABSTRACT (Continue on reverse if necessary and identify by block number) This report documents the results of the transonic, active control wind tunnel program. The wind tunnel model along with its physical characteristics (flexibility, vibration modes, and control system transfer functions) and the wind tunnel test procedures are described in this report. In addition, the results of static aeroelastic tests compared with analytical results are included. These results validated the flexible control power and verified the analytical tools used for design. Results of active control designs and tests, roll control, maneuver load control, and structural mode control designs and tests are also included. Finally, an assessment of the AFW technology provides recommendations for future research and development. <i>Keywords:</i> * Built by Rockwell under in-house funding			
20. DISTRIBUTION/AVAILABILITY OF ABSTRACT UNCLASSIFIED/UNLIMITED <input checked="" type="checkbox"/> SAME AS RPT. <input type="checkbox"/> DTIC USERS <input type="checkbox"/>		21. ABSTRACT SECURITY CLASSIFICATION Unclassified	
22a. NAME OF RESPONSIBLE INDIVIDUAL Edmund Pendleton		22b. TELEPHONE NUMBER (Include Area Code) 57384	22c. OFFICE SYMBOL WRDC/FIBRC

Unclassified

**SECURITY CLASSIFICATION OF THIS PAGE**

Block 3 Cont: Other requests for this document must be referred to WRDC/FIBR  
Wright-Patterson AFB, OH 45433-6553.

Unclassified

FOREWORD

This report satisfies CDRL 2, Final Report, for the Active Flexible Wing (AFW) Technology Contract F33615-85-C-3209. The program was sponsored by the Flight Dynamics Laboratory, Air Force Wright Aeronautical Laboratories, Aeronautical Systems Division (AFSC), United States Air Force, Wright-Patterson Air Force Base, Ohio 45433. Mr. E. W. Pendleton is Air Force project engineer; Mr. G. D. Miller is Rockwell program manager.

Contained herein is a description of the AFW concept and technology and the background of the concept which was independently developed by Rockwell. A description of the actively controlled, transonic wind tunnel model, which was independently built by Rockwell, and the control laws, which were also independently developed and implemented by Rockwell, is included.

Results of laboratory tests which provide the physical characteristics of the model and the static and dynamic wind tunnel tests conducted under the contract are included. Independent Rockwell analyses and comparisons with the test data are also included in this final report.



Accession For	
NTIS CRA&I	<input type="checkbox"/>
DTIC TAB	<input checked="" type="checkbox"/>
Unannounced	<input type="checkbox"/>
Justification	
By	
Distribution/	
Availability Codes	
Dist	Avail and/or Special
C-2	501

## CONTENTS

Section		Page
1.0	INTRODUCTION AND SUMMARY	1-1
	1.1 Introduction	1-1
	1.2 Summary	1-3
2.0	DESCRIPTION OF ACTIVE FLEXIBLE WING (AFW) TECHNOLOGY	2-1
	2.1 Background of the Concept	2-1
	2.1.1 Wing Design Challenge	2-1
	2.1.2 AFW Technology Approach to Problem	2-3
	2.2 Results of AFW Feasibility Study	2-5
3.0	WIND TUNNEL MODEL DESCRIPTION AND CHARACTERISTICS	3-1
	3-1 General	3-1
	3-2 Planform Dimensions	3-5
	3-3 Model Structural and Mechanical Design	3-5
	3.3.1 Flexible Wing Design	3-5
	3.3.2 Fuselage Design	3-5
	3.3.3 Sting Design	3-9
	3.3.4 Hydraulic System	3-9
	3.3.5 Electronic Controller Design	3-11
	3.4 Model Instrumentation	3-11
	3.4.1 Force Balance	3-11
	3.4.2 Strain Gages	3-16
	3.4.3 Hydraulic System Pressure Measurements	3-18
	3.4.4 Angular Position Measurements	3-19
	3.4.5 Accelerometers	3-20
	3.4.6 Wing Static Pressure Measurements	3-20
	3.4.7 Miscellaneous Instrumentation	3-21
	3.5 Static Flexibility Data	3-23
	3.6 Dynamic Vibration Data	3-23
	3.7 Control Surface Actuation Characteristics	3-48
4.0	WIND TUNNEL TESTS, PROCEDURES, FACILITIES, AND EQUIPMENT	4-1
	4.1 Wind Tunnel Tests	4-1
	4.2 Wind Tunnel Test Procedures	4-3
	4.3 Facilities	4-4
	4.4 Equipment	4-4

## CONTENTS

Section		Page
5.0	STATIC AEROELASTIC DATA AND ANALYTICAL CORRELATION	5-1
	5.1 Model Force and Moment Data	5-1
	5.1.1 Data Acquisition and Processing	5-1
	5.1.2 Test Envelope	5-2
	5.1.3 Test Data and Analysis Correlation	5-2
	5.2 Model Pressure Data and CFD-Aeroelastic Calculations	5-17
	5.2.1 CFD-Aeroelastic Calculations	5-32
	5.3 Wing Deflection Calculations	5-37
	5.4 Static Aeroelastic Data Conclusions	5-37
6.0	ACTIVE CONTROL SYSTEMS DESIGN AND TESTS	6-1
	6.1 Roll Control Design and Tests	6-1
	6.1.1 Roll Trim System	6-1
	6.1.2 Roll Control System Design and Implementation	6-3
	6.1.3 Roll Control System Test	6-8
	6.1.4 Roll Control Design and Test Conclusion	6-22
	6.2 Maneuver Load Control Design and Test	6-23
	6.2.1 MLC Using Camber Schedules	6-23
	6.2.2 Test Results of MLC Using Camber Schedules	6-27
	6.2.3 MLC Using Strain Gage Feedback (SGF)	6-27
	6.2.4 Test Results of MLC Strain Gage Feedback	6-31
	6.2.5 MLC Design and Test Conclusion	6-34
	6.3 Structural Mode Control (SMC) System Design and Tests	6-40
	6.3.1 SMC Control Law Development	6-40
	6.3.2 SMC Analysis and Comparison with Test Results	6-49
	6.3.3 SMC System Conclusions	6-60
7.0	EVALUATION OF AFW TECHNOLOGY AND CONCLUSIONS	7-1
	7.1 Model Scaling to Full-Scale	7-1
	7.2 Recommendations for Future Research	7-3
	7.3 Conclusions	7-3
APPENDIX	MEASURED PRESSURE DATA COMPARISON	A-1

# ILLUSTRATIONS

Figure	Title	Page
1-1	Potential Payoff of Active, Flexible, Adaptive Wing Technology. . . . .	1-2
1-2	Low Speed Wind Tunnel Model Test Configuration. . . . .	1-4
2-1	AFW Aeroelastic Tailoring Challenge . . . . .	2-2
2-2	Aircraft Configuration Panel Geometry . . . . .	2-4
2-3	Control Surface Deflections (Max. Roll Rate $M = 1.2$ at S.L.). . . . .	2-6
2-4	Summary of Designs for Aerodynamics and Control Effectiveness Studies. . . . .	2-7
2-5	Flexibility Effects on Transonic Maneuver Drag Due to Lift - 7 g's. . . . .	2-10
2-6	Flexibility Effects on Supersonic Drag Due to Lift . . . . .	2-10
2-7	Reduced TOGW Payoff of AFW Technology . . . . .	2-11
3-1	AFW Model (0.1667-Inch) Installed in the Langley Research Center 16-Foot TDT. . . . .	3-2
3-2	General Arrangement . . . . .	3-3
3-3	AFW Technology Wind Tunnel Model - Side And Top Views. . . . .	3-6
3-4	Wing Box/Fairing Control Surface Design . . . . .	3-7
3-5	Control Surface/Actuator Attachment Design. . . . .	3-8
3-6	Hydraulic System Schematic. . . . .	3-10
3-7	Rotary Vane Actuator. . . . .	3-12
3-8	Static Control Console and Junction Boxes . . . . .	3-13
3-9	Dynamic Wind Tunnel Model Digital Controller. . . . .	3-14
3-10	Dynamic Wind Tunnel Model Instrumentation . . . . .	3-15
3-11	Wing Spar Strain Gage Bridge Locations. . . . .	3-17
3-12	Model SIC Test Setup. . . . .	3-24
3-13	Location of Model Deflection Measurements . . . . .	3-25/3-27
3-14	Test SIC Plot - Symmetric - Point 9 . . . . .	3-28
3-15	Test SIC Plot - Symmetric - Point 42. . . . .	3-29
3-16	Test SIC Plot - Antisymmetric - Point 9 . . . . .	3-30
3-17	Test SIC Plot - Antisymmetric - Point 42. . . . .	3-31
3-18	Exploded View of MSC/NASTRAN Finite Element Model . . . . .	3-33
3-19	GVT Setup in Wind Tunnel. . . . .	3-34
3-20	Mode 1, A/S Measured Modes in Laboratory. . . . .	3-38
3-21	Mode 2, A/S Measured Modes in Laboratory. . . . .	3-39
3-22	Mode 3, A/S Measured Modes in Laboratory. . . . .	3-40
3-23	Mode 4, A/S Measured Modes in Laboratory. . . . .	3-41
3-24	Mode 5, A/S Measured Modes in Laboratory. . . . .	3-42
3-25	Mode 1, Symmetric Measured Modes in Laboratory. . . . .	3-43
3-26	Mode 2, Symmetric Measured Modes in Laboratory. . . . .	3-44
3-27	Mode 3, Symmetric Measured Modes in Laboratory. . . . .	3-45
3-28	Mode 4, Symmetric Measured Modes in Laboratory. . . . .	3-46
3-29	Mode 5, Symmetric Measured Modes in Laboratory. . . . .	3-47

# ILLUSTRATIONS

Figure	Title	Page
3-30	Response of RTEO at Mach 0, $q = 0$ . . . . .	3-52
3-31	Response of LTEO at Mach 0, $q = 0$ . . . . .	3-53
3-32	Response of LTEI at Mach 0, $q = 0$ . . . . .	3-54
3-33	Response of RTEI at Mach 0, $q = 0$ . . . . .	3-55
3-34	Response of LLEO at Mach 0, $q = 0$ . . . . .	3-56
3-35	Response of RLEO at Mach 0, $q = 0$ . . . . .	3-57
3-36	Response of RLEI at Mach 0, $q = 0$ . . . . .	3-58
3-37	Response of LLEI at Mach 0, $q = 0$ . . . . .	3-59
3-38	Typical Step Response for LLEI, LLEO, LTEO, RLEI, RTEI, and RTEO Actuation Systems . . . . .	3-60
4-1	Model Test Envelope . . . . .	4-2
5-1	Test Envelope . . . . .	5-3
5-2	Test - Theory Comparisons of $C_{L\alpha}$ versus $q$ - First Wind Tunnel Entry. . . . .	5-4
5-3	Test - Theory Comparisons of $C_{M\alpha}$ versus $q$ . . . . .	5-6
5-4	Test - Theory Comparisons of $C_{\delta LEI}$ versus $q$ . . . . .	5-7
5-5	Test - Theory Comparisons of $C_{\delta LEO}$ versus $q$ . . . . .	5-8
5-6	Test - Theory Comparisons of $C_{\delta TEI}$ versus $q$ . . . . .	5-9
5-7	Test - Theory Comparisons of $C_{\delta TEO}$ versus $q$ . . . . .	5-10
5-8	Effect on Angle-of-Attack on $C_{\delta LEO}$ , $M = 0.9$ . . . . .	5-11
5-9	Effect on Angle-of-Attack on $C_{\delta LEO}$ , $M = 1.15$ . . . . .	5-12
5-10	Effect on Angle-of-Attack on $C_{\delta TEO}$ , $M = 0.9$ . . . . .	5-13
5-11	Effect on Angle-of-Attack on $C_{\delta TEO}$ , $M = 1.15$ . . . . .	5-14
5-12	Effect on Angle-of-Attack on $C_{\delta TEI}$ , $M = 0.9$ . . . . .	5-15
5-13	Effect on Angle-of-Attack on $C_{\delta TEI}$ , $M = 1.15$ . . . . .	5-16
5-14	Variation of $C_L$ , $C_M$ , $C_q$ with $\delta$ (LEI). . . . .	5-18
5-15	Variation of $C_L$ , $C_M$ , $C_q$ with $\delta$ (LEO). . . . .	5-19
5-16	Variation of $C_L$ , $C_M$ , $C_q$ with $\delta$ (TEI). . . . .	5-20
5-17	Variation of $C_L$ , $C_M$ , $C_q$ with $\delta$ (TEO). . . . .	5-21
5-18	AFW Wind Tunnel Test Results - Super Position; Lift and Pitching Moment LEI and LEO. . . . .	5-22
5-19	AFW Wind Tunnel Test Results - Super Position; Lift and Pitching Moment TEI and TEO. . . . .	5-23
5-20	AFW Wind Tunnel Test Results - Super Position - Rolling Moment TEI and TEO . . . . .	5-24
5-21	Variation of $C_{h\alpha} = 0$ (TEO) with Dynamic Pressure. . . . .	5-25

## ILLUSTRATIONS

Figure	Title	Page
5-22	Variation of $C_{h\alpha} = 0$ (at TEO) with Dynamic Pressure . . . . .	5-26
5-23	Variation of $C_{h\delta LEI}$ (at LEI) with Dynamic Pressure . . . . .	5-27
5-24	Variation of Bending and Torsional Moments with $\delta$ (Leading Edge Inboard) . . . . .	5-28
5-25	Variation of Bending and Torsional Moments with $\delta$ (Leading Edge Outboard). . . . .	5-29
5-26	Variation of Bending and Torsional Moments with $\delta$ (Trailing Edge Inboard). . . . .	5-30
5-27	Variation of Bending and Torsional Moments with $\delta$ (Trailing Edge Outboard) . . . . .	5-31
5-28	AFW Wing Configuration with Control Surfaces - Body Region has Been Modified. . . . .	5-33
5-29	Computational Grid with Leading Edge and Trailing Edge Control Surfaces Deflected. . . . .	5-34
5-30	Roll Coefficient versus Q for the Trailing edge Outboard Control Surface Deflection at $M = 0.9$ . . . . .	5-38
5-31	Roll Coefficient versus Q for the Trailing edge Inboard Control Surface Deflection at $M = 0.9$ . . . . .	5-39
5-32	Roll Coefficient versus Q for the Trailing edge Outboard Control Surface Deflection at $M = 1.15$ . . . . .	5-40
5-33	Roll Coefficient versus Q for the Trailing edge Inboard Control Surface Deflection at $M = 1.15$ . . . . .	5-41
5-34	Wing Deflections Calculated from Test Data $M = 0.9$ , $q = 150$ psf, $\alpha = 0$ , $TEO = +50^\circ$ . . . . .	5-42
5-35	Wing Deflections Calculated from Test Data $M = 0.9$ , $q = 150$ psf, $\alpha = 0$ , $TEO = -50^\circ$ . . . . .	5-43
5-36	Wing Deflections Calculated from Test Data $M = 1.15$ , $q = 340$ psf, $\alpha = 1.50^\circ$ . . . . .	5-44
5-37	Wing Deflections Calculated from Test Data $M = 1.15$ , $q = 340$ psf, $\alpha = 1.50^\circ$ , $TEO = -20^\circ$ . . . . .	5-45
5-38	Wing Deflections Calculated from Test Data $M = 0.9$ , $q = 150$ psf, $\alpha = 0$ , $TEI = 2.75^\circ$ , $TEO = 3.50^\circ$ . . . . .	5-46
5-39	Wing Deflections Calculated from Test Data $M = 0.9$ , $q = 250$ psf, $\alpha = 0$ , $TEO = -2.50^\circ$ , $TEI = 1.25^\circ$ . . . . .	5-47
5-40	Wing Deflections Calculated from Test Data $M = 1.15$ , $q = 340$ psf, $\alpha = 1.50^\circ$ , $TEO = -2.50^\circ$ , $TEI = -1.25^\circ$ , $TEO = -30^\circ$ . . . . .	5-48
6-1	Basic Trim Mechanization . . . . .	6-4
6-2	Basic Roll control Mechanization . . . . .	6-5
6-3	Completed Steady State Roll Rate ( $P_{SS}$ ) vs Dynamic Pressure for $M = 0.9$ . . . . .	6-6
6-4	Percent of Total Steady State Roll Rate vs Dynamic Pressure at $M = 0.9$ . . . . .	6-6
6-5	Wing Locations for Bending and Torsional Moment Data . . . . .	6-8

## ILLUSTRATIONS

Figure	Title	Page
6-6	Test Setup for Frequency Domain Testing . . . . .	6-9
6-7	Bode Plot of the Roll Controller Comparing Test Results and Analytical Predictions . . . . .	6-11
6-8	Correlation of Bode Plots for Three Test Methods . . . . .	6-12
6-9	Progressive Pseudo-Stick Ramps Used Roll System Tests	6-14
6-10	Validation of Roll Gyro Output Using Manually Oscillated Wind-Off Model . . . . .	6-15
6-11	Typical Tunnel Time History for Maximum Roll Input . . . . .	6-17
6-12	Roll Performance Summary . . . . .	6-18
6-13	Rolling Moment vs Dynamic Pressure for Mach = 1.15 . . . . .	6-19
6-14	Effect of Camber on Wing Loads . . . . .	6-21
6-15	Location of Strain Gages, Left Wing Only Shown . . . . .	6-24
6-16	Simple Control System for MLC Utilizing Camber Schedules . . . . .	6-25
6-17	Original Camber Schedules and Maneuver Load Control Camber Schedules to Limit Wing Root Bending Moment . . . . .	6-26
6-18	Utilizing Camber Schedules to Reduce the Wing Root Bending Moment, Analytical and Test Results . . . . .	6-28
6-19	Test Results for a Step Command Show a Significant Reduction in Bending Moment ( $M = 0.9$ , $q = 35$ psf) . . . . .	6-29
6-20	Rockwell's Design Process for Developing the SGF Maneuver Load Controller . . . . .	6-30
6-21	Maneuver Load Control System Utilizing Strain Gage Feedback . . . . .	6-32
6-22	Multiple Methods Used to Measure Open Loop Frequency Response . . . . .	6-32
6-23	Comparison Between Three Methods of Obtaining the Open Loop Frequency Response . . . . .	6-33
6-24	Comparison Between Analytical Modeling and Test Results . . . . .	6-33
6-25	Reduction of Maximum Bending Moment During Ramp and Step Response ( $M = 0.9$ , $q = 35$ psf). . . . .	6-35
6-26	Reduction of Maximum Bending Moment During Ramp and Step Response ( $M = 0.9$ , $q = 100$ psf) . . . . .	6-36
6-27	Nonlinear Aerodynamic Model Showing Reduction of Maximum Bending Moment During Ramp and Step Reponse ( $M = 0.9$ , $q = 35$ psf). . . . .	6-37
6-28	Nonlinear Aerodynamic Model Showing Reduction of Maximum Bending Moment During Ramp and Step Reponse ( $M = 0.9$ , $q = 100$ psf) . . . . .	6-37
6-29	Structural Modal Model Showing Reduction of Maximum Bending Moment During Ramp and Step Responses ( $M = 0.9$ , $q = 35$ psf) . . . . .	6-38
6-30	Structural Modal Model Showing Reduction of Maximum Bending Moment During Ramp and Step Responses ( $M = 0.9$ , $q = 100$ psf) . . . . .	6-38
6-31	Static and Dynamic Reductions of Wing Root Bending Moment Achieved Using the SGF MLC System for Test and Analysis . . . . .	6-39

## ILLUSTRATIONS

Figure	Title	Page
6-32	Generalized Schematic of Structural Mode Control Systems for AFW Model . . . . .	6-41
6-33	Analytical Accelerometer Load Factor Calculations . . . . .	6-42
6-34	AFW Model Control Surfaces and Companion Accelerometer Locations . . . . .	6-44
6-35	Normal Load Factor at Trailing Edge Outboard Control Surface due to TEO Deflections . . . . .	6-45
6-36	Bode Plot of Basic Plant for Symmetric TEO AFW Model Structural Mode Control Systems, $M = 1.15$ , $q = 225$ psf . . . . .	6-46
6-37	Bode Plot of Basic Plant plus Actuator with Preassigned Filters for Symmetric TEO AFW Model Structural Mode Control System, $M = 1.15$ , $q = 225$ psf . . . . .	6-47
6-38	Bode Plot of Basic Plant with Total Compensation Included for Symmetric TEO AFW Model Structural Mode Control System, $M = 1.15$ , $q = 225$ psf . . . . .	6-48
6-39	AFW Model Power Spectral Density Plot for Symmetric TEO Basic and Closed Loop SMC System, $M = 1.15$ , $q = 225$ psf - Basic RMS = 22.388, SMC on RMS = 14.388 . . . . .	6-50
6-40	Normal Load Factor at Control Surface due to Deflection . . . . .	6-52
6-41	Normal Load Factor at Control Surface due to Deflection . . . . .	6-53
6-42	Normal Load Factor at Control Surface due to Deflection - Basic Open Loop . . . . .	6-54
6-43	Normal Load Factor at Control Surface due to Deflection - Basic Open Loop . . . . .	6-55
6-44	Bode Plot of Basic Plant for Symmetric TEO Structural Mode Control System, Analytical Results vs Test, $M = 1.15$ , $q = 225$ psf . . . . .	6-56
6-45	Bode Plot of Basic Plant for Antisymmetric TEO Structural Mode Control System, Analytical Results vs Test, $M = 1.15$ , $q = 225$ psf . . . . .	6-57
6-46	Bode Plot of Basic Plant for Symmetric TEI Structural Mode Control System, Analytical Results vs Test, $M = 1.15$ , $q = 225$ psf . . . . .	6-58
6-47	Bode Plot of Basic Plant for Antisymmetric TEI Structural Mode Control System, Analytical Results vs Test, $M = 1.15$ , $q = 225$ psf . . . . .	6-59
6-48	Bode Plot of Symmetric Normal Load Factor at TEO due to TEI Deflection, $M = 1.15$ , $q = 225$ psf . . . . .	6-61
6-49	Bode Plot of Symmetric Normal Load Factor at TEI due to TEO Deflection, $M = 1.15$ , $q = 225$ psf . . . . .	6-62
6-50	Bode Plot of Basic Plant for Symmetric TEI Structural Mode Control System, Analytical Results vs Test, $M = 0.9$ , $q = 250$ psf . . . . .	6-63
7-1	Model - Full-Scale Aircraft Correlation . . . . .	7-2

TABLES

Table	Title	Page
2-1	Effects on Actuator Requirements . . . . .	2-8
3-1	AFW Dynamics Model Scale Factors . . . . .	3-4
3-2	Strain Gage Bridge Locations . . . . .	3-16
3-3	Hydraulic Supply Pressure Measurements . . . . .	3-18
3-4	Control Surface Differential Pressures . . . . .	3-19
3-5	Control Surface Deflection Measurements . . . . .	3-19
3-6	Accelerometer Locations . . . . .	3-20
3-7	Left-Hand Wing Pressure Orifice Locations . . . . .	3-21
3-8	Scanivalve Hookup . . . . .	3-22
3-9	SIC's Connected by Common Line in Figures 3-14 Through 3-17 . . . . .	3-32
3-10	Ground Vibration Test and Measured Generalized Mass Results . . . . .	3-37
3-11	Ground Vibration Test Control Surface Rotation Modes . . .	3-49
3-12	Summary of Frequency Response Tests of ATW Wind Tunnel Model at Langley With and Without Air Loads . . . .	3-51
5-1	Aerodynamic Forces with Control Surface Deflection For $M_{\infty} = 0.9$ and $\alpha = 0.0$ . . . . .	5-35
5-2	Aerodynamic Forces with Control Surface Deflection For $M_{\infty} = 1.15$ and $\alpha = 0.0$ . . . . .	5-36
5-3	Aerodynamic Forces with Control Surface Deflection For $M_{\infty} = 1.15$ and $\alpha = 1.66$ . . . . .	5-36
6-1	Roll Control Effector Selection and Roll Rate Feedback Gains . . . . .	6-7
6-2	Wind Tunnel Gain and Phase Margins . . . . .	6-11
6-3	Gain and Phase Margin Summary . . . . .	6-12
6-4	Roll Control Effector Selection and Roll Rate Feedback Gains . . . . .	6-18
6-5	Correlation of Analytic Predictions and Wind Tunnel Final Test Results . . . . .	6-22
6-6	Both Ramp and Step Responses Show a Significant Reduction in Bending Moment ( $M_n = 0.9$ , $q = 35$ psf) . . . .	6-29
6-7	MLC Analytical Design Requirements . . . . .	6-30
6-8	Comparison of Analytical and Test $f_n$ and Phase Margins for the SGF MLC System . . . . .	6-34
6-9	Structural Mode Control Law Summary . . . . .	6-51

## 1.0 INTRODUCTION AND SUMMARY

### 1.1 INTRODUCTION

Current aircraft controllability investigations at Rockwell International are developing a technology area which promises significant improvements in size, performance, and controllability for future aircraft. This technology, of special interest to systems requiring high maneuverability, will combine aerodynamics, structures, and flight control sciences to produce an integrated configuration of superior capabilities.

Active flexible wing, (AFW) technology integrates active controls technology with a flexible structure on an advanced aerodynamic wing design to produce enhanced aerodynamic performance and control. The concept uses an innovative solution to the wing roll control (aileron reversal) problem encountered in the design of most modern aircraft (both low-aspect-ratio, high-performance aircraft, and high-aspect-ratio transport aircraft). The solution uses active leading and trailing edge control surfaces on a flexible wing structure to control structural deflections, resulting in optimal roll control effectiveness. Solving the roll control problem without the requirement for high stiffness and accompanying weight results in a flexible structure which also lends itself to aeroelastic tailoring for twist control to improve aerodynamic performance. This is beneficial in achieving the multipoint aerodynamic performance goals required on next-generation fighter aircraft. In addition, control system mechanization requirements (actuator size and power) are reduced because of the optimized control effectiveness design.

Initially, Rockwell developed the AFW concept by conducting a conceptual design study for an advanced fighter wing. The study determined that a significant reduction in aircraft takeoff gross weight could be obtained using the technology.

Figure 1-1 shows the potential payoff of AFW technology in terms of takeoff gross weight (TOGW) changes possible with increasing wing flexibility. Associated technologies required for the various degrees of flexibility are indicated. The basepoint is a conventional fighter aircraft design with a rolling tail to aid in roll performance. The figure shows the large increase in aircraft TOGW to maintain rolling performance with a conventional stiff wing design when the rolling tail is removed. The AFW roll control solution with a flexible wing results in greatly reduced TOGW by reducing wing weight and increasing aircraft performance with the rolling tail removed. TOGW can be further reduced by using active control technologies such as maneuver load control and flutter suppression, which permit greater wing flexibility in later phases of technology development. Figure 1-1 was generated from data presented in Section 2.0 of this document.

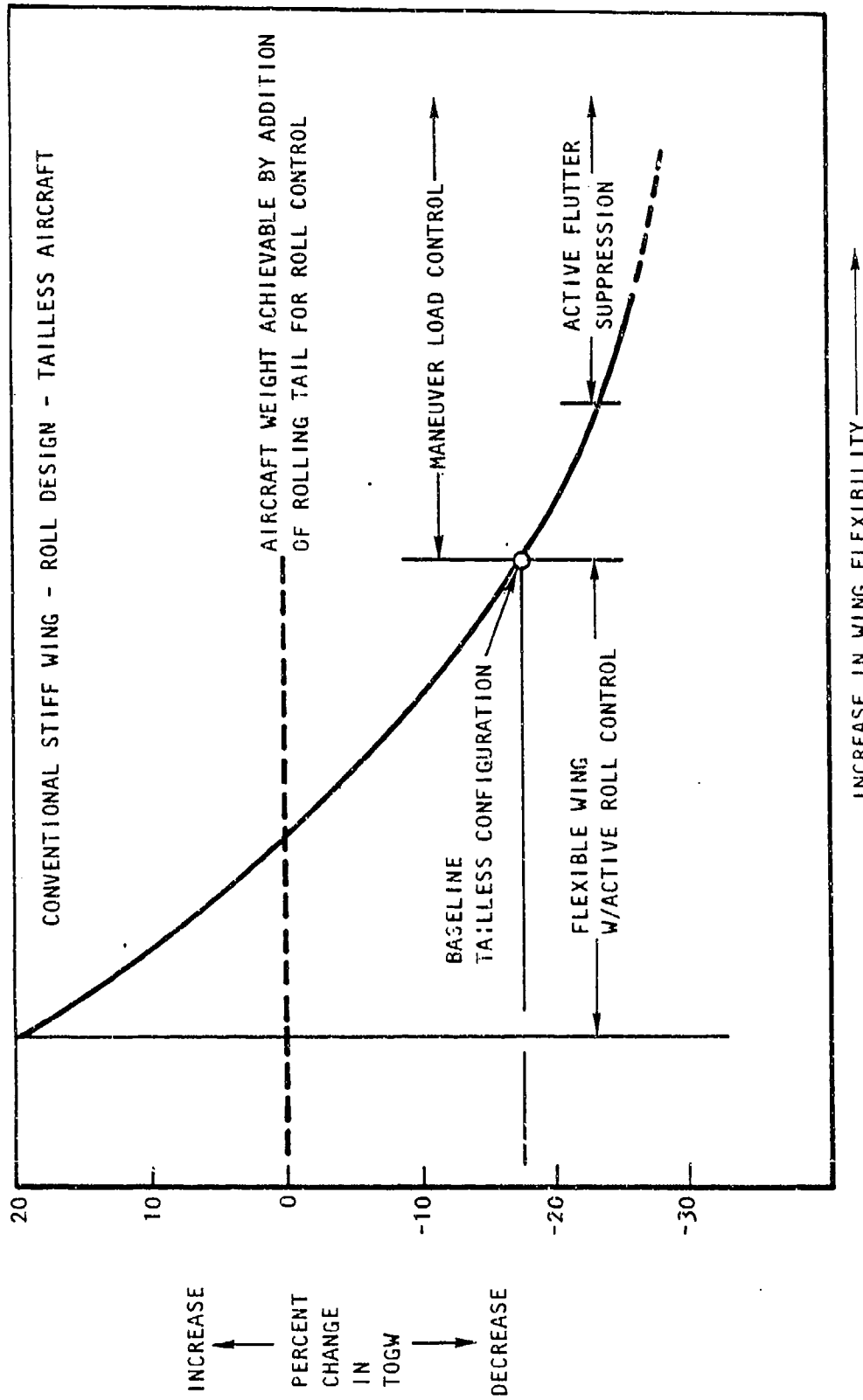


Figure 1-1. Potential Payoff of Active, Flexible, Adaptive Wing Technology

To obtain early verification of the flexible wing control power predicted by the AFW concept, Rockwell designed, built, and tested an aeroelastically scaled static wind tunnel model. Figure 1-2 shows the model in the Rockwell low speed wind tunnel. This wind tunnel test verification along with the conceptual design study proved that the AFW concept was workable and would provide improved performance.

Rockwell designed and built an actively controlled, statically and dynamically scaled, full-span wind tunnel model that was free to roll to evaluate transonic and dynamic effects. This model was designed for testing in the NASA Langley 16-foot transonic dynamics tunnel (TDT). The model would provide test data for both static, transonic aeroelastic control effectiveness and active control results. Rockwell also designed active control laws to control the model during free-to-roll wind tunnel tests.

Under contract to the Air Force, the transonic wind tunnel model was characterized and wind tunnel tests were conducted in two separate tunnel entries in Feb-Mar 1986 and Mar-Apr 1987. The first wind tunnel entry was primarily used to obtain static aeroelastic data. The second wind tunnel entry was primarily used to conduct active control tests which verified the Rockwell developed active control laws.

## 1.2 SUMMARY

This report documents the results of the transonic, active control wind tunnel model program. Additionally, Section 2.0 describes the AFW concept and an estimate of its benefits.

The wind tunnel model along with its physical characteristics (flexibility, vibration modes, and control system transfer functions) are described in Section 3.0. Section 4.0 describes the wind tunnel test procedures.

The results of the static aeroelastic test data along with a comparison of analytical results are shown in Section 5.0. These results validated the flexible control power that was predicted and verified that analytical tools can be used for design.

Section 6.0 presents the results of Rockwell's active control system designs and the contracted wind tunnel tests. Roll control, maneuver load control, and structural mode control designs were developed and tested. The tests verified the active control laws as well as the design methods.

Section 7.0 presents a view of the test results relative to full-scale aircraft, a final assessment of the technology, recommendations for future research and conclusions.

## 2.0 DESCRIPTION OF ACTIVE FLEXIBLE WING (AFW) TECHNOLOGY

AFW technology integrates active control technology with a flexible structure on an advanced aerodynamic wing design to produce enhanced aerodynamic performance and control. The concept uses an innovative solution to the wing roll control (aileron reversal) problem encountered in the design of most modern aircraft (both low-aspect-ratio, high-performance aircraft, and high-aspect-ratio transport aircraft). The solution uses active leading and trailing edge control surfaces on a flexible wing structure to control structural deflections, resulting in optimal roll control effectiveness. Solving the roll control problem without the requirement for high stiffness and accompanying weight results in a flexible structure which also lends itself to aeroelastic tailoring for twist control to improve aerodynamic performance. This is beneficial in achieving the multipoint aerodynamic performance goals required on the next-generation fighter aircraft. In addition, control system mechanization requirements (actuator size and power) are reduced as a result of the optimized control effectiveness design.

### 2.1 BACKGROUND OF THE CONCEPT

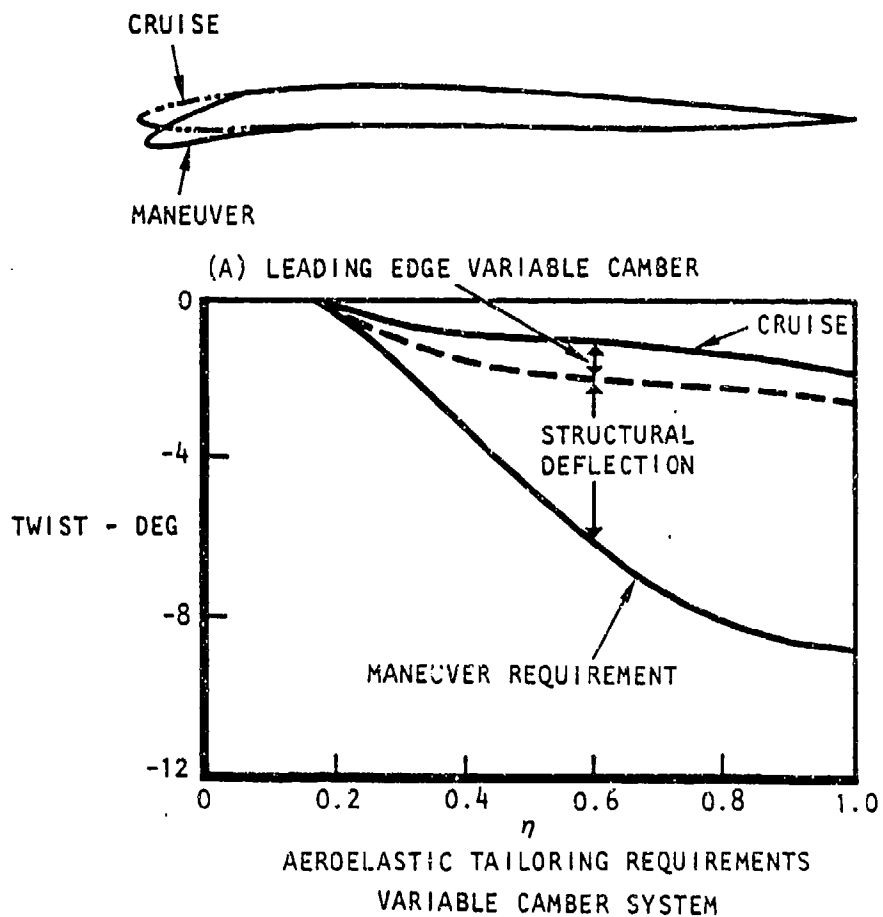
#### 2.1.1 WING DESIGN CHALLENGE

A goal of advanced fighter aircraft design is to provide enhanced performance at several design points (subsonic, transonic, and supersonic). The most significant means to provide improved performance is through the use of a variable twist wing by using variable camber and aeroelastic tailoring. Figure 2-1 illustrates the differential twist required between a cruise and maneuver design of the HiMAT vehicle. The amount that can be realized from variable leading edge camber is shown; the remainder would come from aeroelastic twist.

To obtain the large amount of aeroelastic twist desired between the cruise and maneuver points has always been a design challenge. The wing structure must meet strength and also stiffness constraints such as flutter. Also, high-performance fighter aircraft with aft-swept wings have typically required stiffness increases above strength and flutter design to maintain roll effectiveness. This added stiffness for roll control results in a wing so stiff that its capability to twist under load is almost completely lost, thus reducing the multipoint performance capability of the aircraft. In addition to the reduced performance, the increase in structure associated with the added stiffness represents a significant increase in aircraft weight and resultant size.

The roll control problem on high-performance aircraft results from the aeroelastic twist caused by trailing edge control surface deflections. Control surface deflections produce a lift on the wing which results in rolling moment. Since, the wing is flexible, however, the increase in lift

# HIMAT EXPERIENCE



Note: Aeroelastic Twist Control to Improve Multipoint Aerodynamic Performance

Figure 2-1. AFW Aeroelastic Tailoring Challenge

causes the wing to twist in a direction to reduce the lift. At very high dynamic pressure ( $q$ ) flight conditions, flexibility causes control surface effectiveness that is very small compared with the rigid-wing values. In fact, the effect results in roll reversal at high  $q$ 's. This effect is known as aileron reversal. To prevent aileron reversal, the wing is traditionally stiffened so that conventional control effectiveness are maintained through the aircraft flight envelope. Not only does this result in a heavier structure, but because of the lower roll control effectivenesses, larger control surface deflections are needed to maintain roll rates. This increases actuation requirements thus adding to aircraft weight and system power requirements.

Other fighter aircraft designs, such as the F-15 and F-16, have solved the roll control problem by adding a rolling tail. The resulting larger tail surface, however, adds significant weight to the aircraft and increases supersonic drag thereby reducing aircraft performance. For the advanced fighter design, Rockwell selected a tailless configuration to obtain an improved supersonic persistence capability.

The use of leading edge control surfaces to aid trailing edge surfaces in producing roll has also been used on existing aircraft designs. The F-18 is an example of the use of combined leading and trailing edge control surfaces. Leading edge control surfaces are typically ineffective in producing rolling forces on a rigid or stiff wing, therefore producing only a small amount of the total rolling force required. When the trailing edge control surfaces are constrained to maintain conventional roll control (no aileron reversal) within the flight envelope, the wing must be relatively stiff which results in low leading edge roll control effectiveness. If however, the wing flexibility is maintained near a strength/flutter stiffness boundary, the leading edge control effectiveness is significantly increased at high dynamic pressures.

#### 2.1.2 AFW TECHNOLOGY APPROACH TO PROBLEM

The AFW concept for roll control uses active control technology in a new and innovative approach. The control surfaces are not used as primary control force-producing devices but are used as aerodynamic tabs to control the aeroelastic deformations of the wing. It is the total wing deformations that are used to produce controlling forces.

The AFW concept uses multiple leading and trailing edge control surfaces on the wing. The control surface deflections are optimized as a set to produce the most efficient control at a given flight condition. On a flexible wing this allows use of the surfaces beyond the dynamic pressure where conventional aileron reversal begins. A design case was developed analytically on the configuration in Figure 2-2, which shows the aerodynamic paneling on one of Rockwell's advanced fighter configurations. The wing design was relatively flexible but satisfied strength and flutter design requirements. Four control surfaces on each wing and the body flap were used

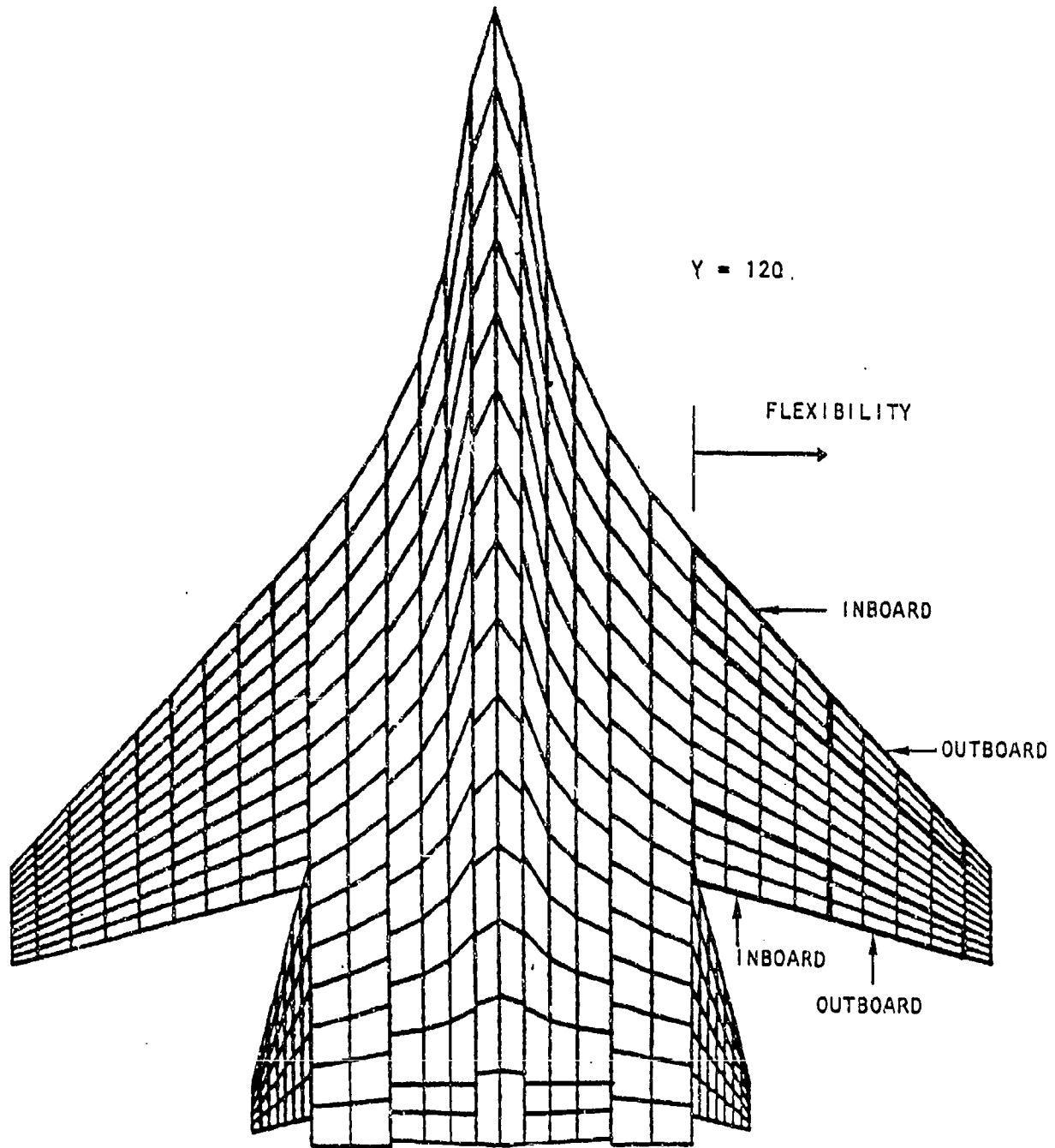


Figure 2-2. Aircraft Configuration Panel Geometry

to produce efficient roll control (minimizing the drag while producing required rolling moments). A 100-degree-per-second roll rate was desired at dynamic pressures ranging from 0 to 2,150 psf ( $M = 1.2$  at sea level). An optimization program was used to determine the optimum control surface deflections to achieve the roll rate for minimum drag. Figure 2-3 illustrates the results of this study. The control surface deflections necessary to maintain a 66-degree-per-second steady-state roll versus dynamic pressure at  $M = 1.2$  are shown. Note that the trailing edge control surface deflections reversed as the dynamic pressure increased. The control surfaces were used beyond conventional aileron reversal. Also, note that the maximum deflection of any control surface was never more than 5 degrees. Typical trailing control surface deflections on a conventional "stiff" wing design were in the range of 30 to 40 degrees to maintain this same roll rate. Thus, the AFW roll control concept resulted in much lower drag during a maneuver than with a conventional design. Also, because of the smaller control surface deflections, the surface hinge moments were reduced resulting in smaller, lighter, and lower power actuators.

In addition to the benefits from the AFW roll control approach, other technologies can be applied. The use of other active control technologies such as maneuver load control (MLC), gust load alleviation, flutter suppression, etc., were used to further reduce wing weight and stiffness. This reduction in stiffness resulted in improvements in overall aerodynamic performance. The overall Rockwell approach for the application of AFW technology used active controls in other modes to reduce strength and stiffness design requirements to practical minimums. The goal was to obtain a wing that was designed by passive clean-wing flutter requirements. Thus, MLC and gust load alleviation were used to reduce strength requirements, and active roll and structure mode controls were used to reduce stiffness requirements.

## 2.2 BENEFITS OF AFW TECHNOLOGY

The benefits of AFW technology were assessed by using data from a design feasibility study conducted by Rockwell previous to the contracted effort. The effects of structural and system weight and aerodynamic performance changes were studied with respect to the use of AFW technology.

Three structural wing designs were developed for the aircraft wing. A "stiff" wing was designed to determine the weight and stiffness of a wing with trailing edge roll effectiveness greater than zero at maximum dynamic pressure. An intermediate wing was designed to obtain the weight and stiffness of a wing without added stiffness for roll effectiveness. This wing satisfied strength, buckling, and flutter requirements. A third wing was designed to satisfy strength and flutter without the buckling or roll control requirements, which was assumed to simulate the effects of maneuver load control on the second design. Figure 2-4 summarizes the three designs in terms of weight and cover sizing. These three wing structural designs were

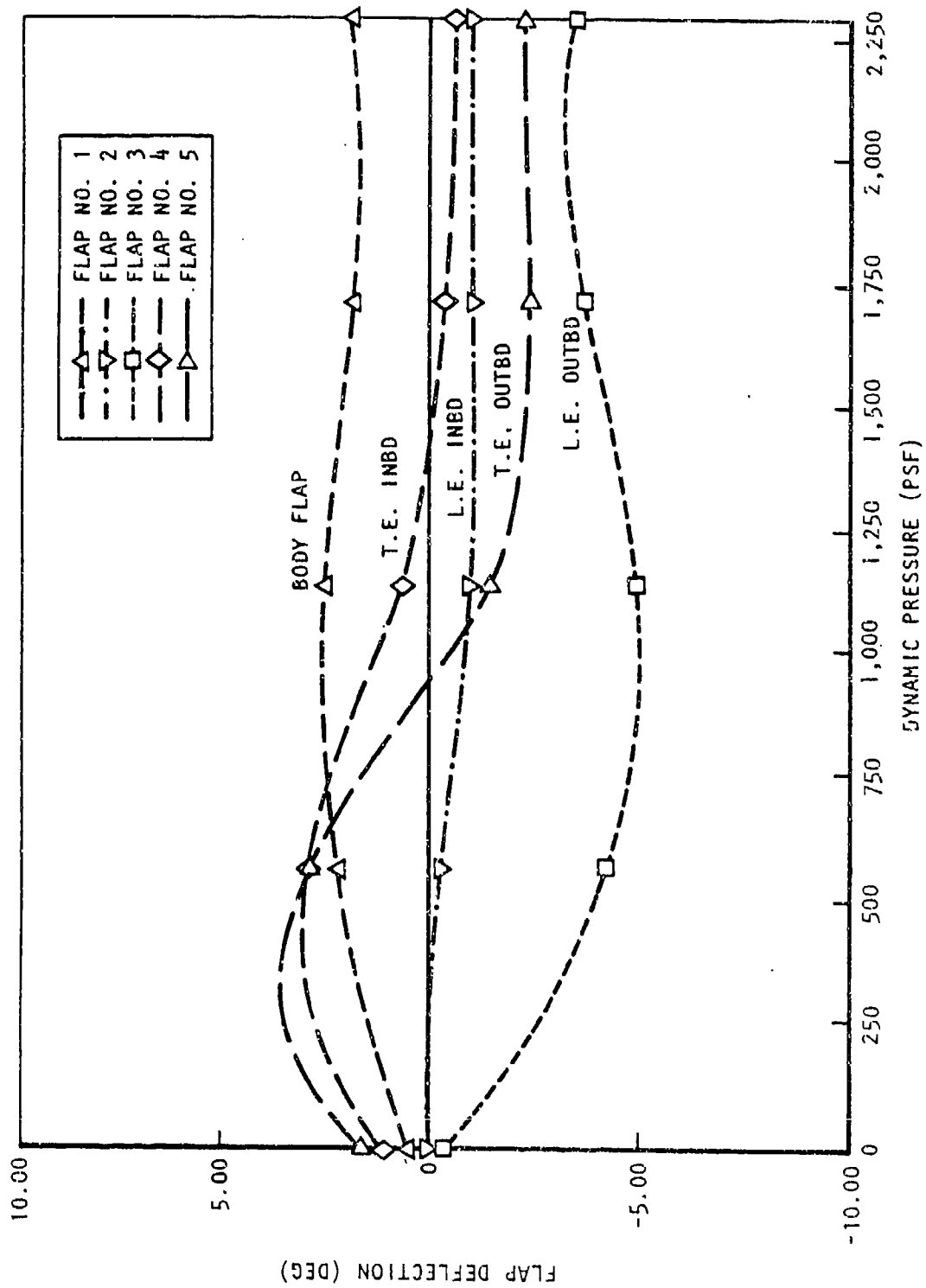


Figure 2-3. Control Surface Deflections (Max Roll  $M = 1.2$  at S.L.)

Design	Intermediate Spars	Structural Box Weight (Strength) (lb/side)	Structural Box Weight (Strength/Buckling) (lb/side)	Wing Skin Thickness (FEM Analysis)	
				Upper Cover	Lower Cover
Stiffness for roll effectiveness	6	1,545	1,545	0.27	0.27
				0.60	0.56
Strength, flutter, buckling	6	-	563	0.20	0.32
				0.20	0.50
Strength, flutter only	6	545	-	0.20	0.22
				0.20	0.38

Figure 2-4. Summary of designs for Aerodynamics and Control Effectiveness Studies

used in the control and aerodynamic feasibility studies. The control study used the intermediate wing design, and the aerodynamic study used all three designs to study performance versus flexibility.

Control power requirements were defined in terms of actuator hinge moment requirements. Table 2-1 presents the comparison of actuator weight and power requirements of the AFW concept relative to a conventional roll control concept using a wing structure design for strength including adequate stiffness to prevent control reversal. The results show that the leading edge surface actuator weight and power were not affected by the use of the AFW concept, but there was a significant reduction in trailing edge surface actuator weight and power. This reduction in actuator weight and power resulted from the reduced surface deflection requirements of the AFW control concept over a conventional approach. This study required the roll control system of each concept to apply the required surface deflections to meet the roll performance requirement of MIL-F-8785C. Required surface deflections were assumed at 80 percent of the actuator stall hinge moment value. Linear aerodynamic data estimated for the aircraft configuration and flex-to-rigid ratio estimates for each wing were applied for the roll control effectiveness and actuator hinge moment computations.

Table 2-1

EFFECTS ON ACTUATOR REQUIREMENTS

Control Surface	Baseline Wing Design With Stiffness			Active Flexible Adaptive Wing*		
	Hinge Moment Per Surf. (in-lb)	Actuator Weight (lb)	Hyd Power HP at Max Rate	Hinge Moment Per Surf. (in-lb)	Actuator Weight (lb)	Hyd Power at Max Rate
Inboard TE (2 per A/C)	0.99x10 <sup>6</sup>	176	132	0.172x10 <sup>6</sup>	19	14
Outboard TE (2 per A/C)	.49x10 <sup>6</sup>	80	39	.155x10 <sup>6</sup>	18	14
Inboard LE (2 per A/C)	.20x10 <sup>6</sup>	20	16	.172x10 <sup>6</sup>	19	14
Outboard LE (2 per A/C)	.18x10 <sup>6</sup>	19	14	.172x10 <sup>6</sup>	19	14
Total per A/C		590	402		150	224

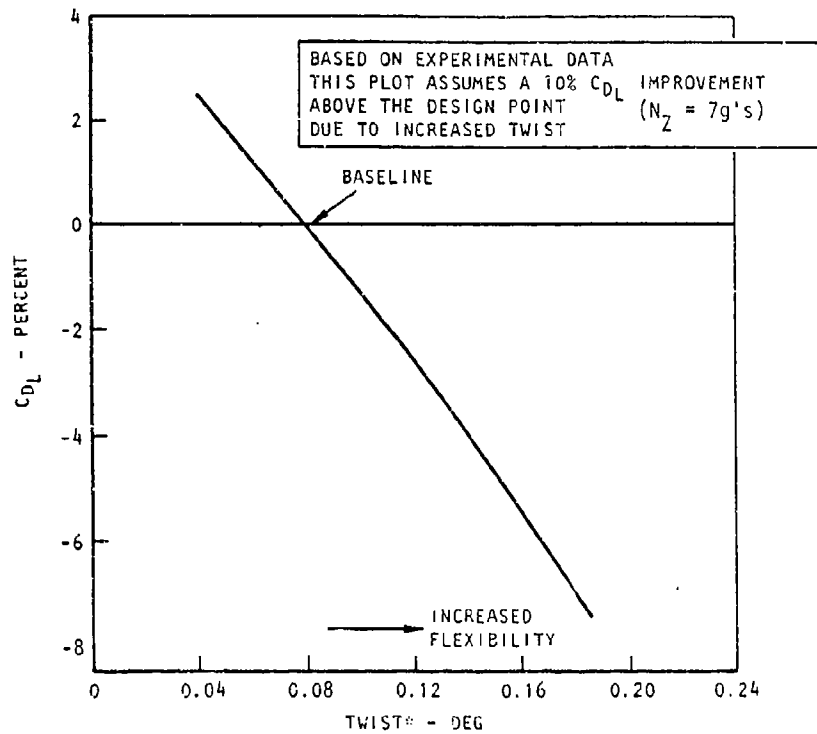
\*Flex-to-rigid Ratio (F/R): 0.18 for inboard TE, 0.90 for outboard TE surface.

The effect of wing flexibility on aerodynamic performance was studied using the three structural designs. Figure 2-5 presents the effect of wing flexibility on transonic drag-due-to-lift. The curve was generated from Rockwell's experimental data base. The effect of supersonic drag-due-to-lift was estimated using linear panel codes. Figure 2-6 presents this data.

The benefits of AFW technology in terms of aircraft take off gross weight (TOGW) reduction were estimated by using the structural and system weight changes from Figure 2-4 and Table 2-1 and the improvements in aerodynamic performance from Figures 2-5 and 2-6. The weights were subtracted from an empirical wing weight estimate for the configuration. These changes in weight were multiplied by the TOGW sensitivity factor for dead weight. The aerodynamic benefits were determined by subtracting the change in drag at a given flexibility from the estimated non-ATW flexibility, and multiplying the difference by the TOGW sensitivity factors for the associated transonic maneuver and supersonic maneuver and cruise drag changes.

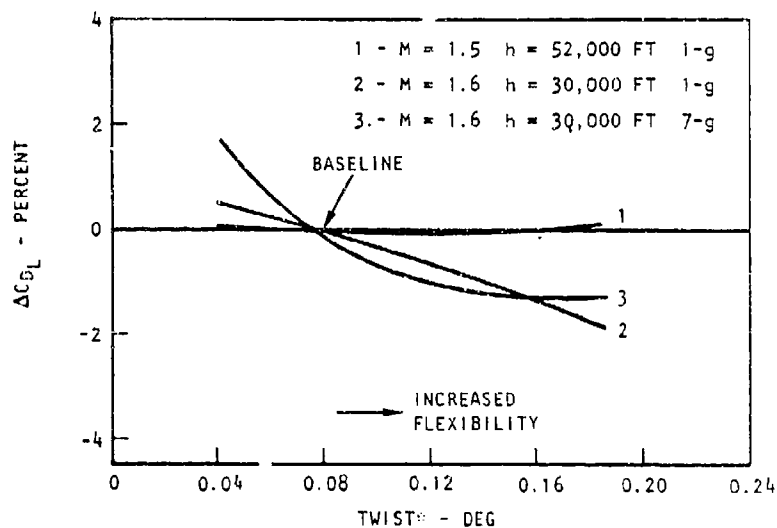
These TOGW results were then plotted versus wing flexibility as shown on Figure 2-7. Three points were plotted, [(1) stiff wing, (2) without MLC wing, and (3) with MLC wing] for both the structural and system weight effects and for the aerodynamic drag effects. The summation of the two effects was also plotted to obtain a total TOGW effect. The zero point on the TOGW axis on Figure 2-7 was calculated by using the empirical weight estimate for a similar, non-ATW aircraft with a rolling tail.

As seen on Figure 2-7, the estimated benefit of AFW technology is a reduction in TOGW of 15 to 30 percent for a constant performing aircraft. Conversely, the technology could be used to obtain significant performance improvements for a fixed TOGW aircraft design.



\*TWIST AT 80% SPAN DUE TO A 1<sup>o</sup> OUTBD TE DEFLECTION  
@ M = 0.9 h = 30K FT

Figure 2-5. Flexibility Effects on transonic Maneuver Drag Due to Lift - 7's



\*TWIST AT 80% SPAN DUE TO A 1<sup>o</sup> OUTBD TE DEFLECTION  
@ M = 0.9, h = 30K FT

Figure 2-6. Flexibility Effects on Supersonic Drag Due to Lift

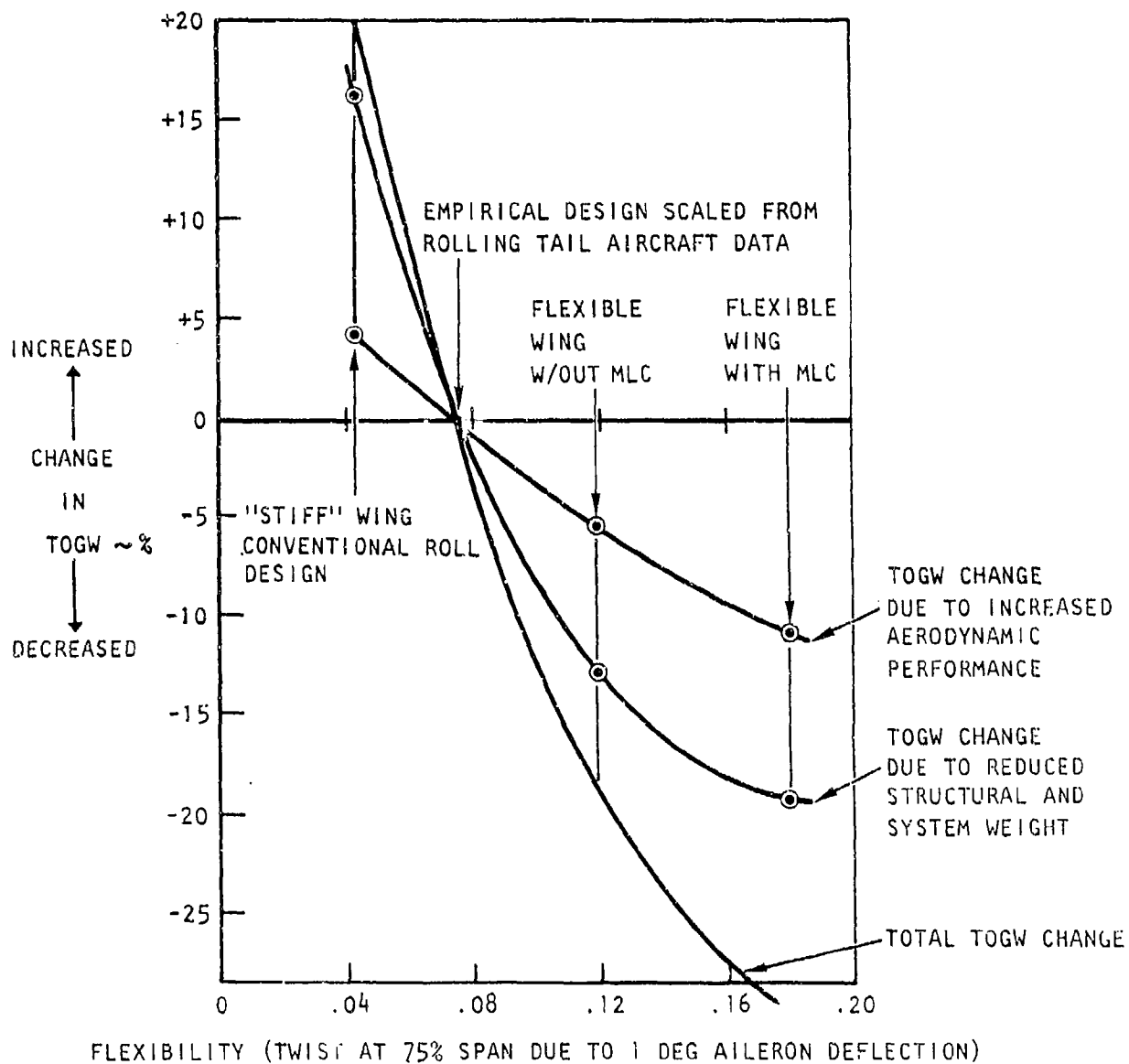


Figure 2-7. Reduced TOGW Payoff of AFW Technology

### 3.0 WIND TUNNEL MODEL DESCRIPTION AND CHARACTERISTICS

#### 3.1 GENERAL

The wind tunnel model is a full-span simulation of a Rockwell International fighter aircraft configuration. (See Figure 3-1.) The lines of the model have been altered in some areas because of construction restraints or test objectives. The fuselage lines aft of the canopy were bulged to facilitate mounting the force balance housing and the pivot bearings. The lower fuselage lines were bulged to mount the model pitch actuator; the centerbody section was deleted to provide clearance for the sting; the wing lower surface lines were bumped to mount the control surface actuators; and the vertical stabilizers were deleted to simplify construction of the wing. The model has eight remotely variable wing control surfaces operated by hinge-line-mounted vane-type rotary actuators powered by an onboard hydraulic system. Model pitch angle relative to the balance is remotely variable, utilizing a linear hydraulic actuator with the head end connected to the fuselage structure and the rod end connected to the force balance housing. Power to this actuator comes from the onboard hydraulic system. The wing structural box is aeroelastically tailored to be representative of the proposed air vehicle structural stiffness. The model has the capability to be free to roll about the sting axis. The sting has a movable section nested in the fixed portion and supported by four ballbearing assemblies. When running in the free-to-roll mode, the movable sting section is restrained by a disc brake actuated by roll limit switches. Hydraulic power for the brake is supplied by the facility system. The two sting sections may be pinned together for static tests. Figure 3-2 shows a general arrangement.

The AFW wind tunnel model is statically and dynamically scaled to simulate a representative full-scale design with a wing span of approximately 52 feet. The geometric scale factor of 1/6 was selected to obtain an 8.67-foot model wing span with a planform area to test section area ratio of 0.141. This area ratio satisfies the recommended ratio of 0.15. The full-scale design point was selected at Mach 1.10 and at the maximum full-scale dynamic pressure of 2150 psf. The wind tunnel model design point that simulates the full-scale design point was selected at Mach 1.10 at a dynamic pressure of 450 psf. These two design points determine the model dynamic, mass, stiffness, force, and aerodynamic scale factors and are shown in Table 3-1. The model wing is aeroelastically and dynamically scaled from these factors. The fuselage was designed to be "rigid." The total roll inertia of the model (wing, fuselage, and rolling sting) was scaled to simulate the full-scale aircraft roll inertia.



Figure 3-1. AFW Model (0.1667 - Inch) Installed in the Langley Research Center 16-Foot TDT

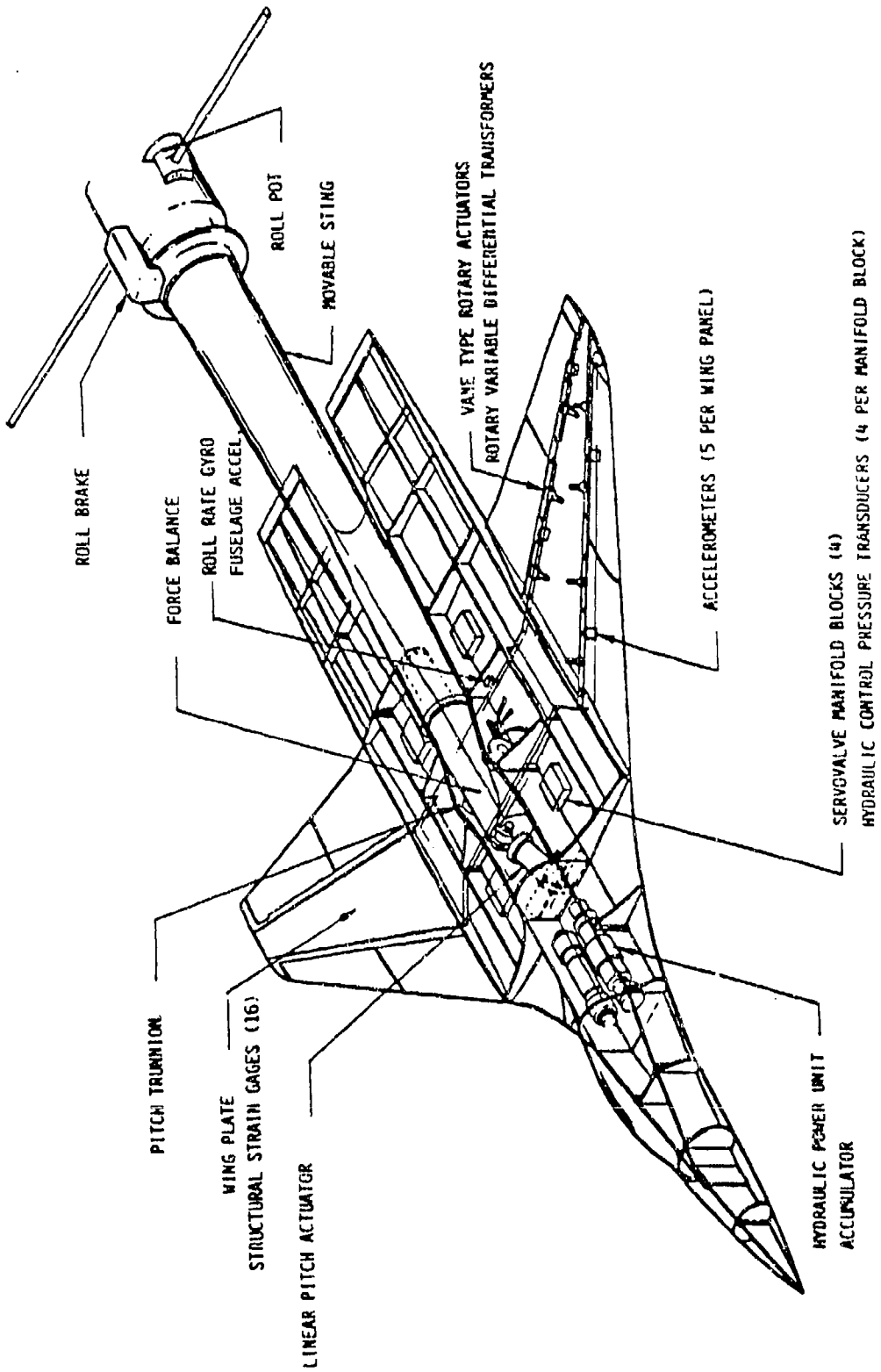


Figure 3-2. General Arrangement

Table 3-1

## AFW DYNAMICS MODEL SCALE FACTORS

Parameter	Value
Mach No. (V/a) fs (Span = 47.43 ft)	1.10
Velocity, Vfs (fps)	1249.2
Dynamic Pressure, $q_{fs}$ , (psf)	2150.0
Density, $\rho$ (slugs/ft <sup>3</sup> )	0.002756
Test Section Design Data	
Mach No.	1.10
Density, $\rho_{ms}$ (slugs/ft <sup>3</sup> )	0.002772
Velocity	569.8
Dynamic pressure $q_{ms}$ (psf)	450.0
Model Scale Factors:	
Geometric, $S_g$	0.1667
Velocity, $S_v = V_{ms}/V_{fs}$	0.4561
Dynamic pressure, $S_q = q_{ms}/q_{fs}$	0.2093
Model velocity margin at design mach no., $M_v$	0.
Density, $S_\rho = (\rho/\rho^0)_{ms}/(\rho/\rho^0)_{fs}$	1.006
Frequency, $S_f = S_v S_g^{-1} (1+M_v)^{-1}$	2.736
Weight/Length, $S_{w/l} = S_\rho S_g^2$	0.02795
Weight, $S_w = S_\rho S_g^3$	0.0046602
Mass inertia/length, $S_{I/l} = S_\rho S_g^4$	0.7767E-3
Mass inertia, $S_I = S_\rho S_g^5$	1.2950E-4
Static unbalance/length, $S_{p/l} = S_\rho S_g^3$	0.0046602
Static unbalance, $S = S_\rho S_g^4$	0.7767E-3
Linear spring, $S_k = S_g S (1+M_v)^{-2}$	0.03489
Rotational spring, $S_c = S_g^3 S (1+M_v)^{-2}$	9.696E-4
Force, $S_f = S_q S_g^2$	0.0058162
Bending moment or torque $S_{bm} = S_q S_g^3$	9.696E-4
Bending or torsional stiffness, $S_{EI} = S_g^4 S_q (1+M_v)^{-2}$	1.6163E-4

### 3.2 PLANFORM DIMENSIONS

Top and side views of the model are shown in Figure 3-3. The thickness-camber profile of the wing and fuselage is scaled from the full-scale aircraft except where deviations are required. The wing lower mold lines are "bumped" to accommodate the thickness of the control surface actuators. The fuselage is modified near the sting interface to accommodate the sting, balance, pitch trunnion, and pitch actuator, and the aft fuselage center body is deleted to allow clearance for the sting when the model is pitched.

### 3.3 MODEL STRUCTURAL AND MECHANICAL DESIGN

The model comprises an aeroelastically tailored composite wing with eight independently driven, computer-controlled, active, wing leading-edge and trailing-edge control surfaces and a semi-rigid fuselage that is supported by a pitch actuation system to a six-component force balance. The force balance is supported by a sting. The sting is free to roll or to be fixed by a dynamic brake system.

#### 3.3.1 FLEXIBLE WING DESIGN

The primary strength and deflection control of the wing is provided by a wing box assembly which consists of an aluminum honeycomb core cocured with tailored plies of graphite/epoxy tape. The thickness and orientation of the graphite plies permit the desired amounts of bending and twist as a function of aerodynamic loads on the wing assembly. The top and bottom surfaces of the wing box are covered with a semi-rigid polyurethane foam to provide an aerodynamic surface without significant contribution to the overall wing stiffness. The wing leading and trailing edge control surfaces consist of polyurethane foam cores with graphite/epoxy cloth skins. The gap between the control surfaces and the wing box is covered with a flexible graphite/epoxy aerodynamic fairing to minimize contribution to wing stiffness. Figure 3-4 illustrates the wing box/fairing/control surface design.

The control surfaces are attached to the wing box by hydraulic rotary actuators. The actuators fit into round holes in titanium inserts in the wing; this provides shear and torsion ties but allows for bending freedom. This attachment minimizes the contribution of the control surfaces to the wing stiffness. Figure 3-5 illustrates the control surface attachment on the wing.

#### 3.3.2. FUSELAGE DESIGN

The model fuselage was designed to provide the basic aerodynamic shape of the configuration and house the onboard model components. The configuration shape was modified to provide room for the sting/balance attachment. Also, a slot was provided near the fuselage trailing edge to allow for the sting cutting through the fuselage when the model is pitched and rolled relative to the sting.

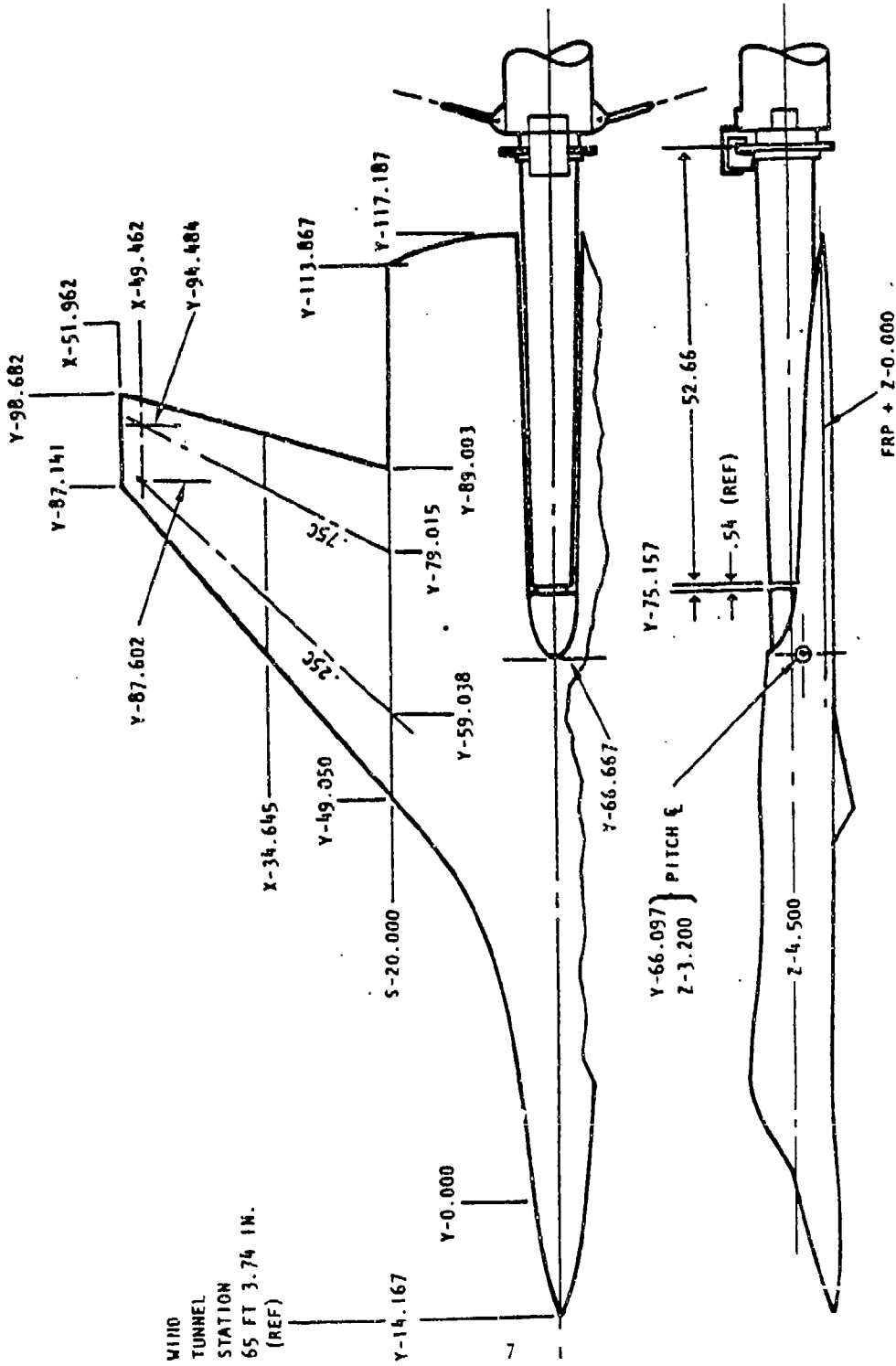
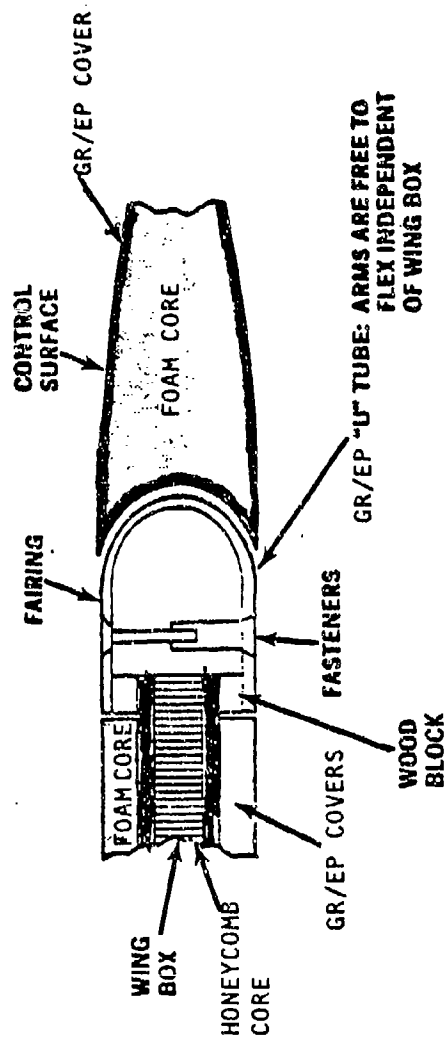
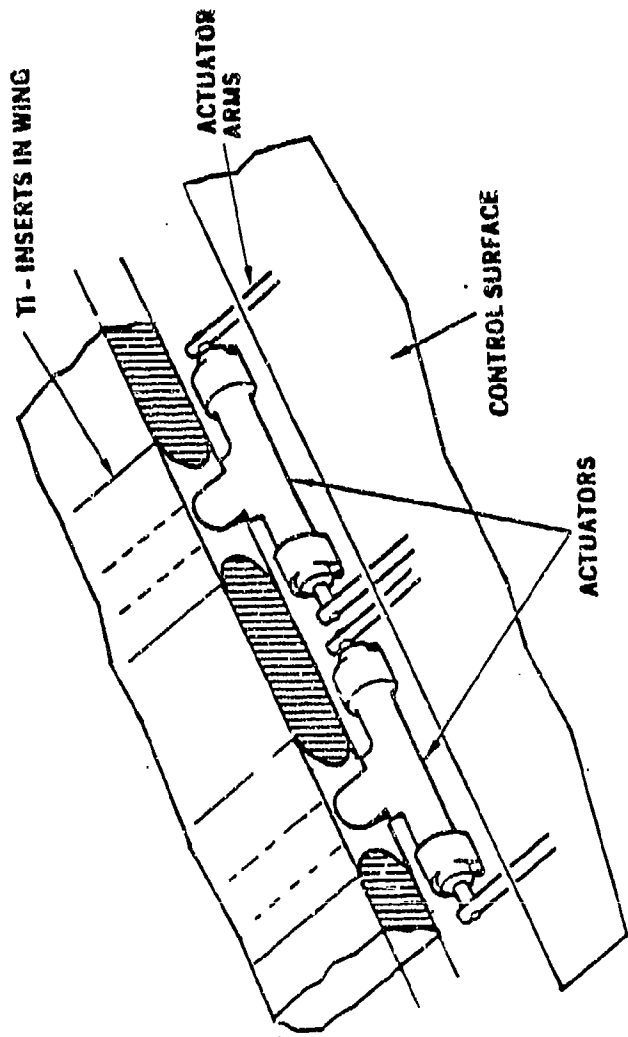


Figure 3-3. AFW Technology Wind Tunnel Model - Side and Top Views



- FAIRINGS ARE DESIGNED TO AERODYNAMICALLY SEAL CONTROL SURFACES
- WITHOUT ADDING STIFFNESS TO THE WING

Figure 3-4. Wing Box/Fairing Control Surface Design



- CONTROL SURFACES ARE ATTACHED TO THE WING BY ACTUATORS THAT ARE "FREE" TO ROLL
- ISOLATING CONTROL SURFACE STIFFNESS FROM WING

Figure 3-5. Control Surface/Actuator Attachment Design

The fuselage was designed to be rigid, not scaled for flexibility. The design uses aluminum stringers and bulkheads forming a substructure with fiberglass skins providing the basic shape and strength. The fuselage was attached to the sting through pitch trunnions and a pitch actuator, thus allowing the model to be pitched at the end of the sting.

### 3.3.3 STING DESIGN

The model sting was designed to be sufficiently stiff so that its response would be small compared with the wing response in the wind tunnel. Also, the sting was required to allow for roll freedom so that the model would be free to perform rolling maneuvers. To provide access for the model electrical power and for the control system wiring, the sting was required to be hollow.

A two-piece sting was designed to meet those requirements. The wind tunnel attachment piece was a 10-inch-diameter steel tube with 1.5-inch wall thickness. This piece attached to the wind tunnel. The other end of the sting was a tapered tube, 4.0 inches on the model end and 7.0 inches on the sting side; this tube was also 1.5-inches thick. The two pieces were joined together by roll bearings which allowed roll freedom. A disk brake was provided to prevent the two pieces from rotating when desired. The fuselage was attached to the sting through a force balance.

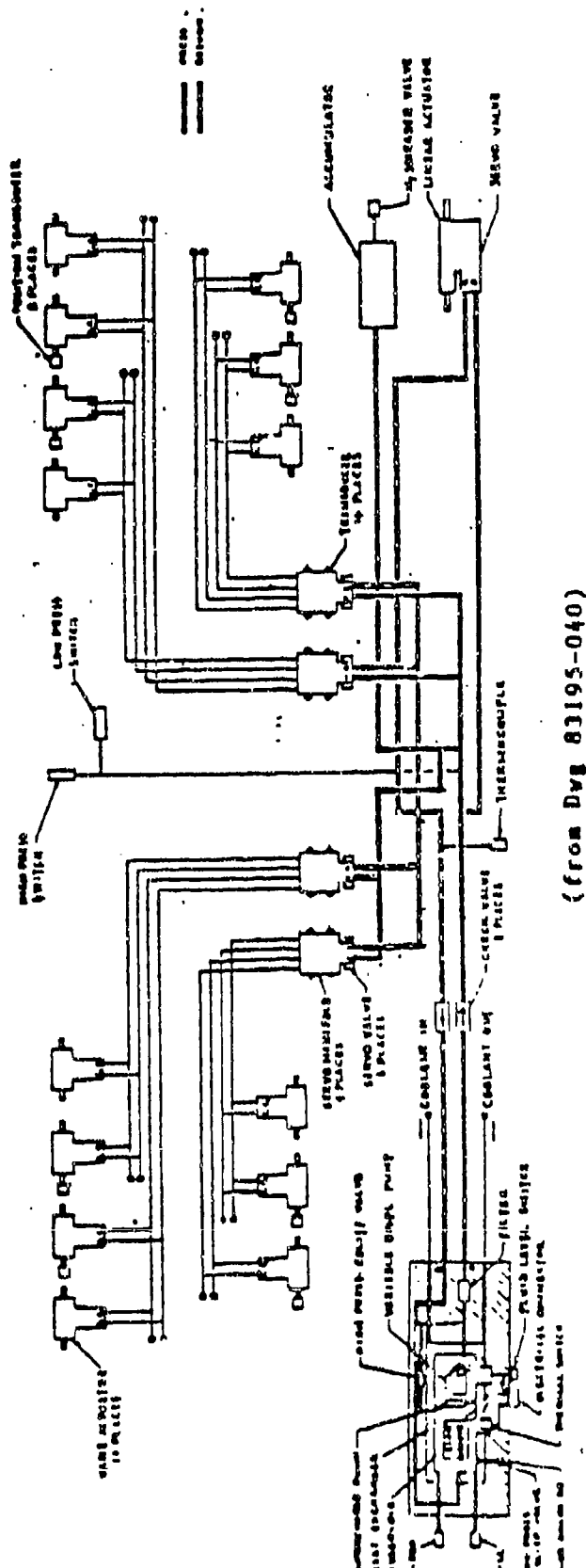
### 3.3.4 HYDRAULIC SYSTEM

The wind tunnel model has a self-contained hydraulic system designed to power the control surfaces and pitch actuation systems. The control system forces, rates, and frequencies were scaled to the full-sized aircraft design; the system forces and rates were used to develop flow rates and power requirements. The system was sized for a 2,000 psi hydraulic supply taking into account line and valve pressure drops, actuator leakage, and servo-valve pilot flows. Figure 3-6 is a schematic drawing of hydraulic system.

The hydraulic supply was provided by a Vickers continuous-duty pump capable of 3.0 gpm at 2,000 psi. The pump, a modified version of one used in a Hughes helicopter, is capable of continuous duty and is powered by a water-cooled electric motor. Electric power and water cooling were routed to the pump (which is located in the model fuselage) through the hollow model sting. A small accumulator was also designed into the system to aid the pump under maximum flow-rate transient conditions.

The model actuators are powered by MOOG Series 30 servo-valves. One servo-valve is used on each control surface and on the pitch actuator.

The model is pitched relative to the sting by a linear hydraulic actuator. The linear pitch actuator has a 3.0-inch stroke which pitches the model between -1.50 and +13.75 degrees angle-of-attack. The actuator



(from Dwg 83195-040)

Figure 3-6. Hydraulic System Schematic

is sized to provide high pitch rates (10 degrees/second) under maximum loads. The actuator stiffness is sized to prevent model divergence at high dynamic pressures.

The wing control surfaces are powered by miniature rotary vane hydraulic actuators. (The actuator design layout is shown in Figure 3-7.) The design requires control surface motion of  $\pm 24$  degrees, a torque capability of 275 in/lb at 2,000 psi, and an estimated no-load rate of 250 degrees/second. The double vane rotary design is also constrained in diameter to fit within the wing mold lines. The actuator had o-ring energized Teflon seals around the vane face and vane ends. Also, a nylon washer was added to the end caps to seal the ends.

### 3.3.5 ELECTRONIC CONTROLLER DESIGN

Two separate electronic controllers were designed and fabricated for the model. The first controller was designed for use during static wind tunnel testing. It uses position potentiometers to manually set the control surface and pitch positions. The second controller was designed for use during dynamic wind tunnel testing. It uses a digital computer for real-time control of the model in free-to-roll and forced pitch maneuvers. Electronically, there is an extensive amount of commonality between the two controllers. The servo-amplifiers, demodulators, transducer-excitation oscillators, dc-signal amplifiers, dc-power supplies, connector panel, and custom-designed continuously-variable lead-lag-attenuator circuit cards are identical in both controllers.

Figure 3-8 shows the controller used for static testing along with the junction boxes that connect it to the model and recording equipment and also provides test points for monitoring all console input and output signals. Figure 3-9 shows the digital controller used for active-control wind tunnel testing.

## 3.4 MODEL INSTRUMENTATION

The model is instrumented with a force balance to measure total model forces, strain gages to measure wing loads, hydraulic pressure transducers to measure control surface hinge moments, transducers to measure control surface deflections and pitch angular position, accelerometers to measure wing and fuselage dynamic response, a roll gyroscope to measure roll rates, and various miscellaneous instrumentation. Figure 3-10 illustrates the model's instrumentation.

### 3.4.1 FORCE BALANCE

Six component force and moment data were obtained using the Task corporation 4.0-inch-diameter MK VI internal strain gage balance. The balance was installed upright in the model and pinned at M.S. 68.71 to utilize the aft balance pin hole.

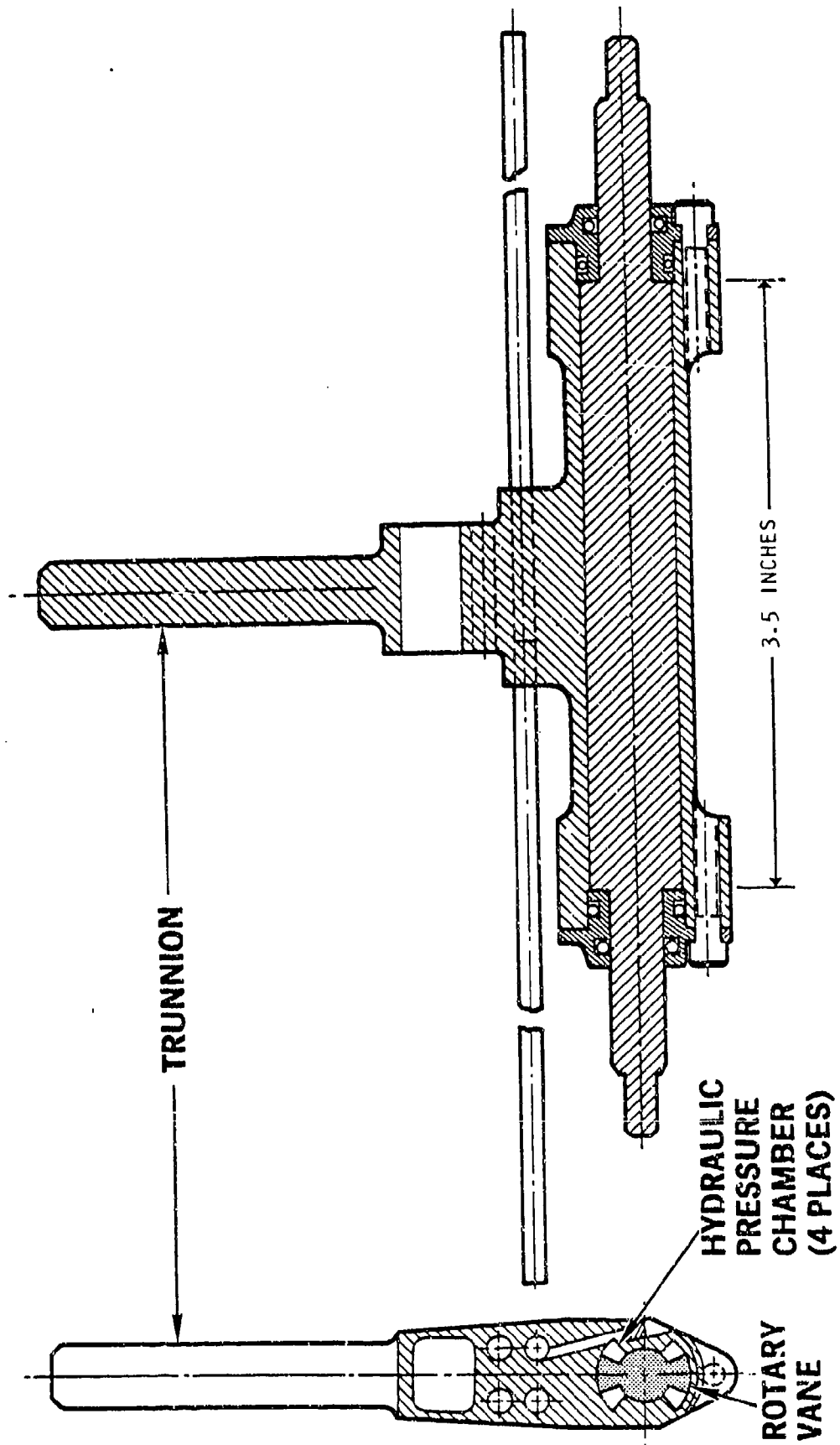


Figure 3-7. Rotary Vane Actuator

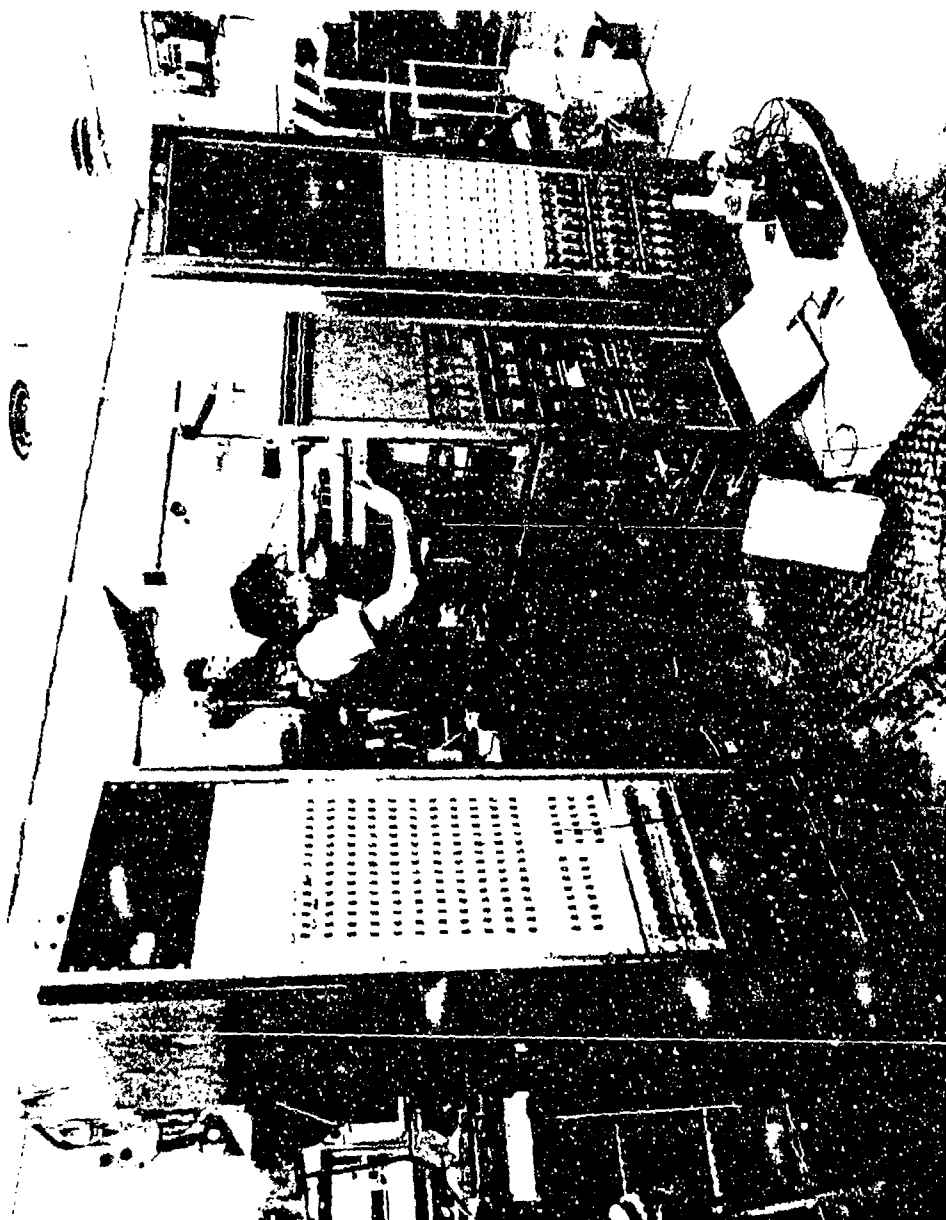


Figure 3-8. Static Control Console and Junction Boxes

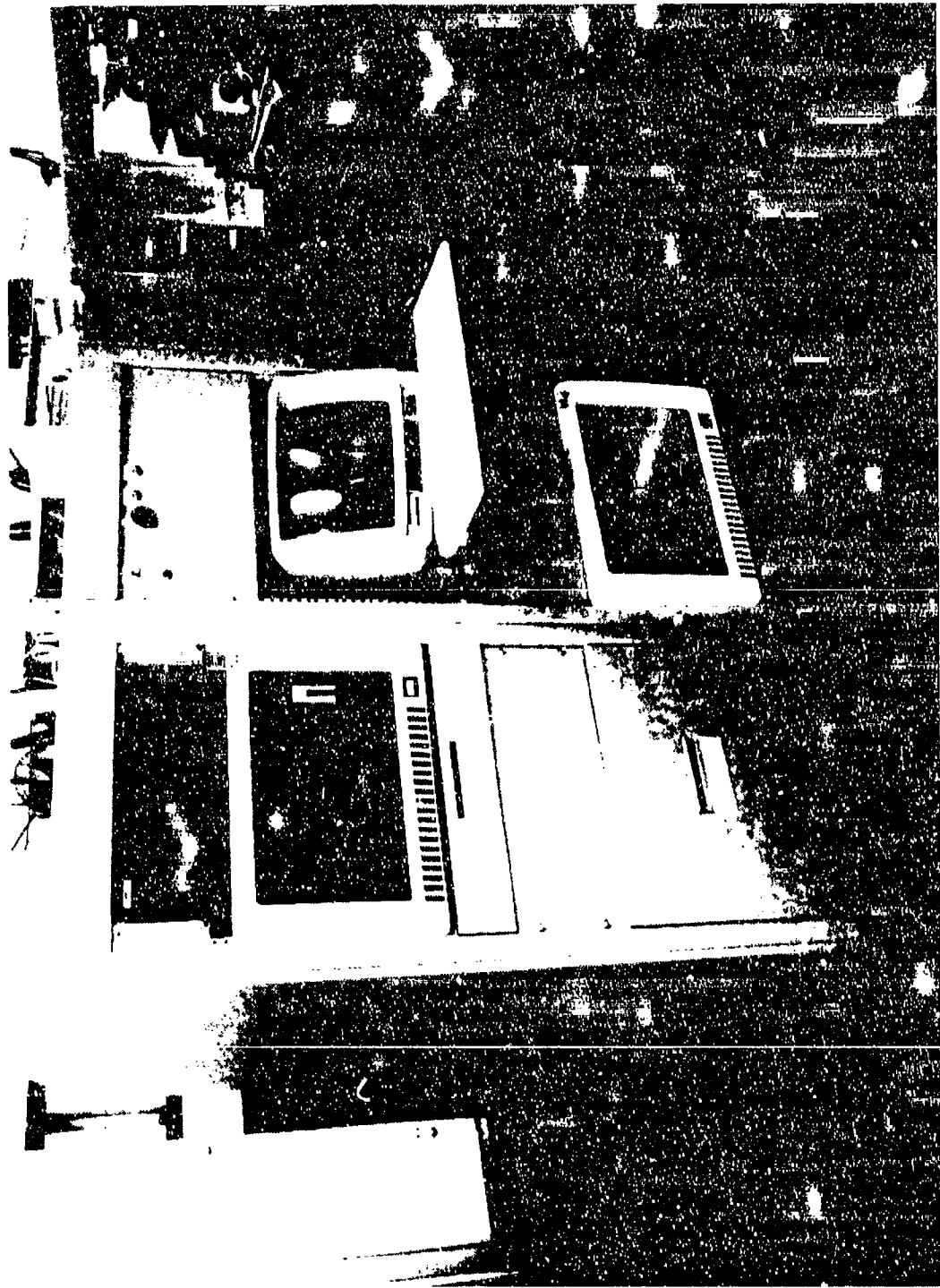


Figure 3-9. Dynamic Wind Tunnel Model Digital Controller

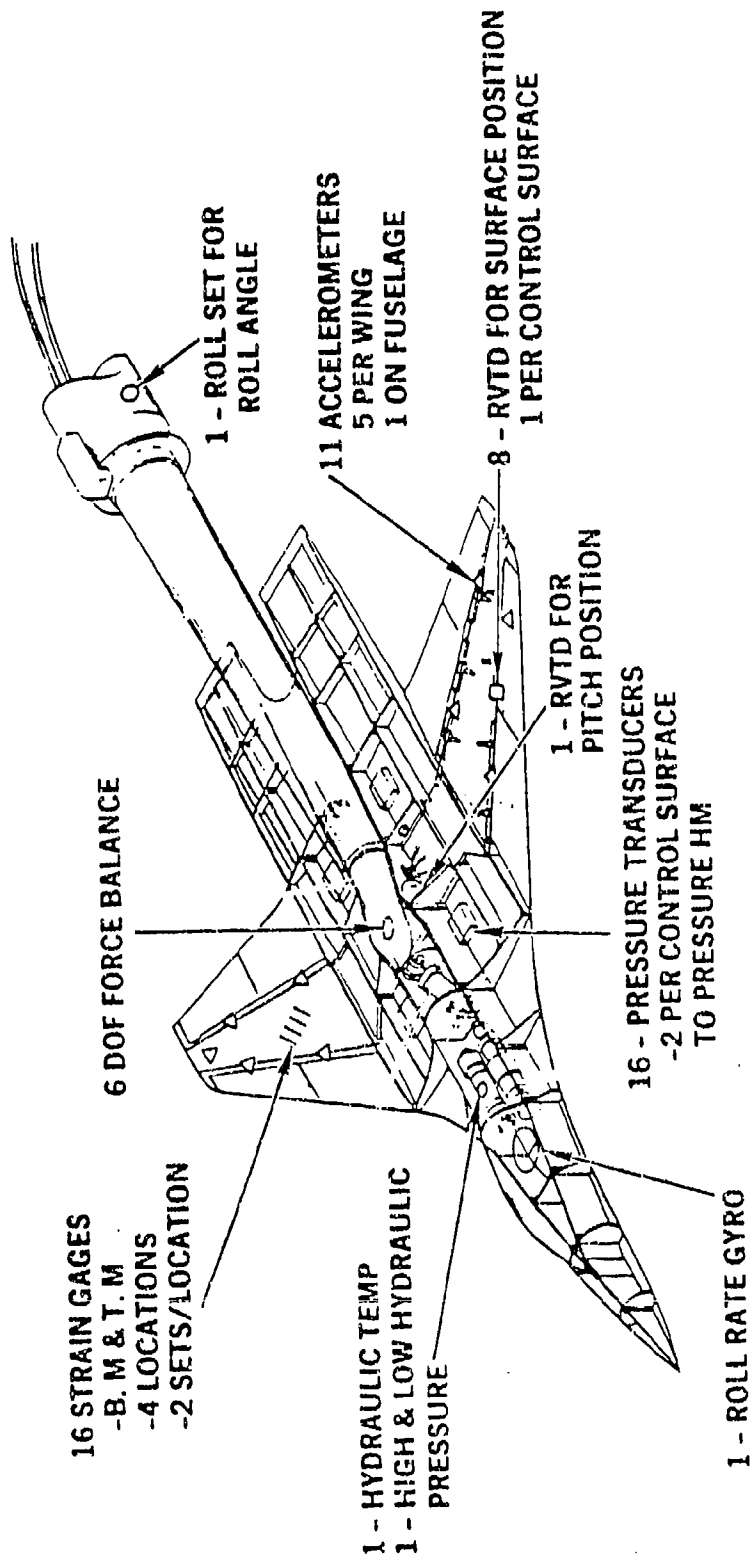


Figure 3-10. Dynamic Wind Tunnel Model Instrumentation

### 3.4.2 STRAIN GAGES

The wing plate is instrumented with 16 strain-gage bridges to measure wing bending and torsional moments at four stations. Gage locations are given in Table 3-2 and illustrated in Figure 3-11. There is a primary and a back-up strain gage at each location with only one recorded at a time. Selection of the primary gage is accomplished during the wing proof loadings.

Table 3-2  
STRAIN GAGE BRIDGE LOCATIONS

Parameter	Description	B.P.	x/c
BML11	Left-hand wing panel, inbd bending moment	9.25	0.50
BML12	Left-hand wing panel, inbd bending moment	10.25	0.50
BML01	Left-hand wing panel, inbd bending moment	31.78	0.50
BML02	Left-hand wing panel, outbd bending moment	32.98	0.50
BMR11	Right-hand wing panel, inbd bending moment	9.25	0.50
BMRO1	Right-hand wing panel, outbd bending moment	31.78	0.50
BMRO2	Right-hand wing panel, outbd bending moment	32.98	0.50
TML11	Left-hand wing panel, inbd torsional moment	9.25	0.50
TML12	Left-hand wing panel, inbd torsional moment	10.75	0.50
TML01	Left-hand wing panel, outbd torsional moment	31.78	0.50
TML02	Left-hand wing panel, outbd torsional moment	32.78	0.50
TMR11	Right-hand wing panel, inbd torsional moment	9.25	0.50
TMR12	Right-hand wing panel, inbd torsional moment	10.75	0.50
TMRO1	Right-hand wing panel, outbd torsional moment	31.78	0.50
TMRO2	Right-hand wing panel, outbd torsional moment	32.98	0.50

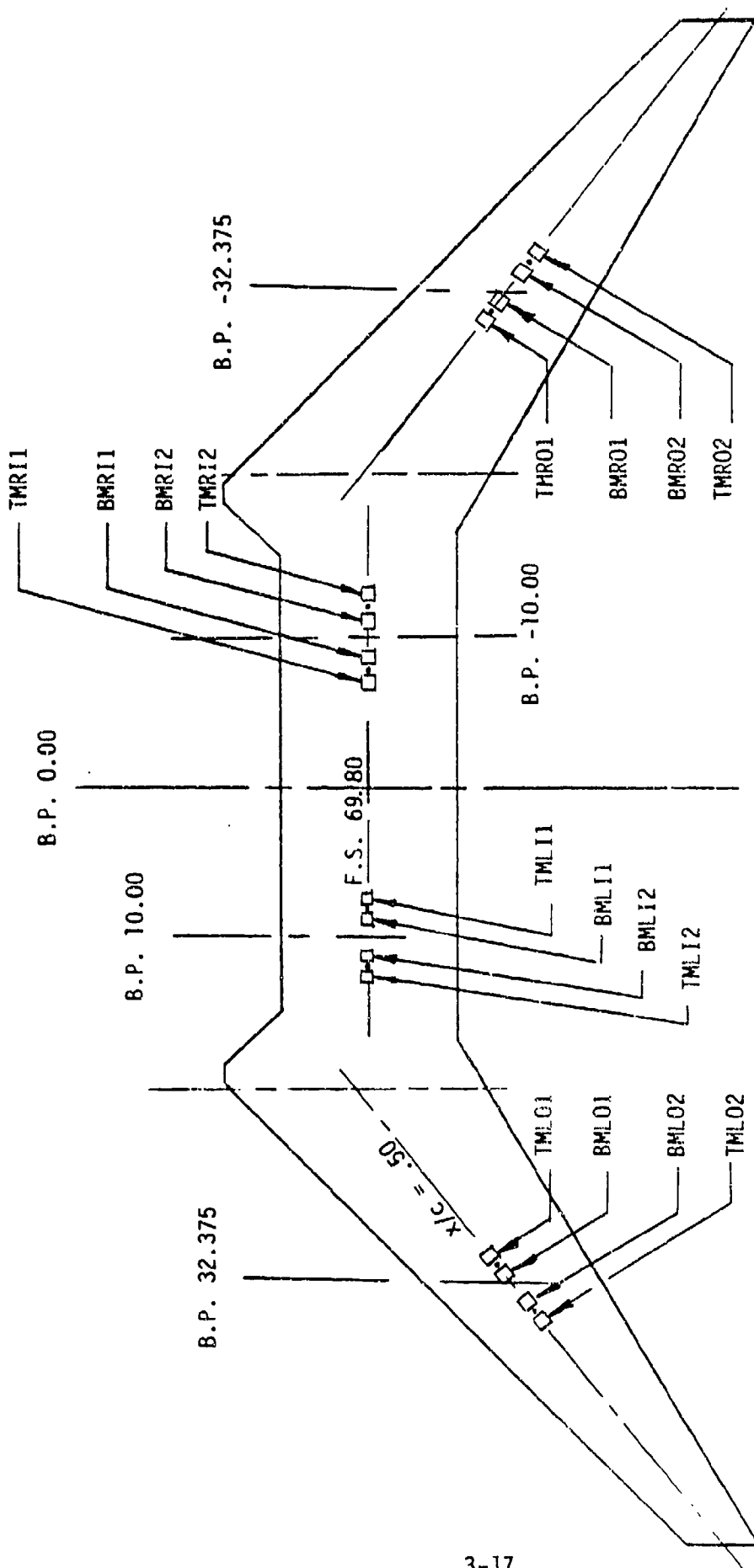


Figure 3-11. Wing Spar Strain Gage Bridge Locations

### 3.4.3 HYDRAULIC SYSTEM PRESSURE MEASUREMENTS

The hydraulic supply pressures on both sides of each vane actuator are measured using Entran Model EPX-141U-2500G pressure transducers. The differential pressure across each vane is electronically output along with the upper vane control pressure. The differential pressure across the vane is proportional to surface hinge moment. Parameter identification is given in Tables 3-3 and 3-4.

Table 3-3

#### HYDRAULIC SUPPLY PRESSURE MEASUREMENTS

Parameter	Description
PLLE11	Left-hand, leading-edge, inbd control surface pressure 1
PLLE12	Left-hand, leading-edge, inbd control surface pressure 2
PLLE01	Left-hand, leading-edge, outbd control surface pressure 1
PLLE02	Left-hand, leading-edge, outbd control surface pressure 2
PLTE11	Left-hand, trailing-edge, inbd control surface pressure 1
PLTE12	Left-hand, trailing-edge, inbd control surface pressure 2
PLTE01	Left-hand, trailing-edge, outbd control surface pressure 1
PLTE02	Left-hand, trailing-edge, outbd control surface pressure 2
PRLE11	Right-hand, leading-edge, inbd control surface pressure 1
PRELE12	Right-hand, leading-edge, inbd control surface pressure 2
PRLE01	Right-hand, leading-edge, outbd control surface pressure 1
PRLE02	Right-hand, leading-edge, outbd control surface pressure 2
PRTE11	Right-hand, trailing-edge, inbd control surface pressure 1
PRTE12	Right-hand, trailing-edge, inbd control surface pressure 2
PRTE01	Right-hand, trailing-edge, outbd control surface pressure 1
PRTE02	Right-hand, trailing-edge, outbd control surface pressure 2

Two hydraulic supply pressure switches are located in the output line of the hydraulic power unit. One switch indicates hydraulic system overpressure if the system pressure is greater than 2600 psi. Activation of this switch commands a rapid angle-of-attack reduction to 0 degrees, nulls all control surfaces, and illuminates a warning light on the control console. The other hydraulic pressure switch actuates if the system pressure drops below 1000 psi. Activation of this switch commands tunnel bypass and nulls the signal to the pitch servo-valve.

Table 3-4

## CONTROL SURFACE DIFFERENTIAL PRESSURES

Parameter	Description
DPLLEI PLLEI1-PLLEI2	Left-Hand, Leading-edge, inbd diff. pressure
DPLLEO PLLEO1-PLLEO2	Left-Hand, Leading-edge, outbd diff. pressure
DPLTEI PLTEI1-PLTEI2	Left-Hand, Trailing-edge, inbd diff. pressure
DPLTEO PLTEO1-PLTEO2	Left-Hand, Trailing-edge, outbd diff. pressure
DPRLEI PRLEI1-PRLEI2	Right-Hand, Leading-edge, inbd diff. pressure
DPRLEO PRLEO1-PRLEO2	Right-Hand, Leading-edge, outbd diff. pressure
DPRTEI PRTEI1-PRTEI2	Right-Hand, Trailing-edge, inbd diff. pressure
DPRTEO PRTEO1-PRTEO2	Right-Hand, Trailing-edge, outbd diff. pressure

## 3.4.4 ANGULAR POSITION MEASUREMENTS

Each control surface is instrumented with an MPC Y88A rotary variable differential transformer (RVDT) mounted to the actuator shaft. Parameter identification is given in Table 3-5. These sensors require 10 VRMS, 1800-hz excitation voltage that is supplied from the model control console. Demodulation and amplification of the sensor output are also accomplished in the control console. Leading edge control surface deflections are positive when the nose is moved down. Trailing edge deflections are positive when the trailing edge is moved down.

Table 3-5

## CONTROL SURFACE DEFLECTION MEASUREMENTS

Parameter	Description
DLLEI	Left-hand, leading-edge, inbd control surface deflection
DLLEO	Left-hand, leading-edge, outbd control surface deflection
DLTEI	Left-hand, trailing-edge, inbd control surface deflection
DLTEO	Left-hand, trailing-edge, outbd control surface deflection
DRLEI	Right-hand, leading-edge, inbd control surface deflection
DRLEO	Right-hand, leading-edge, outbd control surface deflection
DRTEI	Right-hand, trailing-edge, inbd control surface deflection
DRTEO	Right-hand, trailing-edge, outbd control surface deflection

The model pitch angle relative to the balance is measured with an MPC Y88A rotary variable differential transformer mounted to the pivot axis. The output of this transducer is designated "ALP".

The sting/model roll angle is measured using a one-turn Litton 8517 10K ohm potentiometer mounted to the sting driven with a belt attached to the forward movable sting section. The output of this sensor is designated "PHI".

### 3.4.5 ACCELEROMETERS

The fuselage is instrumented with an Entran EGA-125-10D accelerometer with the sensitive axis directed in the model pitch plane. The output of this accelerometer is designated "AFUS." Excitation voltage is provided from power supplies and the signal conditioning mounted in the junction box. The output of this sensor is ac-coupled.

Each wing panel is instrumented with five Entran EGA-125F-100D accelerometers located as shown in Table 3-6. Excitation voltage signal conditioning (consisting of amplification and ac-coupling) is provided from the junction box.

Table 3-6.

ACCELEROMETER LOCATIONS

Parameter	Description	Location	
		% Span	%Chord
ALLEI	Left-hand, leading-edge, inbd accelerometer	0.506	0.304
ALLEO	Left-hand, leading-edge, outbd accelerometer	0.750	0.304
ALTEI	Left-hand, trailing-edge, inbd accelerometer	0.507	0.706
ALTEO	Left-hand, trailing-edge, outbd accelerometer	0.750	0.706
ALTIP	Left-hand, tip accelerometer	0.922	0.304
ARLEI	Right-hand, leading-edge, inbd accelerometer	0.506	0.304
ARLEO	Right-hand, leading-edge, outbd accelerometer	0.750	0.304
ARTEI	Right-hand, trailing-edge, inbd accelerometer	0.507	0.706
ARTEO	Right-hand, trailing-edge, outbd accelerometer	0.750	0.706
ALTIP	Right-hand, tip accelerometer	0.922	0.304

### 3.4.6 WING STATIC PRESSURE MEASUREMENTS

The left-hand wing is instrumented with 141 pressure orifices. The pressures are located on the upper and lower wing surfaces at five spanwise stations. These pressures are measured utilizing a four-barrel scanivalve assembly with Statham PM131-TC-10 PSID pressure transducers. A 1248 BCD

position transmitter is used. The pressure transducers are referenced to tunnel static pressure via a pressure tube routed into the plenum. Pressure tap locations are given in Table 3-7. Scanivalve hookup is shown in Table 3-8. The scanivalve assembly is located in the fuselage nose. An access hatch is provided for maintenance. A backing pressure tube is provided and should be referenced to atmosphere.

### 3.4.7 MISCELLANEOUS INSTRUMENTATION

The model is instrumented with a Bendix Model 302260 roll rate gyroscope. This sensor requires 13 VRMS, 800 Hz power supplied from the model control console; demodulation and amplification of the output are also in the control console.

An Omega Engineering SCASS-062G-2 chromel-alumel thermocouple probe is installed in the hydraulic system return line to monitor fluid temperature. The temperature is displayed on a Doric digital thermocouple indicator supplied by Rockwell.

The hydraulic power unit is equipped with a switch which is actuated by either low-fluid or high-fluid level temperature. When this switch is actuated, a warning light on the model control console is activated.

Table 3-7

#### LEFT-HAND WING PRESSURE ORIFICE LOCATIONS

SPAN STATION (INCHES)										
22.67			30.50		36.33		42.12		48.00	
% Chord	Upper	Lower								
0	P100	---	P200	---	P300	---	P400	---	P500	---
2.5	P101	P121	P201	P221	P301	P321	P401	P421	P501	P521
5.0	P102	P122	P202	P222	P302	P322	P402	P422	P502	P522
10.0	P103	P123	P203	P223	P304	P323	P403	P423	P503	P523
15.0	P104	P124	P204	P224	P305	P324	P404	P424	P504	P524
20.0	P105	P125	P205	P225	P306	P325	P405	P425	P505	P525
30.0	P106	P126	P206	P226	P307	P326	P406	P426	P506	P526
40.0	P107	P127	P207	P227	P308	P327	P407	P427	P507	P527
50.0	P108	P128	P208	P228	P309	P328	P408	P428	P507	P528
60.0	P109	P129	P209	P229	P310	P329	---	P429	P508	---
70.0	P110	P130	P210	P230	P311	P330	P410	P430	---	P529
80.0	P111	P131	P211	P231	P312	P331	---	P431	P510	P530
85.0	P112	P132	P212	P232	P313	P332	P412	P432	P511	P531
90.0	P113	P113	P213	P233	P314	P333	P413	P433	P512	P532
95.0	P114	P134	P214	P234	P315	P334	P414	P434	P513	P533

Table 3-8

## SCANIVALVE HOOKUP

PORT	SCANIVALVE 1		SCANIVALVE 2		SCANIVALVE 3		SCANIVALVE 4	
	Press.	Q.D.No.	Press	Q.D. No.	Press	Q.D. No.	Press	Q.D. No.
Home	Po	-----	Po	-----	Po	-----	Po	-----
1	P100	1-1	P207	3-10	P314	6-5	P527	4-16
2	P200	1-12	P307	3-18	P414	6-14	P128	3-7
3	P300	1-23	P407	4-6	P121	1-7	P228	3-15
4	P400	2-6	P507	4-13	P221	1-18	P328	4-3
5	P500	2-17	P108	3-3	P321	2-1	P428	4-10
6	P101	1-2	P208	3-11	P421	2-12	P528	4-17
7	P201	1-13	P308	3-19	P521	2-23	P129	3-8
8	P301	1-24	P408	4-7	P122	1-8	P229	3-16
9	P401	2-7	P508	4-14	P222	1-19	P329	4-4
10	P501	2-18	P109	3-4	P322	2-2	P429	4-11
11	P102	1-3	P209	3-12	P422	2-13	P529	6-25
12	P202	1-14	P309	3-20	P522	2-24	P130	5-6
13	P302	1-25	-----	-----	P123	1-9	P230	5-16
14	P402	2-8	P509	6-20	P223	1-20	P330	6-6
15	P502	2-19	P110	5-1	P323	2-3	P430	6-15
16	P103	1-4	P210	5-11	P423	2-14	P530	6-26
17	P203	1-15	P310	6-1	P523	2-25	P131	5-7
18	P303	1-26	P410	6-11	P124	1-10	P231	5-17
19	P403	2-9	P510	6-21	P224	1-21	P331	6-7
20	P503	2-20	P111	5-2	P324	2-4	P431	6-16
21	P104	1-5	P211	5-12	P424	2-15	P531	6-27
22	P204	1-16	P311	6-2	P524	2-26	P132	5-8
23	P304	1-27	P-----	-----	P125	1-11	P232	5-18
24	P404	2-10	P511	6-22	P225	1-22	P332	6-8
25	P504	2-21	P112	5-3	P325	2-5	P432	6-17
26	P105	1-6	P212	5-13	P425	2-16	P532	6-28
27	P205	1-17	P312	6-3	P525	2-27	P133	5-9
28	P305	1-28	P412	6-12	P126	3-5	P233	5-19
29	P405	2-11	P512	6-23	P226	3-13	P333	6-9
30	P505	2-22	P113	5-4	P326	4-1	P433	6-18
31	P106	3-1	P213	5-14	P426	4-8	P533	6-29
32	P206	3-9	P313	6-4	P526	4-15	P134	5-10
33	P306	3-17	P413	6-3	P127	3-6	P234	5-20
34	P406	4-5	P513	6-24	P227	3-14	P334	6-10
35	P506	4-12	P114	5-5	P327	4-2	P434	6-19
36	P107	3-2	P214	5-15	P427	4-9	Po	-----
37	Po	----	Po	----	Po	----	Po	-----

### 3.5 STATIC FLEXIBILITY DATA

A static flexibility test was conducted to measure the flexibility characteristics of the wind tunnel model. The model was set up in test configuration in a Rockwell Laboratory and a matrix of 59 structural influence coefficients was measured. Figure 3-12 shows a view of the test setup. Figure 3-13 shows the locations of the 59 points where the SIC measurements were taken. Fifty-one of these points were on the left side of the model (46 on the wing and 5 on the fuselage), 2 were on the fuselage centerline, and 6 were on the right wing. The 6 deflections measured on the right wing monitored the degree of symmetry or antisymmetry in the model response to symmetric and antisymmetric loads. The model deflections at all 59 points were measured when the symmetric and antisymmetric loads were applied.

Forty-nine symmetric loads were applied to the model (42 on both wings, 5 on both sides of the fuselage body, and 2 on the fuselage centerline). The four points on the wing tip were not loaded. Six antisymmetric loads were applied to the wings where the deflections on both wings were measured.

Four plots of the test SIC's reduced from the load-deflection measurements are shown in Figures 3-14 through 3-17. The viewpoint in the plots is normal to the model centerline with the nose to the left and the sting root on the right. The lines connecting the SIC's are in a streamwise direction. Table 3-9 lists which SIC's are associated with which line numbers. The point at which the unit load is applied is circled.

The SIC's were not adjusted to eliminate obvious errors since this would mislead the user as to the accuracy of the test SIC's. In most cases, it is not too difficult to discern visually the probable adjustment from the plots. SIC's with a value of zero in the plots should be disregarded. Two of the channels on the inboard trailing edge control surface consistently produced erroneous data and should be ignored (channels 39 and 45).

Analytical structural influence coefficients were developed for flutter and aerodynamic analyses using a MCS/NASTRAN finite element model (FEM). Figure 3-18 is an exploded view of the NASTRAN FEM. All of the wind tunnel model structural components are modeled in the FEM, including the wing, fuselage, and sting. The FEM was altered based on test SIC's and test GVT data until the analytic SIC's and vibration mode shapes and frequencies satisfactorily matched test data.

### 3.6 DYNAMIC VIBRATION DATA

Ground vibration tests (GVT) were performed with the model installed in the Rockwell Structures Laboratory and in the NASA-Langley transonic dynamics wind tunnel for the purpose of validating analytical vibration analyses. Figure 3-19 shows a view of the GVT test conducted in the wind tunnel.

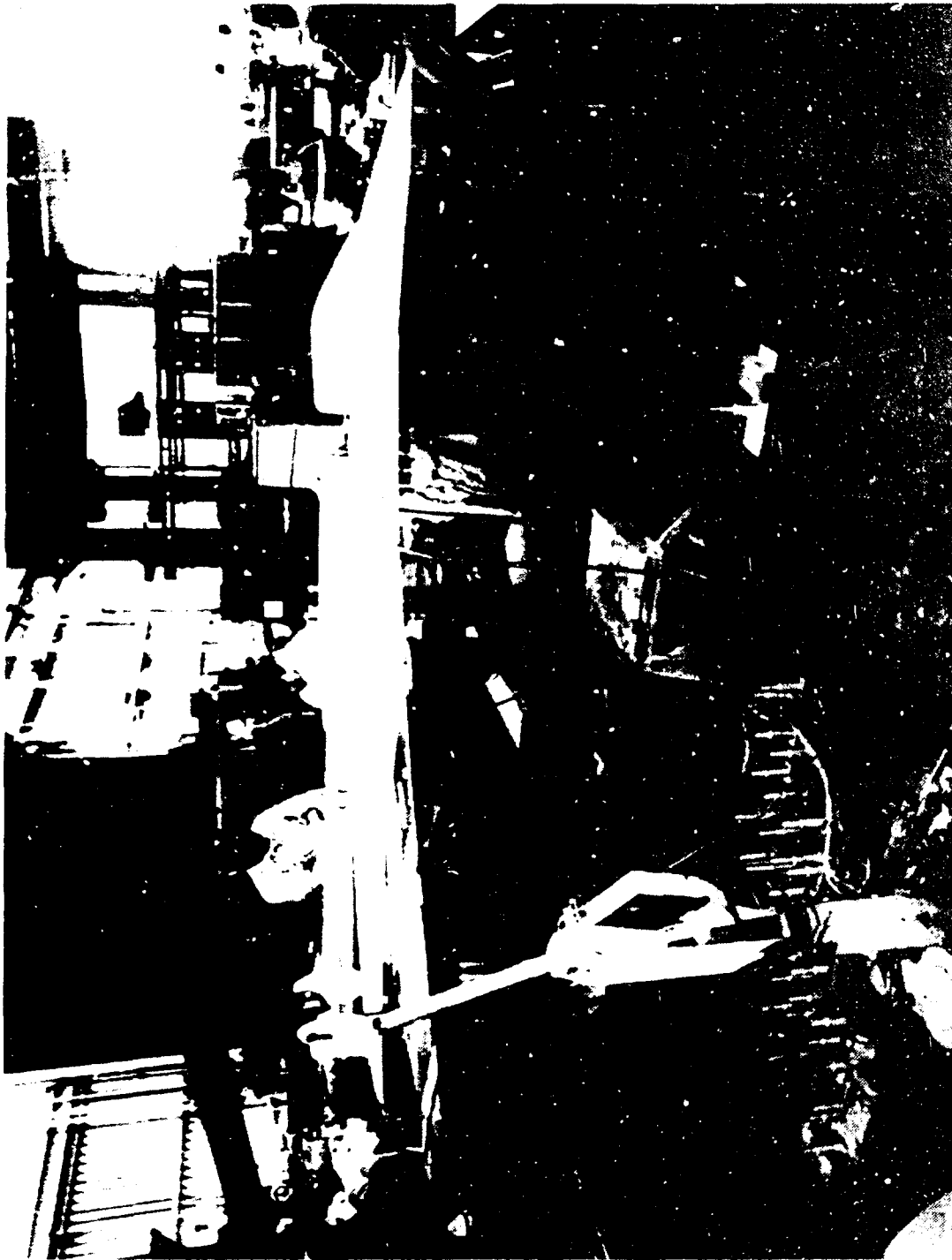


Figure 3-12. Model SIC Test Setup

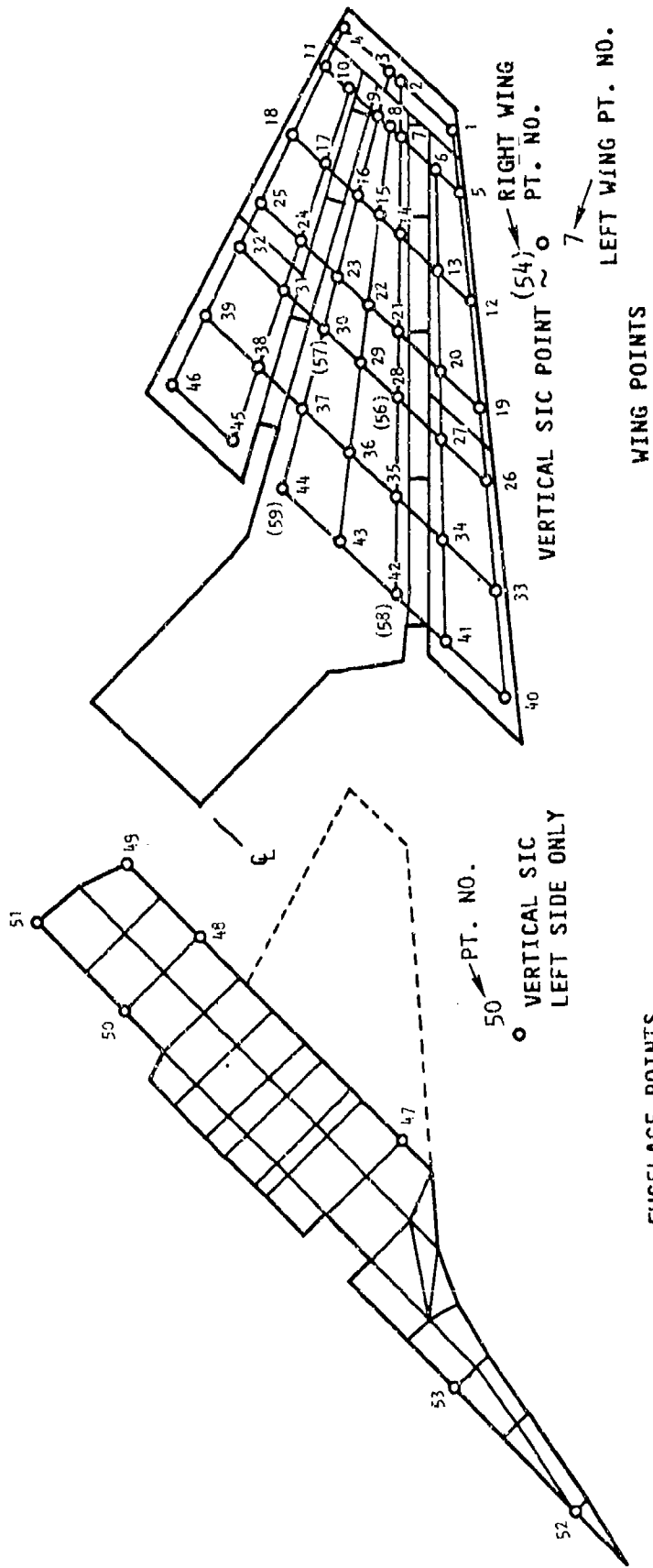


Figure 3-13. Location of Model 1 Deflection Measurements

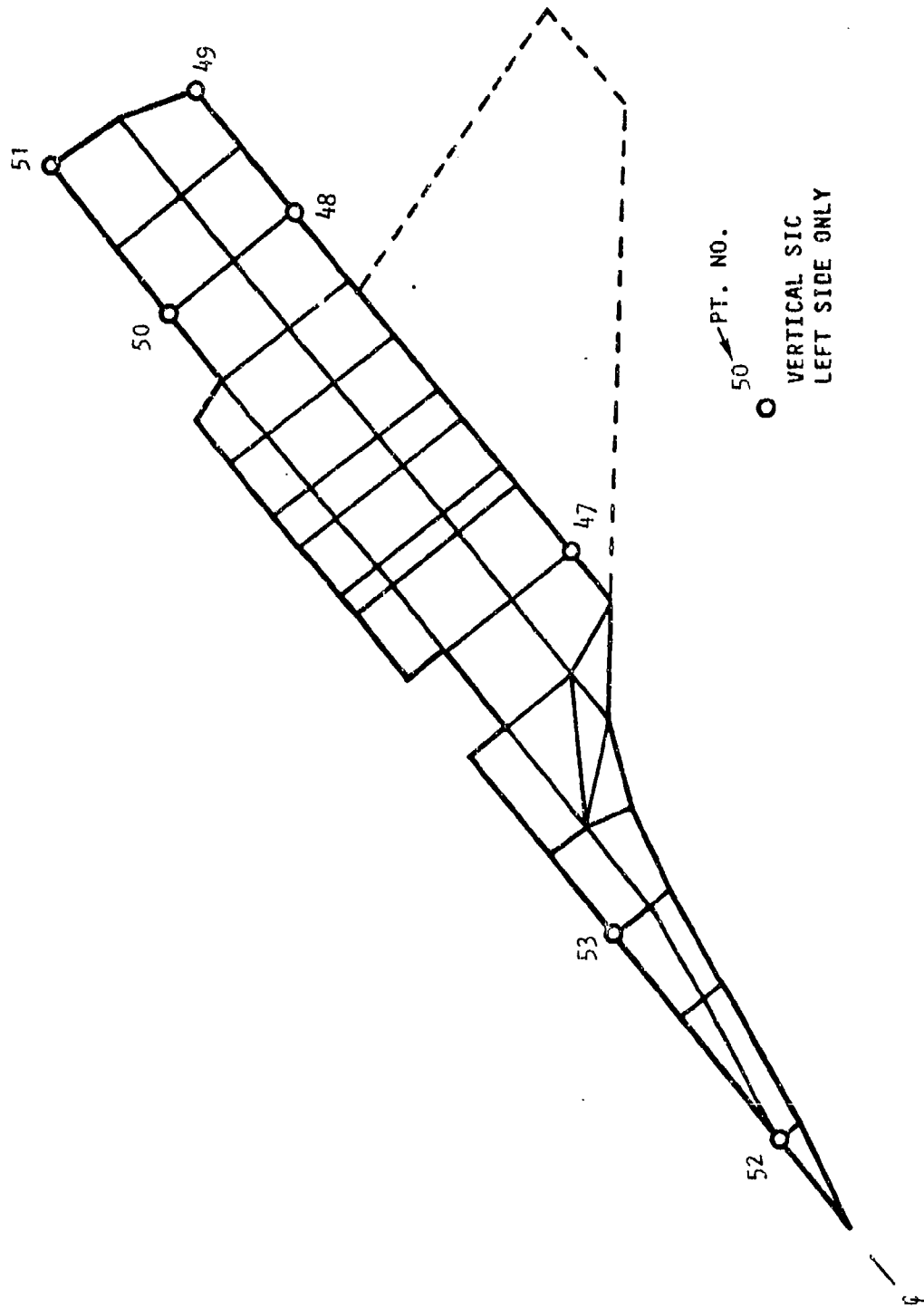


Figure 3-13. Location of Model Deflection Measurements (Continued)

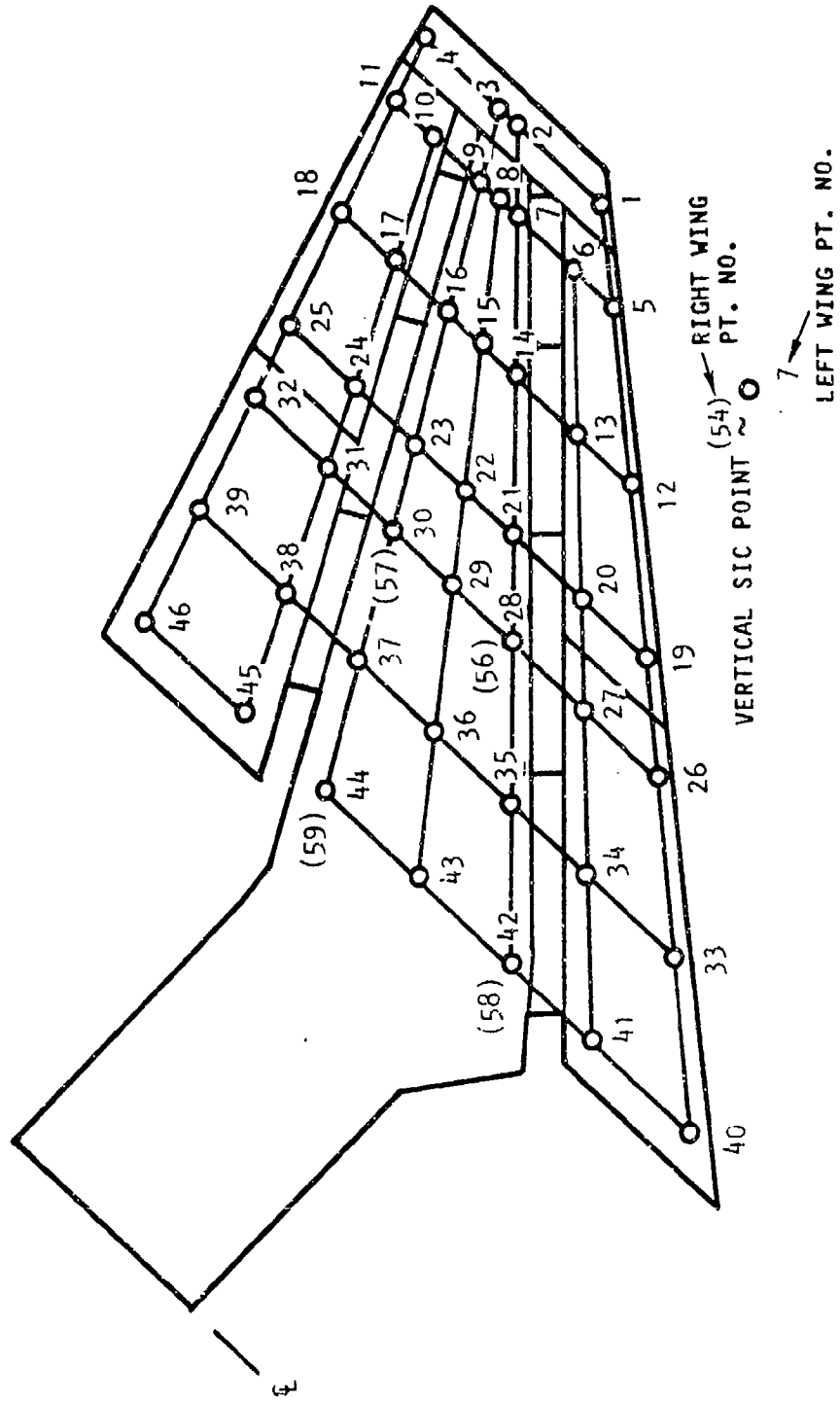


Figure 3-13. Location of Model Deflection Measurements (Concluded)

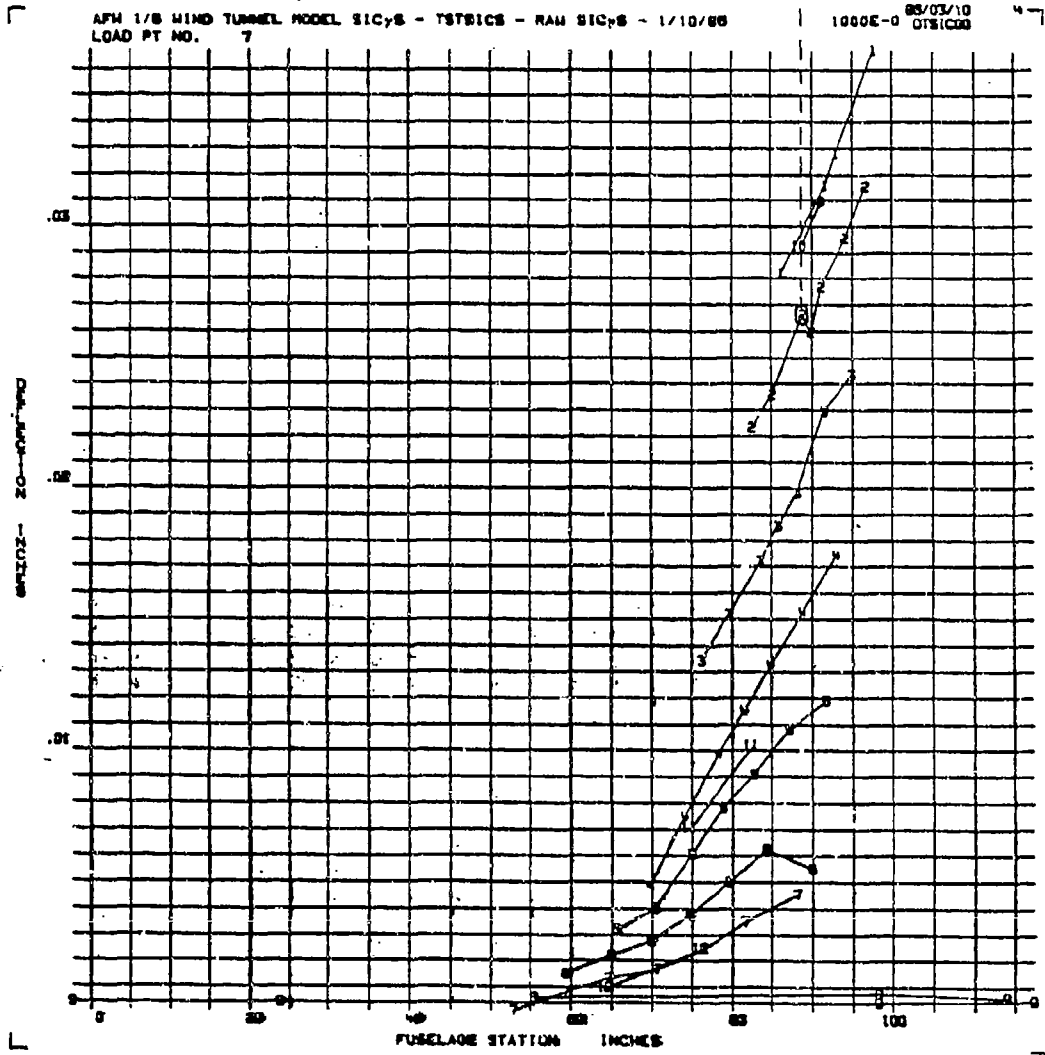
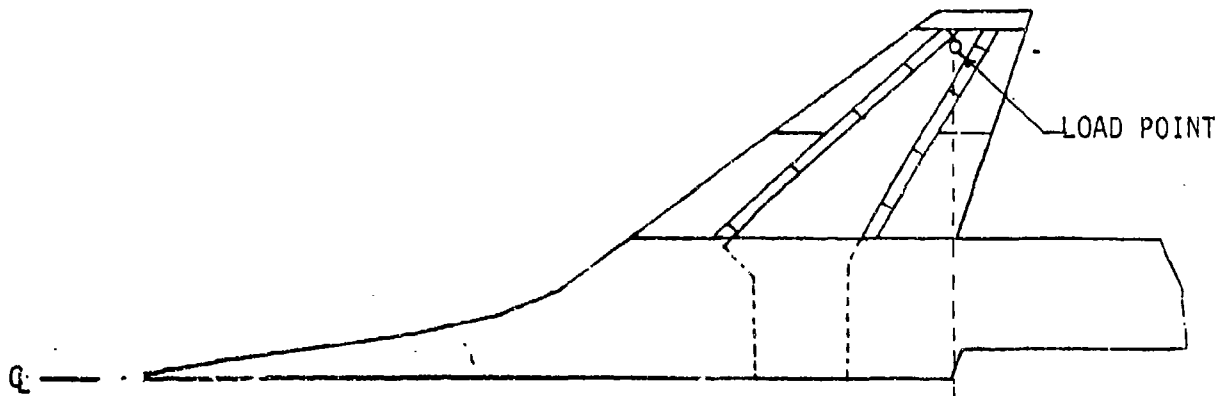


Figure 3-14. Test SIC Plot - Symmetric - Point 9

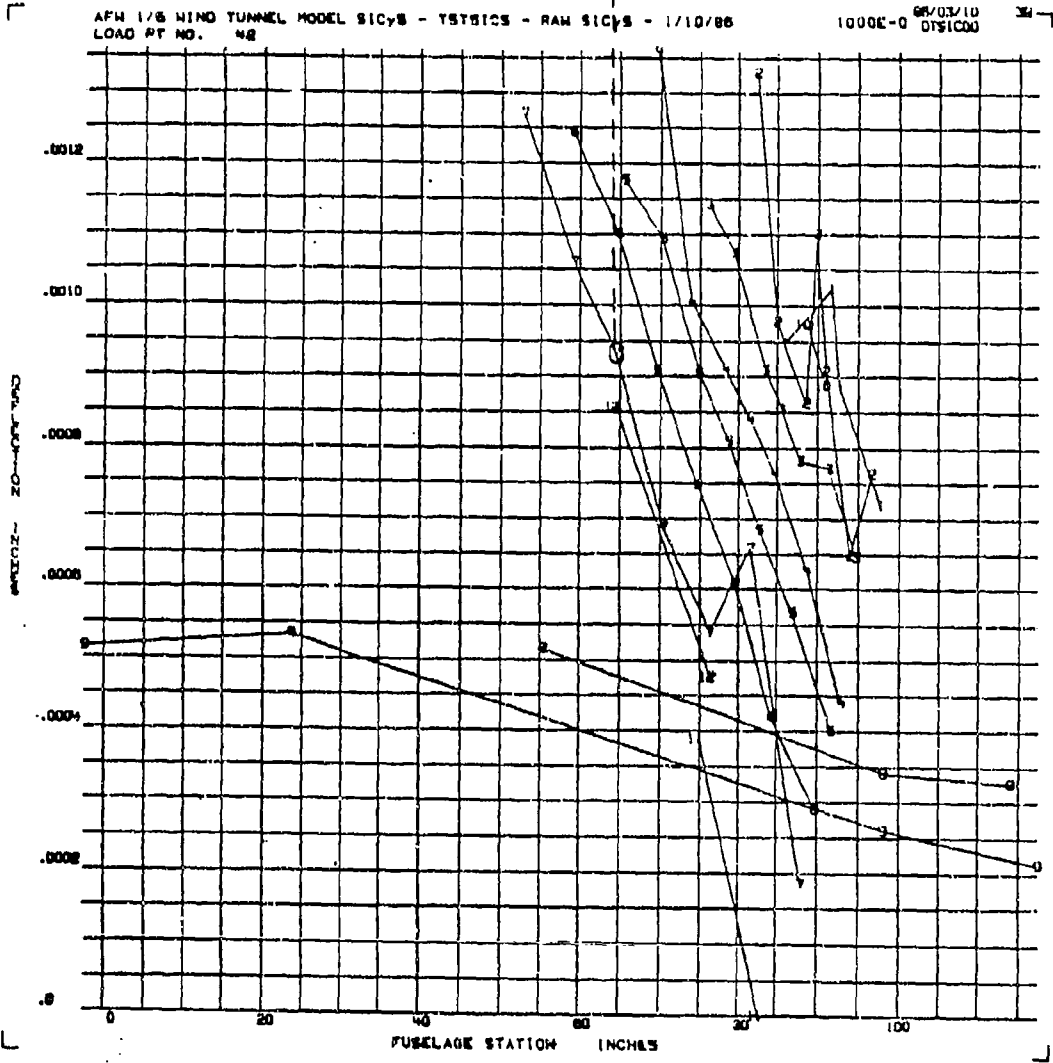
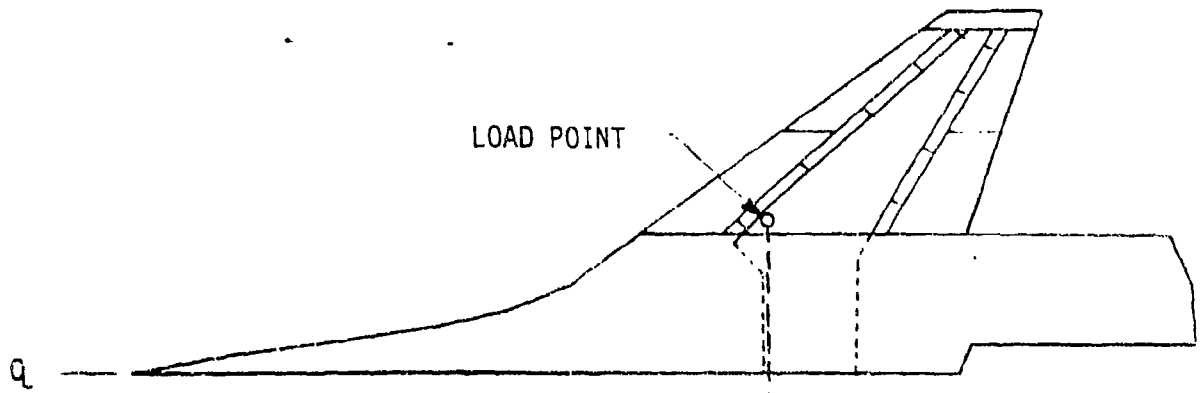


Figure 3-15. Test SIC Plot - Symmetric - Point 42

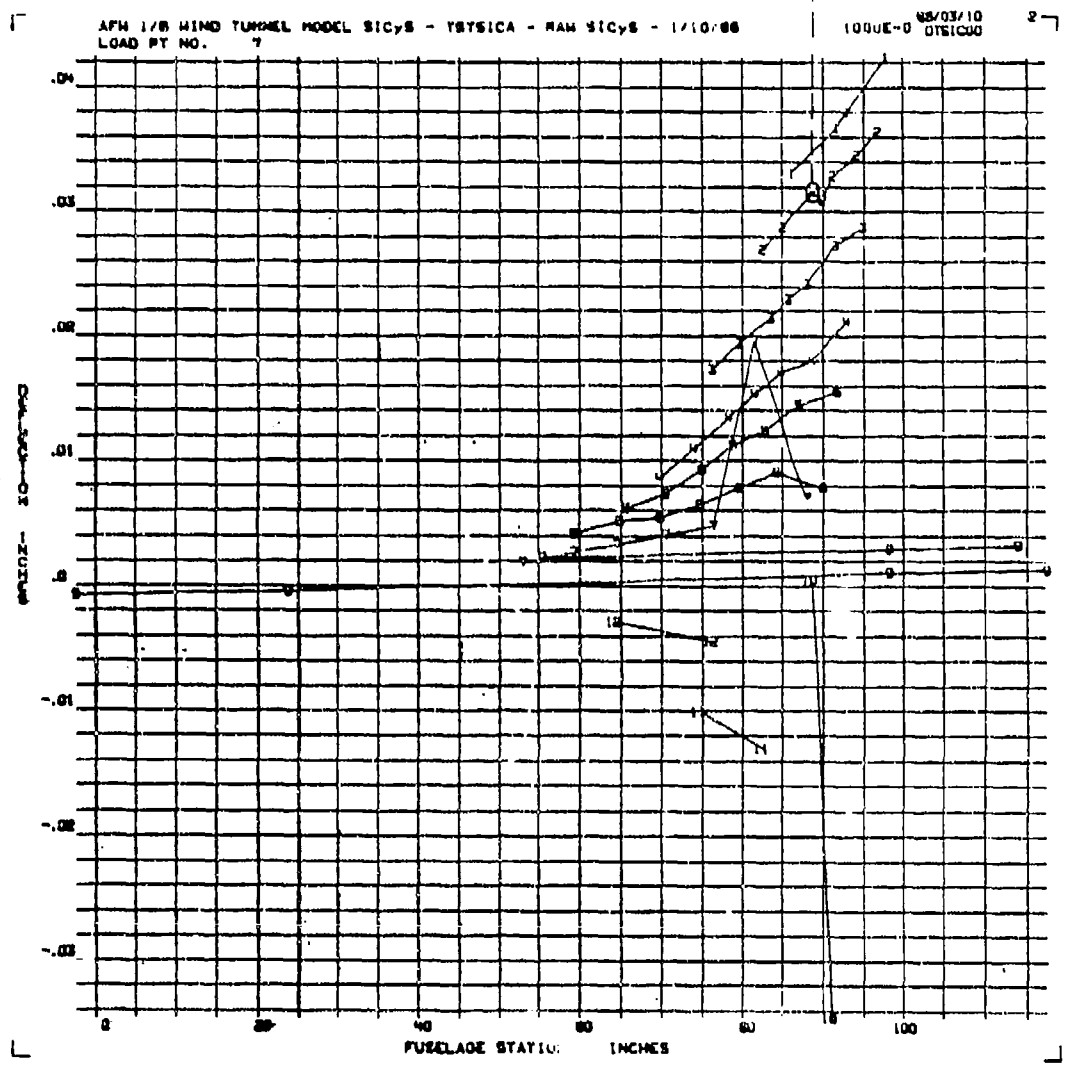
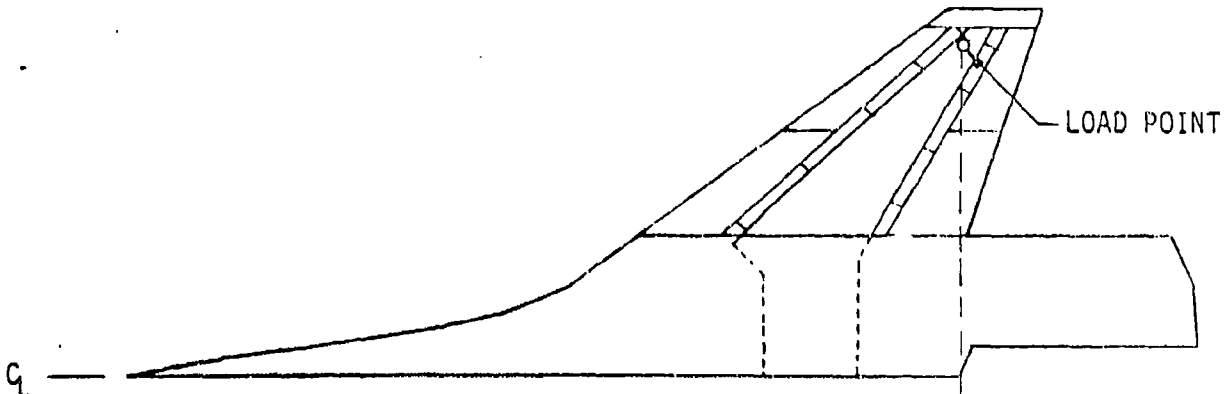


Figure 3-16. Test SIC Plot - Antisymmetric - Point 9

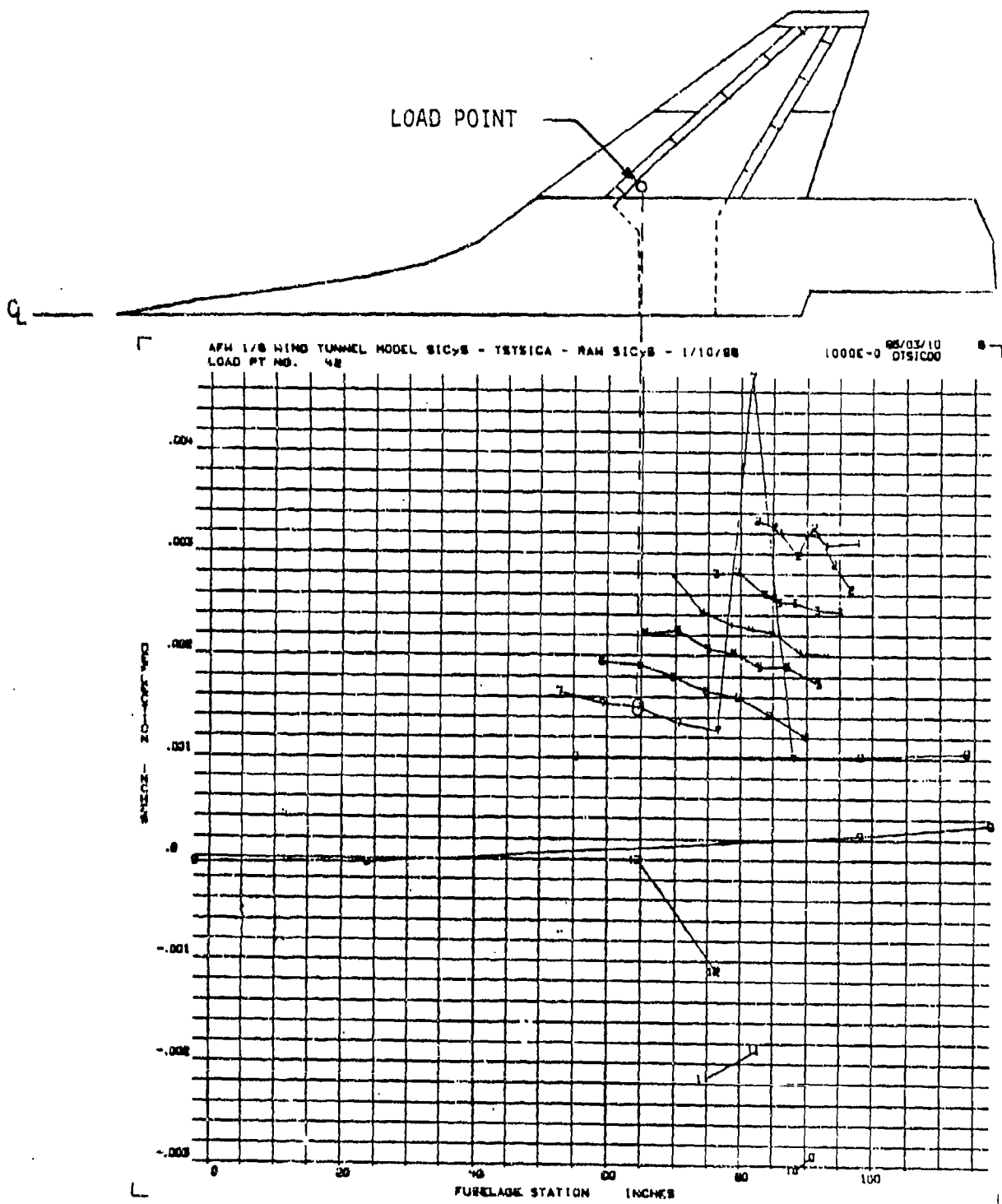


Figure 3 17. Test SIC Plot - Antisymmetric - Point 42

Table 3-9

SIC'S CONNECTED BY COMMON LINE IN FIGURES 3-14 THROUGH 3-17

<u>LINE NUMBER</u>	<u>SIC'S</u>
1	1, 2, 3, 4
2	5, 6, 7, 8, 9, 10, 11
3	12, 13, 14, 15, 16, 17, 18
4	19, 20, 21, 22, 23, 24, 25
5	26, 27, 28, 29, 30, 31, 32
6	33, 34, 35, 36, 37, 38, 39
7	40, 41, 42, 43, 44, 45, 46
8	47, 48, 49
9	52, 53, 50, 51
10	54, 55
11	56, 57
12	58, 59

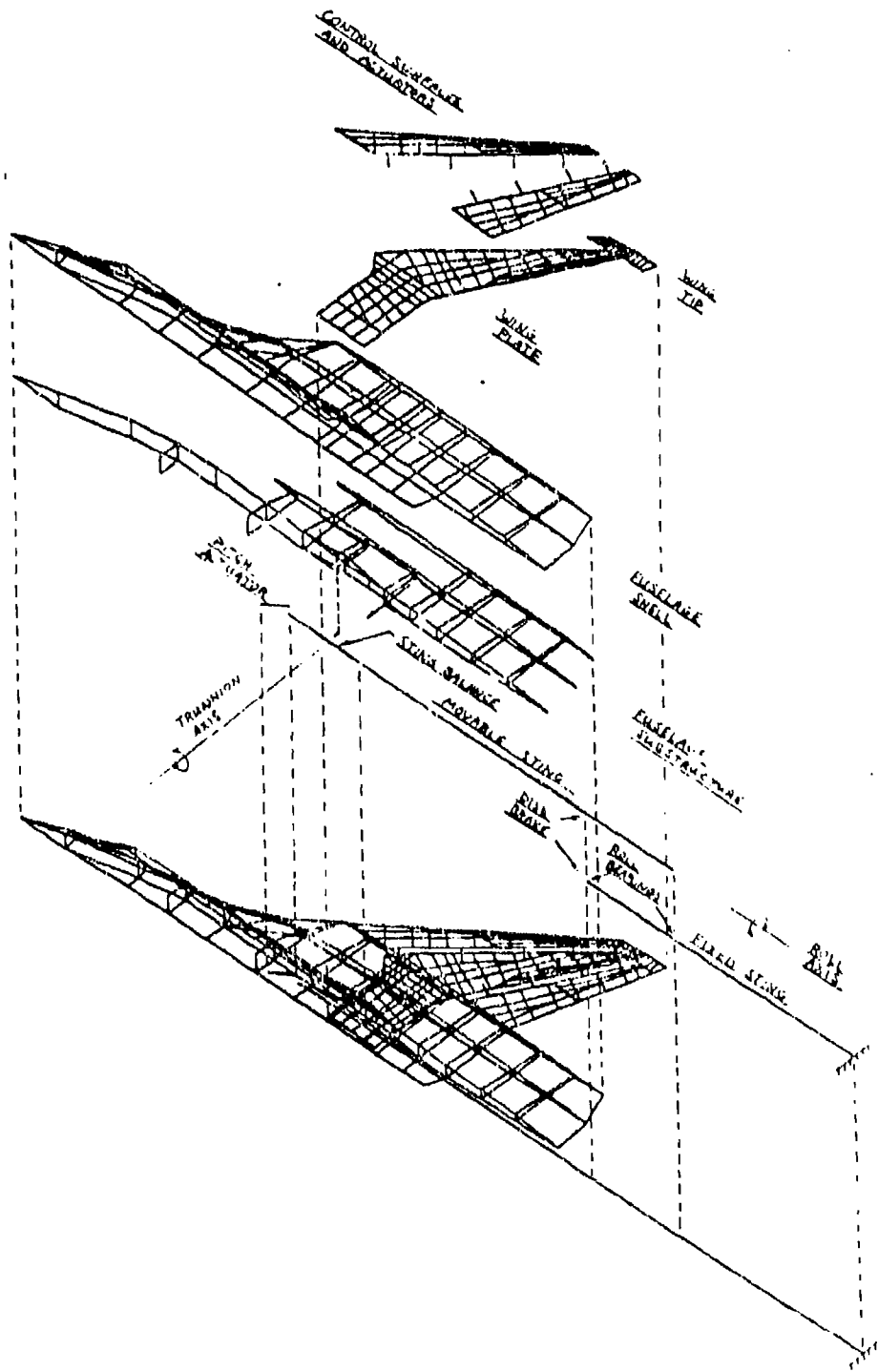


Figure 3 18. Exploded View of MSC/NASIRAN Finite Element Model

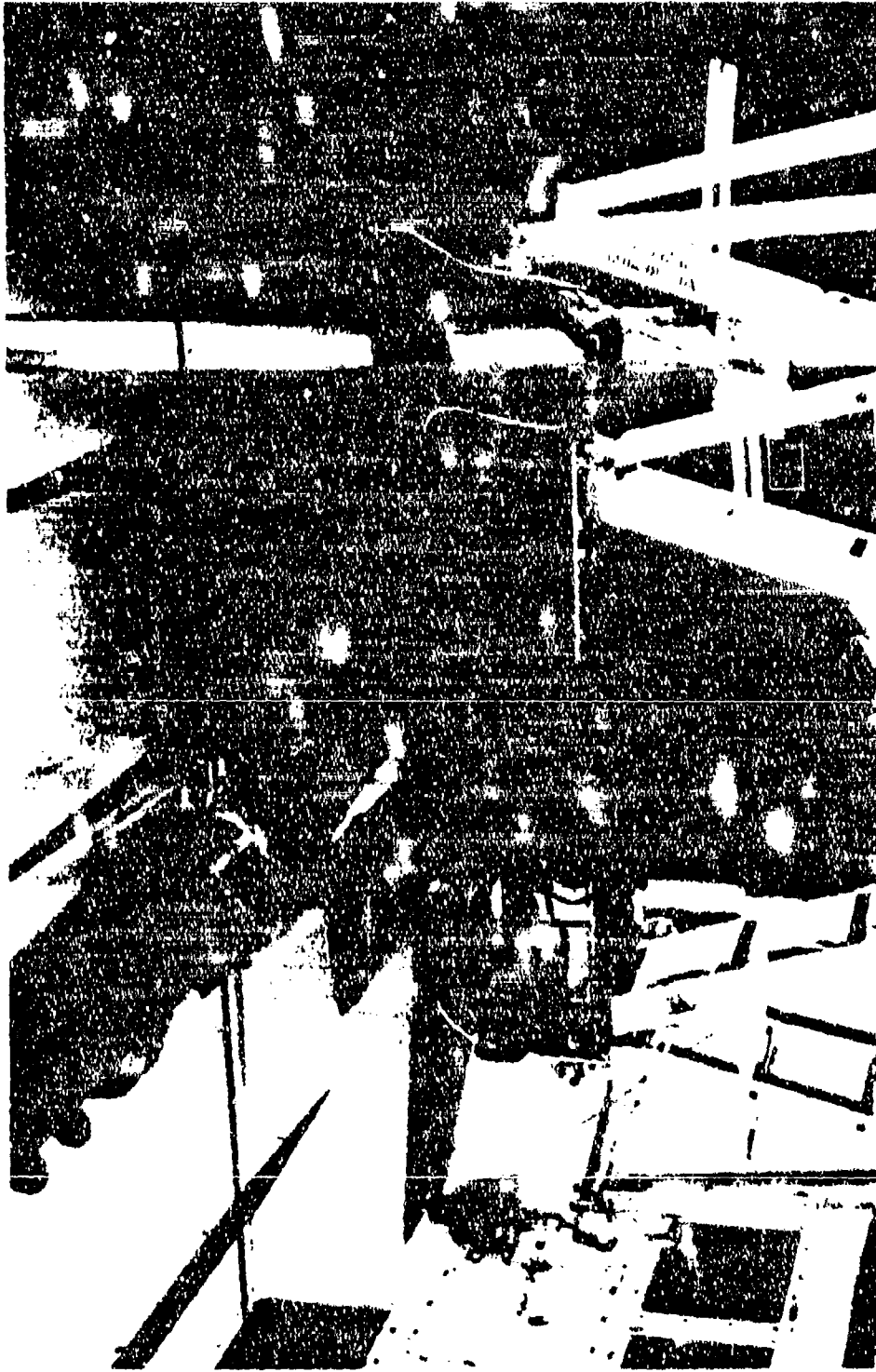


Figure 3-19. GVT Setup in Wind Tunnel

The ground vibration tests were performed for the model mounted on the sting (which was bolted to a laboratory strongback structure) and with the model installed in the wind tunnel. Hydraulic power at 2000 psi (installed in the laboratory by an external hydraulic pump through two hoses that were taped to the back of the model fuselage and connected to the model hydraulic system in the forward fuselage) was supplied to the model. The onboard hydraulic pump was used to supply hydraulic pressure for the tunnel installation GVT. The rotational sting brake was engaged and also pinned to the fixed sting for the brake-on model measurements. The brake was disengaged and the pin removed for the attempted brake-off model measurements. The model pitch angle relative to the sting was zero degrees. Four sets of model data were measured for roll brake-on: 1) symmetric, 2) antisymmetric for the laboratory installation, 3) symmetric, and 4) antisymmetric for the wind tunnel installation. Attempts at measuring valid brake-off modes were unsuccessful because the maximum available shaker forces were inadequate to overcome the breakout friction of the sting roll bearings at most frequencies, because of the bottoming out of the shaker stroke, and because of random shifts in the null roll position of the model.

Multi-shaker sine dwell excitation was used to generate the symmetric and antisymmetric vibration modes. Two shakers were attached to each wing and one shaker was attached to the fuselage. Model frequencies were determined at maximum peak amplitudes from slow frequency sweeps. Modes were then tuned at a constant frequency by adjusting the shaker force amplitude and phases until the responses peaked and decay traces were relatively free of beats. Mode displacement vectors were measured by a roving accelerometer at the structural influence coefficient measurement locations and at locations along the sting. The shakers were the cutoff, and the accelerometer responses measured the free decay which was recorded on a strip chart. The decay trace amplitude-verses-cycle number was then curve-fit with a natural log function to determine the structural damping defined by

$$g = \frac{1}{n\pi} \ln \frac{A_0}{A_n}$$

$n$  = number of cycles

$A_0$  = amplitude at  $n = 0$

$A_n$  = amplitude at  $n^{\text{th}}$  cycle

Control surface hinge-line rotation modes were also obtained with the large mass added to the wing and the wing tip clamped to isolate the control surface from the wing.

Measurements of the model generalized mass were attempted for some of the modes for the laboratory installation. The test procedure involves retuning a given mode after adding distributed masses at 19 locations on the wing and fuselage and measuring the new mode frequency and mode vectors at the 19 added-mass locations. The masses were increased at the 19 locations in three or four increments.

The generalized mass for each mass increment was calculated by

$$M_j = \frac{\sum_{i=1}^{19} (\Delta m_i d_i^2)}{(f_0/f_j)^2 - 1}$$

- where
- $M_j$  = generalized mass for the  $j^{\text{th}}$  increment, lbs
  - $d_i$  = mode normalized deflections at the  $i^{\text{th}}$
  - $m_i$  = incremental mass added to the  $i^{\text{th}}$  location, lbs.
  - $f_0$  = mode frequency, no added mass
  - $f_j$  = mode frequency, for the  $j^{\text{th}}$  added mass increments

The generalized mass for each mass increment was then plotted versus the total mass added and a straight line was fitted to the data and extrapolated to zero added mass, where the generalized mass for the basic mode was determined.

The GVT measured frequencies, damping, and generalized masses for the complete model mounted on the sting in the laboratory are tabulated in Table 3-10 for two configurations antisymmetric with the sting brake-on and symmetric. Mode shapes were measured for the two configurations. The measured mode shapes were manually smoothed and interpolated to the analytical degrees-of-freedom. The first five modes for each configuration are shown in Figures 3-20 through 3-29. Sources of error in the mode shapes came from control surface vibrations induced by the hydraulic control system not related to the external shakers and because the model was slightly unsymmetric in terms of mass or stiffness distribution, which caused the right and left wing to have different responses at the model frequency. The accuracy of mode 3 for the antisymmetric case and mode 5 for the symmetric case is very questionable because of poor orthogonality.

Table 3-10

## GROUND VIBRATION TEST AND MEASURED GENERALIZED MASS RESULTS

SYM	BRAKE	MODE	FREQ GVT (Hz)	Damping GVT	MEAS. GEN. MASS (lbs.)	CALCULATED GEN. MASS ②
LABORATORY INSTALLATION						
A/S ④	ON	STING 1B WING 1B FUS. 1B WING 2B WING 1T WING/FUS. WING 3B	6.2 9.29 16.02 ② 19.0 36.24 39.70 45.50	.0268 .0910 .0760 ② .0374 .0644 .0729 .0549	93.5 3.83 NOT MEAS. 13.33 5.62 2.46 NOT MEAS.	107.5 7.48 38.00 8.22 8.81 2.31 1.94
SYM ④	ON	STING 1B WING 1B FUS. 1B WING 2B WING 1T FUS. 2B WING 2T	6.28 11.11 14.76 32.48 37.73 ③ 39.17 76.53	.0175 .1650 .0368 .0770 .1249 .1079 .042	NOT MEAS. 4.26 20.76 1.10 NOT MEAS. 20.62 NOT MEAS.	77.66 4.01 21.01 4.49 7.255 2.73 1.254
WIND TUNNEL INSTALLATION						
A/S	ON	STING 1B WING 1B FUS. YAW WING 2B WING 1T	6.57 9.29 16.53 20.2 36.36		NOT MEAS.	
SYM	ON	STING 1B WING 1B FUS. 1B WING 2B WING 1T	5.78 11.03 13.10 32.47 36.10			

1 Calculated G.M. =  $\frac{t}{d} \frac{M}{d}$   
GVT analy. GVT

2 Mode retuned at 14.39 Hz for G.M. measurement

3 Mode later retuned AT 41.9 Hz

4 Model mounted to laboratory strong back, no lateral sting cables

AFW 1/6 MODEL - A/S, MEASURED MODES

VIBRATION MODE NO. 1

FREQUENCY 6.20 HZ.

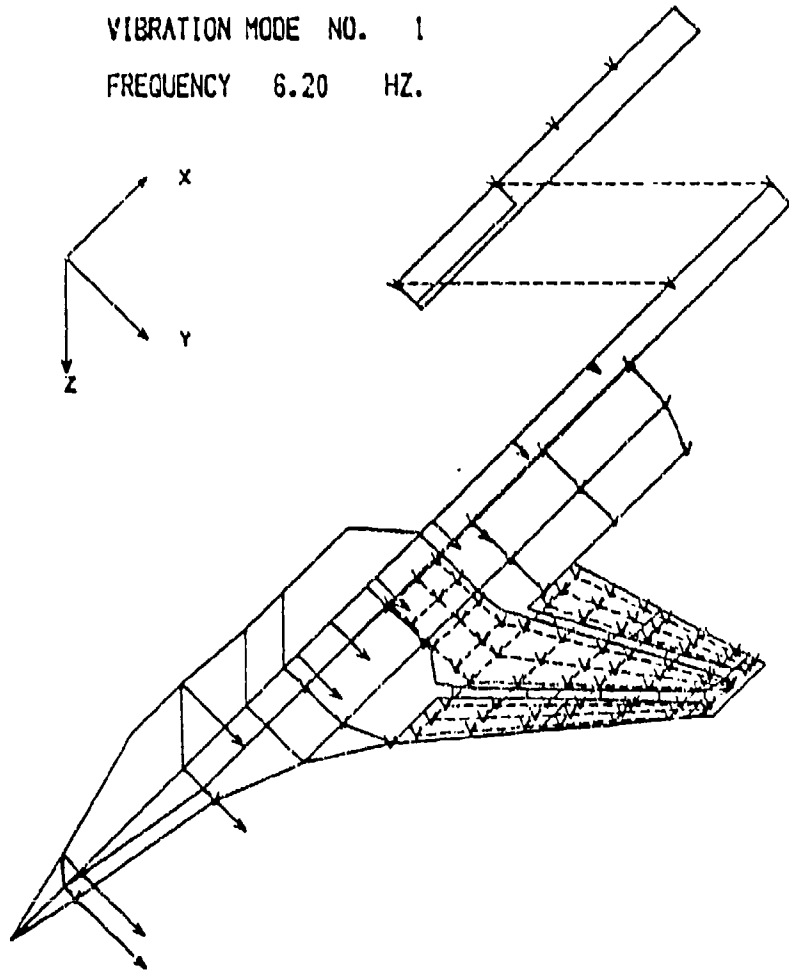


Figure 3-20. Mode 1, A/S Measured Modes in Laboratory

AFW 1/6 MODEL - A/S, MEASURED MODES

VIBRATION MODE NO. 2

FREQUENCY . 9.29 HZ.

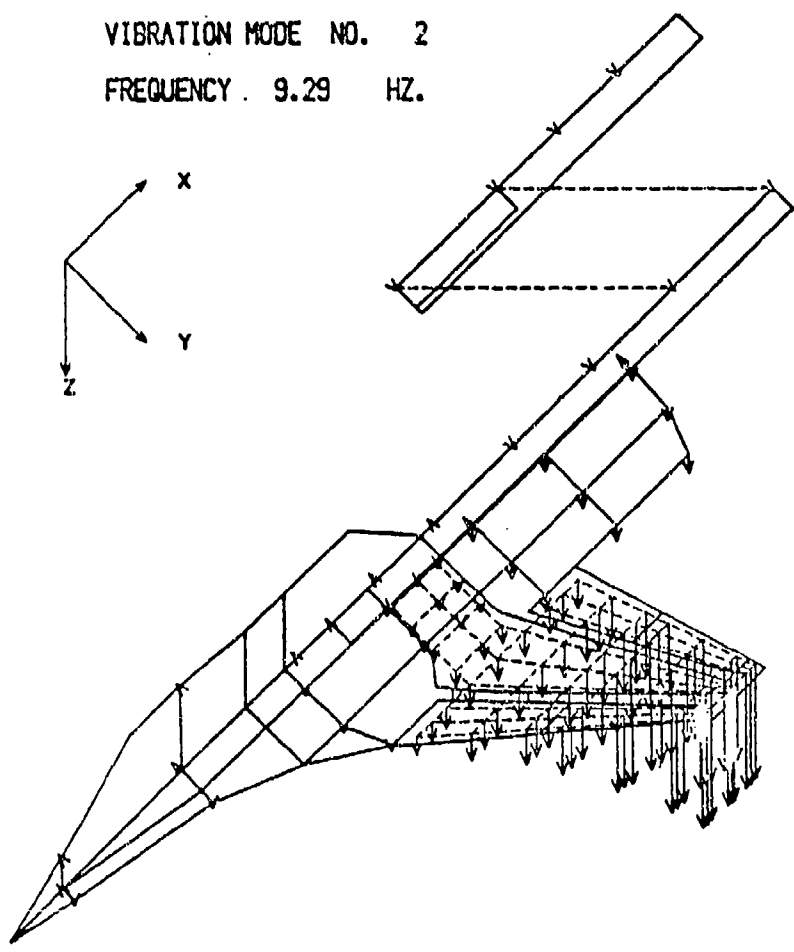


Figure 3-21. Mode 2, A/S Measured Modes in Laboratory

AFW 1/6 MODEL - A/S, MEASURED MODES

VIBRATION MODE NO. 3

FREQUENCY 16.02 HZ.

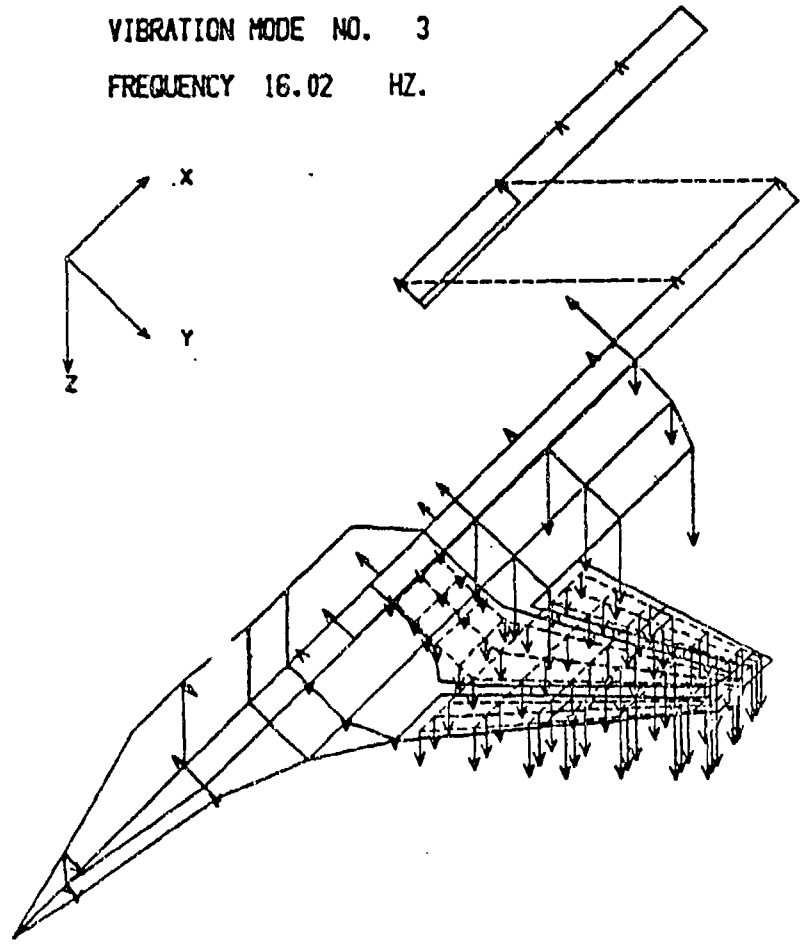


Figure 3-22. Mode 3, A/S Measured Modes in Laboratory

AFW 1/6 MODEL - A/S, MEASURED MODES

VIBRATION MODE NO. 4

FREQUENCY 19.00 HZ.

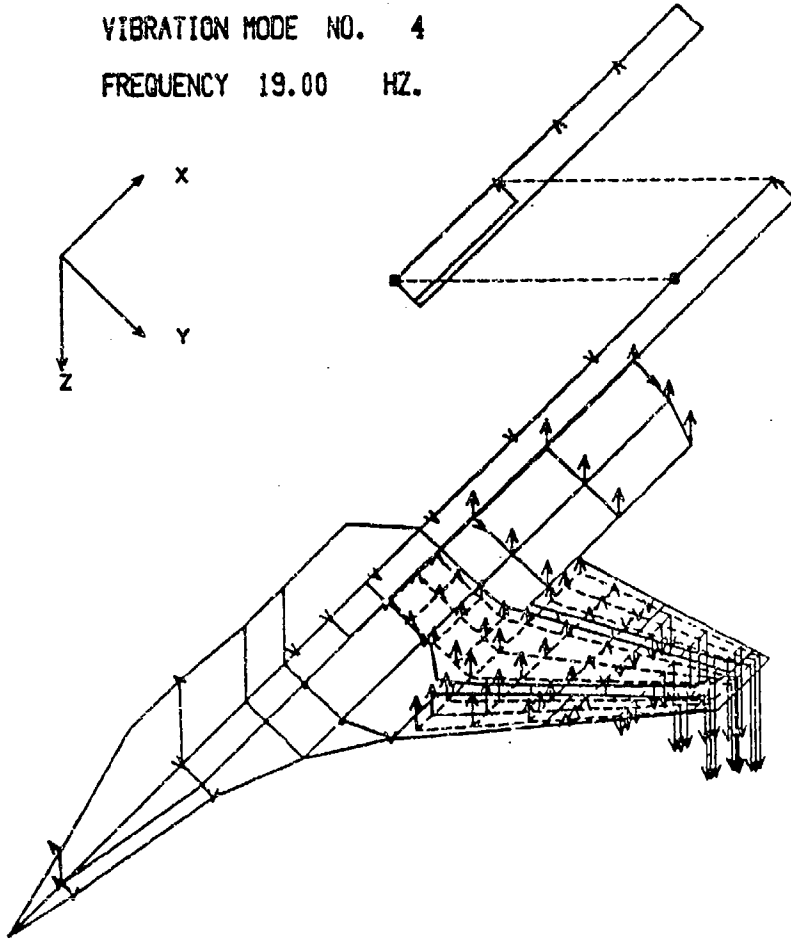


Figure 3-23. Mode 4, A/S Measured Modes in Laboratory

AFW 1/6 MODEL - A/S MEASURED MODES

VIBRATIC. MODE NO. 5

FREQUENCY 36.24 HZ.

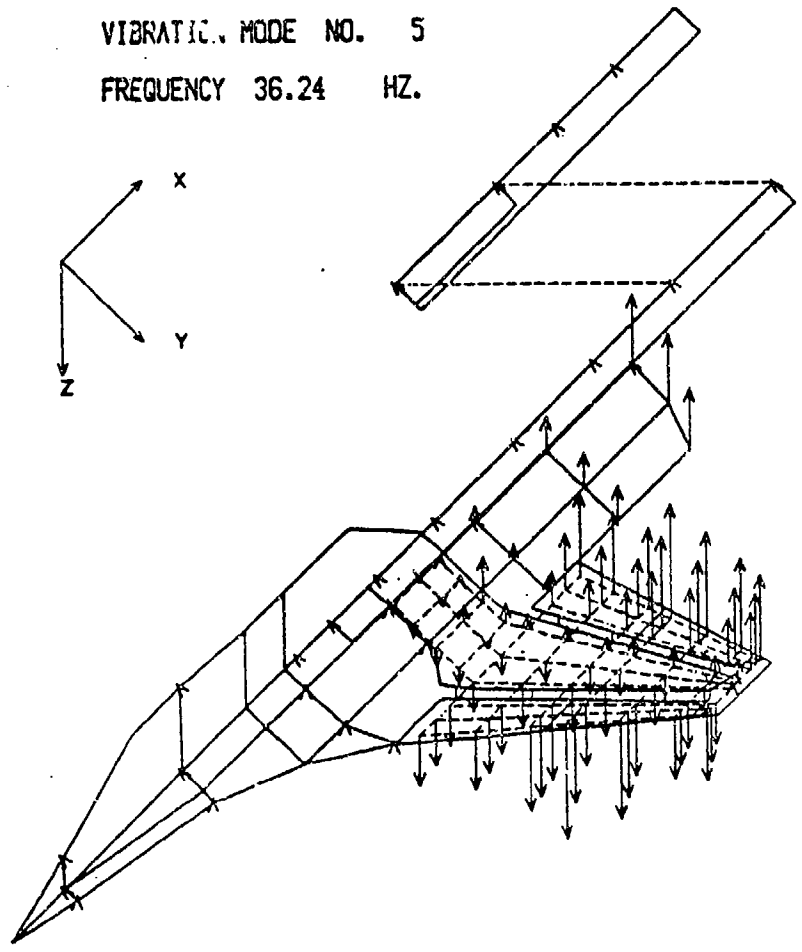


Figure 3-24. Mode 5, A/S Measured Modes in Laboratory

AFW 1/6 MODEL - SYM. MEASURED MODES

VIBRATION MODE NO. 1

FREQUENCY 6.28 HZ.

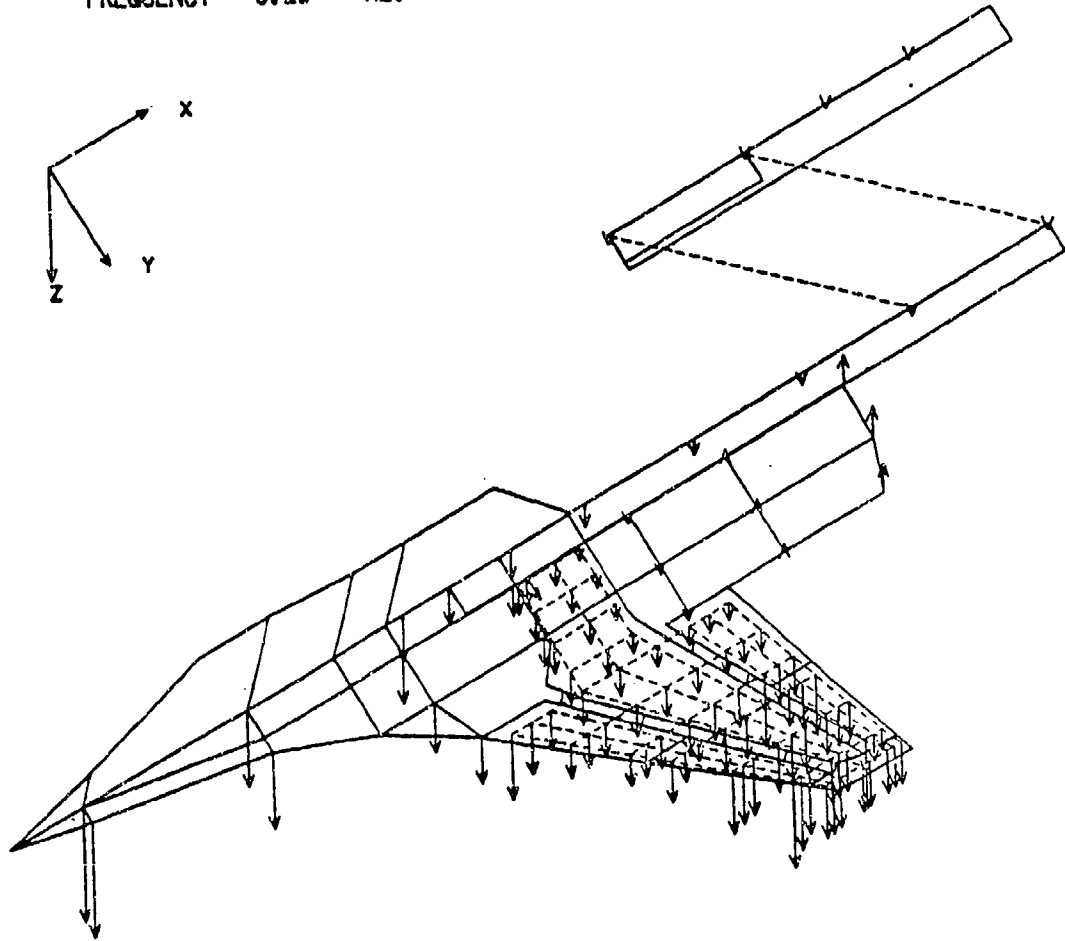


Figure 3-25. Mode 1, Symmetric Measured Modes in Laboratory

AFW 1/6 MODEL - SYM, MEASURED MODES

VIBRATION MODE NO. 2

FREQUENCY 11.11 HZ.

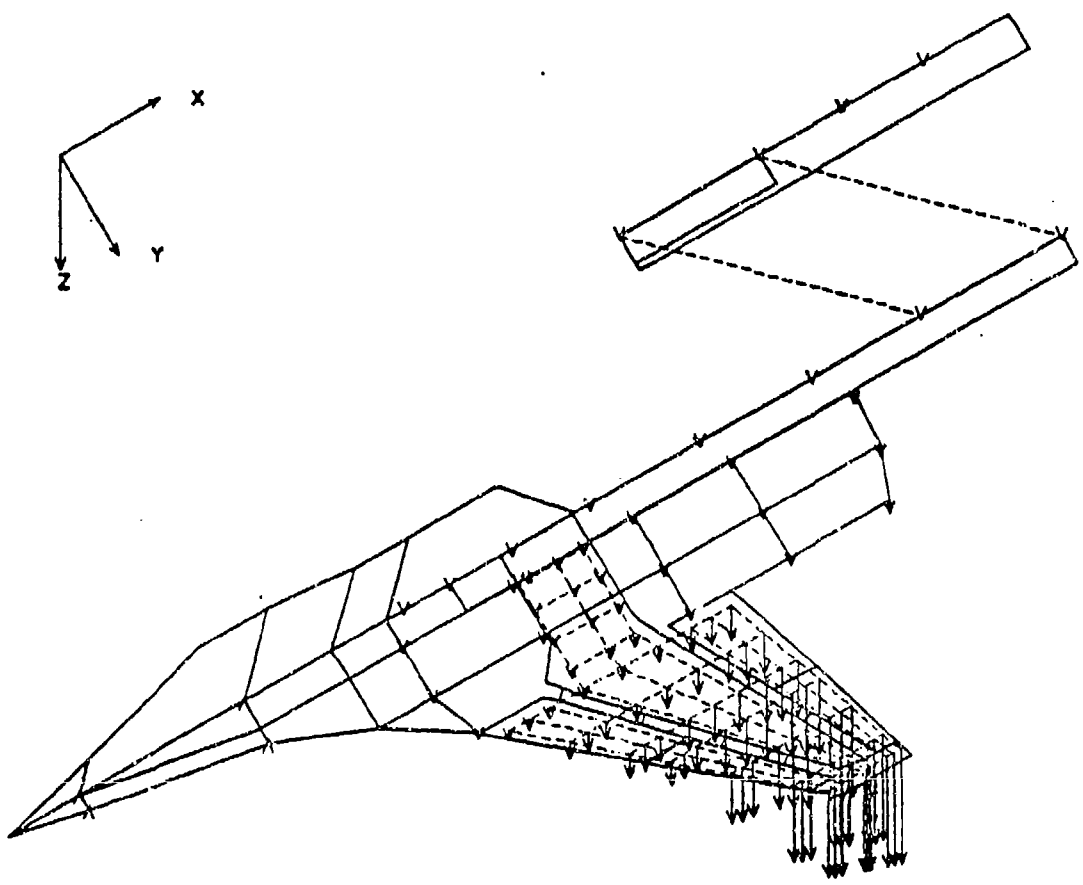


Figure 3-26. Mode 2, Symmetric Measured Modes in Laboratory

AFW 1/6 MODEL - SYM, MEASURED MODES

VIBRATION MODE NO. 3

FREQUENCY 14.76 HZ.

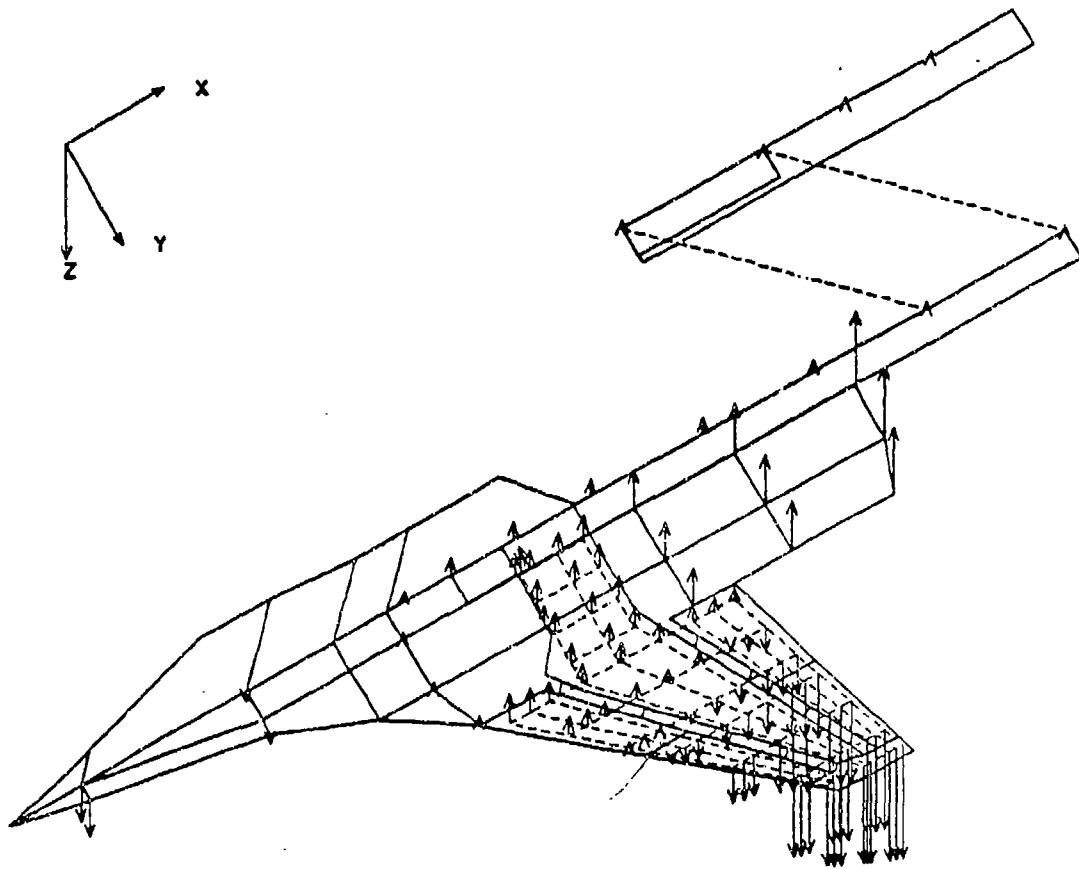


Figure 3-27. Mode 3, Symmetric Measured Modes in Laboratory

AFW 1/6 MODEL - SYM. MEASURED MODES  
VIBRATION MODE NO. 4  
FREQUENCY 32.48 HZ.

88/02/17  
DPLT000

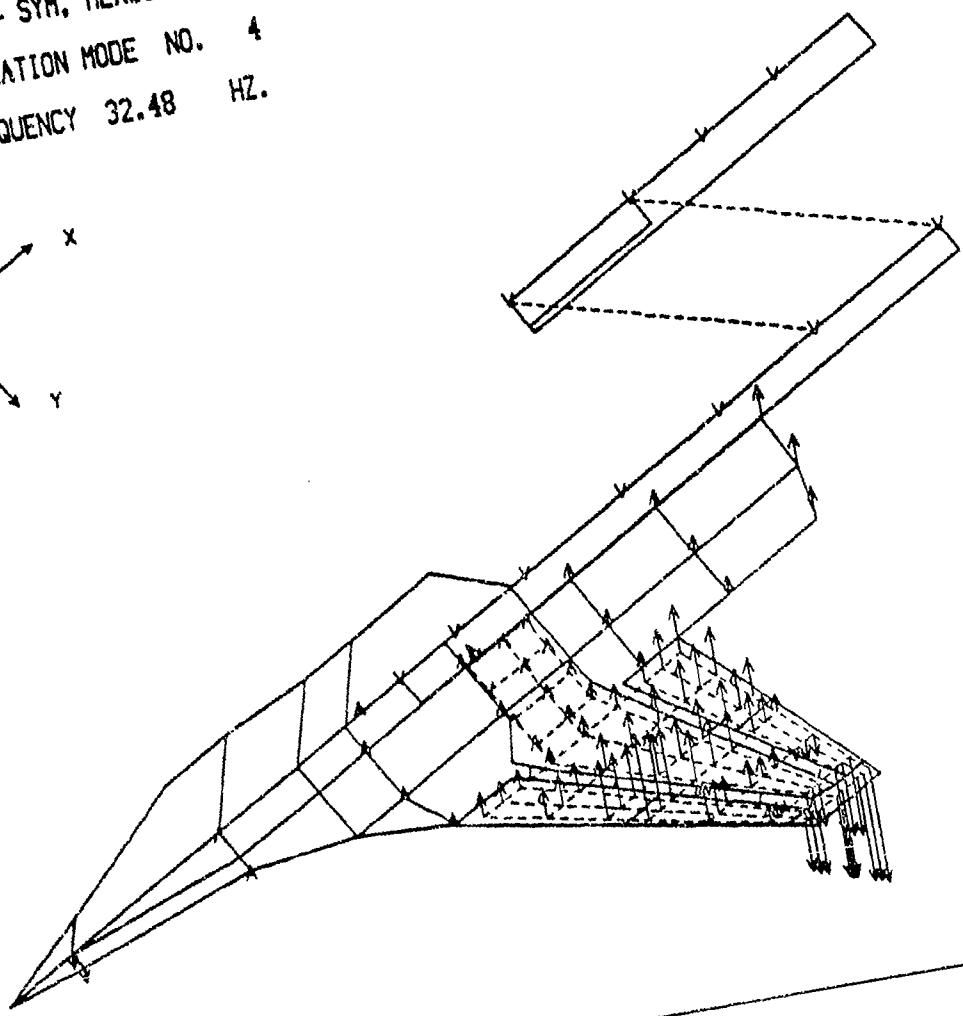
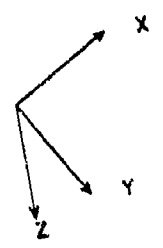


Figure 3-28. Mode 4, Symmetric Measured Modes in Laboratory

AFW 1/6 MODEL - SYM. MEASURED MODES  
VIBRATION MODE NO. 5  
FREQUENCY 37.73 HZ.

05/02/17  
DPLT500

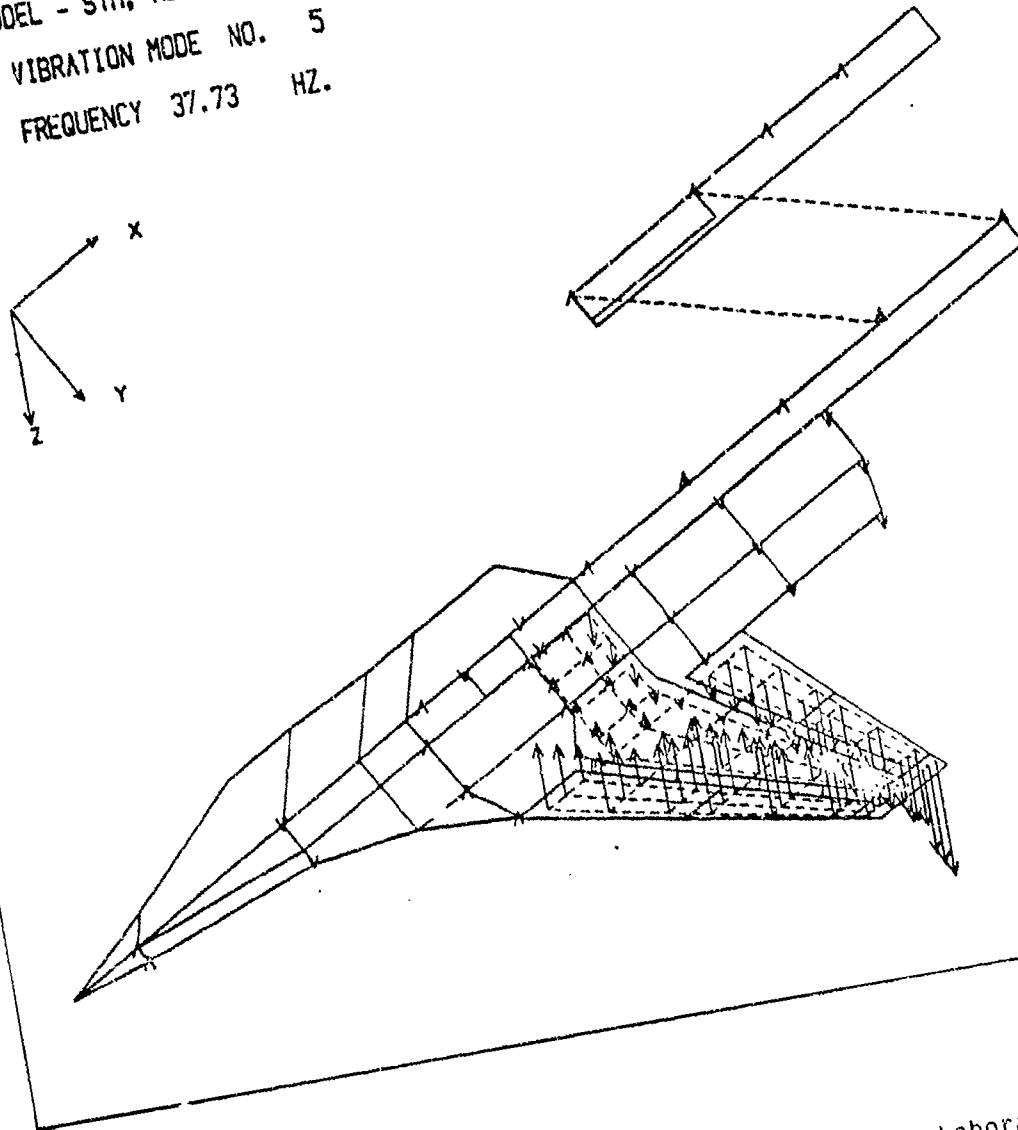


Figure 3-29. Mode 5, Symmetric Measured Modes in Laboratory

The results of the ground vibration test performed with the model installed in the wind tunnel (lateral sting cables connected) and roll brake-on are summarized in Table 3-10 also. Node-line locations were measured and model vectors were measured at approximately 20 locations. Five antisymmetric and five symmetric modes were measured with the sting fixed in roll (brake-on). Because of limitations on available shaker stands, wing shakers and fuselage shakers could not be simultaneously installed. The accuracy of the modes that involved large deflections of both the wing and fuselage, therefore, may be somewhat less than that attainable in the laboratory.

Comparisons of the model frequencies measured in the laboratory and in the wind tunnel (Table 3-10) show that the model frequencies only had minor changes between the two installations.

Control surface hinge-line rotation modes measured for the eight control surfaces are summarized in Table 3-11.

### 3.7 CONTROL SURFACE ACTUATION CHARACTERISTICS

One of the basic requirements for the wing surface actuators was to maintain an amplitude ratio between command and surface position of not more than 2 decibels and not less than minus 3 decibels for all frequencies of less than 26 Hertz. In addition, above 26 Hertz, a rolloff of 40 decibels per decade is allowed. The phase shift requirement was to be less than 120 degrees of lag at 26 Hertz.

Prior to shipping the model and control system to Langley, the electronic gain adjustments internal to the control console were set to twice the gain necessary to cause the onset of limit cycling. This was accomplished by setting the external, graduated, gain control to 50 percent and by increasing the internal gain control until the onset of limit cycling was achieved. Response data were then taken at 25, 50, and 75 percent of the limit cycle gain. From the response data it was determined that leading edge control and trailing edge inboard gains should be set at 40 percent of the limit cycle gain. The trailing edge outboard gain was optimal at 20 percent of the limit cycle gain and, in addition, a lead at 15 Hertz with a lag at 50 Hertz was needed to achieve acceptable responses. The settings of the external controls are summarized below.

CONTROL SURFACE NAMES	GAIN SETTINGS		LEAD SETTINGS		LAG SETTINGS	
	% LCG	POT	Hz	POT	Hz	POT
LEI	40	0.200	50	1.000	50	1.000
LEO	40	0.200	50	1.000	50	1.000
TEI	40	0.200	50	1.000	50	1.000
TEO	20	0.100	15	0.300	50	1.000

Table 3-11

## GROUND VIBRATION TEST CONTROL SURFACE ROTATION MODES

CONTROL SURFACE	SIDE	FREQUENCY (Hz)
Trailing Edge Inboard	R	144.
	L	141.
Trailing Edge Outboard	R	241.
	L	220.
Leading Edge Inboard	R	143.
	L	138.
Leading Edge Outboard	R	283.
	L	271.

- Notes:
1. Large weights added to wing, wing-tip braced
  2. Node-line along hinge-line of each control surface
  3. Hydraulic power turned on

Frequency response data were taken at five tunnel conditions for the right wing actuation systems and at two tunnel conditions for the left wing actuation systems. The data are as follows:

	<u>RIGHT WING ACTUATION SYSTEMS</u>					<u>LEFT WING</u>	
Mach No.	0.0	0.9	0.9	0.9	1.15	0.0	0.9
Q (psf)	0.0	36.5	106.	252.	230.	0.0	252.

Table 3-12 summarizes the frequency response characteristics at the above conditions. Figures 3-30 through 3-37 show the Mach/q equal zero frequency response curves.

The control surfaces responses due to step commands were also determined. Typical response curves are shown in Figure 3-38. Note that the trailing edge outboard responses are more rounded than other surfaces. This is a result of lower gain required for stability due to only one actuator for those surfaces instead of the two used on all other surfaces.

Table 3-12

SUMMARY OF FREQUENCY RESPONSE TESTS OF ATW WIND TUNNEL MODEL  
AT LANGLEY WITH AND WITHOUT AIR LOADS

SURFACE NAME	MACH NO.	"Q" psf	MAGNITUDE RESULTS	PHASE @ 26 HZ
RTEO	0	0	-1.4 TO 2.0 db @ < 47 HZ	-60
LTEO	0	0	-1.9 TO 2.0 db @ < 50 HZ	-60
RTEO	0.9	36.5	-1.9 TO 2.0 db @ < 47 HZ	-65
RTEO	0.9	106	-1.4 TO 2.0 db @ < 47 HZ	-60
LTEO	0.9	252	-2.5 TO 0.8 db @ < 50 HZ	-65
RTEO	0.9	252	-1.4 TO 2.0 db @ < 47 HZ	-60
RTEO	1.15	230	-1.9 TO 1.2 db @ < 50 HZ	-60
LTEI	0	0	-26. TO 4.0 db @ < 50 HZ	-140
RTEI	0	0	-6.0 TO 3.5 db @ < 50 HZ	-85
RTEI	0.9	36.5	-5.3 TO 2.3 db @ < 50 HZ	-90
RTEI	0.9	147	-3.7 TO 0.5 db @ < 50 HZ	-90
LTEI	0.9	252	-26. TO 1.2 db @ < 50 HZ	-150
RTEI	0.9	252	-1.5 TO 0.0 db @ < 50 HZ	-90
RTEI	1.15	230	-1.4 TO 0.0 db @ < 50 HZ	-85
LLEO	0	0	-5.2 TO 0.5 db @ < 50 HZ	-90
RLEO	0	0	-4.8 TO 0.0 db @ < 50 HZ	-90
RLEO	0.9	36.5	-10. TO 3.8 db @ < 50 HZ	-130
RLEO	0.9	148	-6.0 TO 0.4 db @ < 50 HZ	-95
LLEO	0.9	252	-2.0 TO 2.1 db @ < 50 HZ	-80
RLEO	0.9	252	-4.4 TO 0.8 db @ < 50 HZ	-95
RLEO	1.15	230	-5.2 TO 0.6 db @ < 50 HZ	-100
RLEI	0	0	-4.9 TO 0.0 db @ < 50 HZ	-105
LLEI	0	0	-1.6 TO 0.9 db @ < 50 HZ	-95
RLEI	0.9	36.5	-5.2 TO 0.0 db @ < 50 HZ	-110
RLEI	0.9	148	-5.2 TO 0.0 db @ < 50 HZ	-110
LLEI	0.9	252	-1.7 TO 2.9 db @ < 50 HZ	-95
RLEI	0.9	252	-3.1 TO 2.4 db @ < 50 HZ	-110
RLEI	1.15	230	-4.4 TO 4.0 db @ < 50 HZ	-115

28 March 1986

DRTO/COMMAND

M = 0  
q = 0

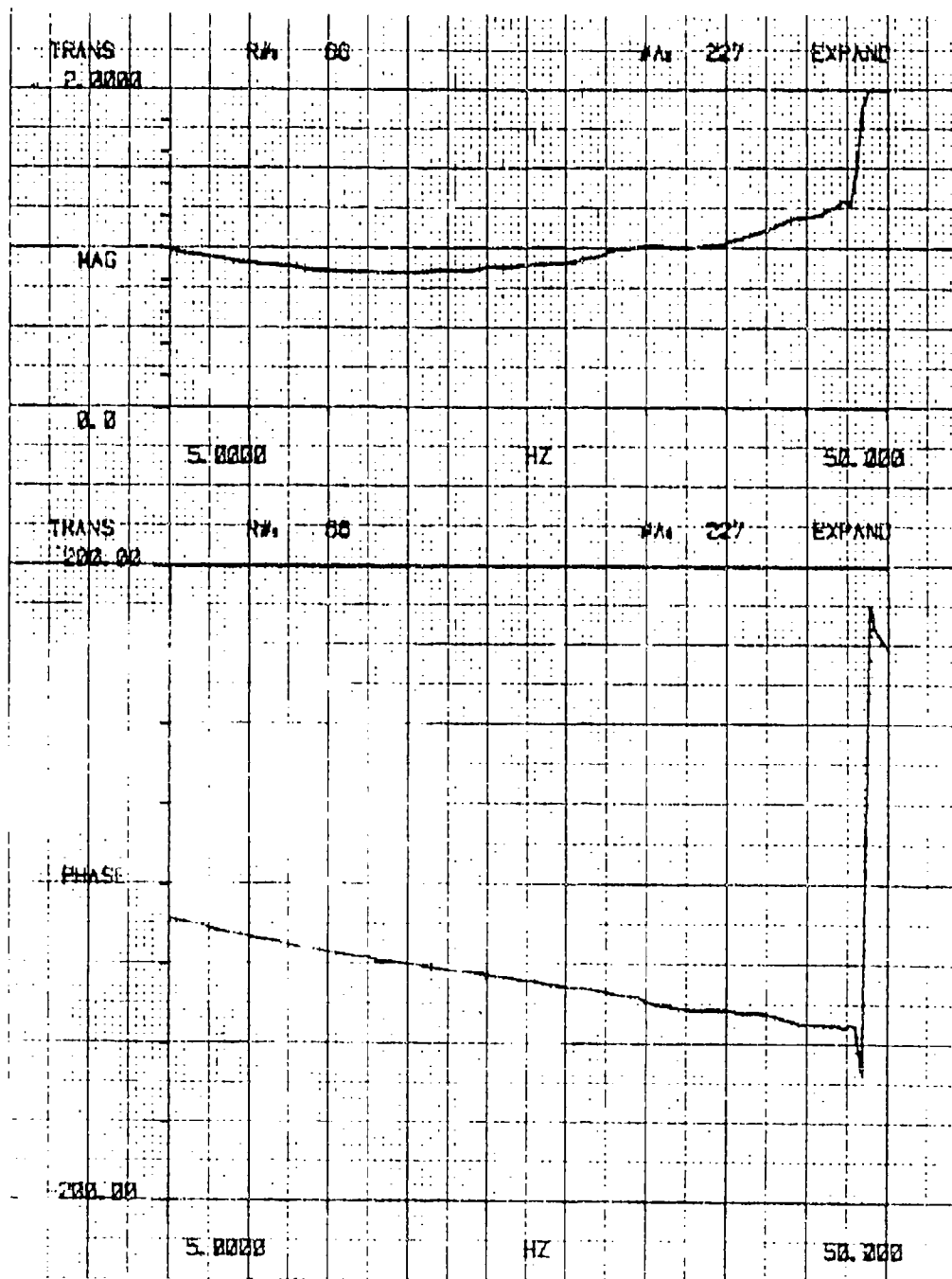


Figure 3-30. Response of RTE0 at Mach 0, q = 0

28 March 1986

DLTO/COMMAND

M = 0  
q = 0

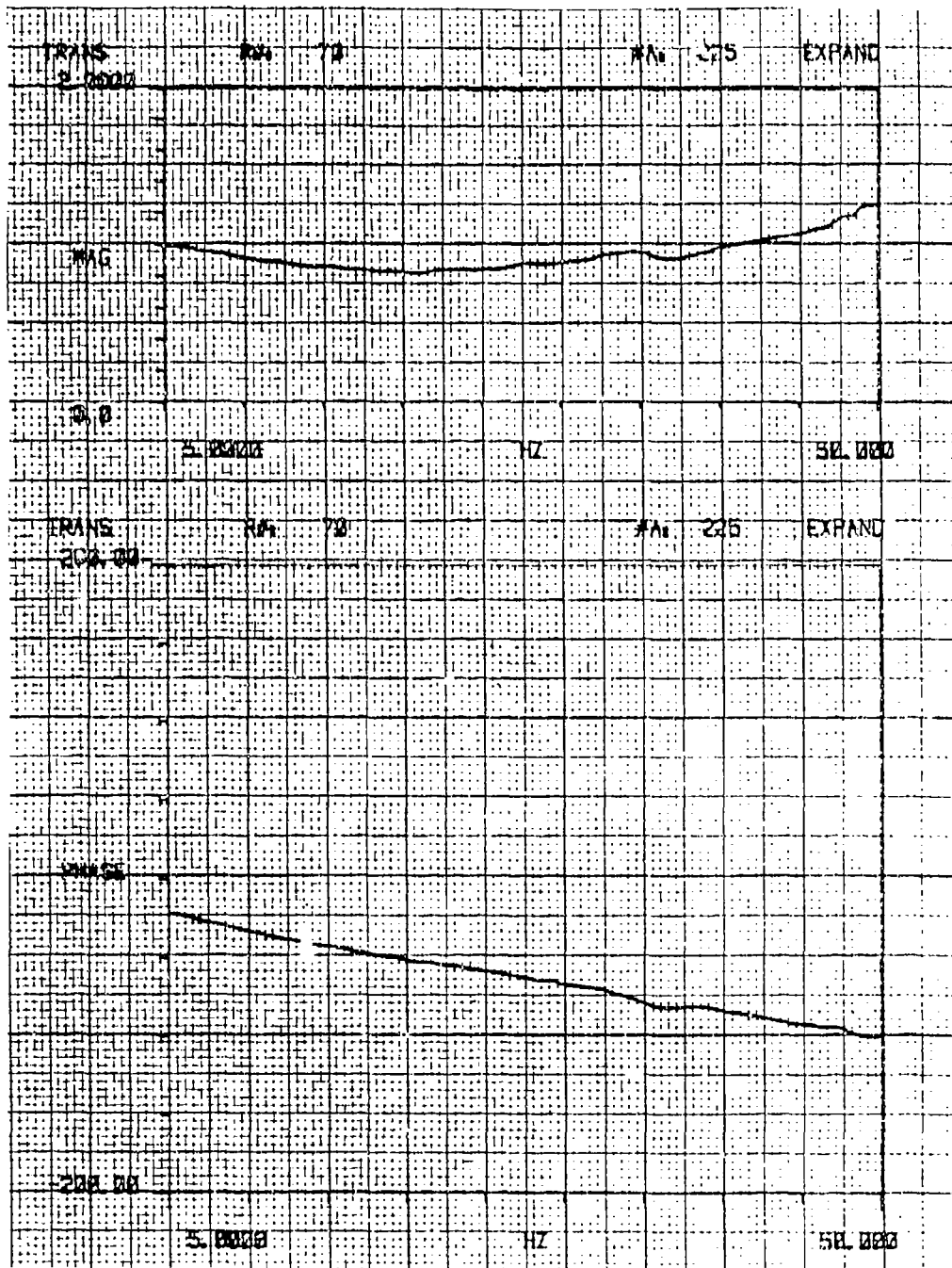


Figure 3-31. Response of LTE0 at Mach 0,  $q = 0$

28 March 1986

DLTI/COMMAND

M = 0  
q = 0

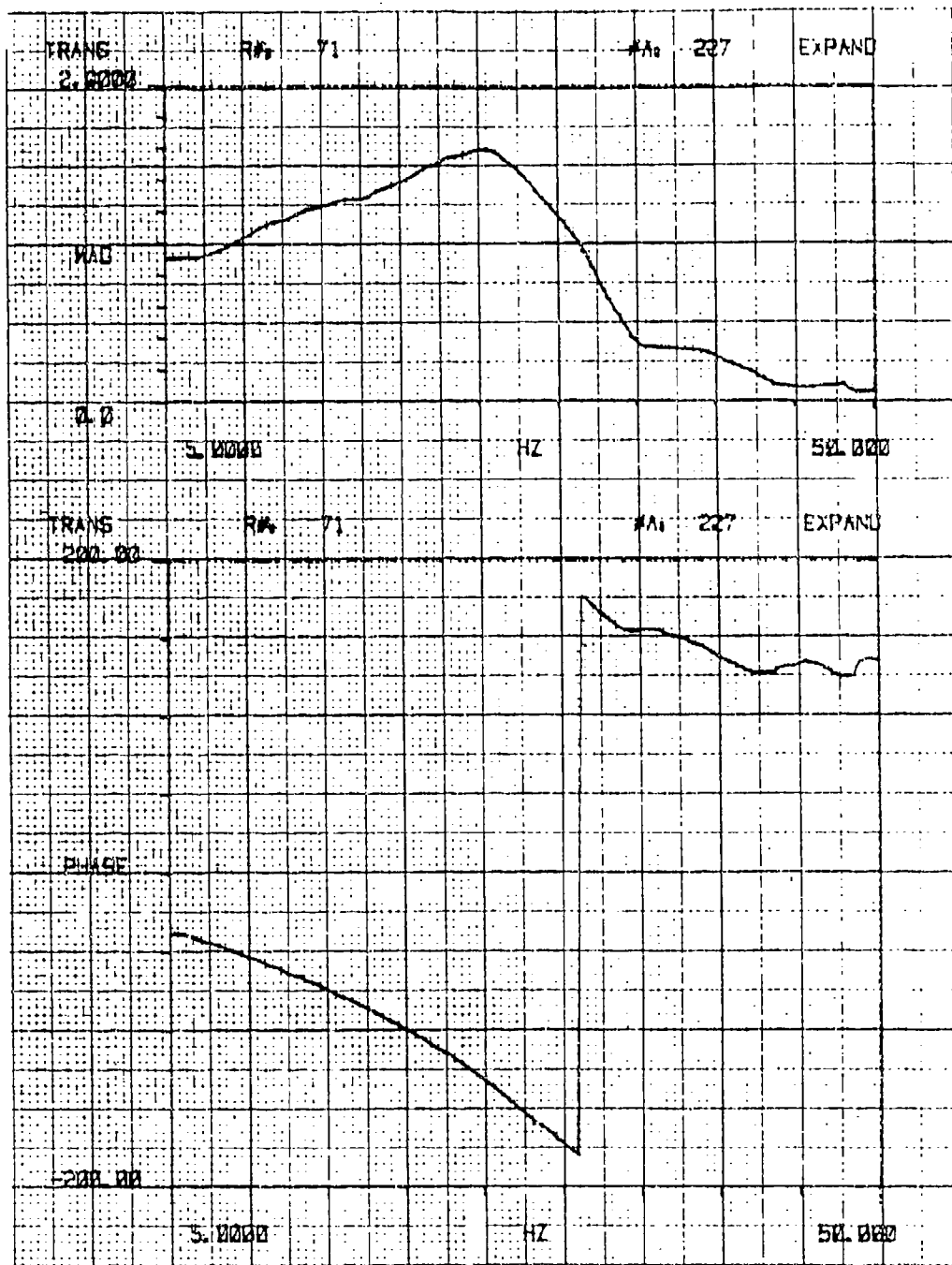


Figure 3-32. Response of LTEI at Mach 0, q = 0

28 March 1986

DRTI/COMMAND

M = 0  
q = 0

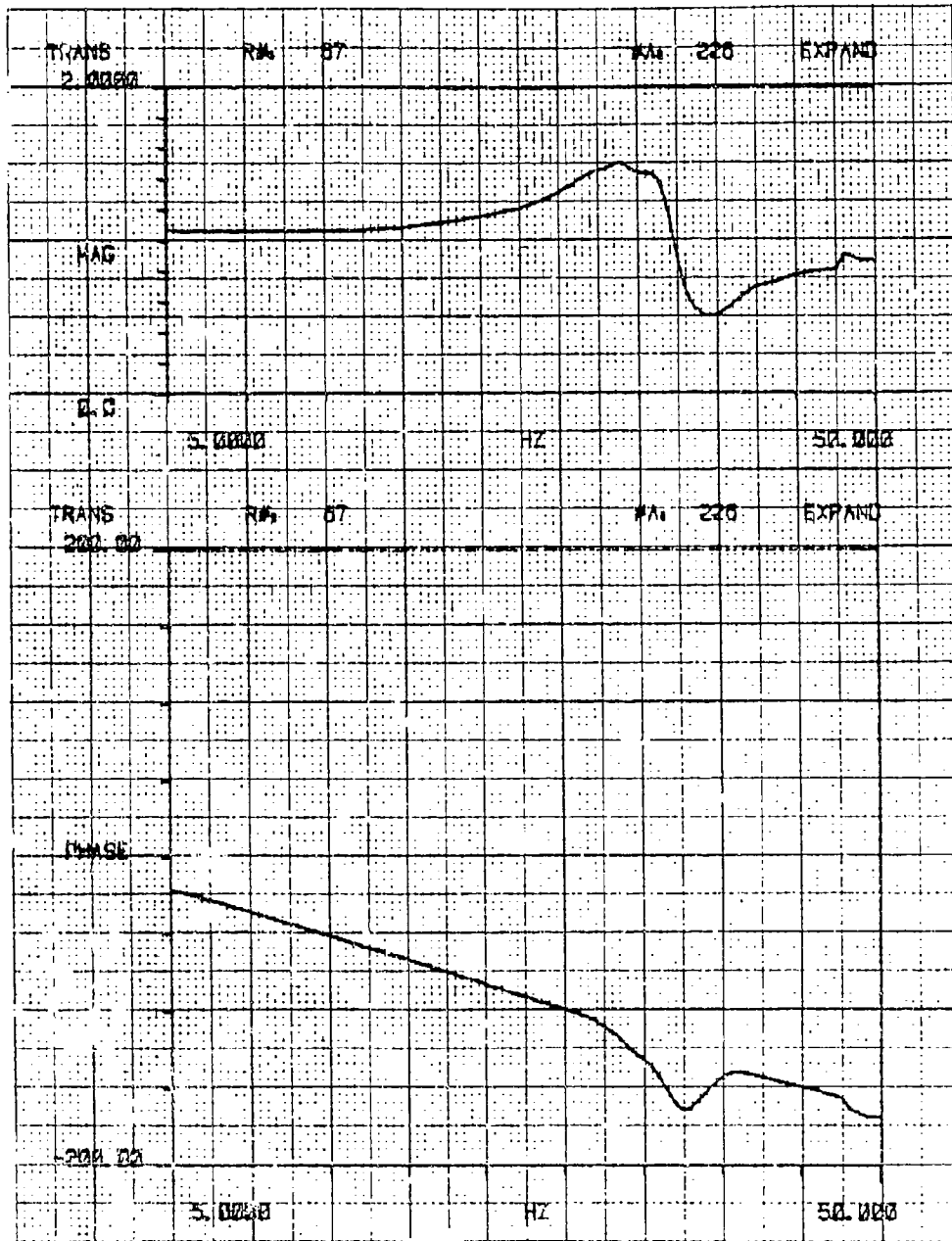


Figure 7-33. Response of RTEI at Mach 0,  $q = 0$

M = 0  
q = 0

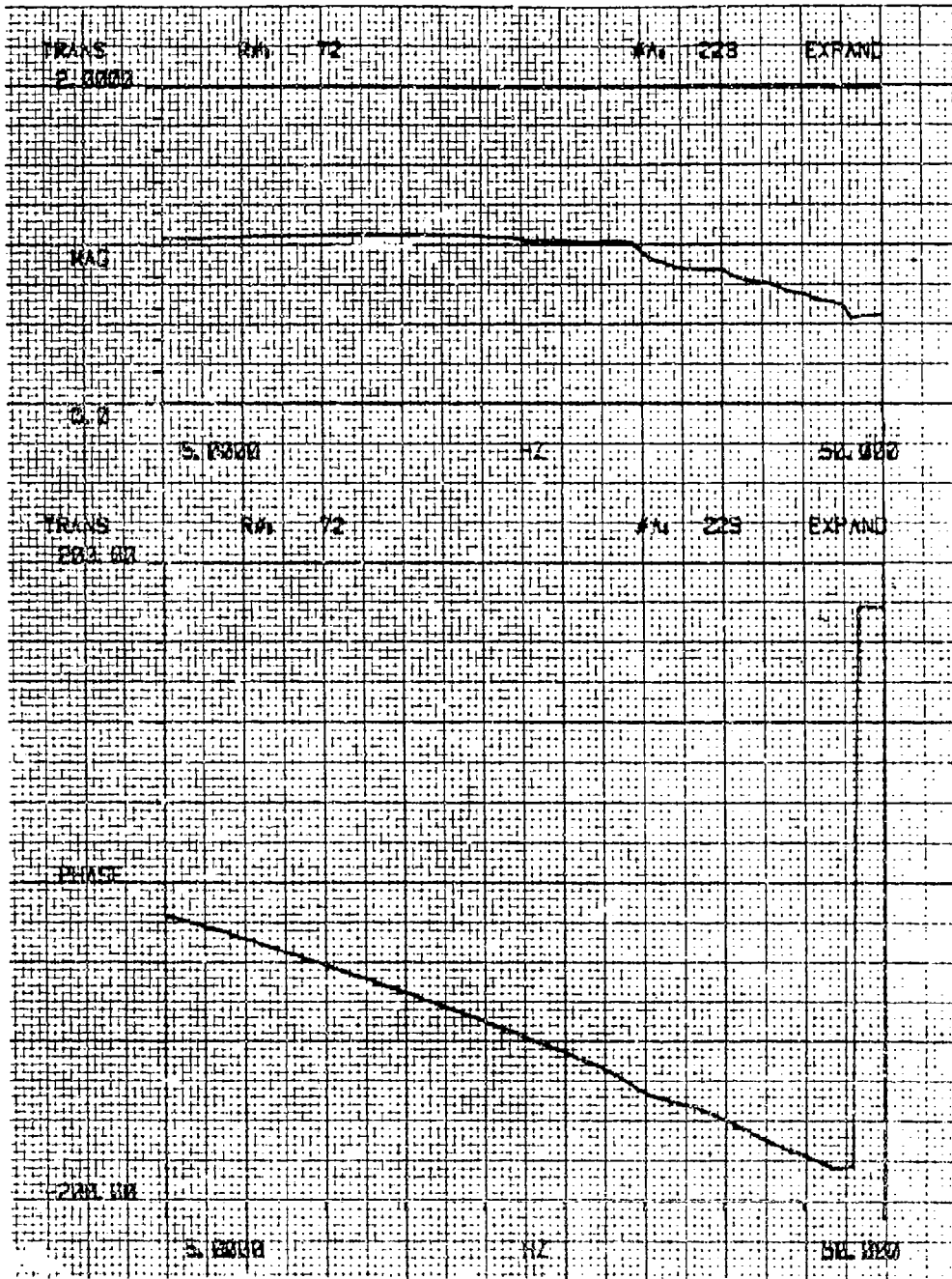


Figure 3-34. Response of LLEO at Mach 0, q = 0

28 March 1986

DRLO/COMMAND

M = 0  
q = 0

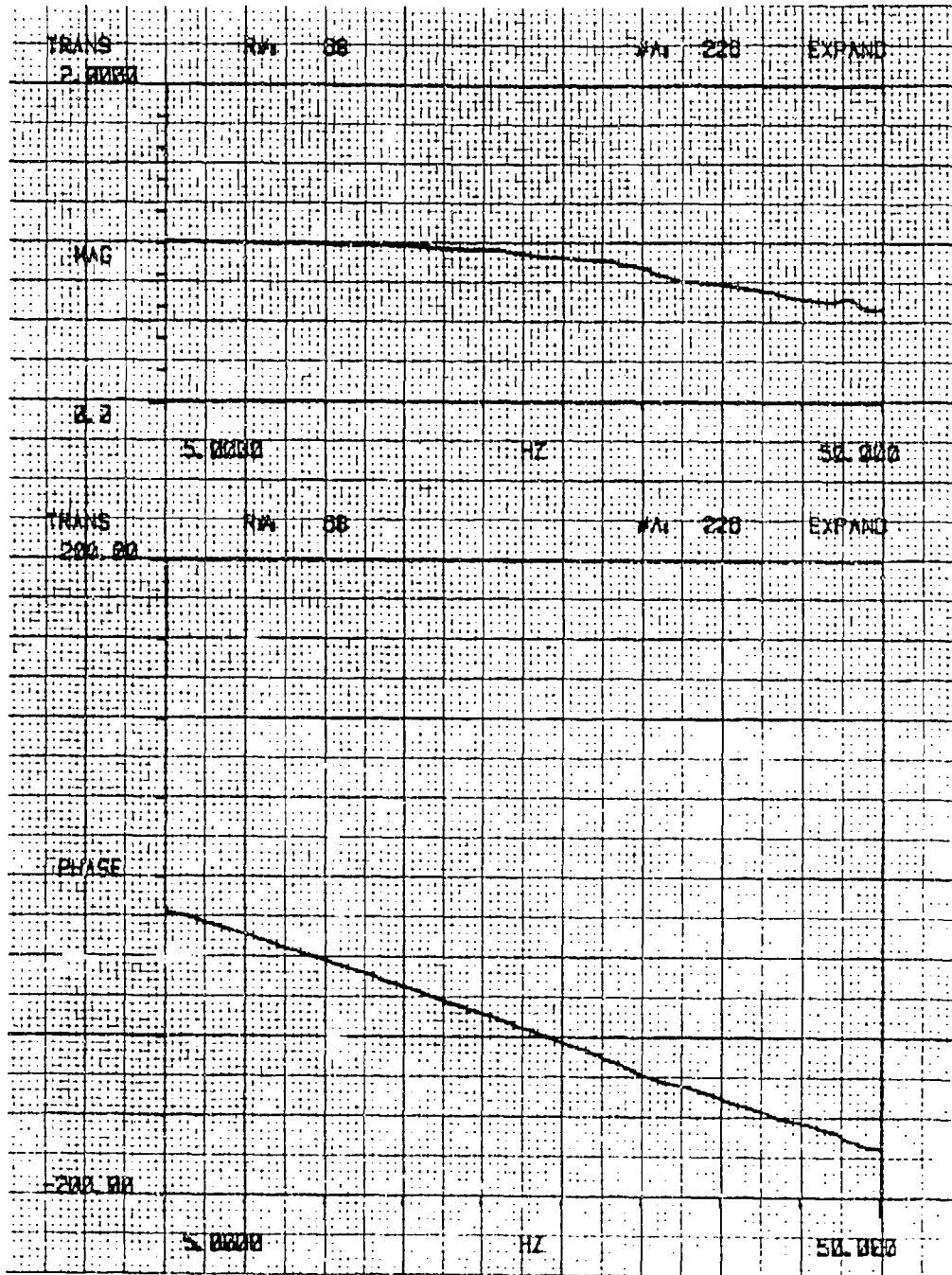


Figure 3-35. Response of RLEO at Mach 0, q = 0

28 March 1986

DLJT/COMMAND

M = 0  
q = 0

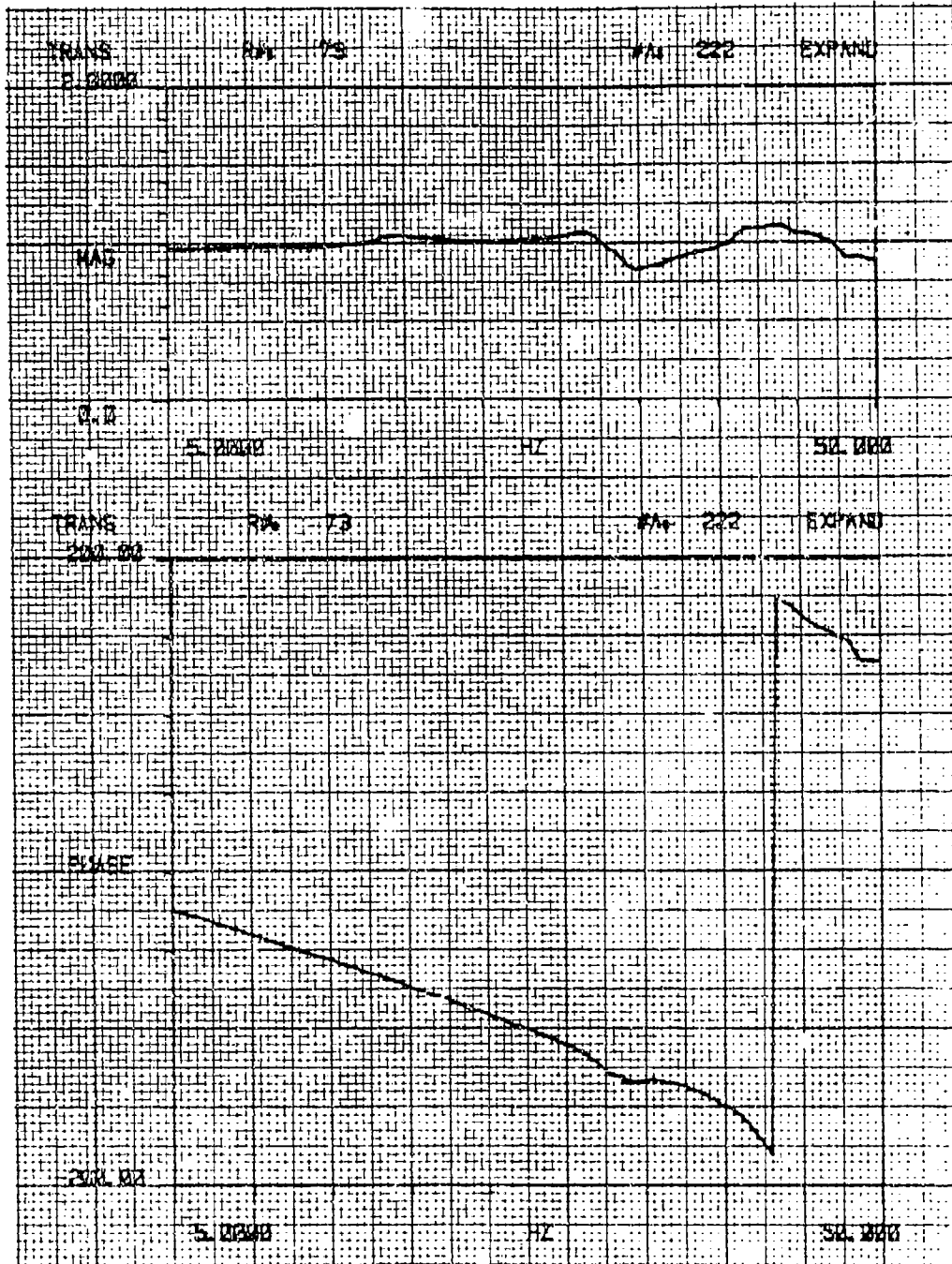


Figure 3-36. Response of RLEI at Mach 0, q = 0

3/18/86

DRLI/COMMAND  $\pm 1^\circ$

Pt. 59  
M = .90  
q - 36.5

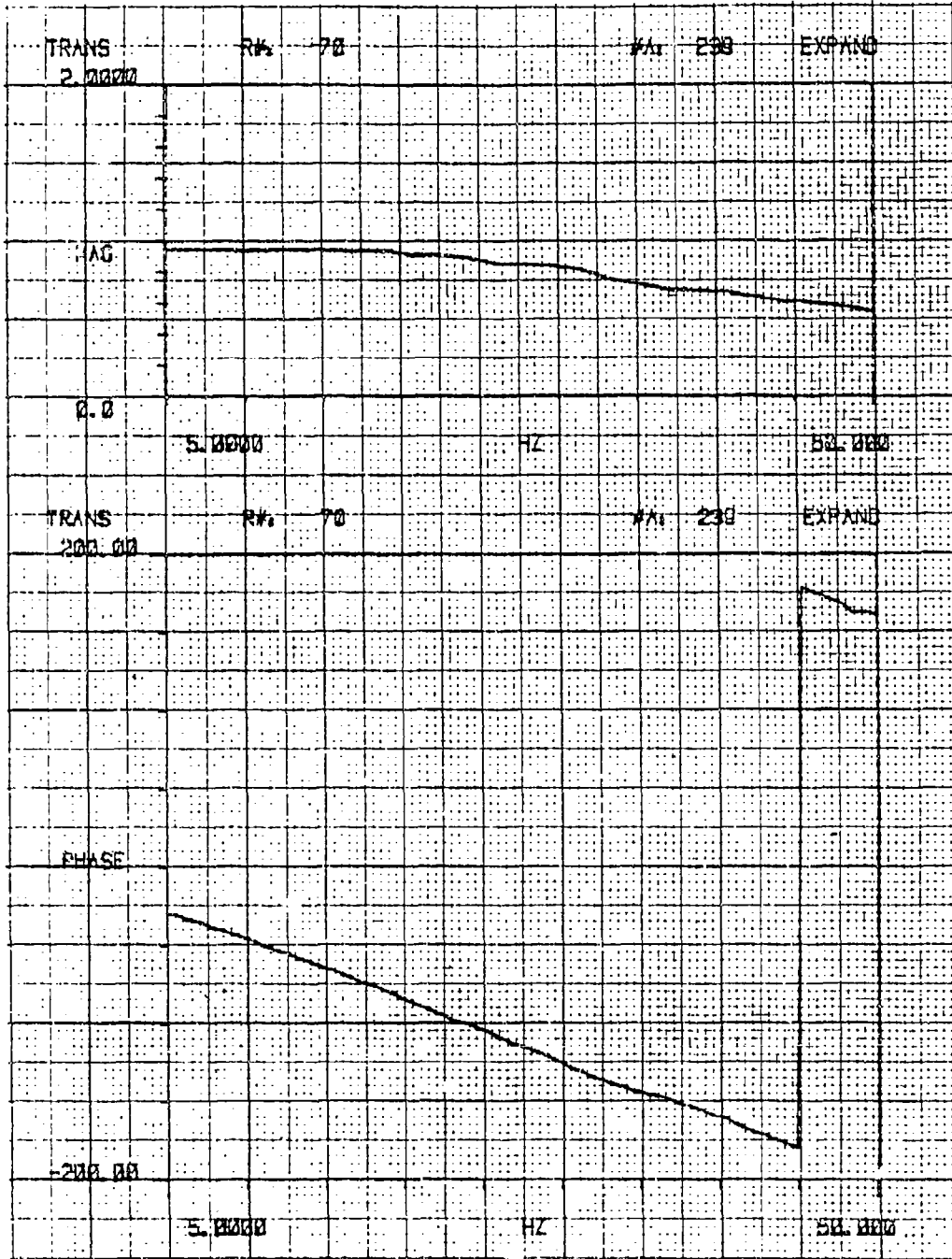


Figure 3-37. Response of LLEI at Mach 0,  $q = 0$

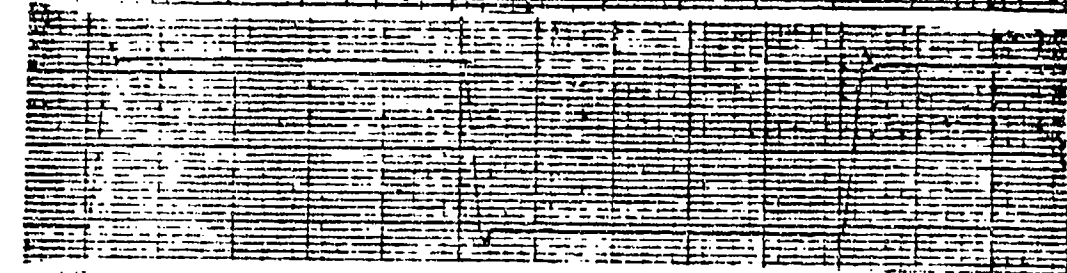
LLEI



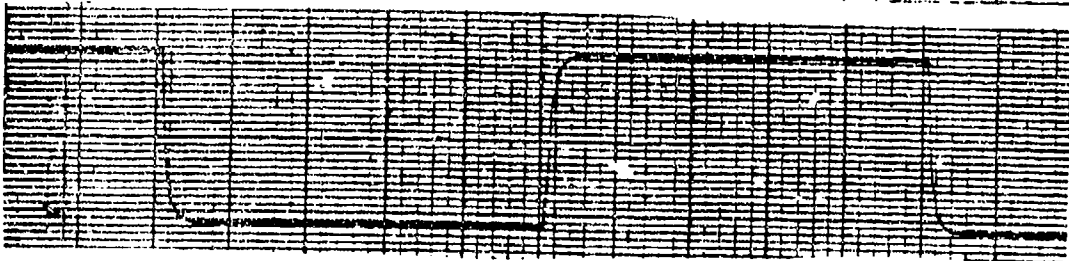
LLEO



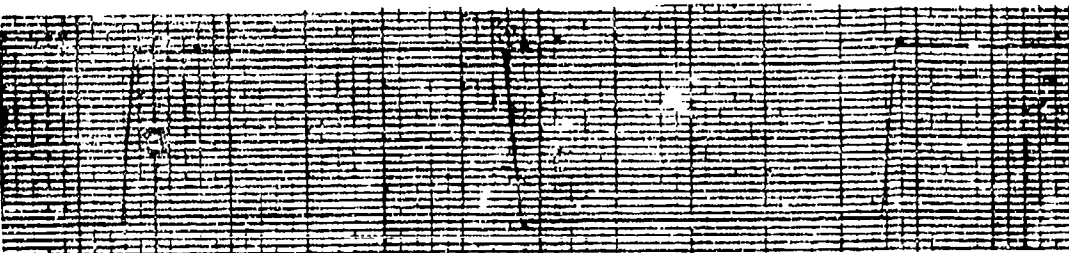
LTEO



RLEI



RTEI



RTEC



Figure 3-38. Typical Step Response for LLEI, LLEO, LTEO, RLEI, RTEI, and RTEC Amplification Systems

## 4.0 WIND TUNNEL TESTS, PROCEDURES, FACILITIES, AND EQUIPMENT

### 4.1 WIND TUNNEL TESTS

Two separate wind tunnel entries were made in the NAS Langley Transonic Dynamics Tunnel (TDT). The entries were in March and April of 1986 and February and March of 1987. The model was tested across the transonic sweep regime. The test envelope is shown in Figure 4-1.

During the first wind tunnel entry, the following tests were conducted:

- The model test envelope was checked to assure that adequate flutter margins existed.
- Static force and moment data were measured for combinations of model angle-of-attack and control surface deflections across the test envelope.
- Dynamic control surface characteristic data were obtained at selected Mach/dynamic pressure points.

During the second wind tunnel entry, the following tests were conducted:

Static wing pressure were measured for combinations of angle-of-attack and control surface position across the test envelope.

- Roll control tests were conducted at 6 Mach/dynamic pressure points.
- Maneuver load control tests were conducted at 2 Mach/dynamic pressure points.
- Structural mode control tests were conducted at 1 Mach/dynamic pressure point.

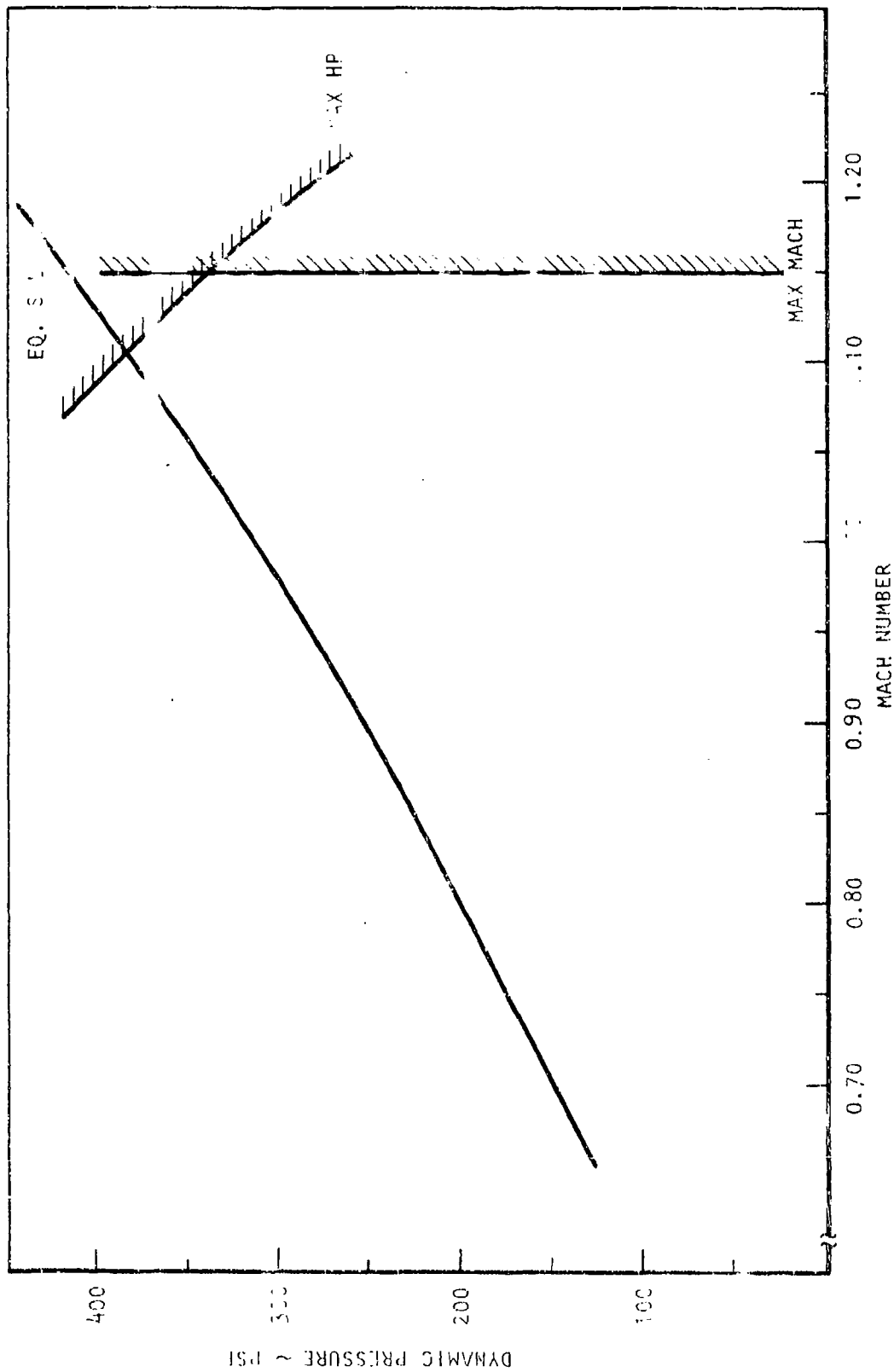


Figure 4. Model Test Envelope

#### 4.2 WIND TUNNEL TEST PROCEDURES

Various test procedures were used during the tunnel tests. The method used for the flutter clearance tests involved maintaining model attitude at zero degrees angle-of-attack at each new test condition while monitoring wing spar strain gage output using a two-channel Hewlett-Packard signal analyzer. The magnitude of the strain gage output at each structural frequency was tracked and plotted versus dynamic pressure at each Mach number.

Control surface effectiveness and longitudinal stability and control data were obtained by setting the model attitude and the control surface deflections with the controller to the required angles at each test condition and then recording the data. Hinge moment data obtained from differential hydraulic pressure measurements made across the vane actuators were also recorded with each steady state data point.

Control system characteristics and stability margins were obtained by inputting either a sine-wave sweep or a 0.5 Hz square wave (simulating a step input) into the appropriate control surface or pitch servo loop. Transfer functions were recorded through the Fast Fourier Transform (FFT) analyzers during the sine-wave sweeps. The sine-wave sweeps were generally run over a 5-to-50 Hz frequency range using nominal 1-degree peak-to-peak control surface deflection. The sine-wave sweep signal was capable of being input into a single surface, symmetrically into a surface pair, or antisymmetrically into a surface pair.

The static data (taken during these tests) using Langley's Data Acquisition System were sampled 1000 times per second and were averaged over a 1-second period.

Periodically, using cameras mounted on the tunnel sting support and on the west wall window inside the control room, high-speed movies were taken during testing.

Roll control tests were conducted using the model's digital computer controller. Two kinds of roll tests were conducted, roll transient and roll control stability. In the roll transient tests, the model was trimmed to a given bank angle by the controller using a roll trim control law; then it was commanded to roll through 90 degrees at a commanded rate whereupon it was commanded to stop rolling using a separate roll control law in the controller. The model was then returned to the roll trim mode to hold at the final bank angle. Commanded roll ratios were increased until a maximum roll rate (minimum roll time to 90 degrees) was achieved. Roll control stability tests were conducted by insertion of a sine-wave sweep signal into the roll rate amplifier summing junction and recording the system response at test points provided in the electronics. Both open and closed loop response was obtained by monitoring the appropriate test points.

Maneuver load control tests were conducted by forcing the model to pitch with ramp commands from the digital computer. Control laws provided commands to move the model control surfaces to reduce wing bending moments. Maneuver load control open and closed loop stability tests were conducted by inputting a sine-wave into model pitch command signal and measuring the appropriate responses.

Structural mode control (SMC) tests were conducted using the digital computer with SMC control laws. The model was excited by forcing control surface deflections with a sine-wave generator. Model dynamic responses were measured with the SMC control law both on and off to determine performance. Open and closed loop stability tests were conducted inputting a sine-wave into the computer accelerometer sensor input and measuring appropriate responses.

#### 4.3 FACILITIES

The facility for this tunnel entry is a continuous flow, closed return wind tunnel which operates from Mach numbers near 0 to 1.20 at total pressures ranging from 0.2 psi (pounds per square inch) absolute to atmospheric pressure within the structural and power limitations of the tunnel. A test medium of either air or Freon -12 (dichlorodifluoromethane) may be used. For the tests described in this report the Freon -12 test medium was used. The test section is approximately 16.0-foot square with corner fillets. The ratio of area contraction of the entrance section is 8.9 to 1. Longitudinal slots along the floor and ceiling provide a means for alleviating blockage resulting from a model and give an open area of 2.1 percent. Slots in the sidewalls give an additional 2.3-percent open area. Models may be mounted to the tunnel west sidewall, cable-mounted along the tunnel centerline, or on the sting supported on the tunnel centerline. The sting mount was used during the test described herein. A method for quick reduction of the tunnel dynamic pressure and Mach number was incorporated into the tunnel design. This consists of four 36-inch-diameter, quick-opening valves located in bypass lines which connect the test chamber and the tunnel return leg downstream of the drive motor nacelle.

#### 4.4 EQUIPMENT

The following test equipment was used during this tunnel entry:

- Hewlett-Packard Model 3582A Signal Analyzer
- Hewlett-Packard Model 5423A Signal Analyzer
- Spectral Dynamics Model SD104A Sweep Generator
- Rockwell Automatic Dynamic Trip System (6 Channel)
- Rockwell Automatic Static Trip System (12 Channel)

## 5.0 STATIC AEROELASTIC DATA AND ANALYTICAL CORRELATION

The wind tunnel model was analyzed and test data were obtained during the two tunnel entries to determine its static aeroelastic characteristics. The analytical results were compared with test results to determine the validity of the analytical tools to predict adequately the flexible characteristics of the model. Flexible force and moment data were calculated as well as those derivatives with respect to angle-of-attack and control surface deflections. Also, pressure data were measured on one wing panel and were used to calculate wing deflections. (The pressure data were obtained only during the second wind tunnel entry.) The pressure data can also be used as a data base for correlations with nonlinear CFD aerodynamic calculations.

### 5.1 MODEL FORCE AND MOMENT DATA

#### 5.1.1 DATA ACQUISITION AND PROCESSING

Each steady-state data point was acquired through the Langley Research Center's Data Acquisition System, processed on the Sigma 5 computer, and recorded on digital magnetic tape for transmittal to Rockwell. The magnetic tape format generated at Langley was not compatible with Rockwell's mainframe computer tape drive, thus extensive data manipulation was performed to reformat the data.

Data reduction at Rockwell consisted of five phases. In the first phase the data were transferred to the disk from magnetic tape. During Phase 2, the data were sorted by Mach number and dynamic pressure and bad points were edited. In Phase 3, the data were reformatted and only 31 variables were retained. The results of this phase were tabulated. The fourth phase consisted of curve fitting, selected coefficient data and extracting linear derivatives for effectiveness calculations. In the fifth phase, the data were again formatted (for use by the Flight Control Group) and then plotted. The parameters retained during Phase 3 constitute the static aerodynamic data base used to develop the required control laws for roll and maneuver load control. These parameters are:

- a. Six-component force and moment data from the internal balance
- b. Wing bending moment (four) and torsional moment (four) data from the wing spar strain gages
- c. Control surface hinge moments (eight)
- d. Control surface deflections (eight)
- e. Model pitch angle

Control surface effectiveness data were obtained by curve fitting the coefficient data versus surface deflection angle using a least squares linear fit over a small deflection range about zero degrees and taking the derivative. Lift and pitching moment curve slopes were determined in a similar manner by curve fitting the coefficient data-versus-angle-of-attack over a small angle-of-attack range and computing the derivatives. The hinge moment coefficients of the deflected surface and the surface upstream or downstream of the deflected surface were curve fitted using a linear least squares method when the data were linear enough to justify use. When non-linearity was exhibited, the data were hand-plotted to evaluate the slopes. Wing spar inboard and outboard torsional and bending moment coefficients were curve fitted similarly.

### 5.1.2 TEST ENVELOPE

Testing was conducted over the Mach number-dynamic pressure envelope presented by Figure 5-1. Low angle-of-attack, small surface deflection data were obtained for each condition indicated by the symbol "L". At test conditions, shown with the symbol "H", high surface deflection, low angle-of-attack data were gathered. The symbol  $\textcircled{H}$  indicates conditions at which high angle-of-attack, high surface deflections were tested. Control system transfer functions and response to step inputs were obtained at the conditions shown by the symbol "T". The symbol "M" denotes test conditions at which multiple surface deflection data were obtained to validate the linear superposition theory. Free-to-roll testing was accomplished at the test point shown by the symbol "F".

### 5.1.3 TEST DATA AND ANALYSIS CORRELATION

A comparison between the data obtained in the first entry and the theoretical results of the Rockwell FA475 Flexible Unified Distributed Panel (FUDP) program is provided when available. The FUDP program is a chordwise linearly-varying doublet panel code. It is an extensively modified version of the original Ames (Woodward) Wing-Body program. Several new features were incorporated into the program in addition to alleviating some of the computational problems inherent in the original version.

Flexible configurations are analyzed by combining an externally calculated structural influence coefficient (SIC) matrix with the aerodynamic influence coefficient matrix to produce flexible characteristics for any given free-stream dynamic pressure. The program cannot predict drag, and the test procedure and test instrumentation in the wind tunnel model cannot predict drag accurately. Drag predictions are beyond the scope of this test.

The effect of flexibility (i.e., dynamic pressure) on the lift-curve slope is shown in Figure 5-2. The figure shows that the theoretical curves follow the same trends as the experimental curves. However, theory indicates a higher lift-curve slope for the Mach number and dynamic pressure range

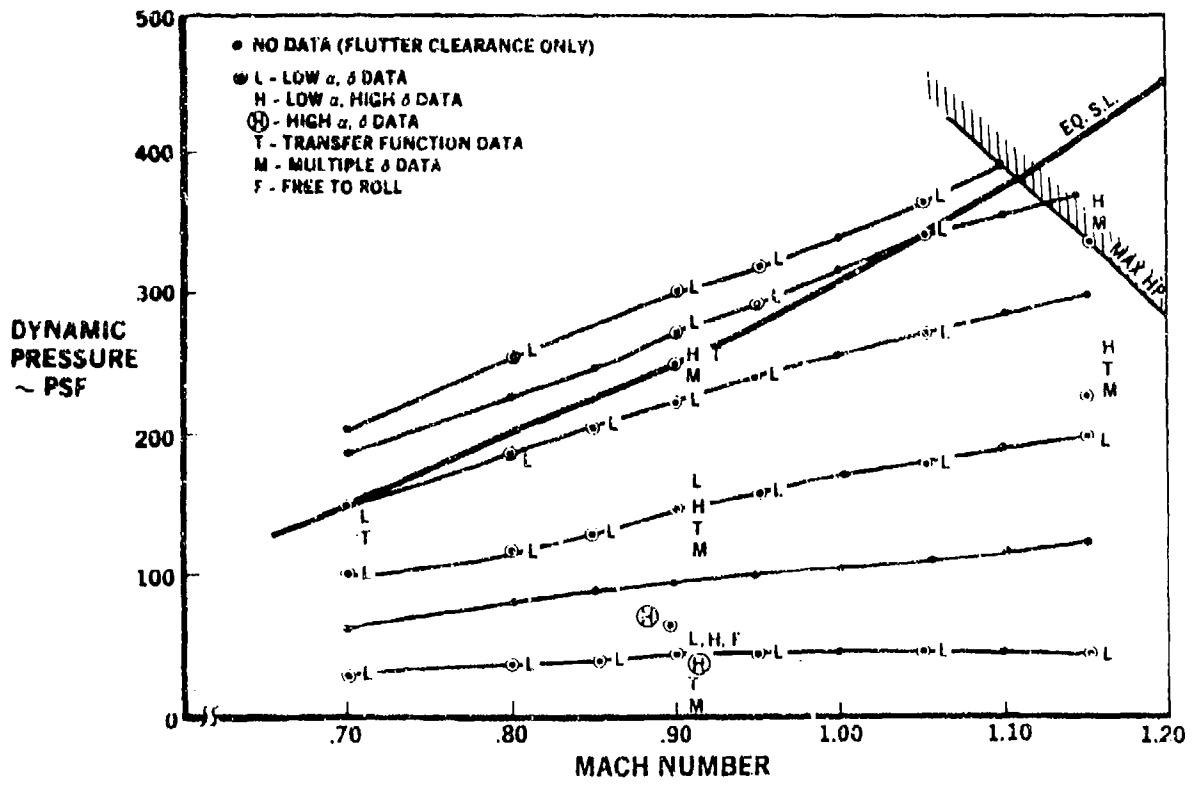


Figure 5-1. Test Envelope

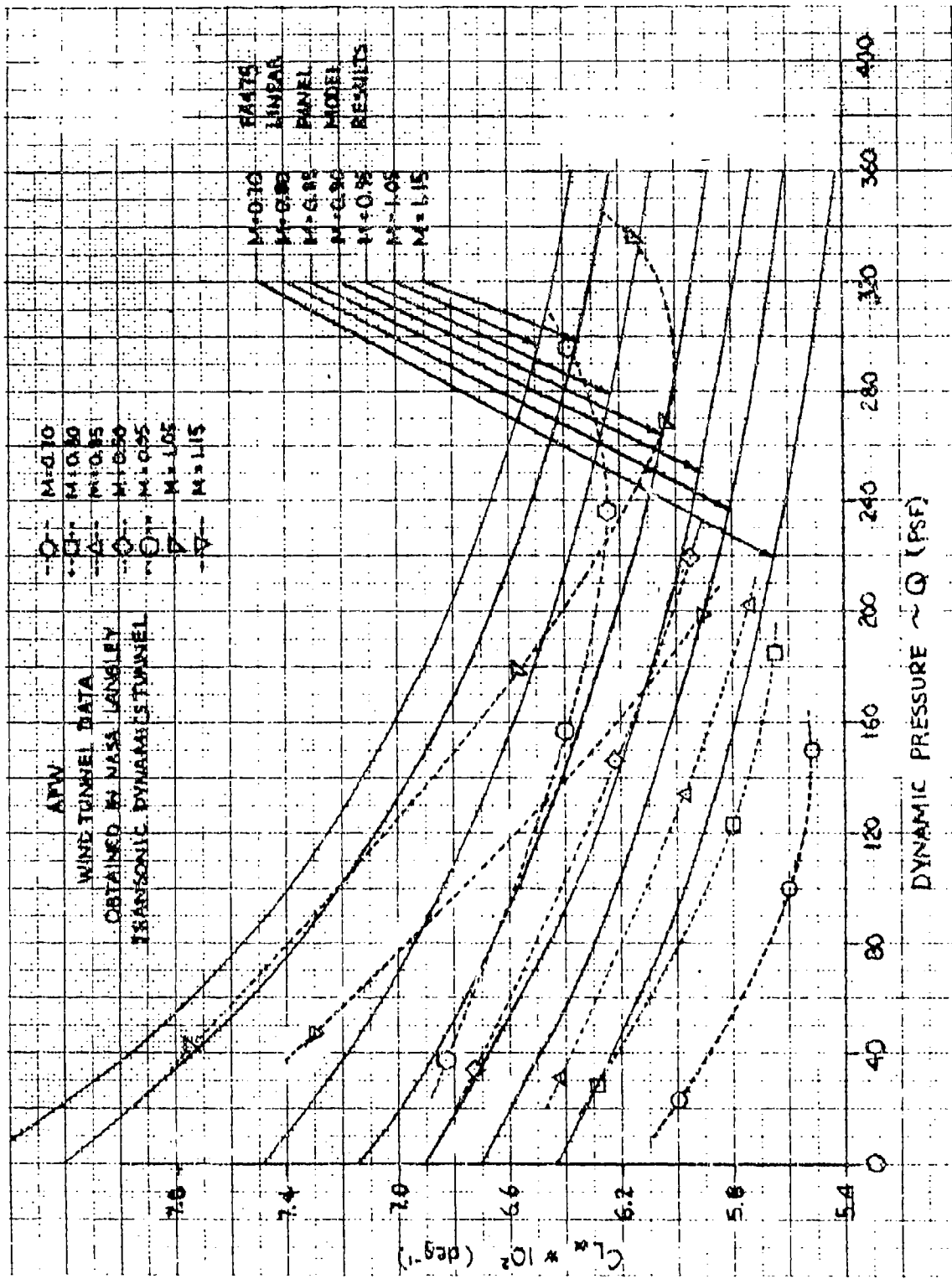


Figure 5-2. Test - Theory Comparisons of  $C_{L\alpha}$  Versus  $q$  - First Wind Tunnel Entry

tested. The two test data curves for the experimental results at supersonic Mach numbers display similar trends. However, these curves differ from the subsonic experimental curves in that the lift-curve slope is more sensitive to flexibility in the supersonic regime. This results in the crossover of the subsonic and supersonic experimental curves. These crossovers cannot be predicted using linear theory because they occur in the nonlinear transonic region.

Figure 5-3 presents the effect of flexibility (i.e., dynamic pressure) on the longitudinal stability ( $C_{m_\alpha}$ ) for the Mach number and dynamic pressure range tested. The experimental curves follow the same trends as the theoretical curves, but FUDP results predict a greater stability than the experimental data. The figures indicate that  $C_{m_\alpha}$  becomes more sensitive to flexibility as the transition is made from the subsonic to supersonic regime. The longitudinal stability increases with increasing Mach number and decreases with increasing flexibility.

Figures 5-4 through 5-7 illustrate the effect of dynamic pressure (i.e., flexibility) on the roll control effectiveness ( $C_{l_g}$ ) for four surfaces: leading-edge inboard, leading-edge outboard, trailing-edge inboard, and trailing-edge outboard. The experimental curves follow the same trends as the theoretical curves for the four control surfaces. The largest discrepancies occur at supersonic Mach numbers. For the outboard leading-edge surface, theory underpredicts the control effectiveness, while for the trailing-edge surfaces theory overpredicts the effectiveness. Experimental reversal points occur prior to theoretical predictions.

Roll control effectiveness of the outboard leading-edge surface increases with Mach number and increasing flexibility except at  $M = 1.15$ , where it remains relatively constant with dynamic pressure. At moderate angles of attack (approximately  $4^\circ$ ) the control effectiveness is increased as shown in Figures 5-8 and 5-9. Of the control surfaces tested, the outboard leading-edge surface is the least sensitive to flexibility. For the trailing-edge surfaces, roll control effectiveness generally decreases with increasing Mach number and flexibility. At moderate angles of attack (approximately  $4^\circ$ ), there is no change in effectiveness of the trailing edge surfaces; however, at high angles of attack (approximately  $10^\circ$ ), effectiveness is reduced. (See Figures 5-10 through 5-13.) The inboard trailing-edge surface is the most effective surface for lateral control in the Mach number-dynamic pressure range tested. Figures 5-8 through 5-13 also show the repeatability of the test data.

It is important to note from the data that as the trailing-edge surface loses its effectiveness, the leading-edge surface increases in effectiveness.

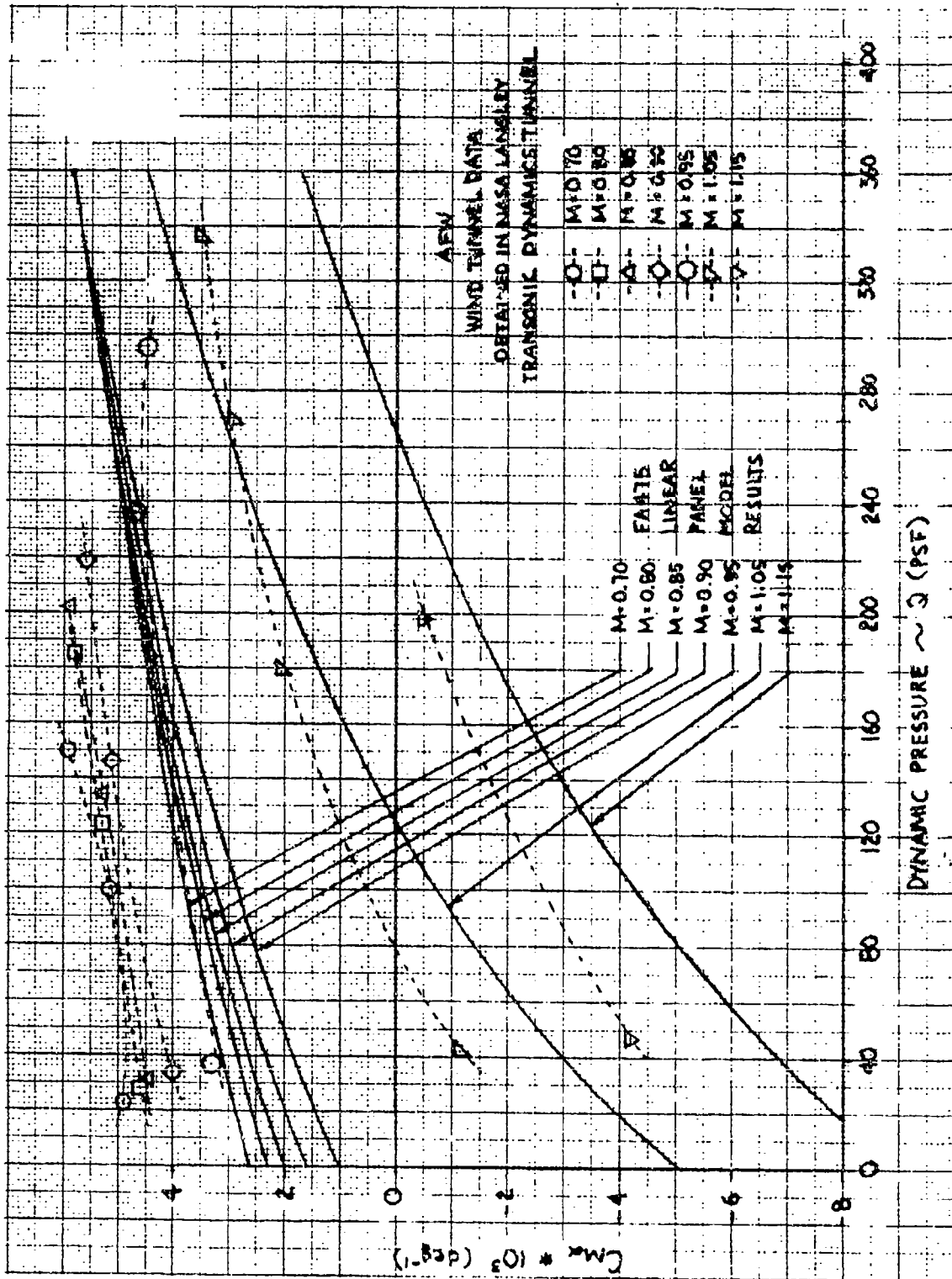


Figure 5-3. Test - Theory Comparisons of  $C_{m\alpha}$  Versus  $q$

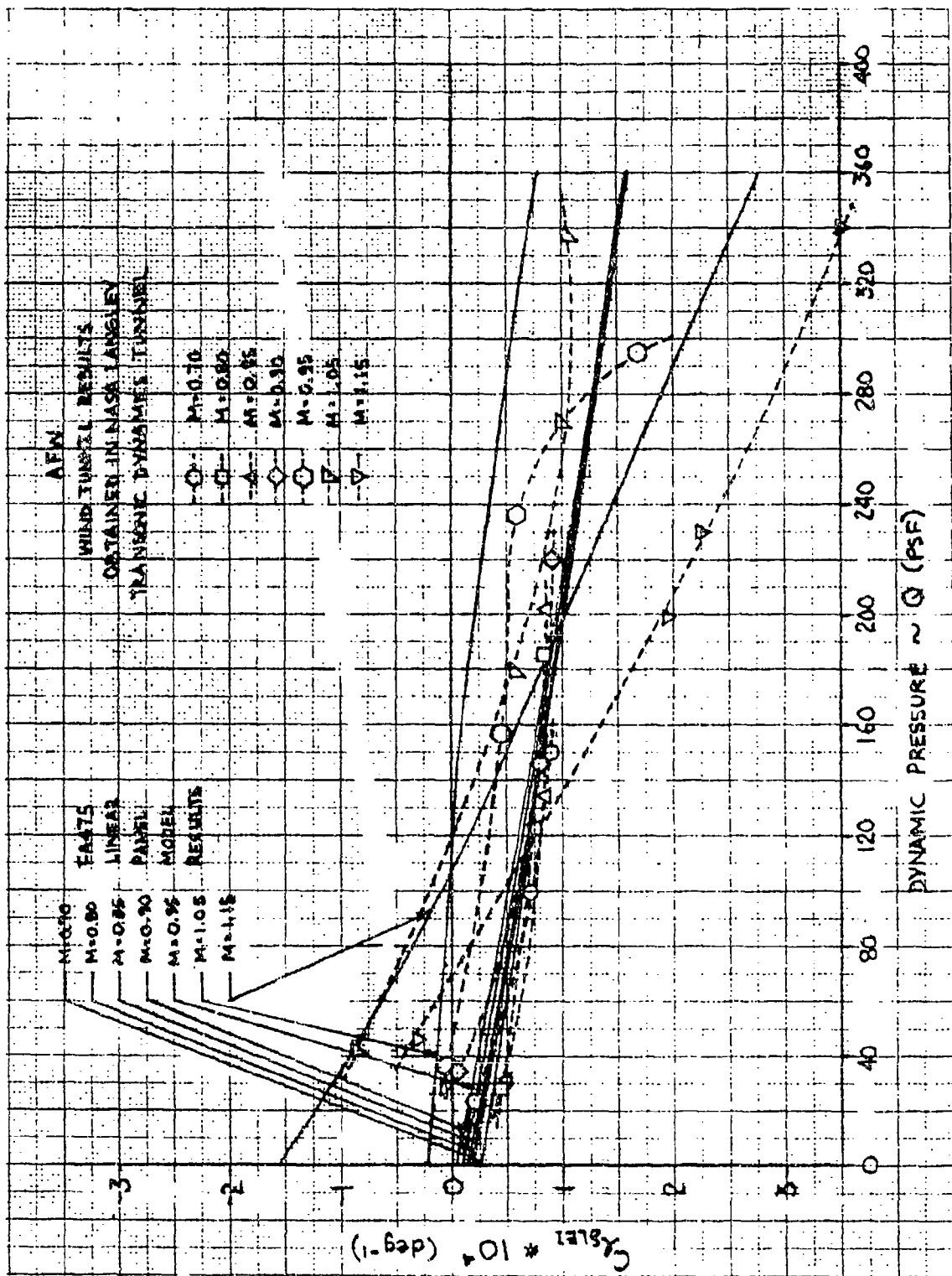


Figure 5-4. Test - Theory Comparisons of  $C_L \delta_{LEI}$  Versus  $q$

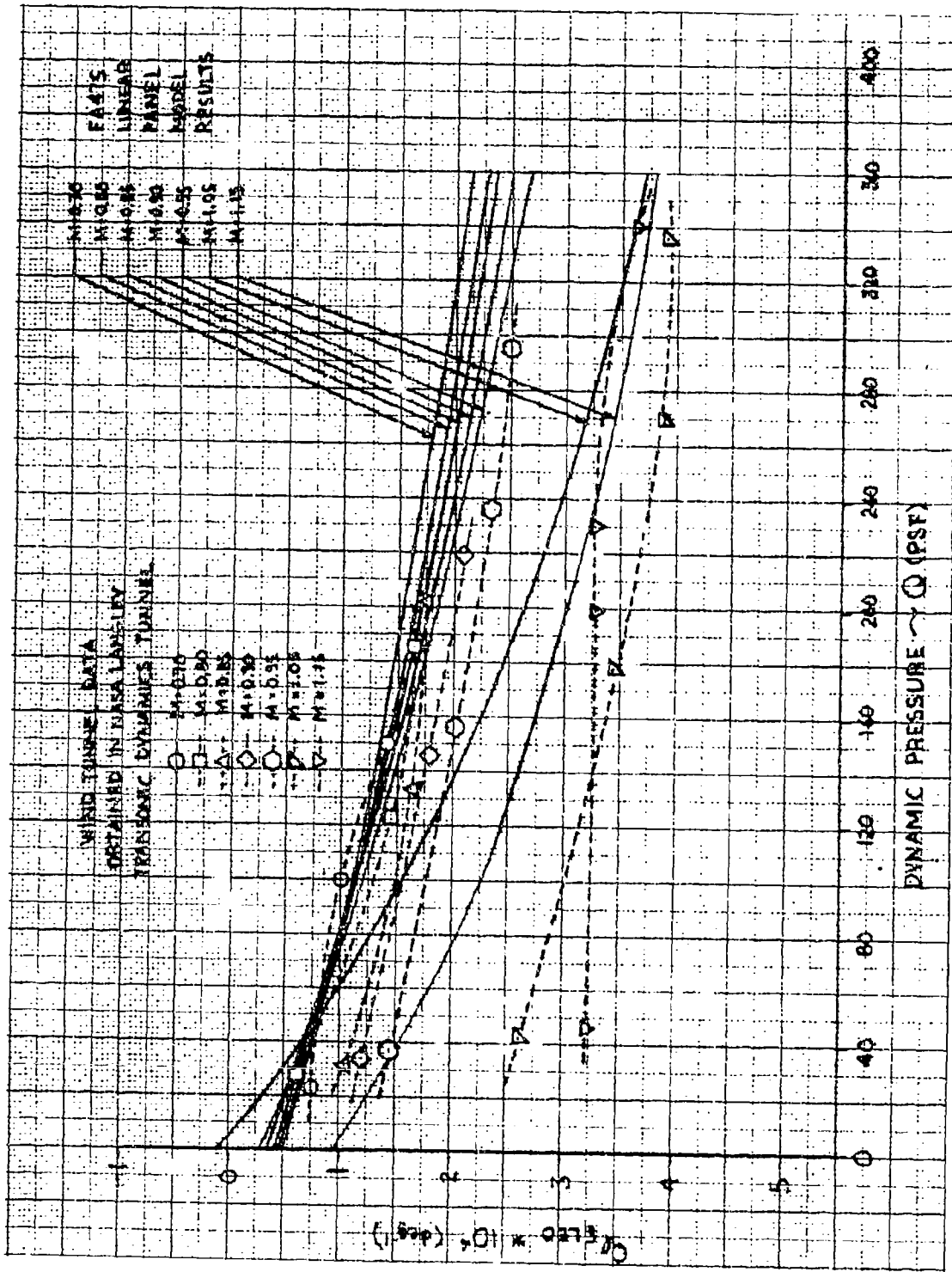


Figure 5-5. Test - Theory Comparisons of  $C_{l \delta LE0}$  Versus  $q$

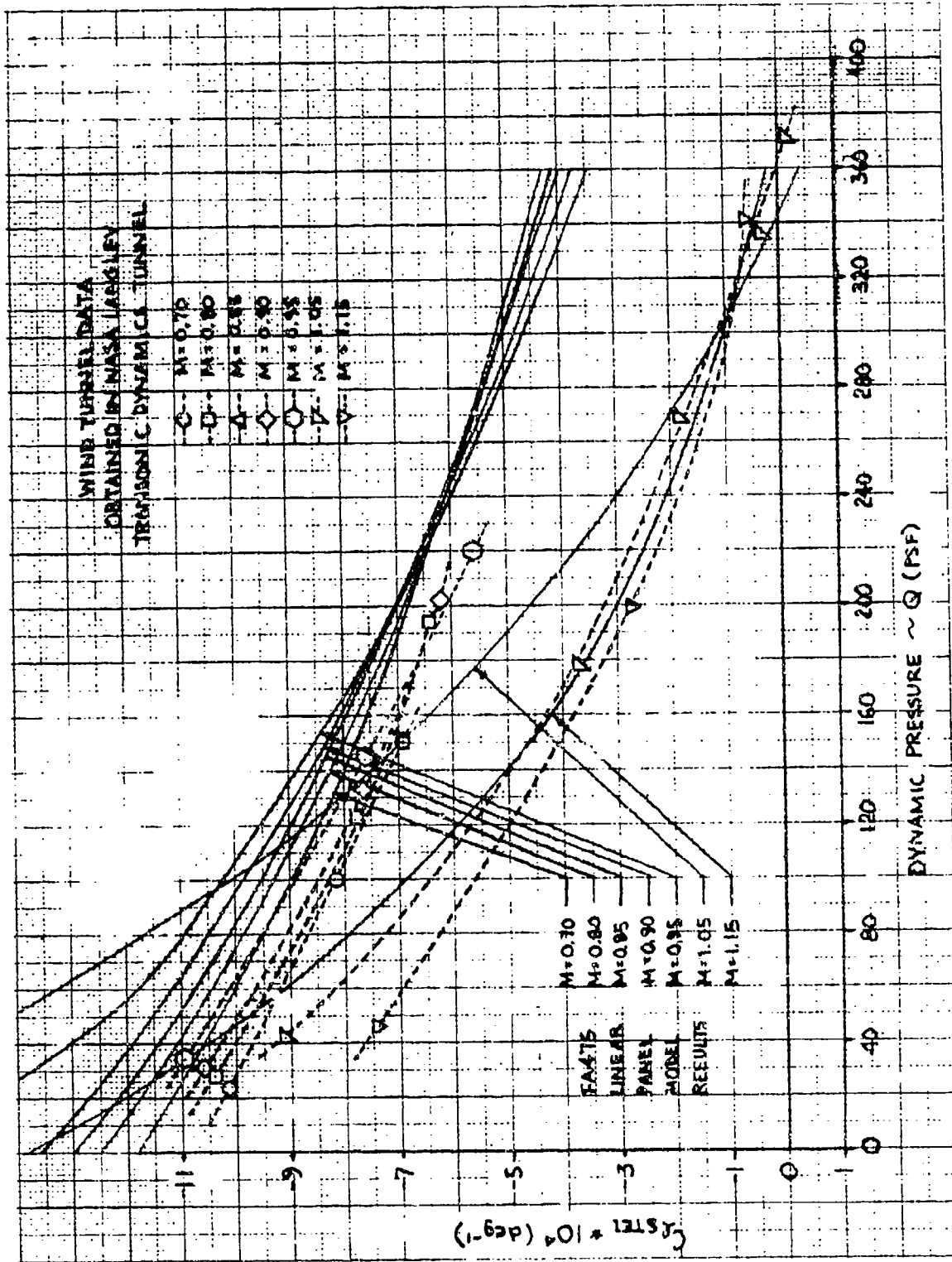


Figure 5-6. Test - Theory Comparisons of  $C_{l_{\delta TEI}}$  Versus  $q$



OUTBOARD LEADING EDGE

AFW  
WIND TUNNEL DATA  
OBTAINED IN NASA LANGLEY  
TRANSONIC DYNAMICS TUNNEL  
FEB 1987  
 $M = 0.90$

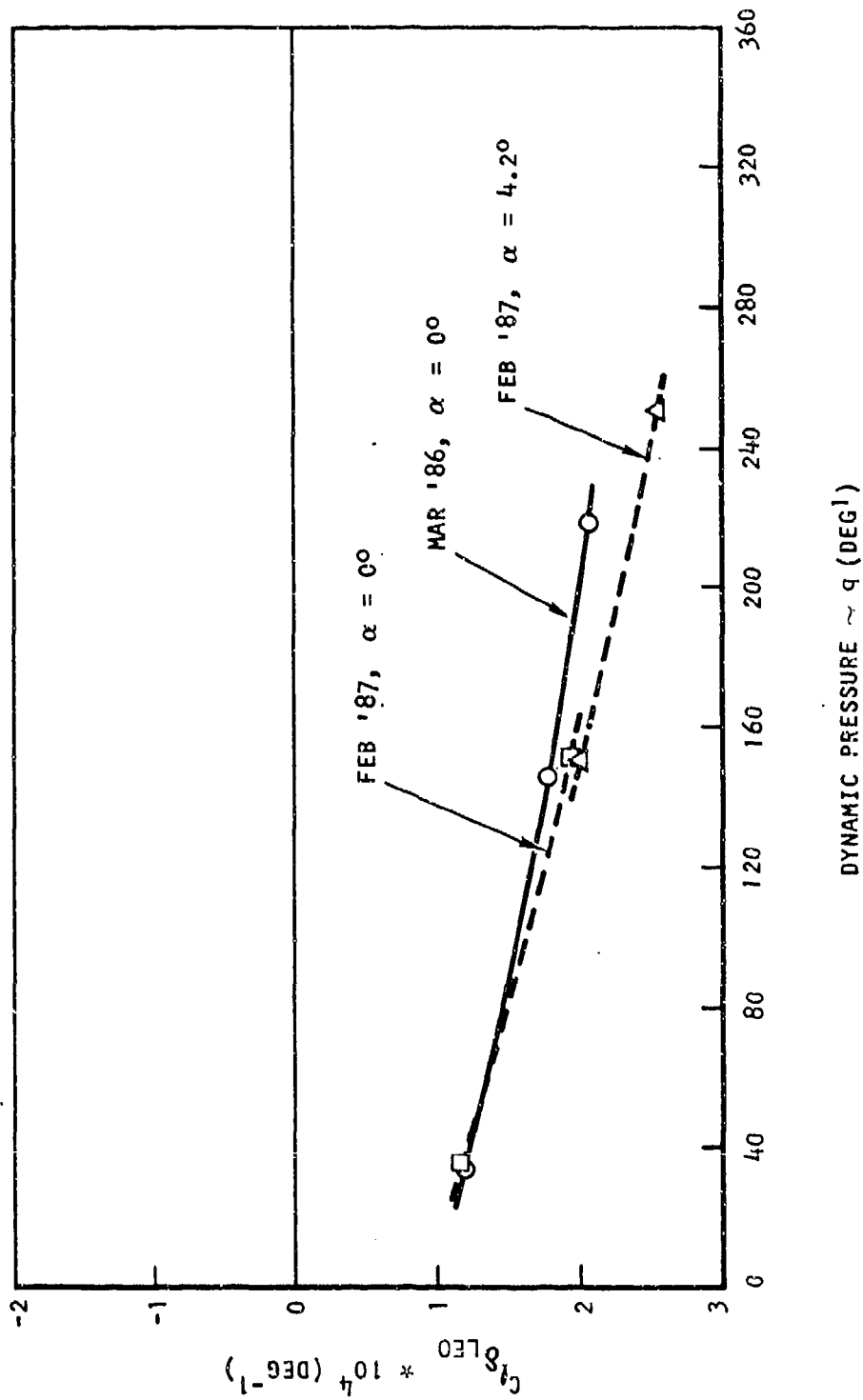
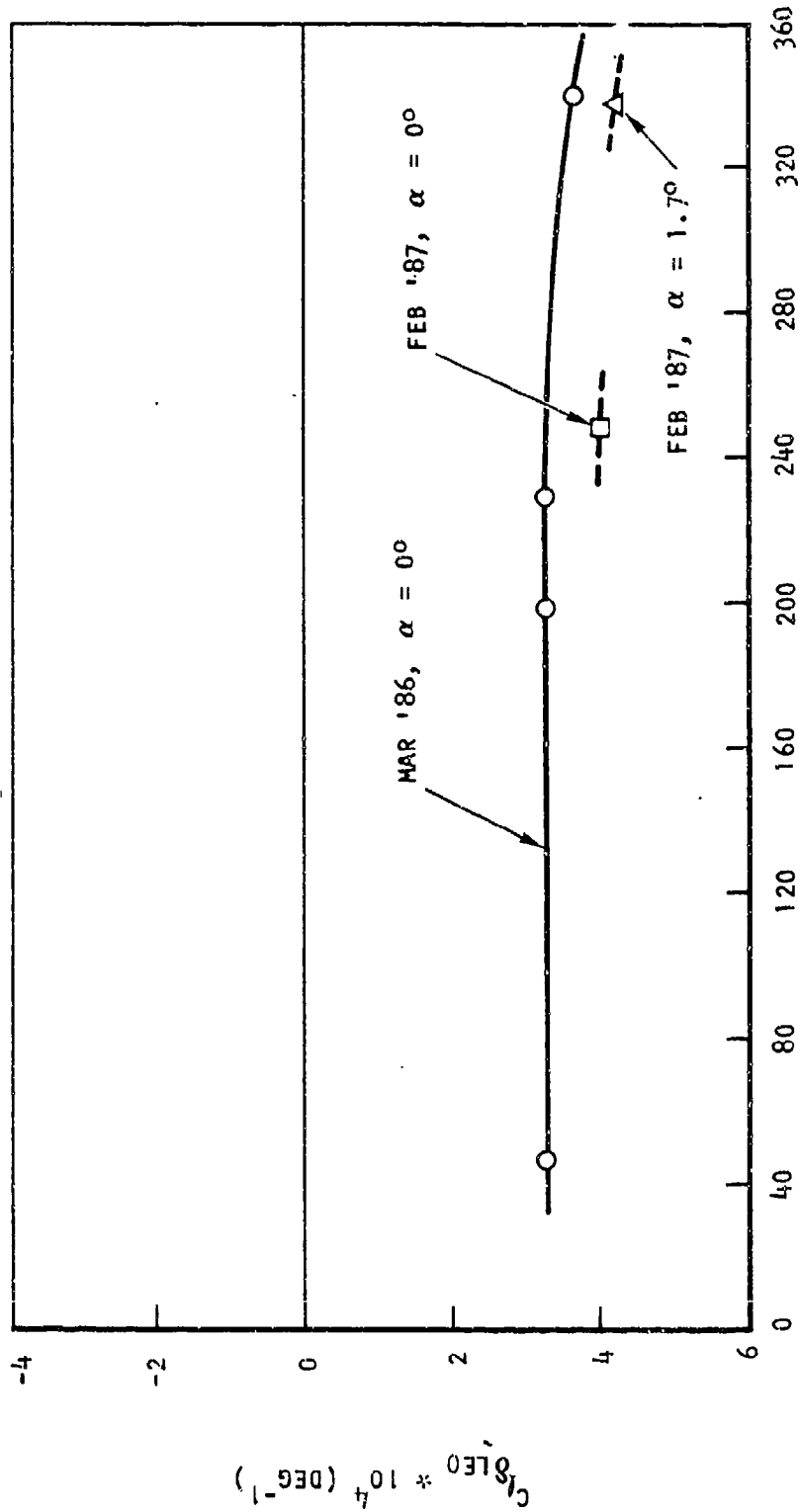


Figure 5-8. Effect on Angle of Attack on  $C_{\delta_{LEO}}$ ,  $M = 0.9$

OUTBOARD LEADING EDGE

AFW  
WIND TUNNEL DATA  
OBTAINED IN NASA LANGLEY  
TRANSONIC DYNAMICS TUNNEL  
FEB 1987  
M = 1.15

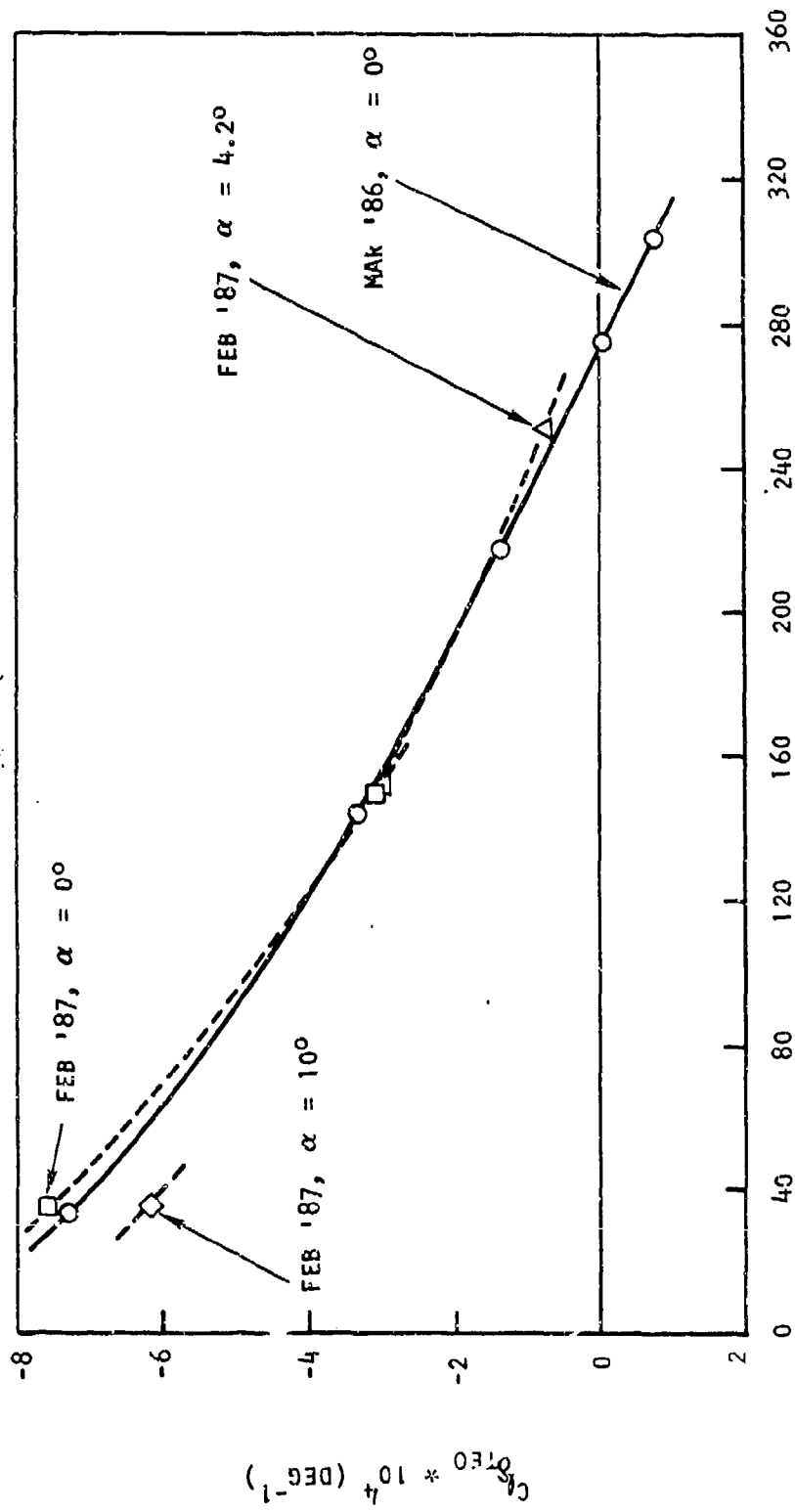


DYNAMIC PRESSURE  $\sim q$  ( $\text{DEG}^1$ )

Figure 5-9. Effect on Angle of Attack on  $C_{l_{\delta_{LEO}}}$ ,  $M = 1.15$

OUTBOARD TRAILING EDGE

AFW  
WIND TUNNEL DATA  
OBTAINED IN NASA LANGLEY  
TRANSONIC DYNAMICS TUNNEL  
FEB 1987  
M = 0.90



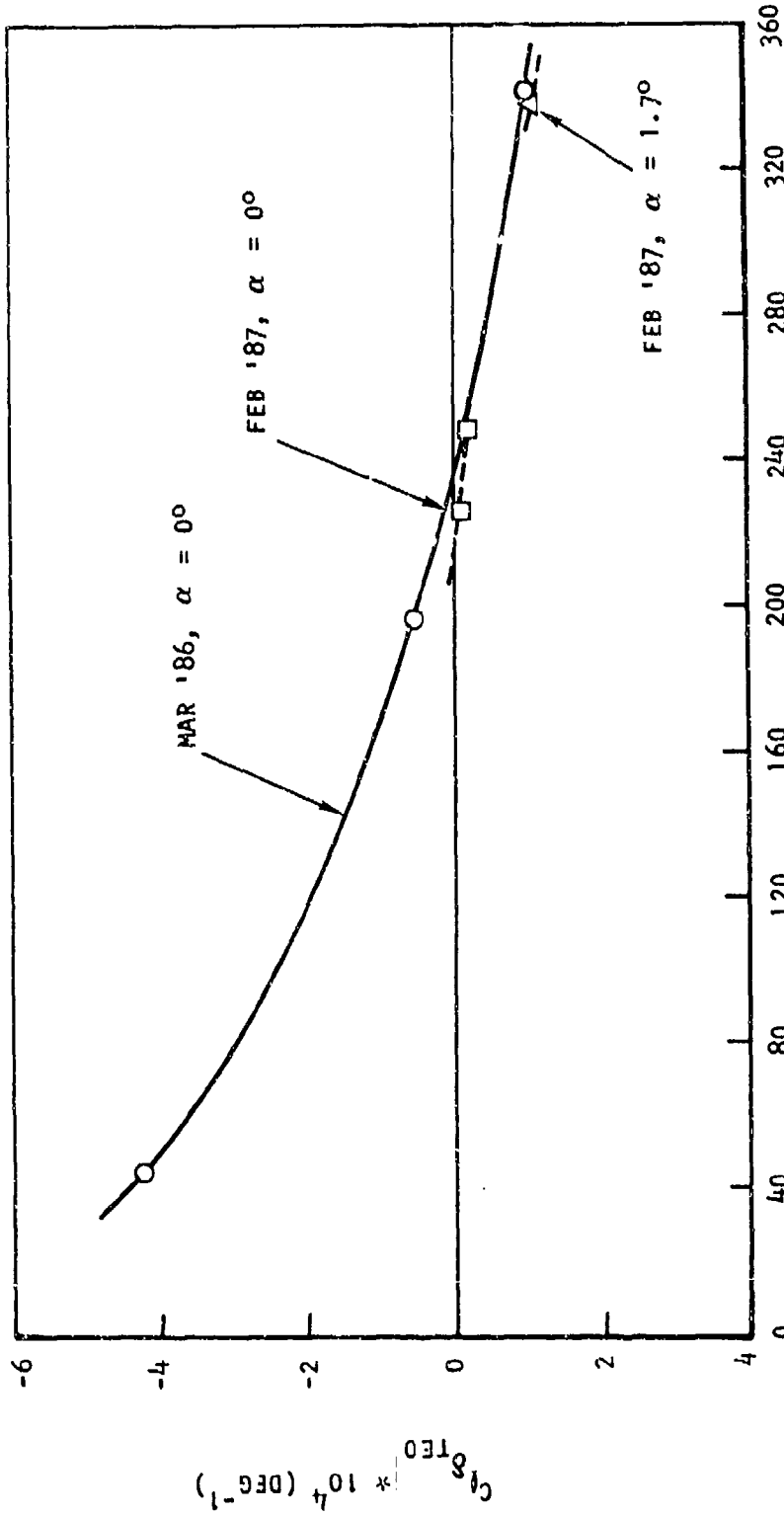
DYNAMIC PRESSURE  $\sim q$  (PSF)

FIG 5-10.

Figure 5-10. Effect on Angle of Attack on  $C_{l_{TEO}}$ ,  $M = 0.9$

OUTBOARD TRAILING EDGE

AFW  
WIND TUNNEL DATA  
OBTAINED IN NASA LANGLEY  
TRANSONIC DYNAMICS TUNNEL  
FEB 1987  
M = 1.15



DYNAMIC PRESSURE  $\sim q$  (PSF)

FIG 5-11.

Figure 5-11. Effect on Angle of Attack on  $C_{D,TEO}$ ,  $M = 1.15$

INBOARD TRAILING EDGE

AFW  
WIND TUNNEL DATA  
OBTAINED IN NASA LANGLEY  
TRANSONIC DYNAMICS TUNNEL  
FEB 1987  
M = 0.90

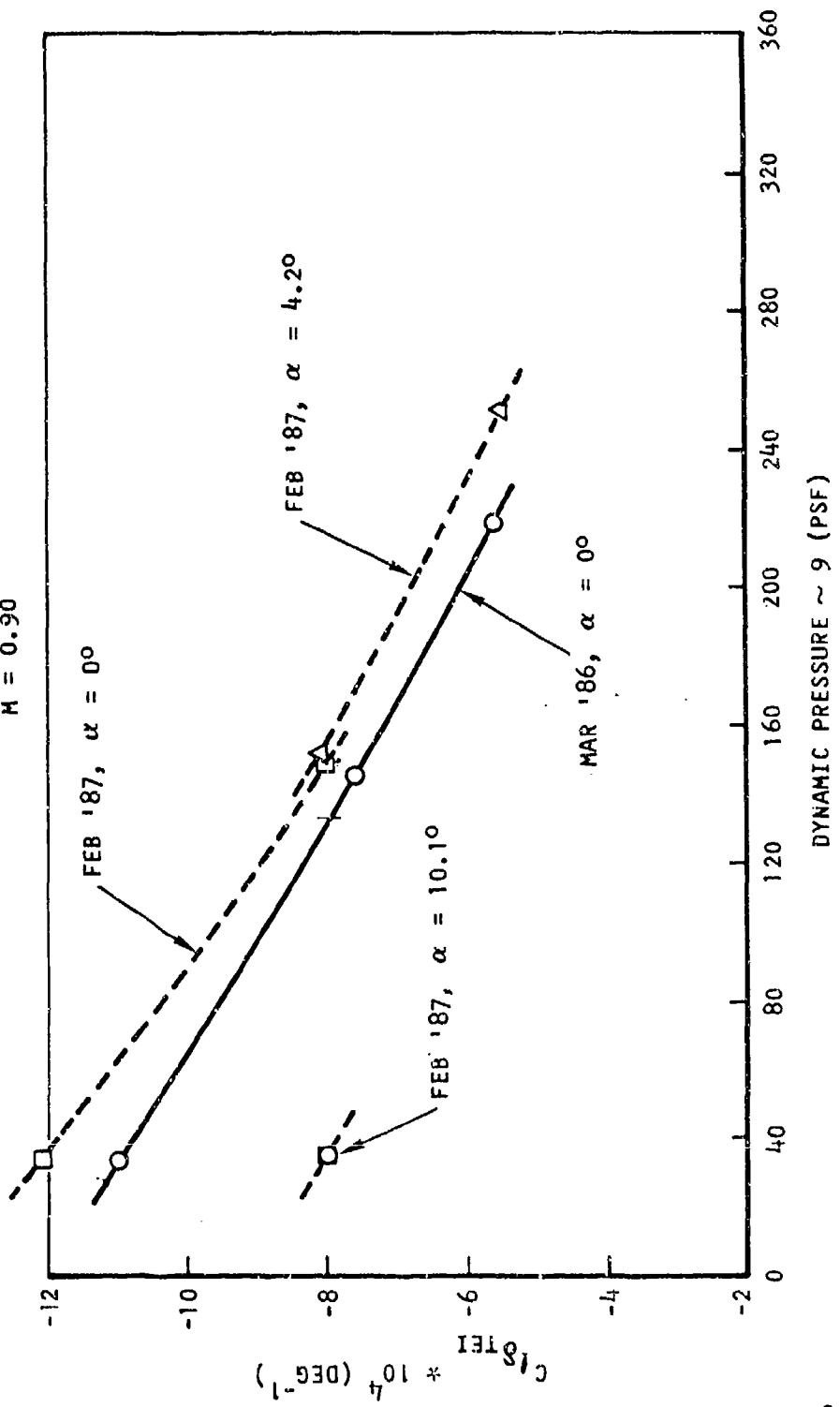


Figure 5-12. Effect on Angle of Attack on  $C_{l_{TEI}}$ , M = 0.9

INBOARD TRAILING EDGE

AFW  
WIND TUNNEL DATA  
OBTAINED IN NASA LANGLEY  
TRANSONIC DYNAMICS TUNNEL  
FEB 1987  
M = 1.15

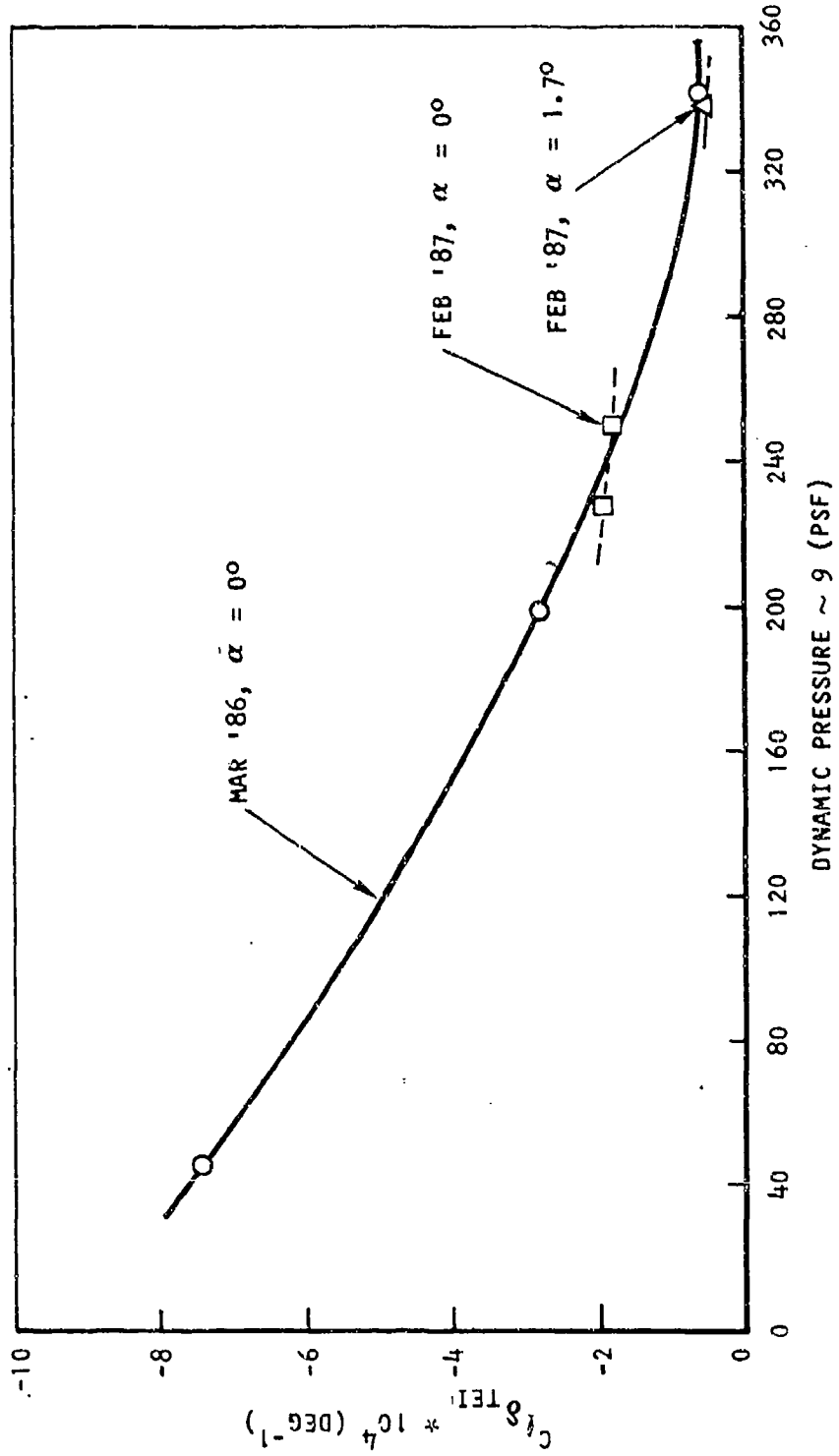


Figure 5-13. Effect on Angle of Attack on  $C_{l_{\delta_{TEI}}}$ , M = 1.15

Figures 5-14 through 5-17 present the effect of individual control surface deflections on lift, pitching moment, and rolling moment at zero angle-of-attack. Reasonable linearity is exhibited with the exception of the effect of leading edge outboard control surface deflection on pitching moment. Pitching moment reverses direction for leading edge outboard deflections because the leading edge surface is located very close to the pitch reference axis.

Figure 5-18 through 5-20 present a comparison of data generated through superposition of individual control surface deflections versus actual multiple control surface deflections. The data obtained by superposition show excellent agreement with the multiple surface deflection data.

Figures 5-21 through 5-23 present some samples of the control surface hinge moment coefficient data obtained during the test. Figure 5-21 shows the variation of the outboard trailing edge control surface hinge moment at zero angle-of-attack as a function of dynamic pressure. Figure 5-22 shows the variation of  $C_{H\alpha}$  of the outboard trailing edge control surface with dynamic pressure. Figure 5-23 presents the variation of  $C_{H\delta}$  of the leading edge inboard surface with dynamic pressure.

The accuracy of these data are questionable because of measured inaccuracies caused by friction to the actuators and hydraulic line pressure losses between the actuators and pressure measurement instrumentation.

The effects of individual control surface deflections on wing plate bending and torsional moment coefficients are shown by Figures 5-24 through 5-27. The data are, for the most part, linear over the range of control surface deflections tested, except for the LEO surface. This surface exhibits nonlinear behavior on some of the sensors, probably because of sensor location.

## 5.2 MODEL PRESSURE DATA AND CFD-AEROELASTIC CALCULATIONS

Static pressure data were measured on one wing panel. Pressure data were obtained at five span stations at both upper and lower surface locations. Refer to Section 2.3 for a description of the pressure measurement locations. Pressures were measured at many of the points where force data were obtained (see Figure 5-1).

The pressure data obtained during the wind tunnel test were printed on paper and recorded on a computer file. Unfortunately, the computer file was incorrectly recorded, and therefore could not be used. Therefore, the original paper copy of the measured pressure data is all that was obtained.

Q = 36 PSF  
MACH = .90

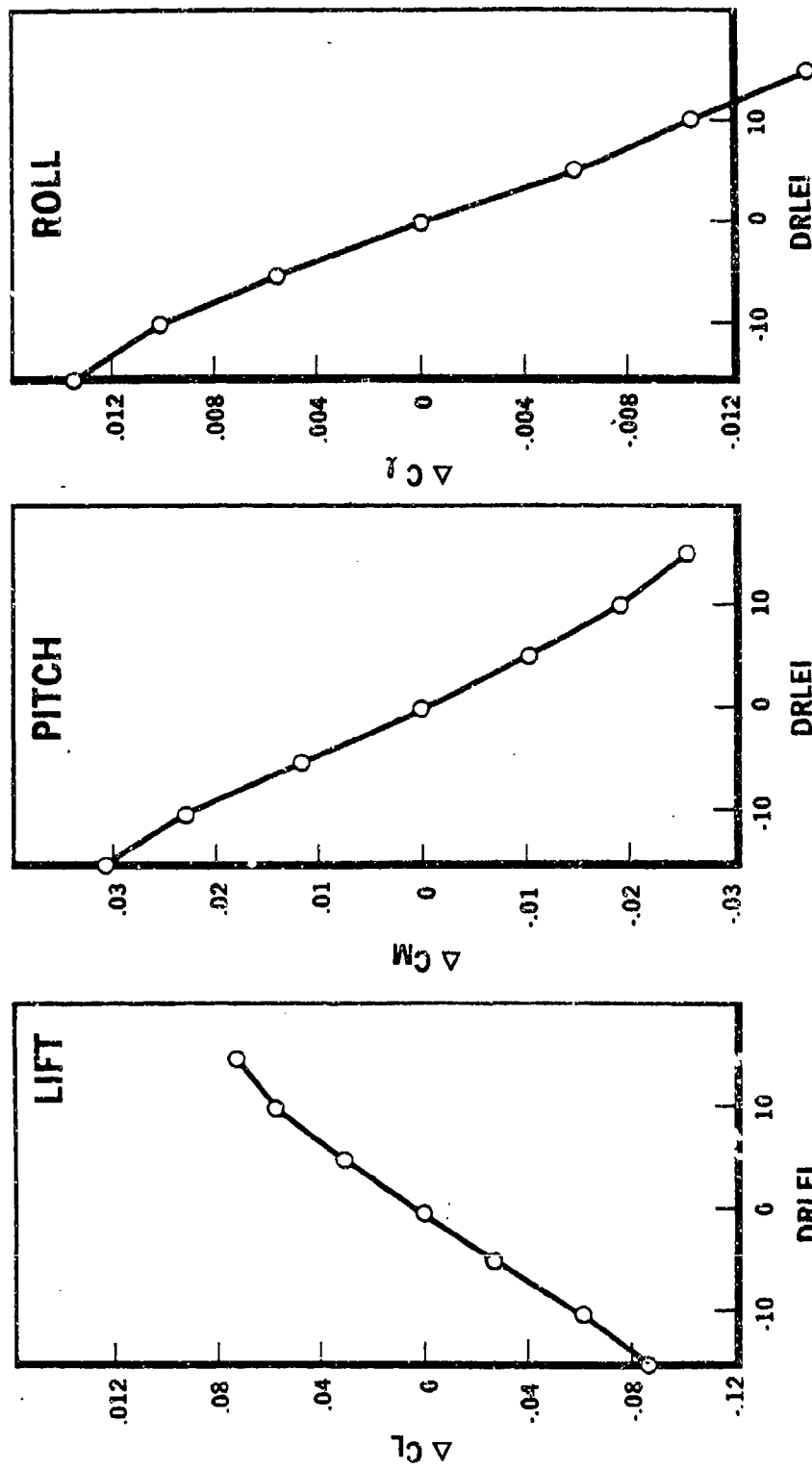
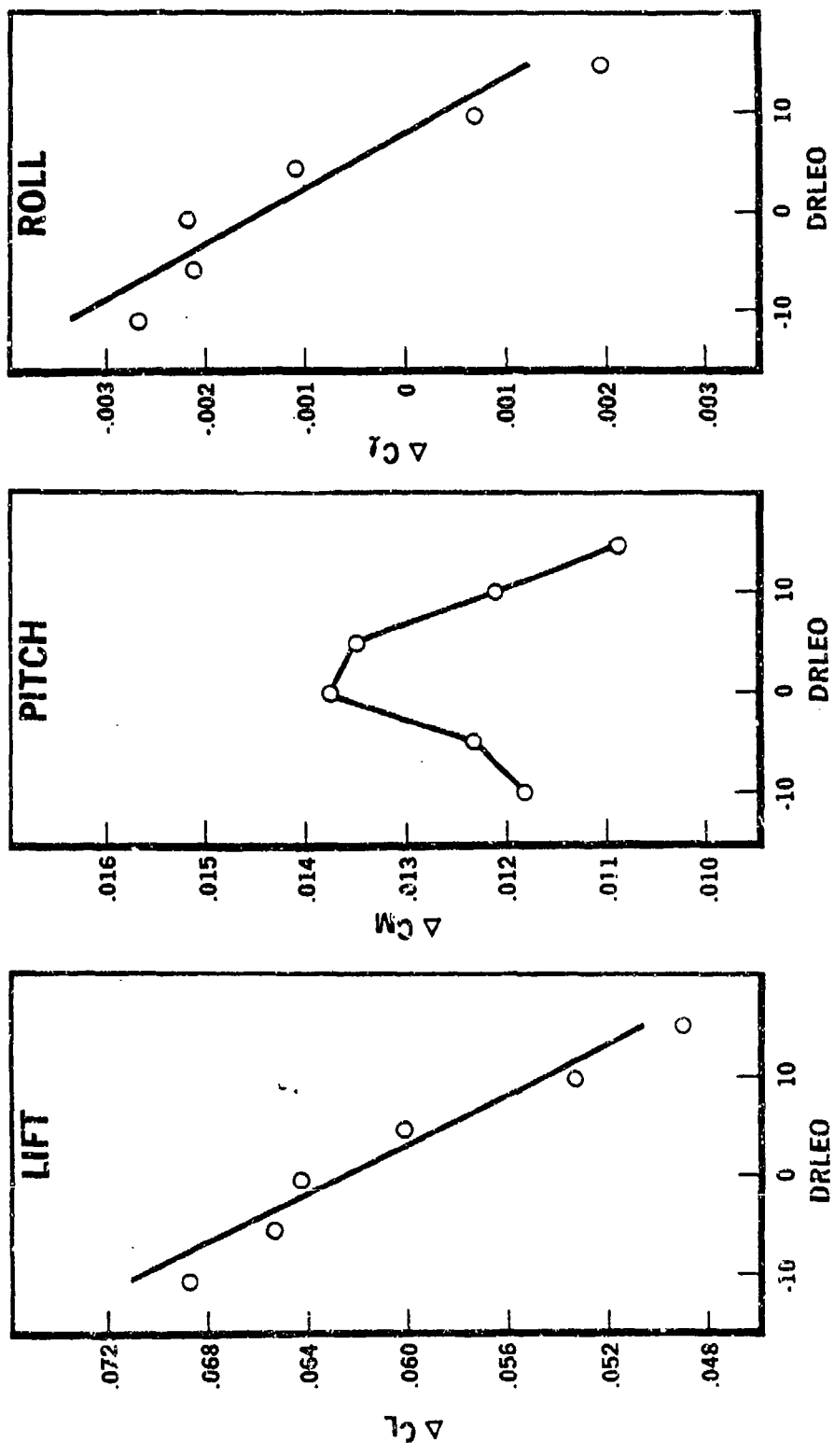
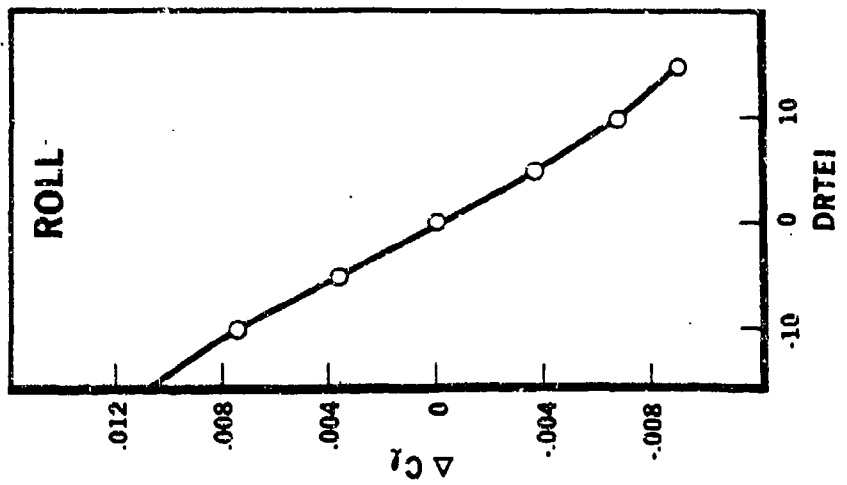
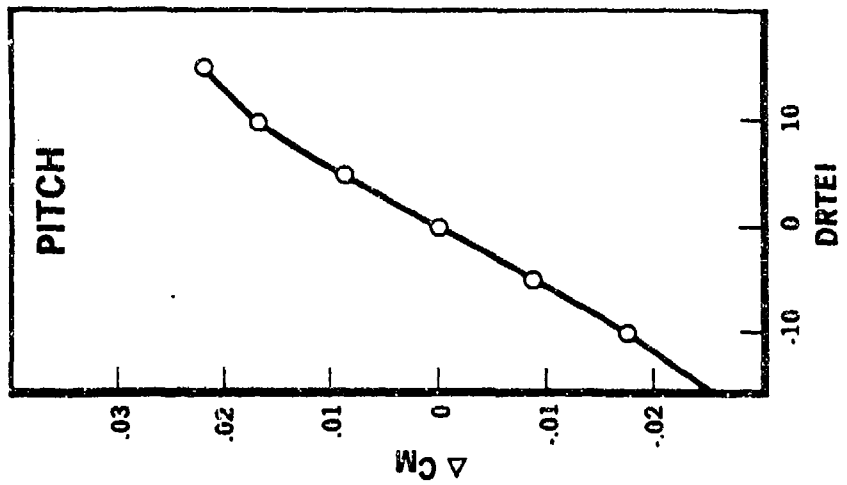
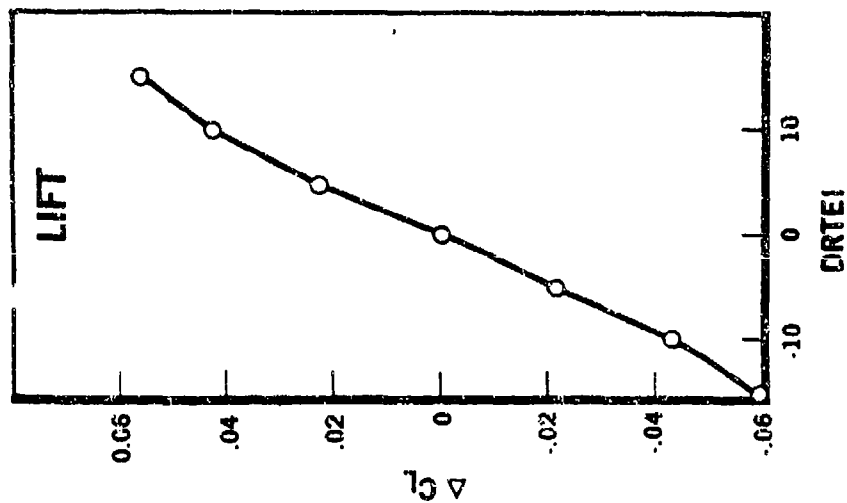


Figure 5-14. Variation of  $C_L$ ,  $C_M$ ,  $C_R$ , with  $\delta$  (Leading Edge Inboard)



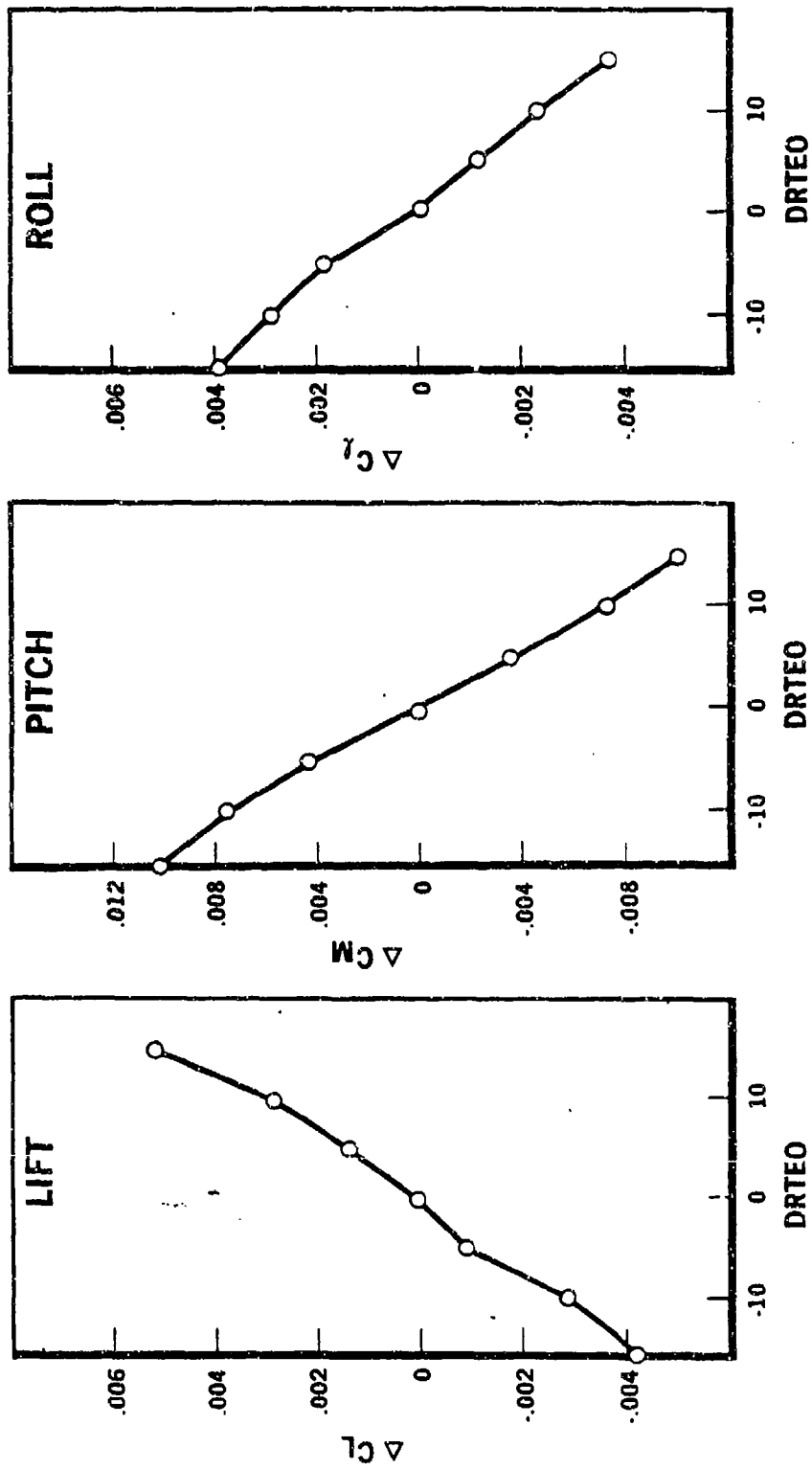
MACH = 0.90  
 Q = 35 PSF

Figure 5-15. Variation of  $C_L$ ,  $C_M$ ,  $C_l$ , with  $\delta$  (Leading Edge Outboard)



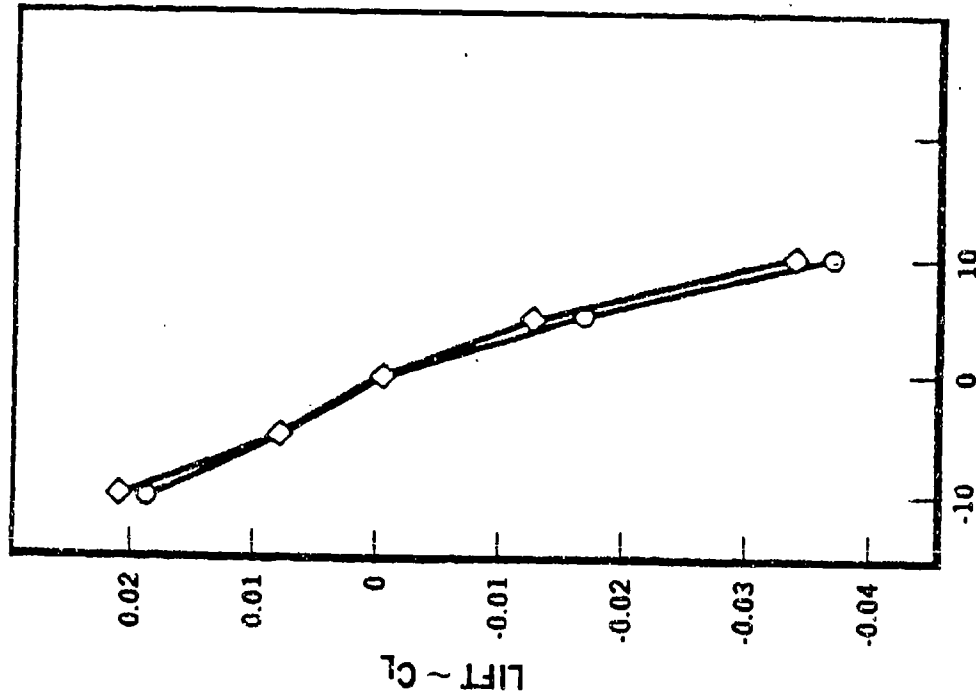
**Mach = .90**  
**Q = 151 PSF**

Figure 5-16. Variation of  $C_L$ ,  $C_M$ ,  $C_l$ , with  $\delta$  (Trailing Edge Inboard)



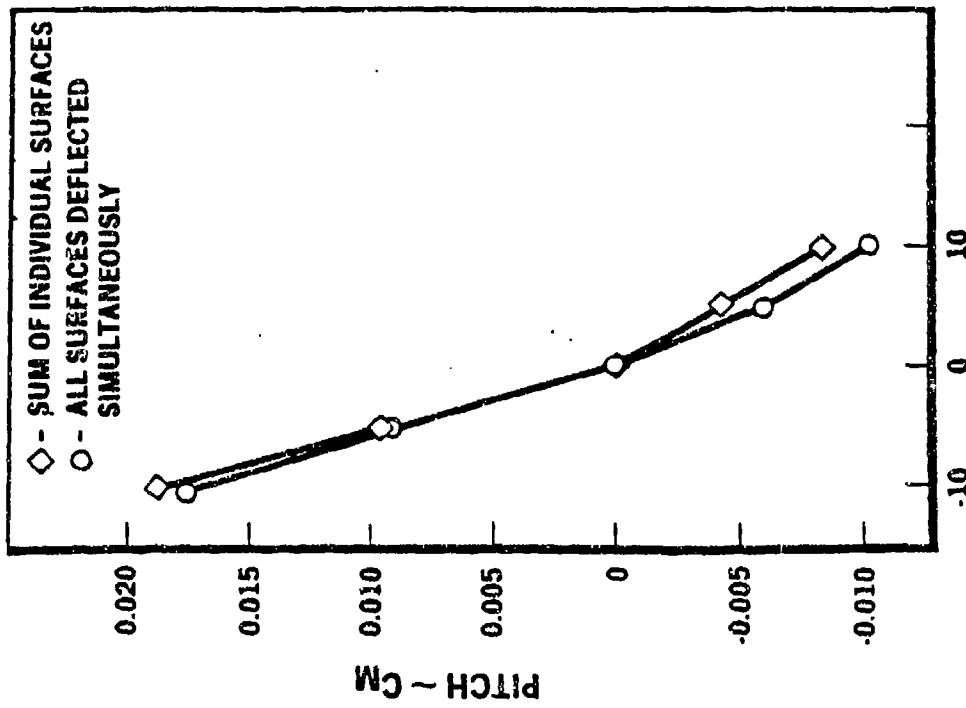
**M = 0.90**  
**Q = 151.0**

Figure 5-17. Variation of  $C_L$ ,  $C_M$ ,  $C_L$ , with  $\delta$  (Trailing Edge Outboard)



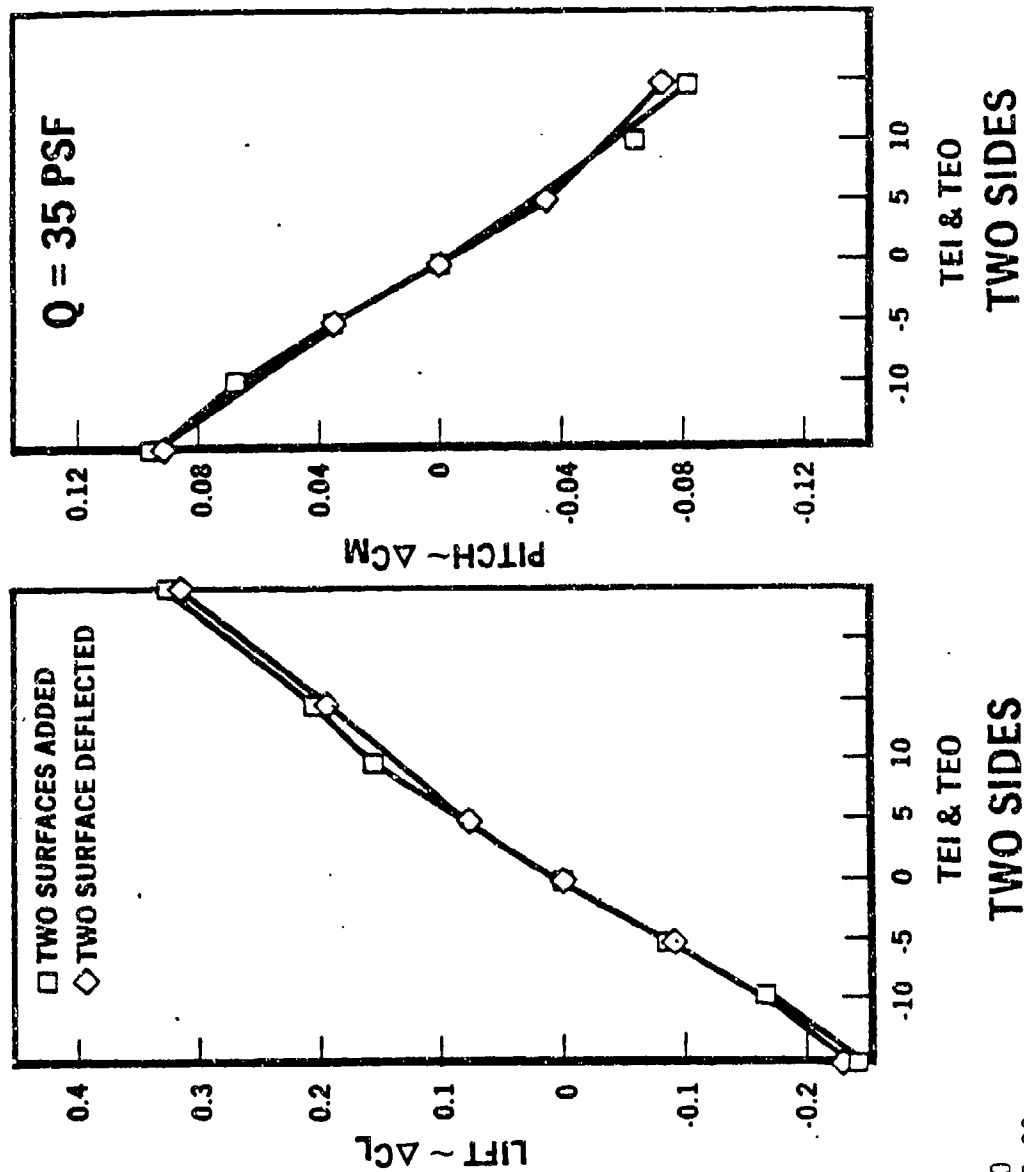
**TWO SIDES LEI & LEO**

$\alpha = 0$   
MACH = 0.90  
Q = 36 PSF



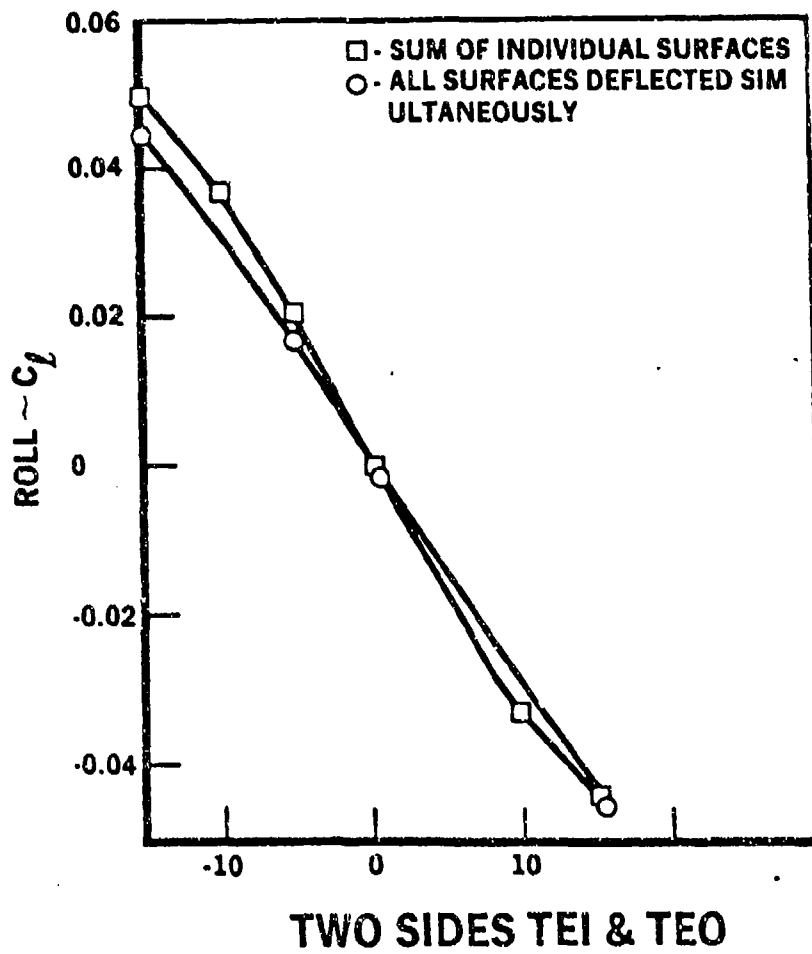
**TWO SIDES LEI & LEO**

Figure 5-18. AFW Wind Tunnel Test Results - Super Position; Lift and Pitching Moment LEI and LEO



$\alpha = 0$   
 MACH = 0.90  
 Q = 36 PSF

Figure 5-19. AFW Wind Tunnel Test Results - Super Position; Lift and Pitching Moment TEI and TEO



$\alpha = 0$   
 MACH = 0.90  
 Q = 36 PSF

Figure 5-20. AFW Wind Tunnel Test Results - Super Position - Rolling Moment TEI and TEO

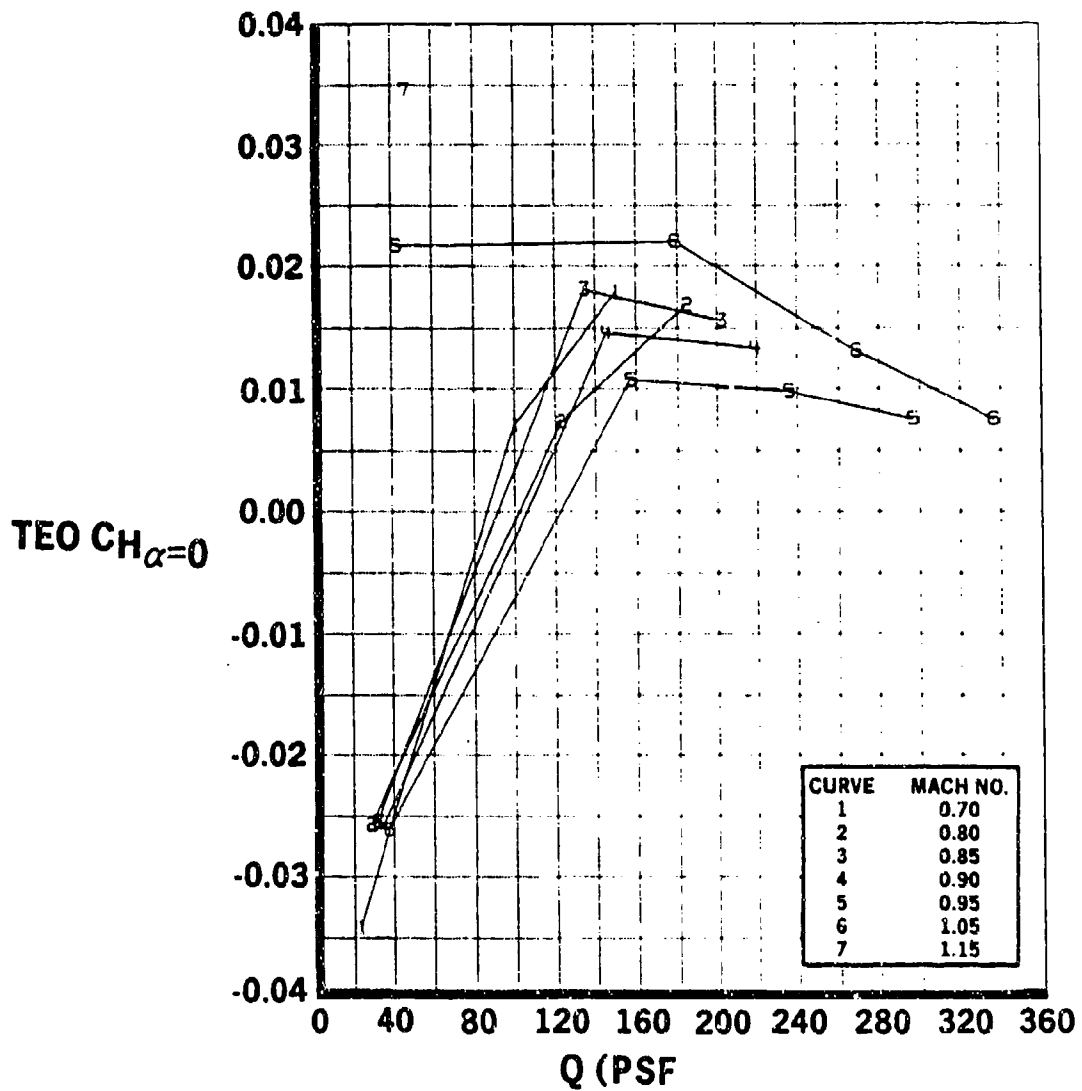


Figure 5-21. Variation of  $Ch_{\alpha} = 0$  (TEO) with Dynamic Pressure

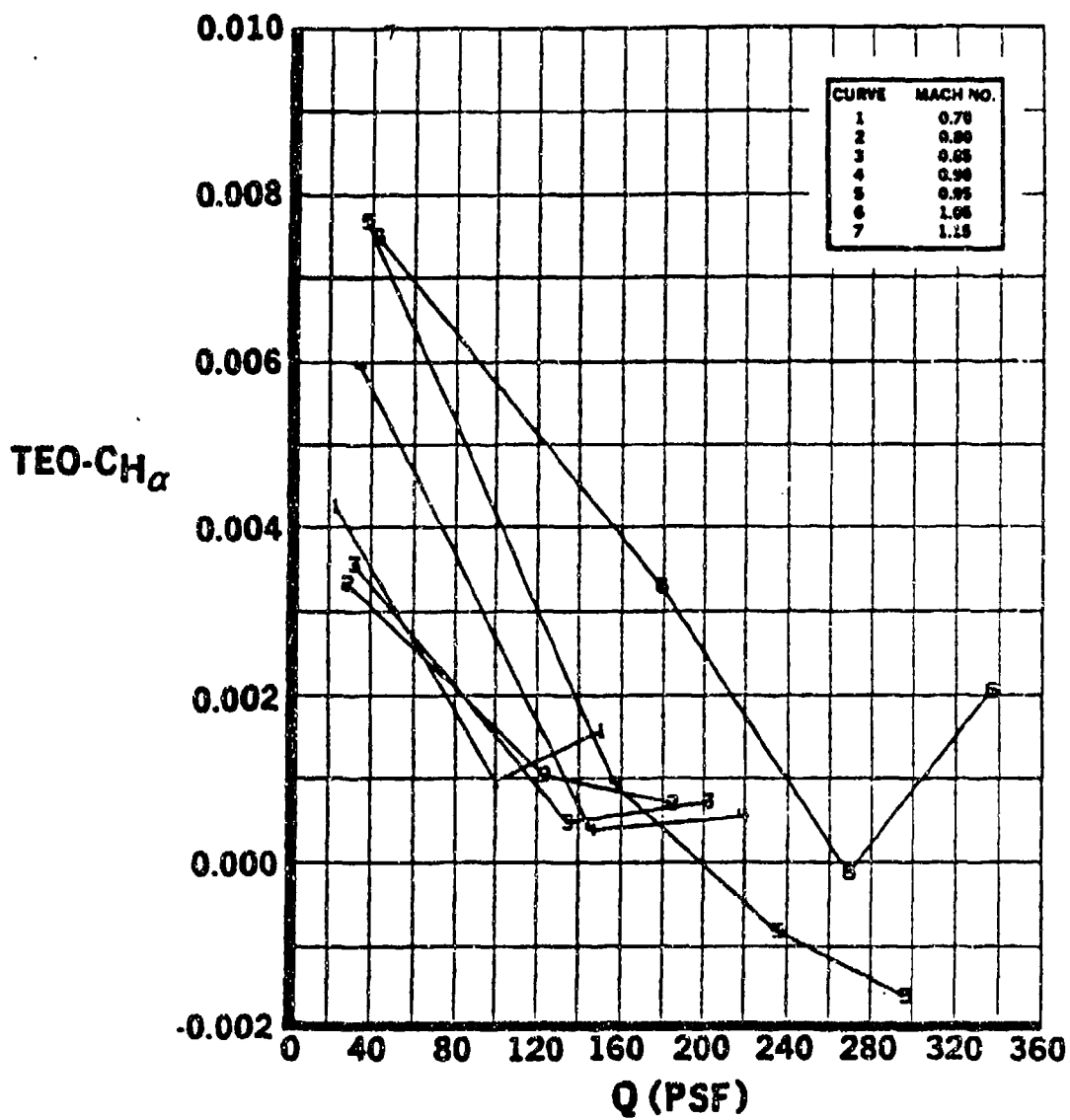


Figure 5-22. Variation of  $CH_\alpha$  (at TEO) with Dynamic Pressure

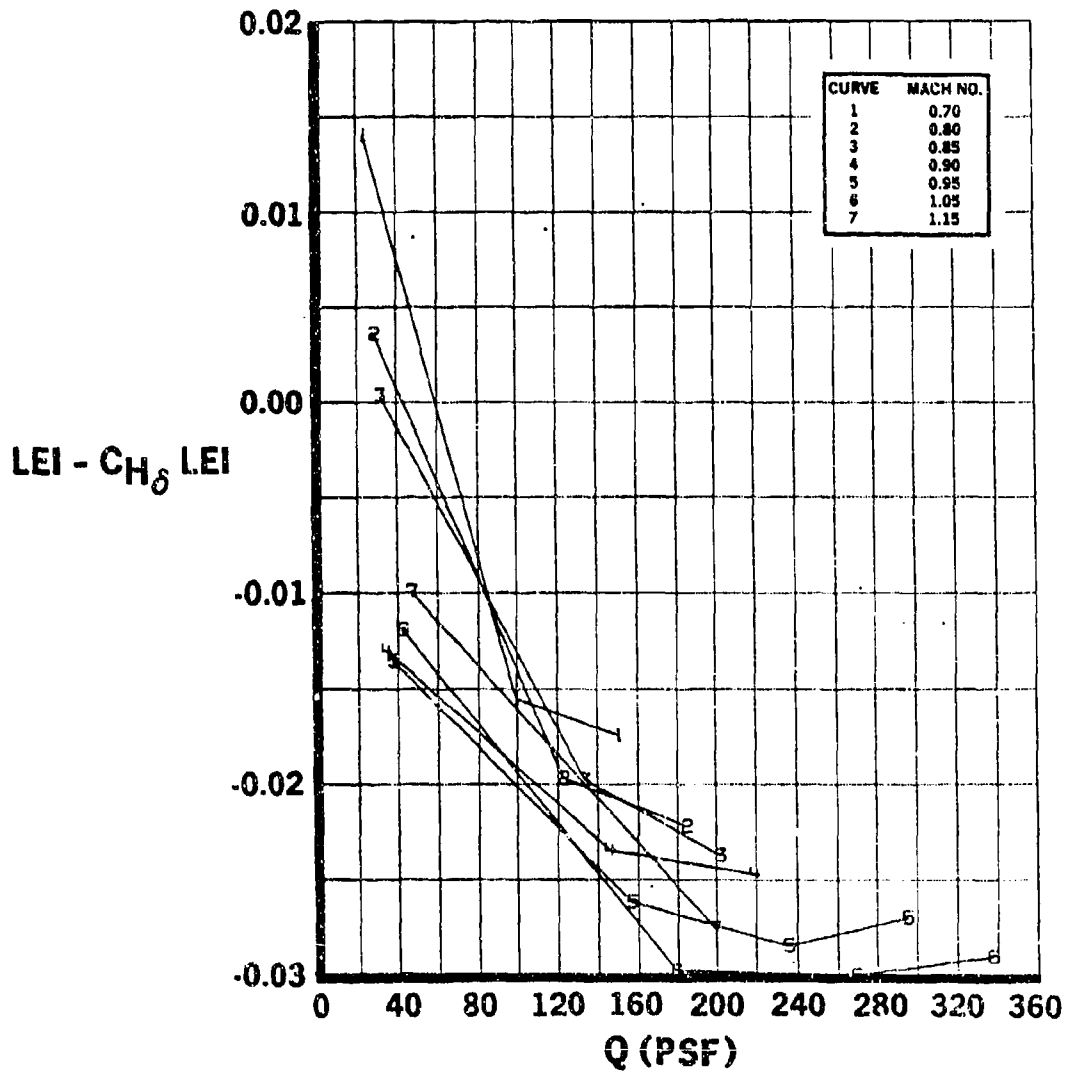
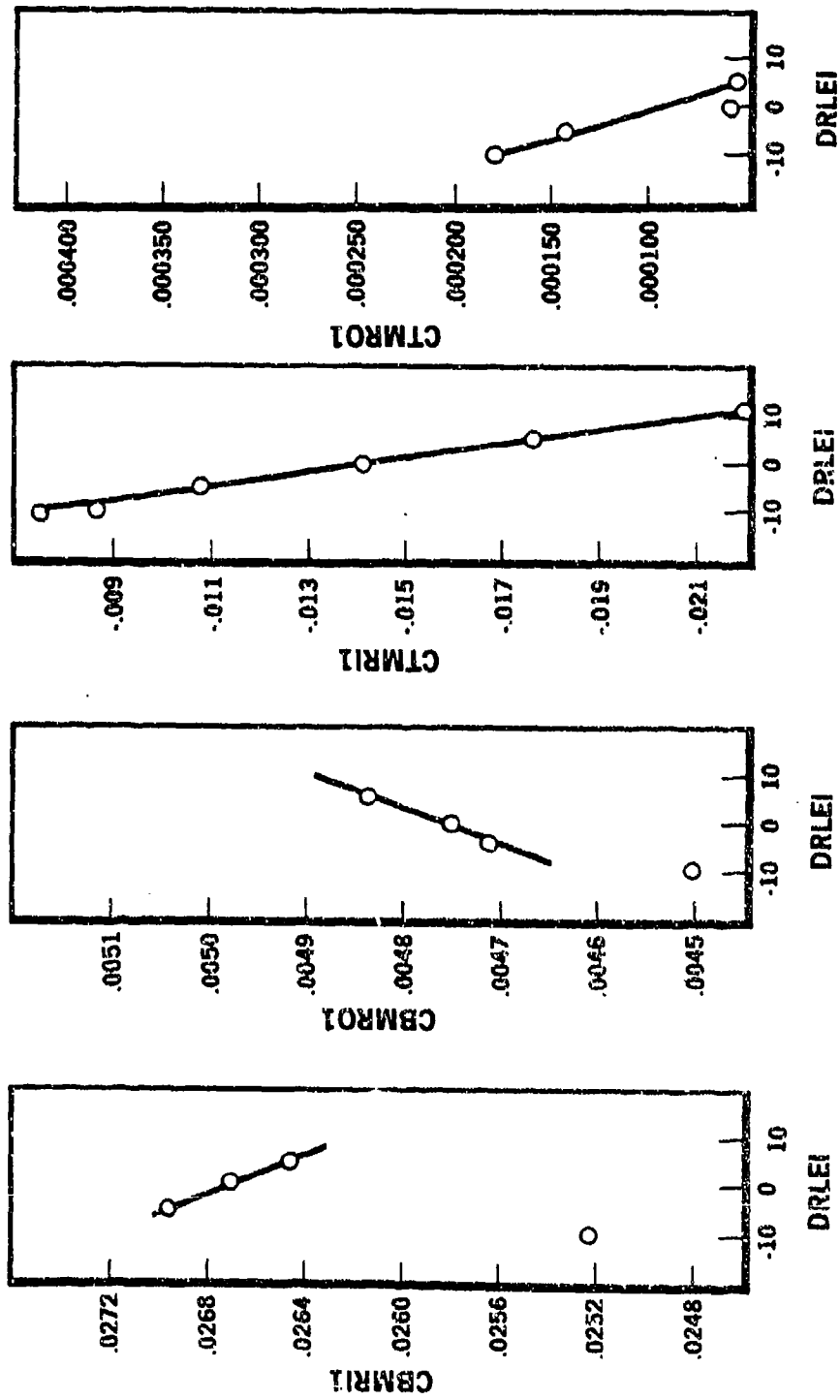
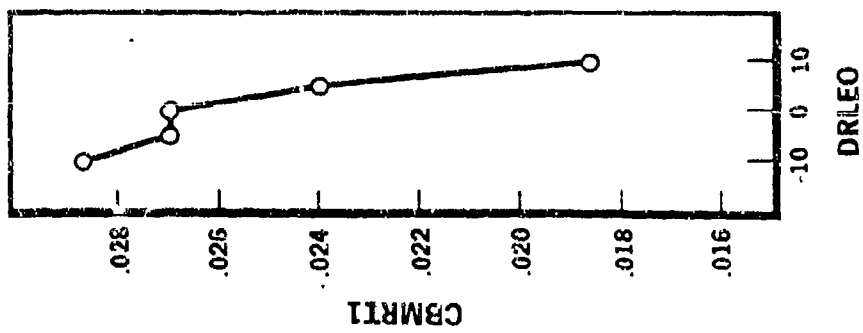
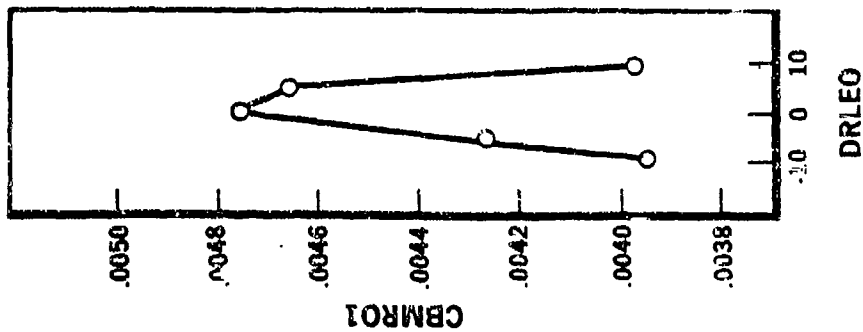
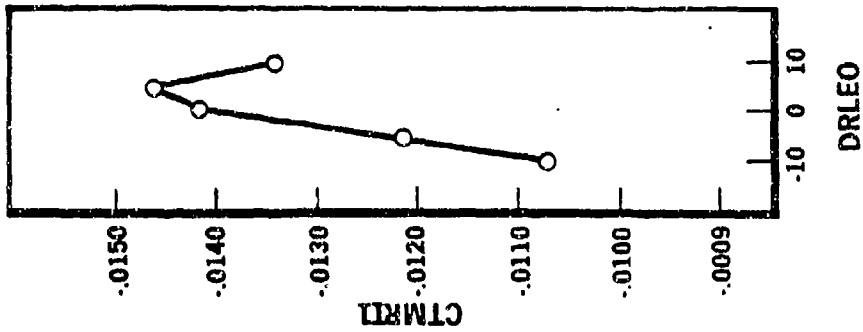
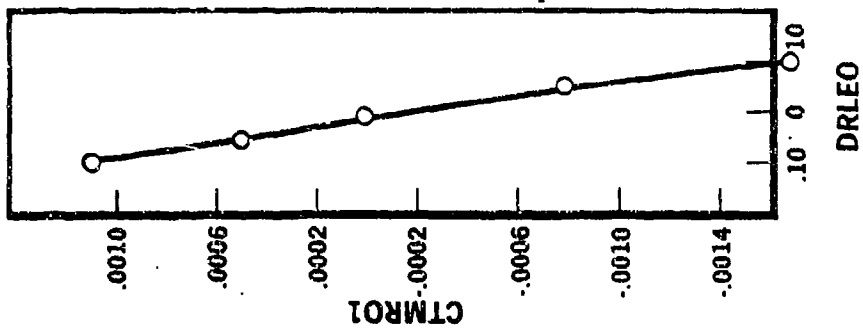


Figure 5-23. Variation of  $CH_{\delta}$  LEI (at LEI) with Dynamic Pressure



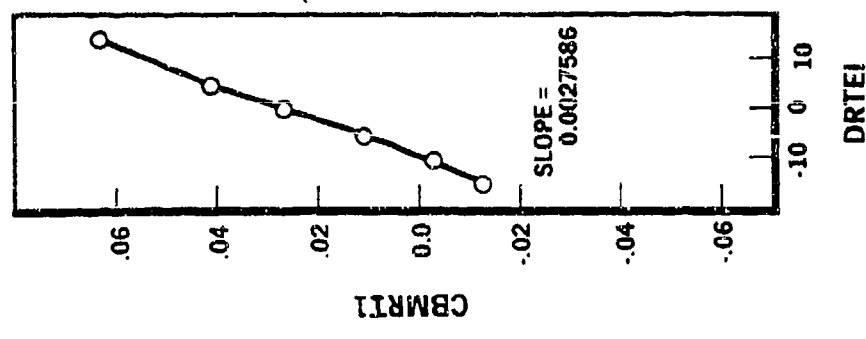
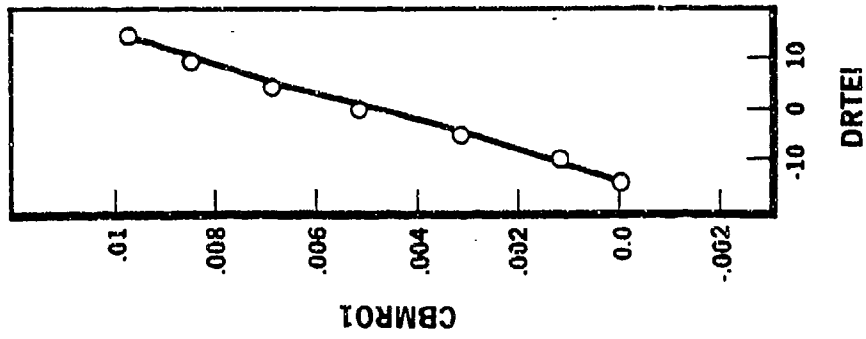
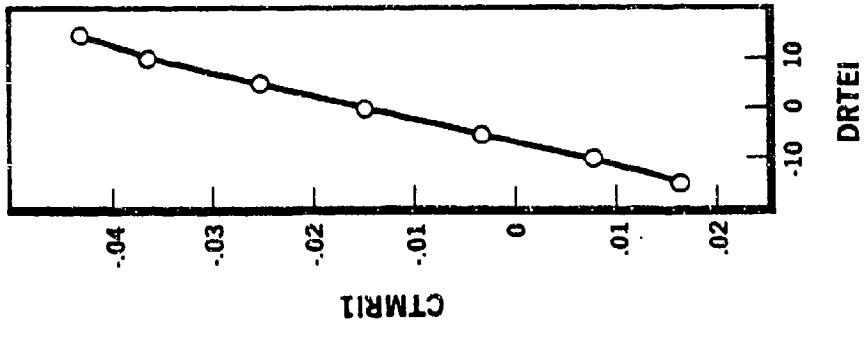
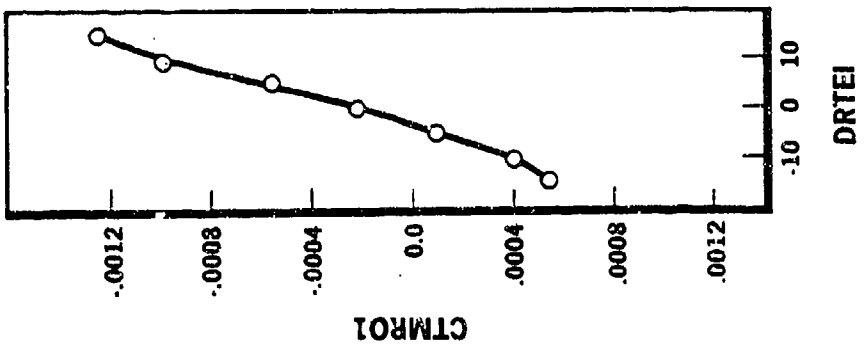
**MACH = 0.90**  
**Q = 35 PSF**

Figure 5-24. Variation of Bending and Torsional Moments with  $\delta$  (Leading Edge Inboard)



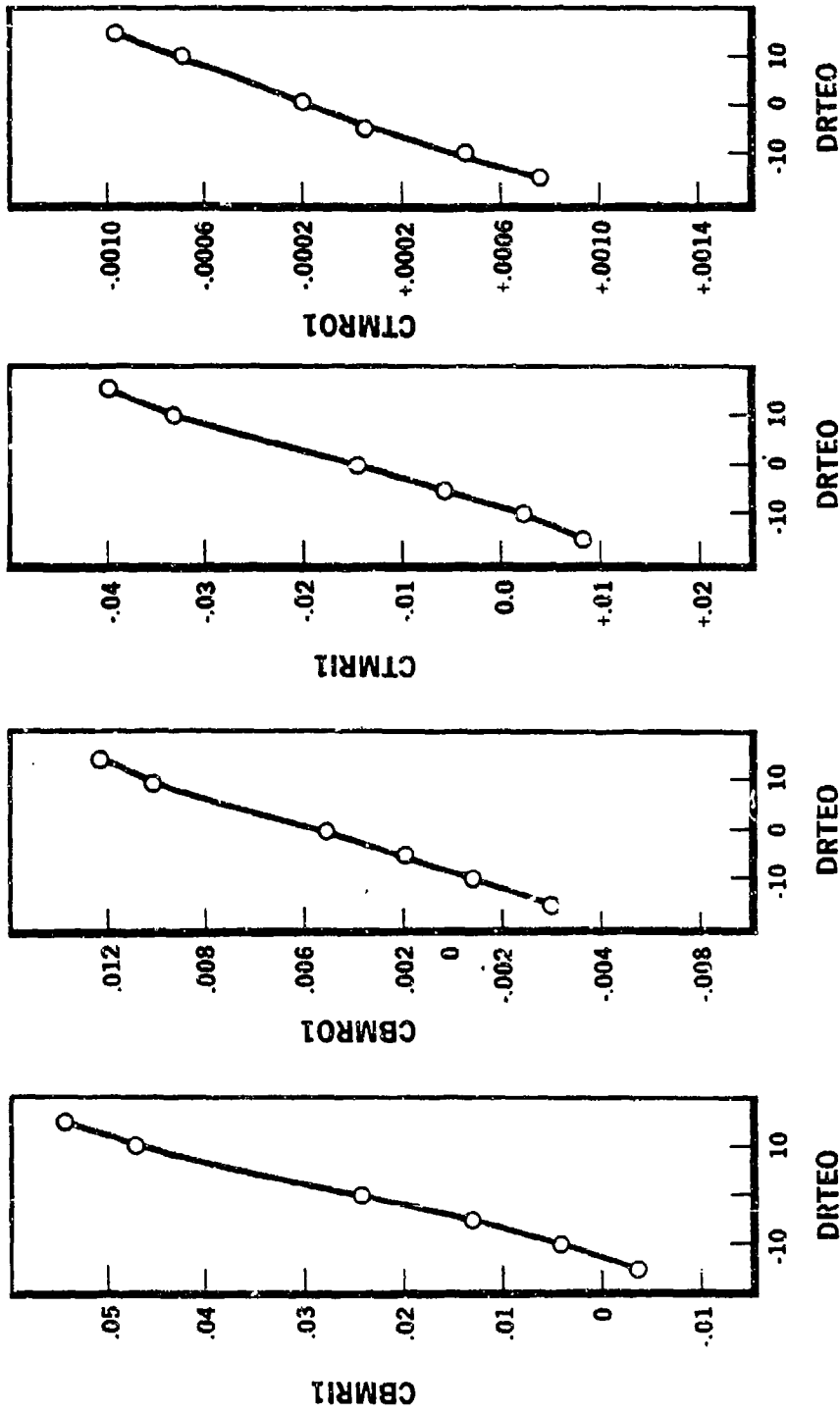
$\alpha = 0$   
**MACH = 0.90**  
**Q = 35 PSF**

Figure 5-25. Variation of Bending and Torsional Moments with  $\xi$  (Leading Edge Outboard)



$\alpha = 0$   
**MACH = 0.90**  
**Q = 35 PSF**

Figure 5-26. Variation of Bending and Torsional Moments with  $\delta$  (Trailing Edge Inboard)



$\alpha = 0$   
**MACH = 0.90**  
**Q = 35 PSF**

Figure 5-27. Variation of Bending and Torsional Moments with  $\delta$  (Trailing Edge Outboard)

## 5.2.1 CDF-AEROELASTIC CALCULATIONS

Rockwell's full potential/aeroelastic CFD code was applied for the AFW model configuration with control surfaces. Two Mach numbers,  $M = 0.9$  and  $M = 1.15$ ; three dynamic pressures,  $q = 0.25$  psi,  $q = 1.75$  psi and  $q = 2.3$  psi; and zero angle-of-attack were selected for the flight conditions. Also, each control surface (leading edge inboard, leading edge outboard, trailing edge inboard, and trailing edge outboard) was deflected  $\pm 2$  or  $\pm 5$  degrees to calculate lift, moment, and roll forces.

To avoid the complexity of the CFD gridding of the body and for economic reasons, the wind tunnel model was modified near the body. This modification allows inclusion of approximated aerodynamic body effects. Details are shown in Figure 5-28. The streamwise lines represent CFD grid lines. A total of 32,000 points (100 chordwise by 16 spanwise by 20 vertical) were used. Also, 480 points (40 by 12) were used for the structural control points of the wing. A typical CFD grid with control surfaces deflected is shown in Figure 5-29.

For lift force calculation, the pressure coefficient is calculated on the CFD grid of the body for each iteration and finite difference area which corresponds to the grid point is calculated at the same time. Pressure force is then determined by multiplying  $\Delta C_p$  and the area for a given  $Q$ . Pressure force, which is a perpendicular component to the incoming flow direction, is summarized along the chordwise direction for specified span stations. These local forces are later integrated along the span direction to get the total lift force.

For pitch moment calculations, each pressure load is multiplied by the longitudinal arm referenced by the CG location (wing tunnel sting connection point). These individual moment forces are integrated over the entire wing area to obtain the moment force.

For roll moment calculations, after spanwise pressure loads are calculated from the lift force calculation, the lateral moment arms referenced by the centerline of the model are multiplied. Again, these moment forces are added together for the total roll moment.

The current full potential code is based on a symmetrical configuration. In the case of antisymmetrically deflected control surfaces (control surface deflection angles on the right wing are different from control surface deflection angles on the left wing), an independent analysis was conducted for each side, since only one side can be taken by the full potential flow solver.

Thus, lift and moment forces in this case are averaged values of right and left wing analyses. For the total roll moment calculation, differences between the right and left roll coefficient values are taken. In the case, one of the rolling directions (left roll or right roll) is considered as the positive roll direction.

A TYPICAL PLANFORM SHAPE OF A FIGHTER CONFIGURATION WITH MODIFIED BODY. STATIONS ARE LOCATION OF COMPUTATIONAL GRID

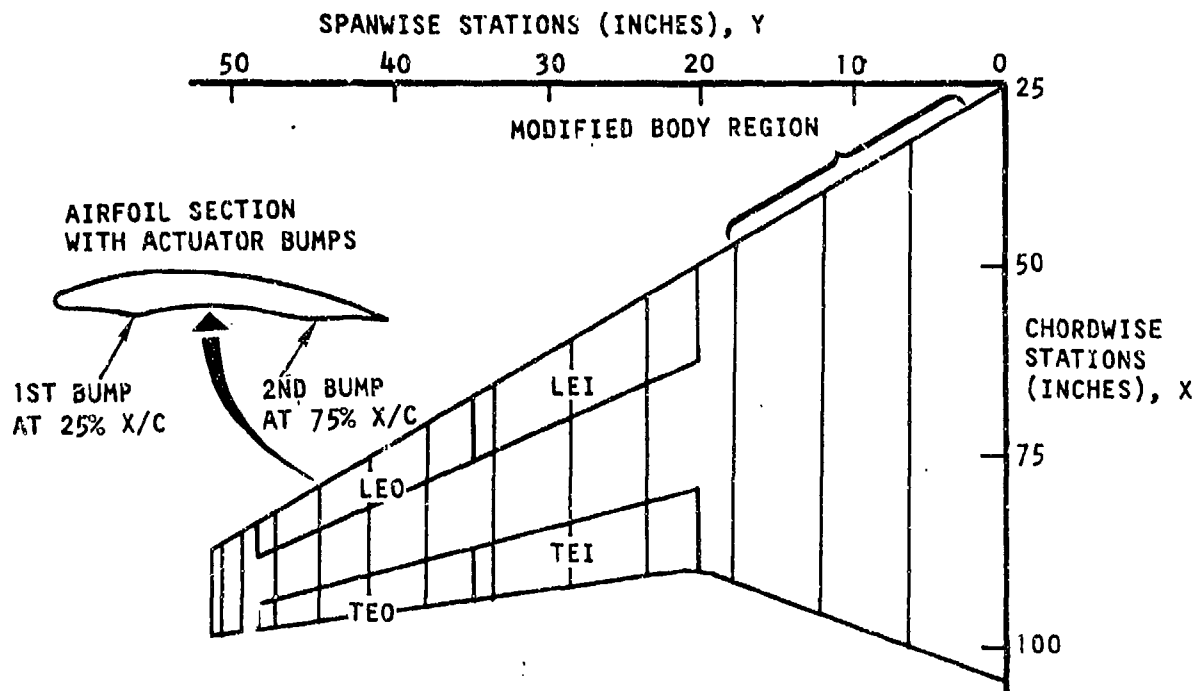


Figure 5-28. AFW Wing Configuration with Control Surfaces. Body Region has been Modified

SECTION I-5

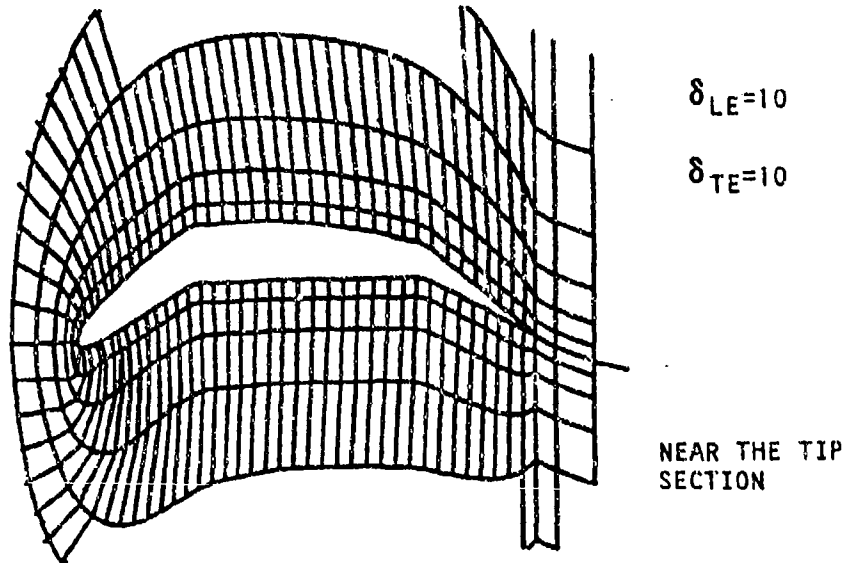
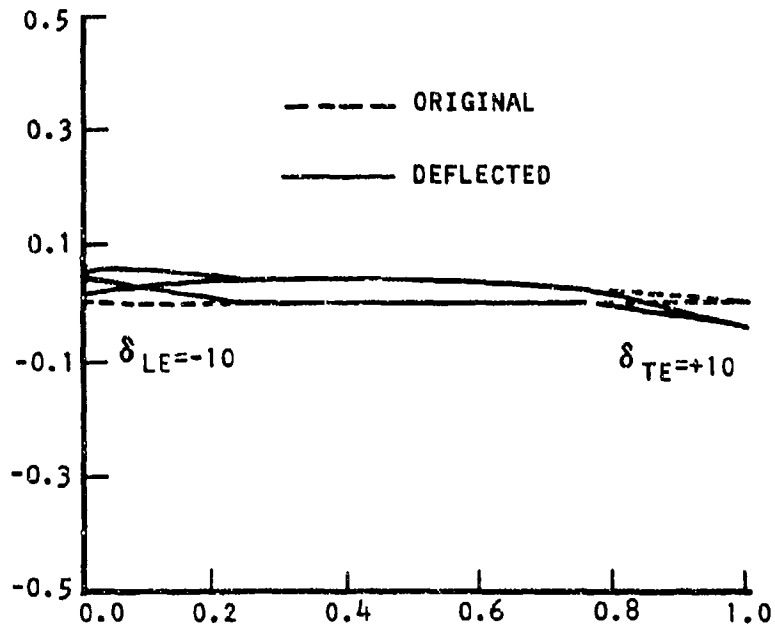


Figure 5-29. Computational Grid with Leading Edge and Trailing Edge Control Surfaces Deflected

Two Mach numbers,  $M = 0.9$  and  $M = 1.15$ , were selected for zero angle of attack flow conditions. Each one of four control surfaces, LEI, TEI, LEO, and TEO were deflected by at least two different angles,  $\delta = \pm 2$  or  $\pm 5$  at a time. Although capability exists for all four control surface analyses, only two control surfaces, TEI and TEO, were used for this study. In the aeroelastic study, three dynamic pressures were selected for each Mach number. A summary of the analyses for  $M = 0.9$  is shown in Table 5-1 and analyses for  $M = 1.15$  are shown in Table 5-2. Also, extra flow conditions for  $M = 1.15$  and  $\alpha = 1.66$  are shown in Table 5-3.

Table 5-1

AERODYNAMIC FORCES WITH CONTROL SURFACE DEFLECTION FOR  
 $M_{\infty} = 0.9$  and  $\alpha = 0.0$

Q(Psi)	$\delta_{TEO}$	$\delta_{TEI}$	$C_L$		$C_M$		$C_{ROLL}$	
			DATA	FULL POT	DATA	FULL POT	DATA	FULL POT
0.25	0	0	.1117	.0913	-.0120	-.0081		
	5	0	.1302	.1227	-.0250	-.0137		
	-5	0	.0869	.0636	.0000	-.0040		
	0	-5	.1754	.1806	.0350	-.0182		
	0	-5	.0399	.0105	.0109	-.0008		
	$\pm 5$	0	.1129	.1085	-.0121	-.0125	.0075	.0080
	0	$\pm 5$	.1159	.0956	-.0115	-.0095	.0120	.0137
1.05	0	0	.0716	.0681	-.0066	-.0076		
	5	0	.0728	.0790	-.0145	-.0120		
	-5	0	.0676	.0615	.0014	-.0044		
	0	5	.1176	.1339	-.0252	-.0170		
	0	-5	.0243	.0085	.0119	-.0008		
	+5	0	.0736	.0703	-.0063	-.0082	.0031	.0035
	0	+5	.0734	.0712	-.0064	-.0088	.0079	.0113
1.74	0	0	.0527	.0519	-.0040	-.0069		
	2	0	.0491	.0486	-.0058	-.0080		
	-2	0	.0546	.0547	-.0017	-.0052		
	0	2	.0643	.0687	-.0101	-.0105		
	0	2	.0399	.0336	-.0022	-.0044		
	$\pm 2$	0	.0517	.0513	-.0040	-.0066	.0003	.0003
	0	$\pm 2$	.0522	.0512	-.0040	-.0074	.0022	.0031

Table 5-2

AERODYNAMIC FORCES WITH CONTROL SURFACE DEFLECTION FOR  
 $M_\infty = 1.15$  and  $\alpha = 0.0$

Q(psi)	$\delta_{TEO}$	$\delta_{TEI}$	$C_L$		$C_M$		$C_{ROLL}$	
			DATA	FULL POT	DATA	FULL POT	DATA	FULL POT
0.25	0	0	.0647	.0556	-.0145	-.0101		
	2	0		.0585		-.0101		
	-2	0		.0503		-.0089		
	0	2		.0704		-.0121		
	0	-2		.0396		-.0068		
	$\pm 2$	0		.0549		-.0095		.0017
	0	$\pm 2$		.0549		-.0095		.0316
1.73	0	0	.0144	.0179	-.0015	-.0073		
	2	0	.0122	.0106	-.0019	-.0073		
	-2	0	.0155	.0182	-.0003	-.0060		
	0	2	.0191	.0186	-.0045	-.0089		
	0	-2	.0086	.0103	.0013	-.0057		
	$\pm 2$	0	.0143	.0144	-.0011	-.0067	.0004	.0004
	0	$\pm 2$	.0130	.0144	-.0020	-.0073	.0007	.0007
2.35	0	0		.0031		-.0061		
	2	0		-.0055		-.0067		
	-2	0		.0066		-.0061		
	0	2		.0044		-.0073		
	0	-2		.0005		-.0044		
	$\pm 2$	0		-.0012		-.0065		-.0003
	0	$\pm 2$		.0025		-.0059		-.0000

Table 5-3

AERODYNAMIC FORCES WITH CONTROL SURFACE DEFLECTION FOR  
 $M_\infty = 1.15$  and  $\alpha = 1.66$

Q(psi)	$\delta_{TEO}$	$\delta_{TEI}$	$C_L$		$C_M$		$C_{ROLL}$	
			DATA	FULL POT	DATA	FULL POT	DATA	FULL POT
2.35	0	0	.1055	.1142	.0036	-.0040		
	2	0	.1024	.1161	.0033	-.0044		
	-2	0	.1088	.1192	.0045	-.0032		
	0	2	.1079	.1229	.0003	-.0060		
	0	-2	.1037	.1119	.0076	-.0024		
	$\pm 2$	0	.1059	.1176	.0042	-.0038	.0004	.0005
	0	$\pm 2$	.1052	.1174	.0041	-.0043	.0004	.0005

The calculated data were reduced to determine control surface deflection derivatives. Figures 5-30 through 5-33 show the static rolling moment derivatives with respect to each control surface deflection. Also shown on Figure 5-30 through 5-33 are the linear theory at test calculation in matching test results.

Comparison between CFD and test pressure data is presented in the appendix.

### 5.3 WING DEFLECTION CALCULATIONS

The wind tunnel pressure data were used to calculate wing deflections for a few selected test conditions. The pressure data were used to calculate a distributed grid of vertical forces. Those forces were used to multiply the model measured structural flexibility matrix to calculate wing deflections.

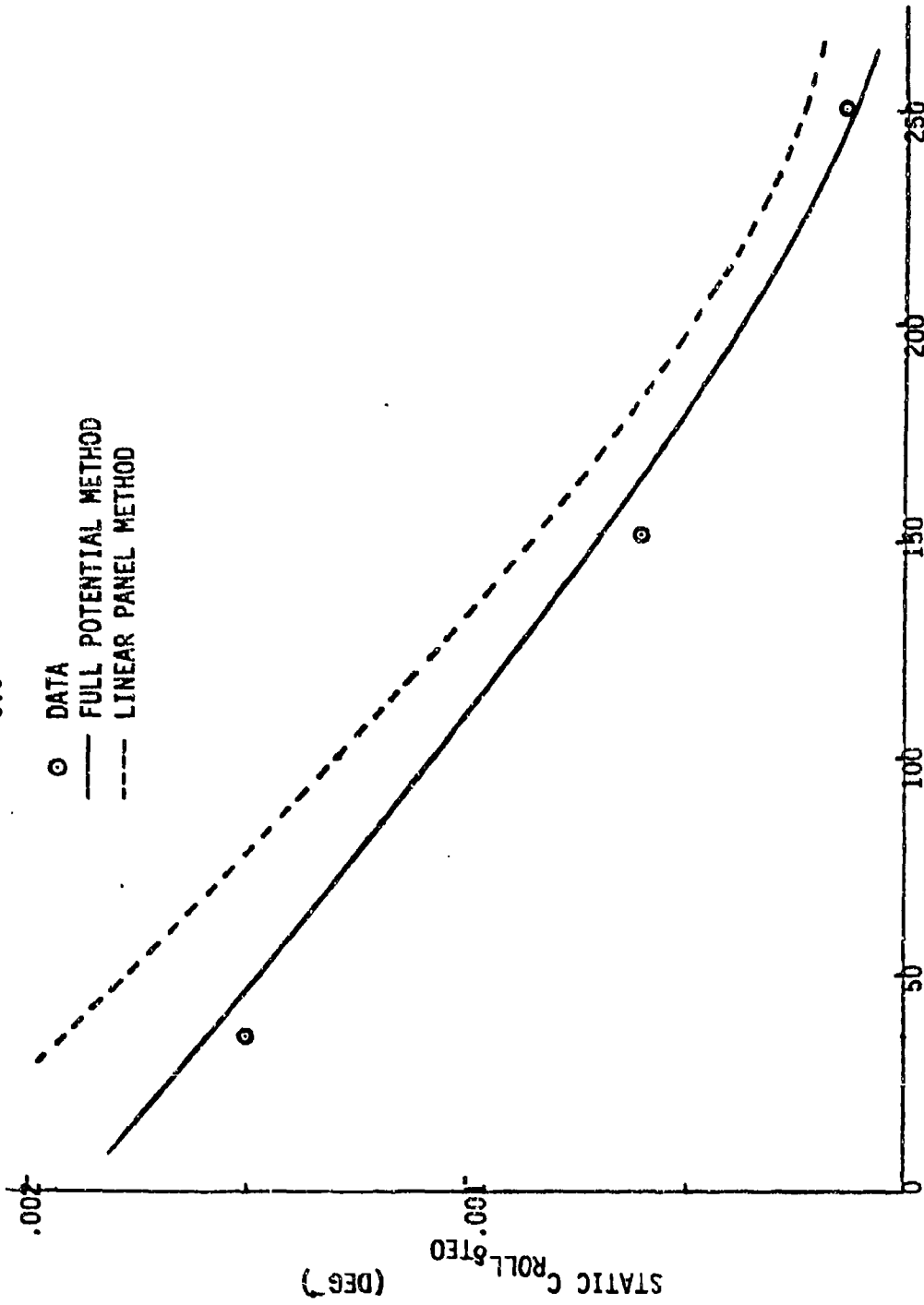
Figure 5-34 through 5-37 present wing deflections due to single control surface rotations or angle-of-attack. Figures 5-38 through 5-40 present deflections due to typical roll control surface deflections. Figure 5-38 presents deflections due to a typical low q rolling maneuver, where both trailing control surfaces are used. Figure 5-39 presents deflections for a medium q rolling maneuver where the LE0 and TEI surfaces are used (at this condition, the TE0 surface has approximately zero rolling effectiveness). Figure 5-40 presents deflections for a high q rolling maneuver where the TE0, in the reversed direction, and the LE0 surfaces are used (the TEI surface was used for trim at this condition). These deflection calculations (using measured pressure and structural flexibility data) agreed very well with the analytical deflection calculations generated by the method described in section 5.1.3.

### 5.4 STATIC AEROELASTIC DATA CONCLUSIONS

The static aeroelastic test and analytical data generally showed fairly good agreement. The results of the linear panel model analyses with flexibility followed the trends of the experimental data fairly closely. Therefore, linear methods will serve as good tools for early conceptual and preliminary design in determining flexible control surface effectiveness and sizing. The CFD-aeroelastic analyses compared well with experimental values in most cases. However, some supersonic CFD code correlations were not as good. These cases were for areas where the body model was simplified. It is felt that if the actual complete model geometry were modeled, the CFD code would provide very accurate results in the lower angle-of-attack (less than 10 degrees) and control surface deflection (less than 10 degrees) regimes. However, to determine high angle-of-attack or high control surface deflection data, wind tunnel tests would be required.

AFW WIND TUNNEL MODEL

M = 0.9  
 $\alpha = 0.0$



DYNAMIC PRESSURE, Q, PSF

Figure 5-30. Roll Coefficient Versus Q for the Trailing Edge Outboard Control Surface Deflection at M = 0.9

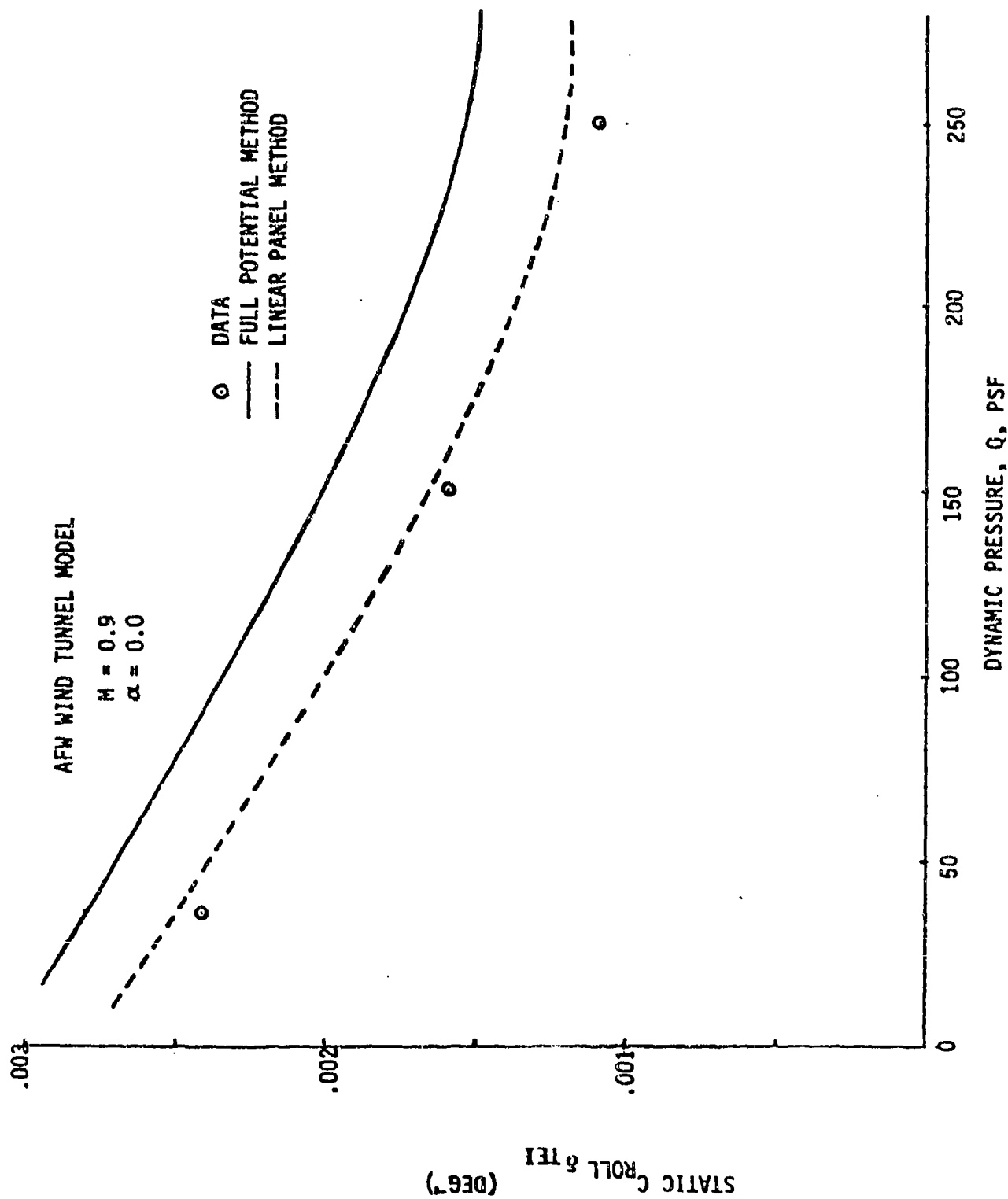


Figure 5-31. Roll Coefficient Versus Q for the Trailing Edge Inboard Control Surface Deflection at  $M = 0.9$

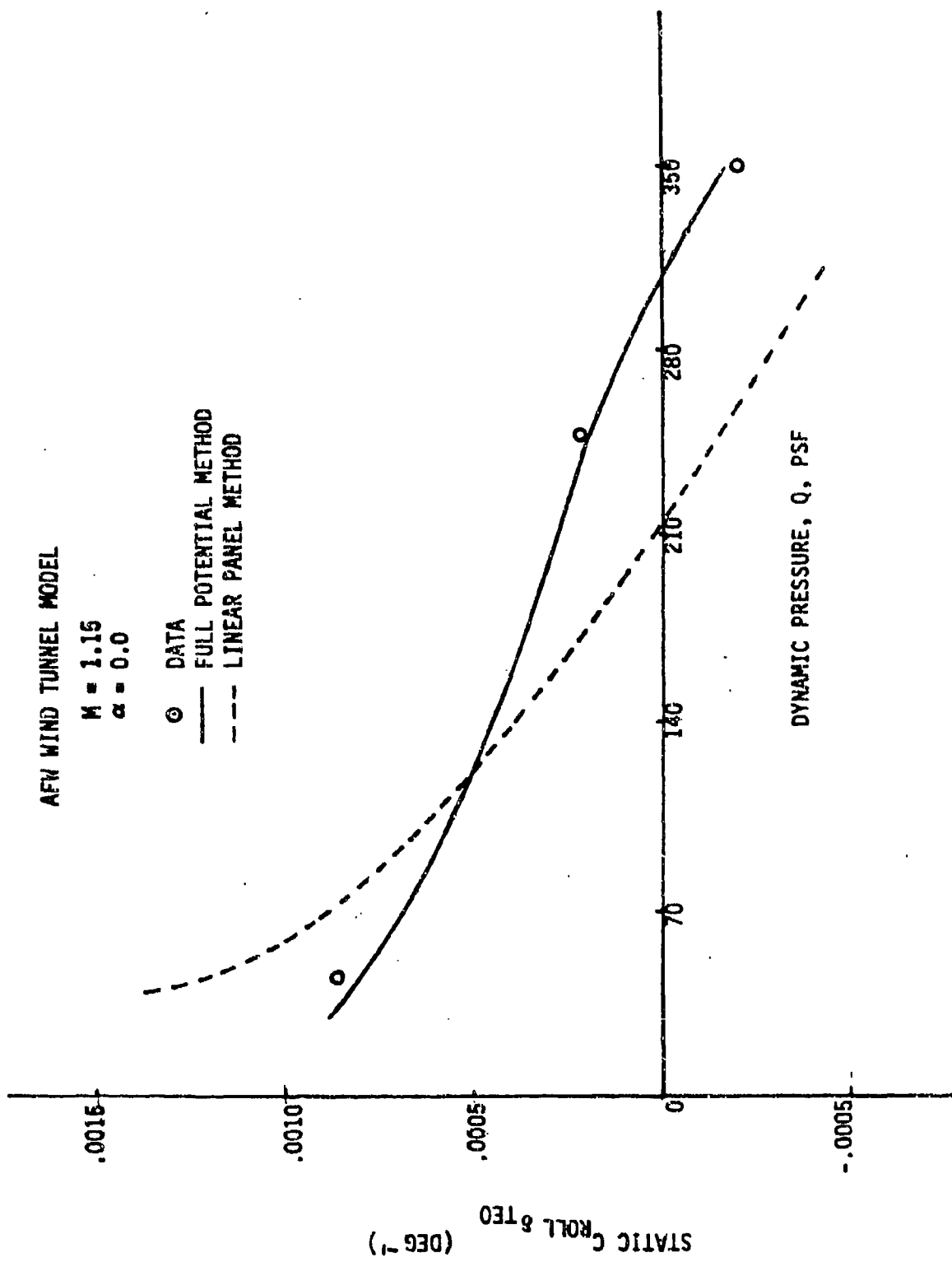


Figure 5-32. Roll Coefficient Versus Q for the Trailing Edge Outboard Control Surface Deflection at  $M = 1.15$

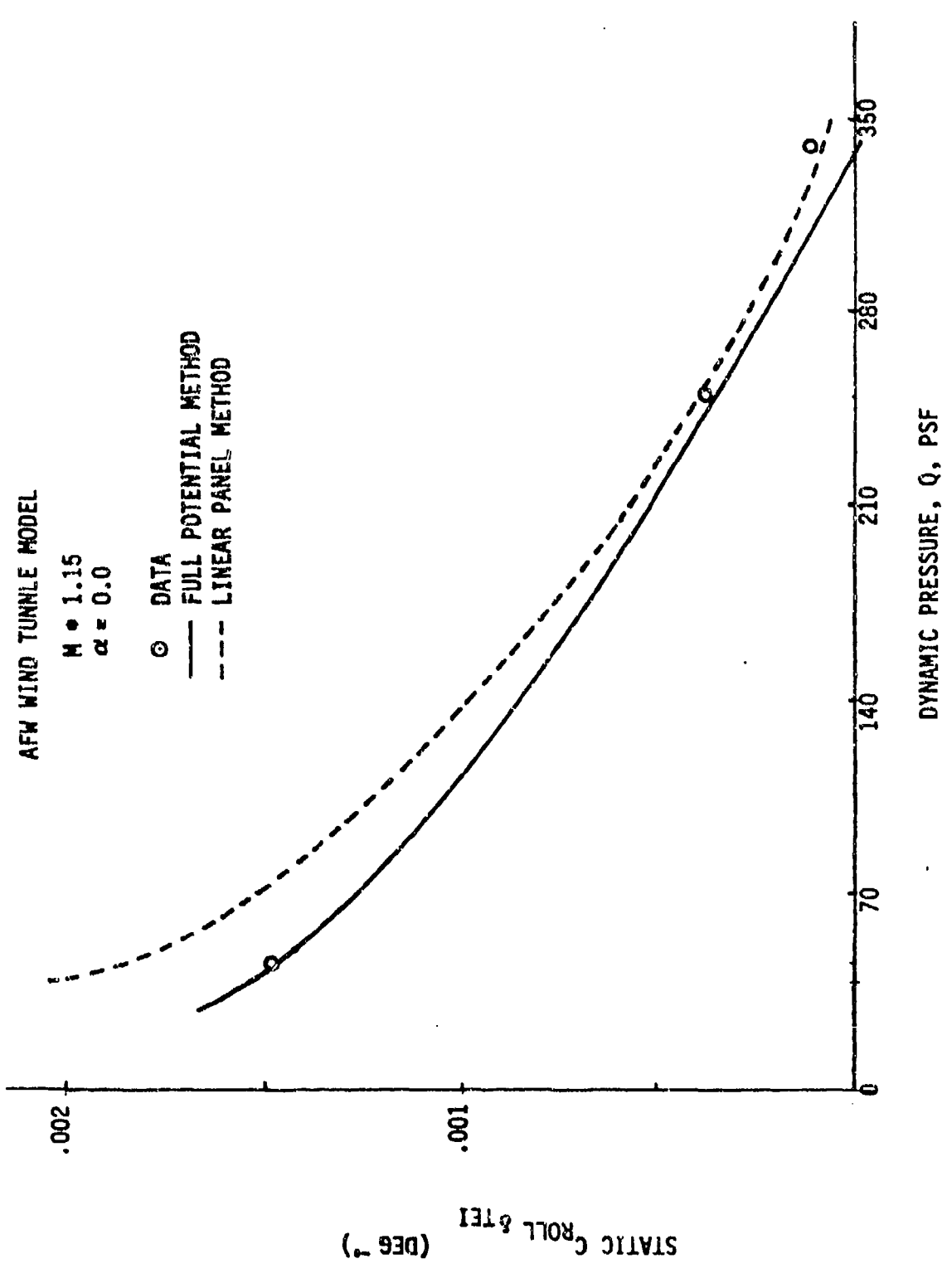


Figure 5-33. Roll Coefficient Versus Q for the Trailing Edge Inboard Control Surface Deflection at M = 1.15

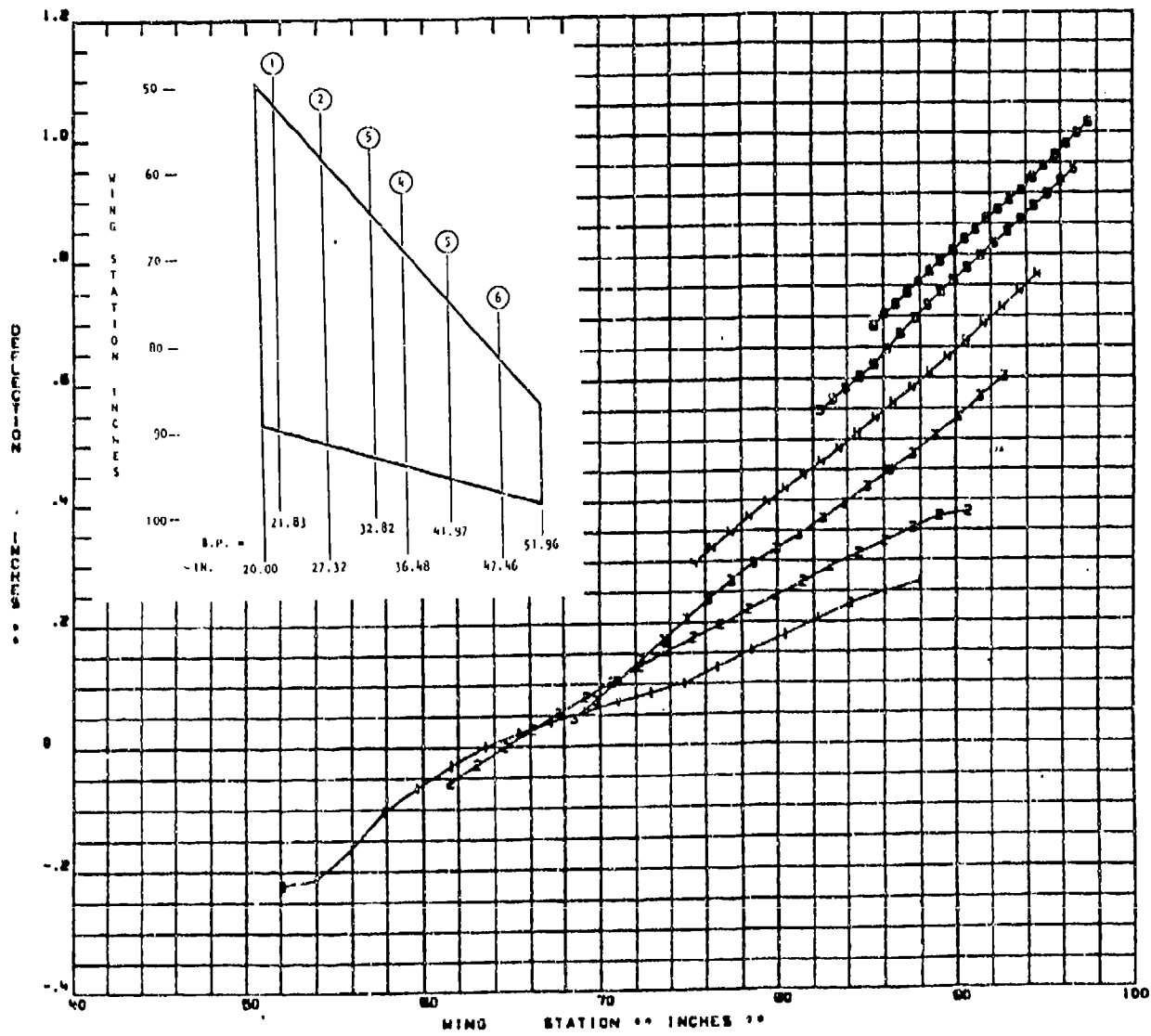


Figure 5-34. Wing Deflections Calculated from Test Data  
 $M = 0.9$ ,  $q = 150$  psf,  $\alpha = 0$ ,  $TEO = +5^\circ$

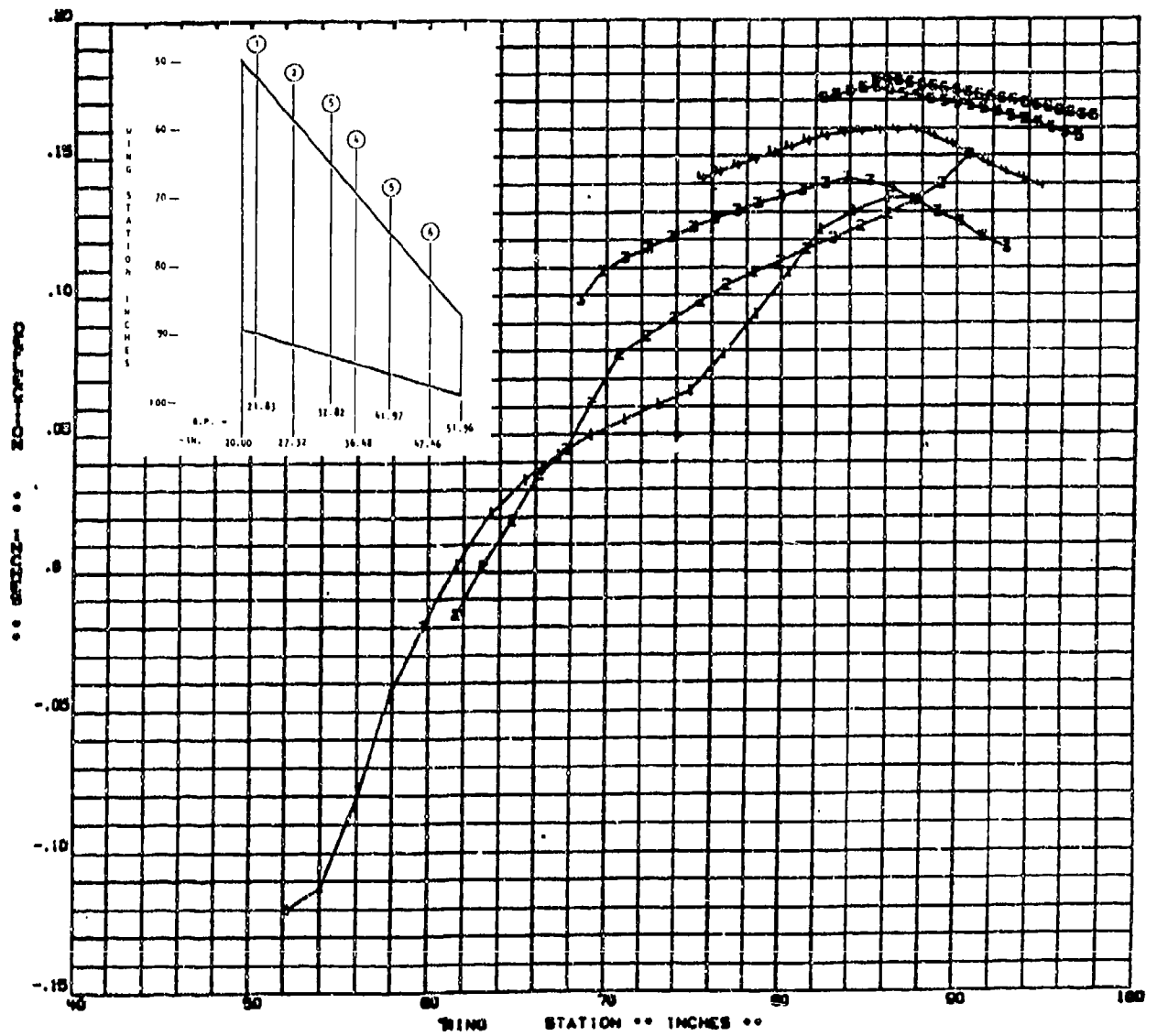


Figure 5-35. Wing Deflections Calculated from Test Data  
 $M = 0.9$ ,  $q = 150$  psf,  $\alpha = 0$ ,  $TEO = -5^\circ$

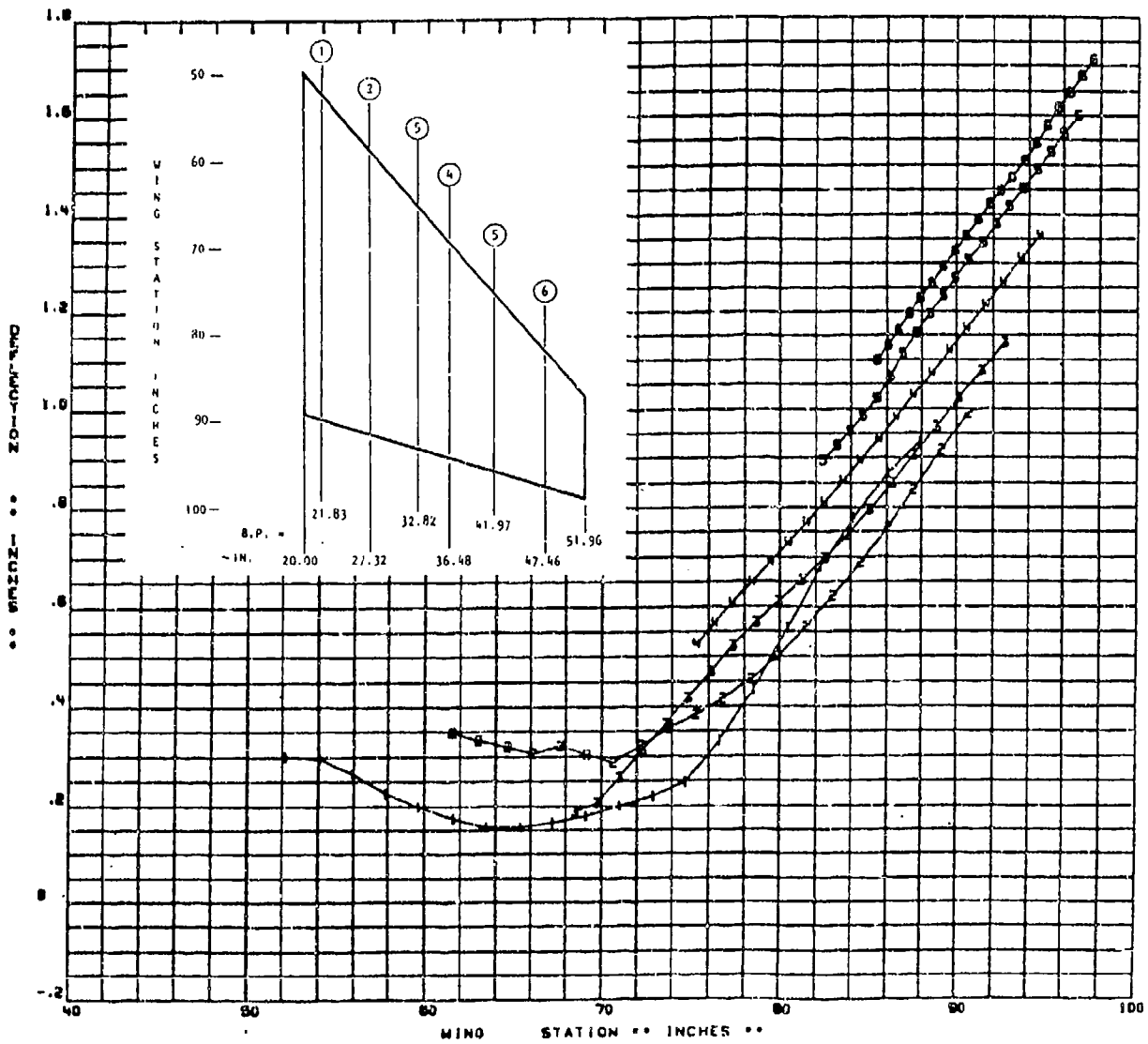


Figure 5-36. Wing Deflections Calculated from Test Data  
 $M = 1.15$ ,  $q = 340$  psf,  $\alpha = 0$ ,  $TEO = 1.5^\circ$

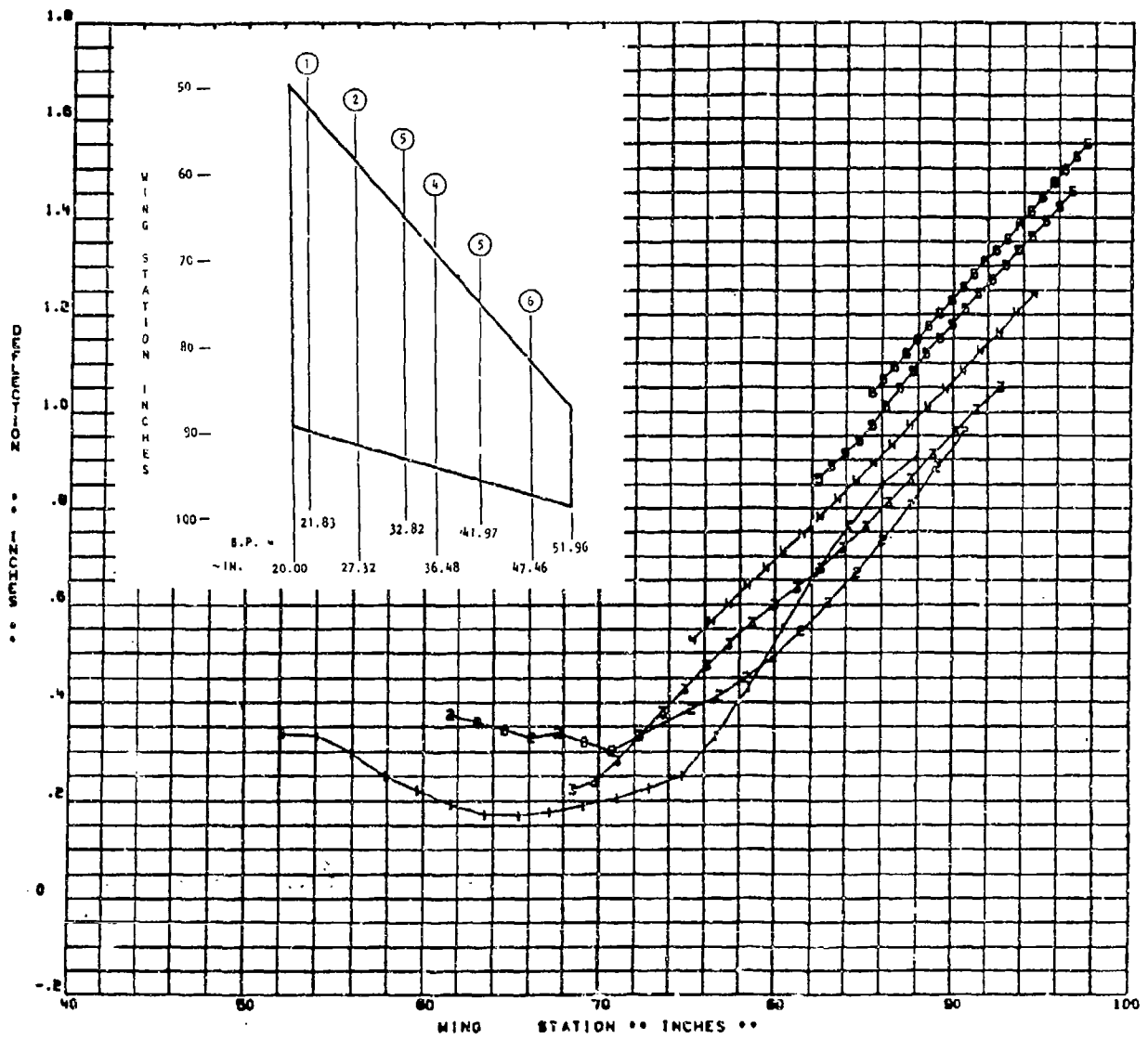


Figure 5-37. Wing Deflections Calculated from Test Data  
 $M = 1.15$ ,  $q = 340$  psf,  $\alpha = 0$ ,  $TEO = -2^\circ$

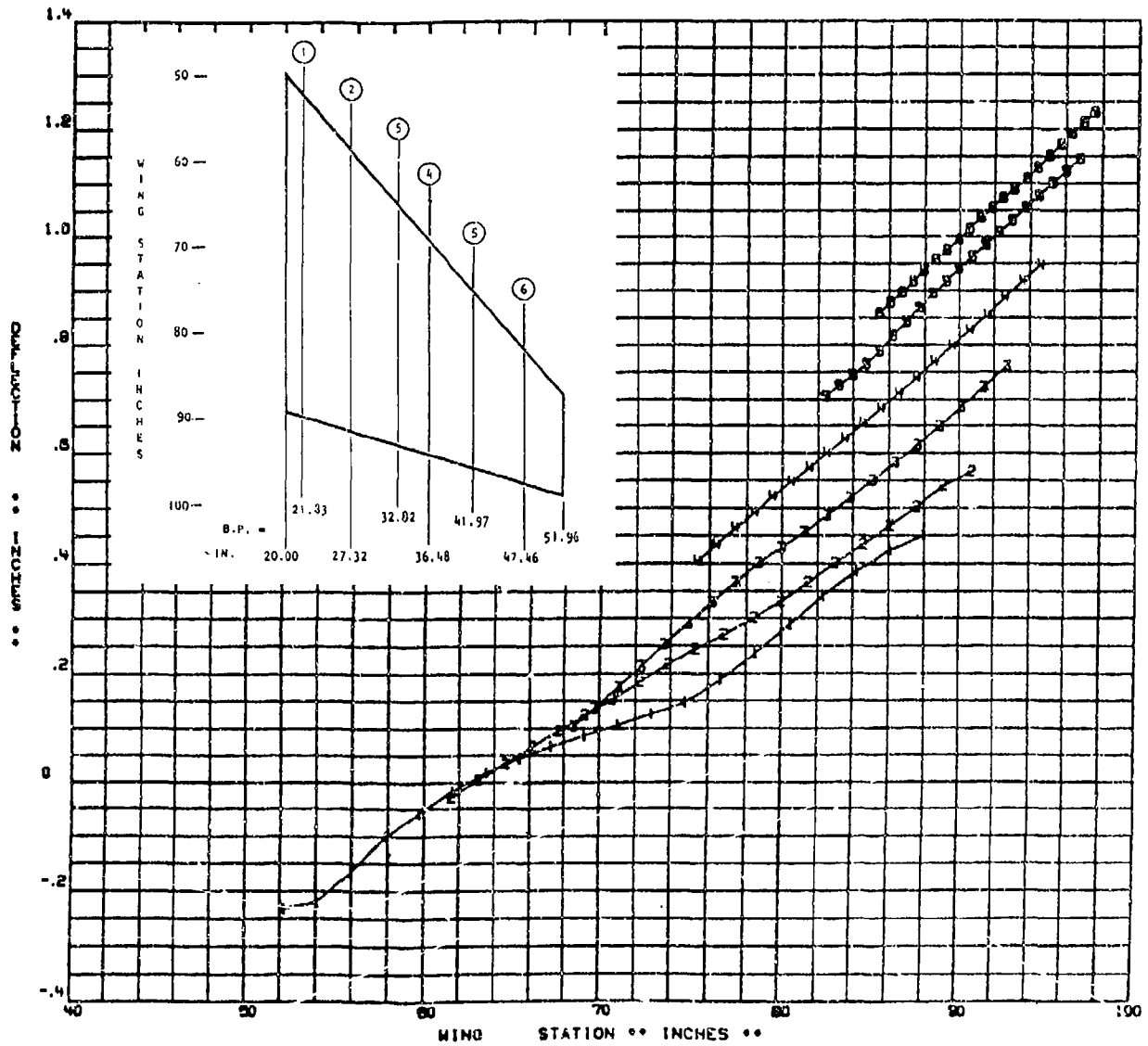


Figure 5-38. Wing Deflections Calculated from Test Data  
 $M = 0.9$ ,  $q = 150$  psf,  $\alpha = 0$ ,  $TEI = 2.75^\circ$ ,  $TEO = -2^\circ$

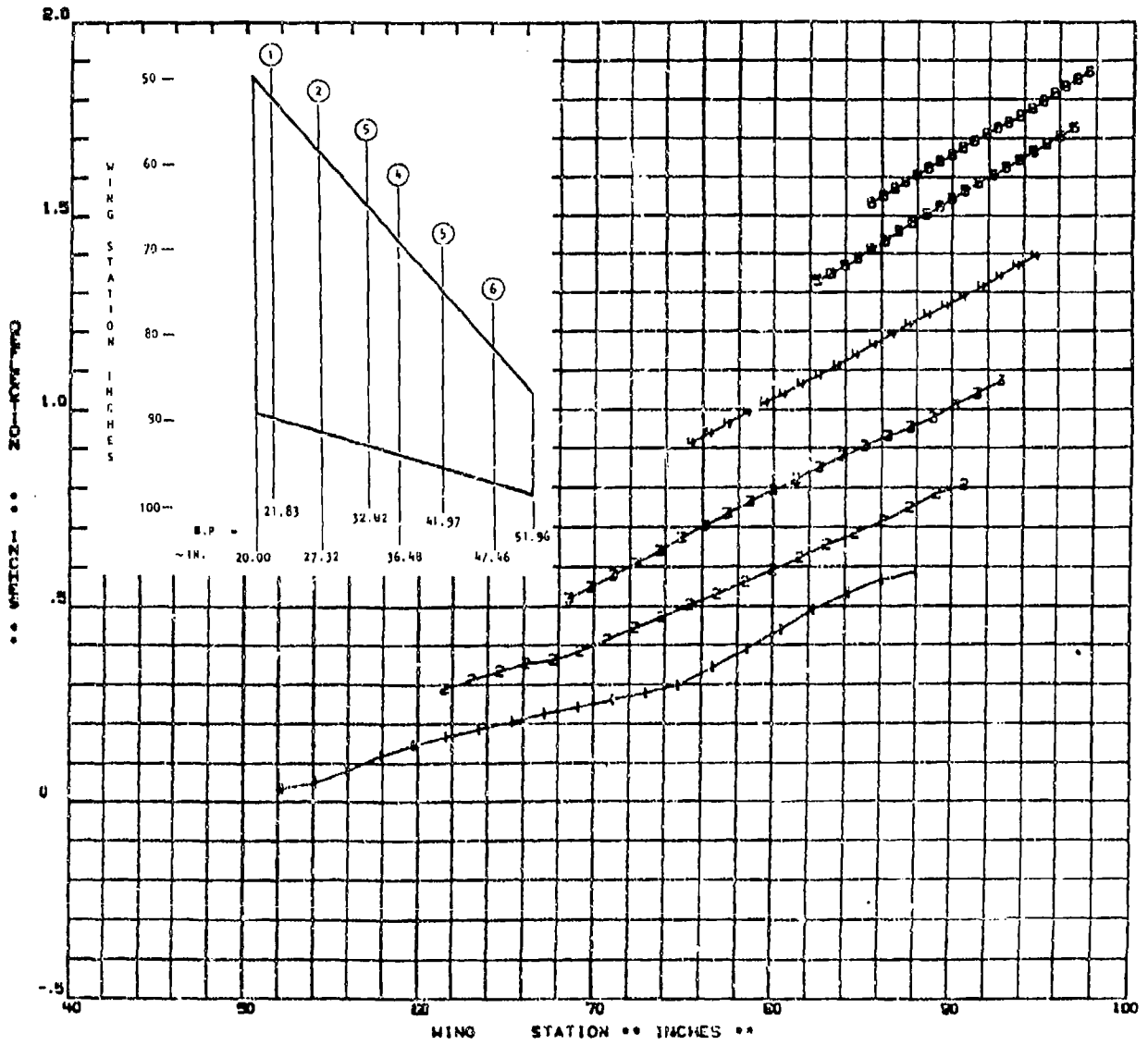


Figure 5-39. Wing Deflections Calculated from Test Data  
 $M = 0.9$ ,  $q = 250$  psf,  $\alpha = 0$ ,  $TEC = -2^\circ$ ,  $TEI = 2.75^\circ$

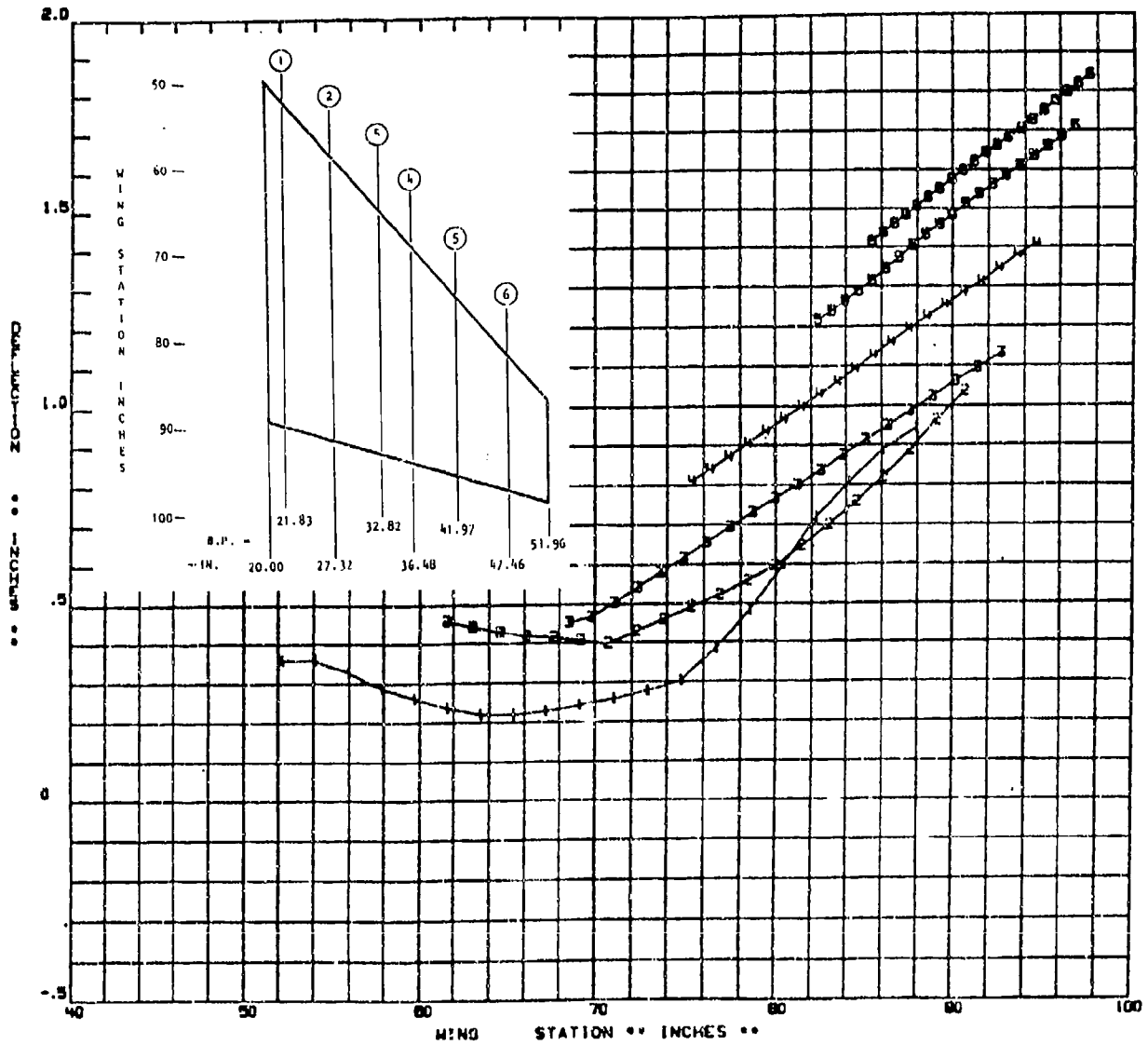


Figure 5-40. Wing Deflections Calculated from Test Data  
 $M = 1.15$ ,  $q = 340$  psf,  $\alpha = 1.5^\circ$ ,  $TEI = 1.25^\circ$ ,  $TEP = -3^\circ$

## 6.0 ACTIVE CONTROL SYSTEMS DESIGN AND TESTS

Three separate active control modes were developed and wind tunnel tested. They were 1) roll control, 2) maneuver load control, and 3) structural mode control. Analytical models were developed, control laws were designed, software was coded in the model digital controller, and wind tunnel tests were conducted for each mode.

The roll control mode was developed to show that high roll rates could be attained in the high end of the Mach/dynamic pressure flight envelope. The maneuver load control (MLC) system was developed to show that wing loads could be significantly lowered using MLC, and the structural mode control system was developed to show that wing dynamic response to control surface input and/or turbulence could be reduced using active controls.

Wind tunnel tests of the roll control and maneuver load control systems indicated that these objectives were met. The structural mode control system was not successfully tested because of problems in implementation of the software. The test data, however, verified the analytical design which showed that the objective would be met.

### 6.1 ROLL CONTROL DESIGN AND TESTS

The roll control system of the AFW wind tunnel model was designed to achieve high dynamic roll response from high subsonic through low supersonic flight regimes. The model roll control system duplicated the proposed full-scale implementation and mechanization including sample rates and filter values authority distribution. Roll control laws were designed for six tunnel test conditions and were implemented in a control system mechanization which was applicable to the entire test envelope. Testing was conducted to duplicate full-scale vehicle roll stick input in order to extract MIL-F-8785C specification performance data and MIL-F-9490D stability data for evaluation. Also, the data were used for correlation and corroboration of the analytic tool used in the modeling and control synthesis and analysis efforts.

#### 6.1.1 ROLL TRIM SYSTEM

The AFW roll trim control system was developed to allow positioning of the model at any bank angle as commanded by the user of the system. The primary use of this system was for positioning the model at an initial position prior to performing roll maneuvers. For most roll maneuvers, the model was trimmed at -90 degrees of bank angle (right wing up). This allowed the model a full 180 degrees to accelerate and decelerate during the roll system tests (as opposed to 90 degrees if rolled from straight and level). The roll trim system was also used for holding a bank angle after a roll maneuver was completed and then for returning the model to straight and level or a new bank angle from which a new roll maneuver could be initiated.

Since the model center of gravity was below the axis of rotation of the model, a rolling moment (39.3 ft-lbs of moment at -90 degrees bank angle) was required to hold the model at any non-zero bank angle. This moment was offset by deflecting the control surfaces differentially to balance the restoring force produced by the center of gravity offset.

The design goal of the roll trim system was to roll the model to a commanded position at a rate not to exceed 15 deg/sec. This rate was determined by weighing considerations of the amount of time the model would take to get to the desired angle and the maximum allowable rate that was considered reasonable during a trimming maneuver. Also required was a design that had minimal complexity where a single line of feedback and a single set of gains for all flight conditions could be achieved. The system also had to be completely decoupled from the roll controller(s). This allowed alternate control mechanizations to be implemented without alteration of the trim system. Constructing the trim system as an outer loop to the roll systems, as in the conventional implementation in trim systems, would require the evaluation of all roll controllers with the trim system. With the roll trim system decoupled, re-evaluation of unique roll controllers would not have to be conducted within the context of the trim system. The net effect of this was to facilitate "plug in" roll controllers in the second tunnel test in addition to future tests.

The basic roll trim mechanization was characterized by a bank angle feedback system (see Figure 6-1) where the feedback signal originates from a roll potentiometer mounted at the roll bearing on the sting. The roll trim and control systems were computed at 200 Hz sample frequency. The input command to the system was a step command of the magnitude of the desired bank angle. The step input was rate limited to 12 deg/sec to produce a steady ramp input command. This was provided to maintain a roll rate below 15 deg/sec (the 12 deg/sec limit takes care of the overshoot). The gain before the limiter assured that the ramp command had a fast response (i.e., always at or near the rate limits).

The error between the commanded bank angle and the actual bank angle was fed a proportional-plus-integral whose output was distributed to a set of four control surface selector gains. These gains were the same as those used in the roll system for control surface selection and their values were either +1, -1 or 0. The selection of the surfaces was based on their effectiveness in the roll system. Selecting the same control effectors for trim as for roll guaranteed that roll was initiated from the same non-zero surface deflections and allowed for trim with smaller overall surface deflections.

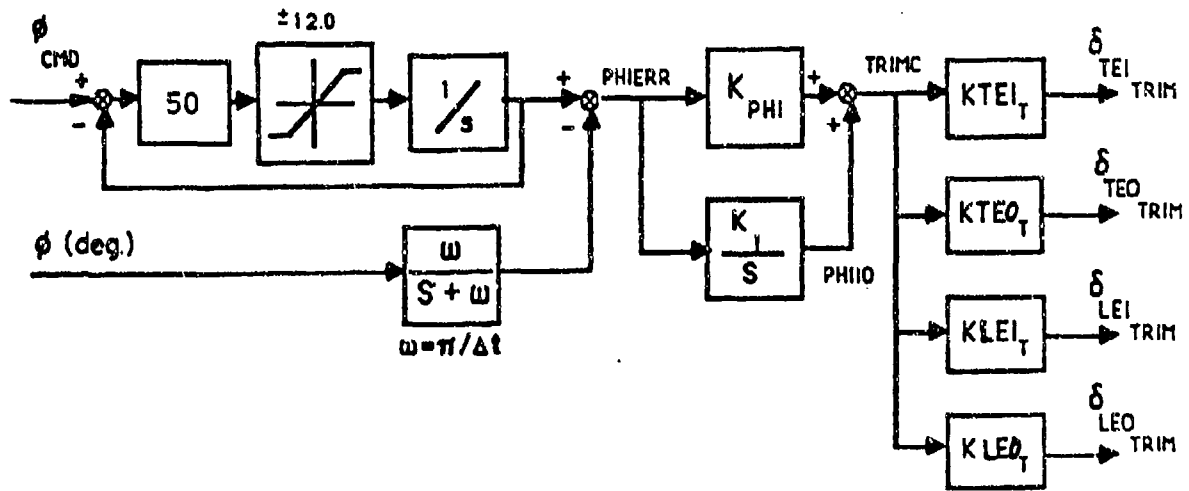


Figure 6-1. Basic Trim Mechanization

### 6.1.2 ROLL CONTROL SYSTEM DESIGN AND IMPLEMENTATION

The roll control system provided roll stability and command performance of the AFW model. The roll control system was demonstrated at six flight conditions. The six design flight conditions were selected to cover the flight envelope given the unique properties of the AFW wing system. Rockwell-designed controllers were demonstrated at all six conditions while a NASA Langley controller was developed and demonstrated for two conditions (this report does not cover the NASA-Langley design).

Performance and stability design requirements for the roll control system were based on MIL-F-8785C and MIL-F-9490D respectively. Roll performance is specified by MIL-F-8785C time to 90-degree bank angle ( $T_{90}$ ) requirements for medium and high speed combat flight regime which were scaled for the model. These  $T_{90}$  values for a full-scale vehicle are 1.0 and 1.4 seconds for medium and high speed envelopes, respectively. These  $T_{90}$  values were scaled by the model frequency scale factor to 0.385 and 0.538 seconds for the model. Note that a model frequency scale factor of 2.6 was used for the roll control system scaled requirements, while the frequency scale factor from Table 3-1 was 2.7. This difference was due to different assumptions of operating tunnel temperature, both of which were within the tunnel operating range. Stability requirements from MIL-F-9490D consisted of 6db of gain margin and 45 degrees of phase margin. In addition to these requirements, there were specific wind tunnel model requirements for avoidance of hinge, bending and torsion moment exceedance.

The basic controller was characterized by a simple roll rate feedback system. The roll rate signal was derived from a rate gyro (which has a maximum output of 470 deg/sec) mounted on the model fuselage. After being filtered, the roll gyro signal passed through a second order filter which was used for rejection of higher order modes beyond the basic rigid body roll mode of prime concern. Each signal was then applied to a roll rate feedback gain. This section formed the basic feedback portion of the system. The controller was structured to allow both the Rockwell and NASA Langley designed controllers to operate within the confines of the same mechanization thus simplifying the real time implementation. Figure 6-2 presents the basic block diagram of the roll control law mechanization.

The input command to the system took the form of a fictitious roll stick (referred to as the pseudo-stick) step which was generated by the real-time controller. This input command passed through a first order lag and a scaling gain which was then split into four paths, one for each pair of surfaces. Each signal was then applied to an individual authority gain. These gains were used to control surface selection at individual flight conditions and to adjust the authority allocated to each surface pair. The command signals were combined with the proper feedback signals applied to a unit proportional plus adjustable gain integrator thus completing the system. As with all other controllers on the model, the roll system operated at a digital sample rate of 200 Hz.

The AFW roll controller was designed to allow for selection of surfaces which have the maximum control power at a given flight condition. Preliminary surface selection for proper allocation of control authority was based on steady state roll rate ( $P_{SS}$ ) approximations for individual surfaces. The model was essentially a one-degree of freedom system while in the roll mode, if only rigid body dynamics were considered. Thus, approximations based on rolling moment due to deflection angle ( $L_{\delta x}$ ) and rolling moment due to roll rate ( $L_p$ ) were quite good. Figure 6-3 presents the computed steady state roll rates (deg/sec/deg) for each pair of control surfaces as a function of dynamic pressure for Mach 0.9. It can be seen that as the dynamic pressure increased, certain effectors become less effective while others became more effective. Figure 6-4 presents a more illustrative way of viewing roll control power as a function of total control power at given flight conditions. Here it can be seen which surfaces should be selected for maximum effectiveness. Similar plots were generated for the entire flight envelope thus providing a guide to selection of control effectors at any of the conditions. Based on the selection of control surfaces, roll feedback gains were generated for the selected surface combinations.

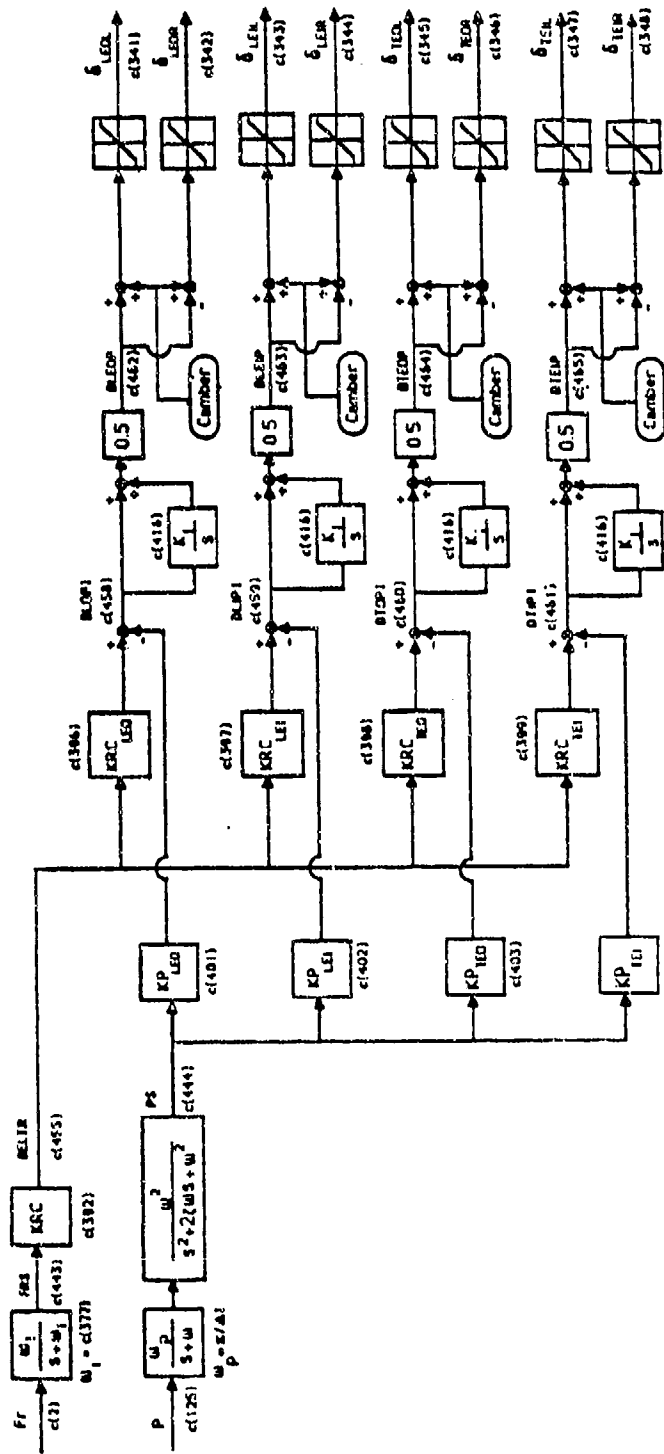


Figure 6-2. Basic Roll Control Mechanization

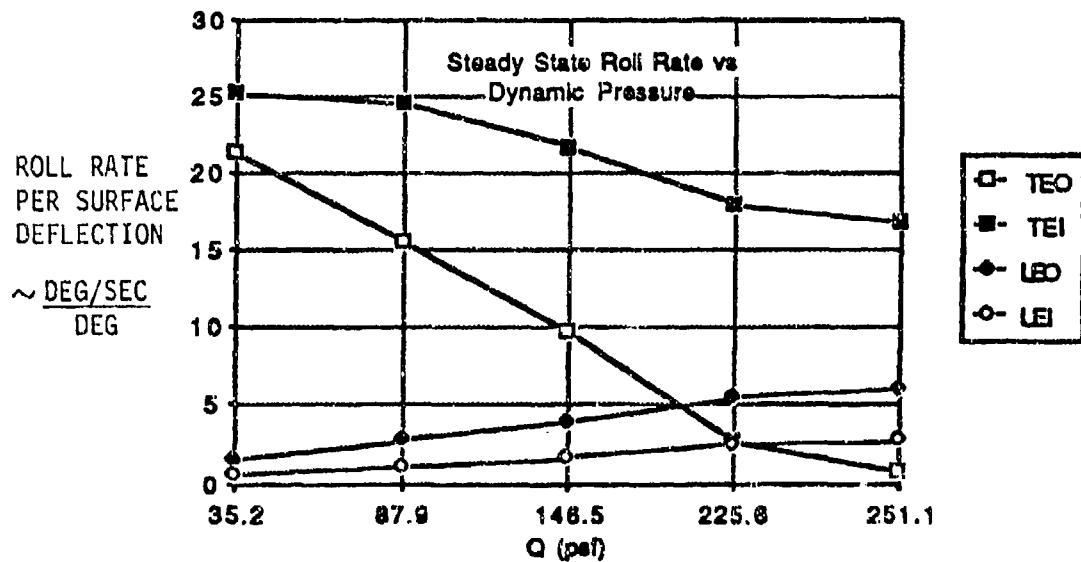


Figure 6-3. Computed Steady State Roll Rate ( $P_{SS}$ ) Versus Dynamic Pressure for  $M = 0.9$

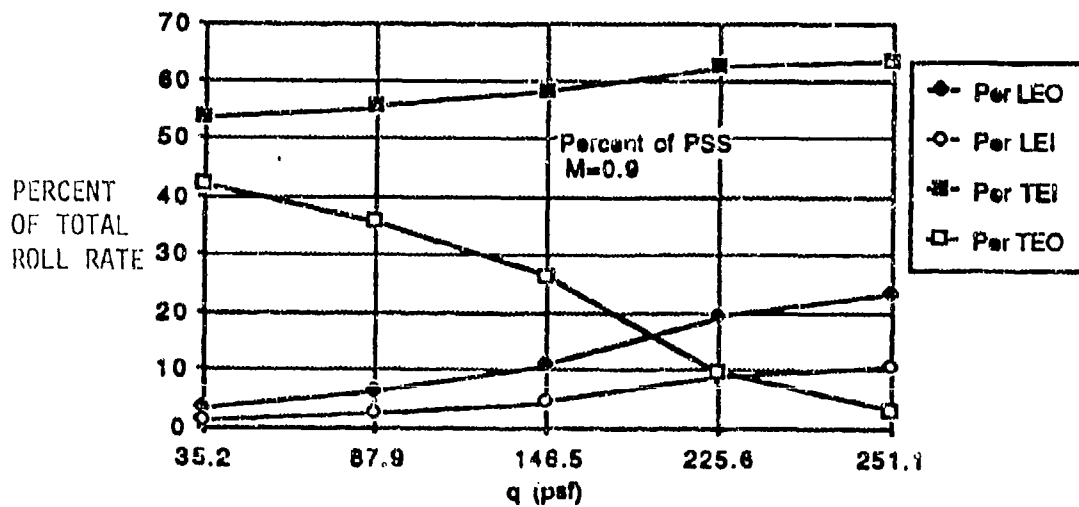


Figure 6-4. Percent of Total Steady State Roll Rate Versus Dynamic Pressure at Mach = 0.9

The preliminary design roll feedback gains ( $K_p$ ) (shown in Table 6-1) were selected based on the assumption that the model was a perfect single degree-of-freedom system in which actuator dynamics could be ignored. Gains could then be computed based on achieving a desired time constant through augmenting the basic roll damping of the model (i.e.,  $L_{pAUG} = L_p + K_p \cdot L_{\delta x}$ ). This effectively altered the roll subsidence break frequency. The desired time constant was determined to be 0.0384 sec. (a factor of 2.6 from the conventional fighter value of 0.1 sec). Since the ratio of total selected roll control power to unaugmented roll damping was essentially constant over the spectrum of the design flight conditions, the gains exhibited little variation. Following selection of the gains, a full frequency domain analysis was conducted with the complete AFW system modeled in order to "fine tune" the system gains.

Roll control surface deflection limiters were implemented to prevent exceedance of hinge moment and bending and torsion moment limits in addition to preventing leading edge surface departure. The limiter design process took a two step approach: First, deflection envelopes were developed for candidate surface pairs for a given set of hinge, bending and torsion moments. Torsion and bending limits were developed based on Locations 1 and 3 in Figure 6-5 which correspond to the wing root and mid-span strain gage locations on the model. The hinge moments were developed for each individual control surface. These envelopes allowed selection of surface deflection pairs for the surfaces that could be varied while maintaining a constant maximum hinge, bending or torsion moment load. Since these allowable surface deflection envelopes were also a function of angle-of-attack, separate envelopes were developed for several candidate test angles-of-attack.

Table 6-1

ROLL CONTROL EFFECTOR SELECTION AND ROLL RATE FEEDBACK GAINS

Flight Cond.		Surfaces			$k_p$
Mach	q(psf)	TEO	TEI	LEO	
0.7	150.0	X	X	—	0.21
0.9	150.0	X	X	—	0.22
0.9	250.0	—	X	X	0.19
1.05	340.0	-X	—	X	0.20
1.15	250.0	—	X	X	0.27
1.15	340.0	-X	—	X	0.23

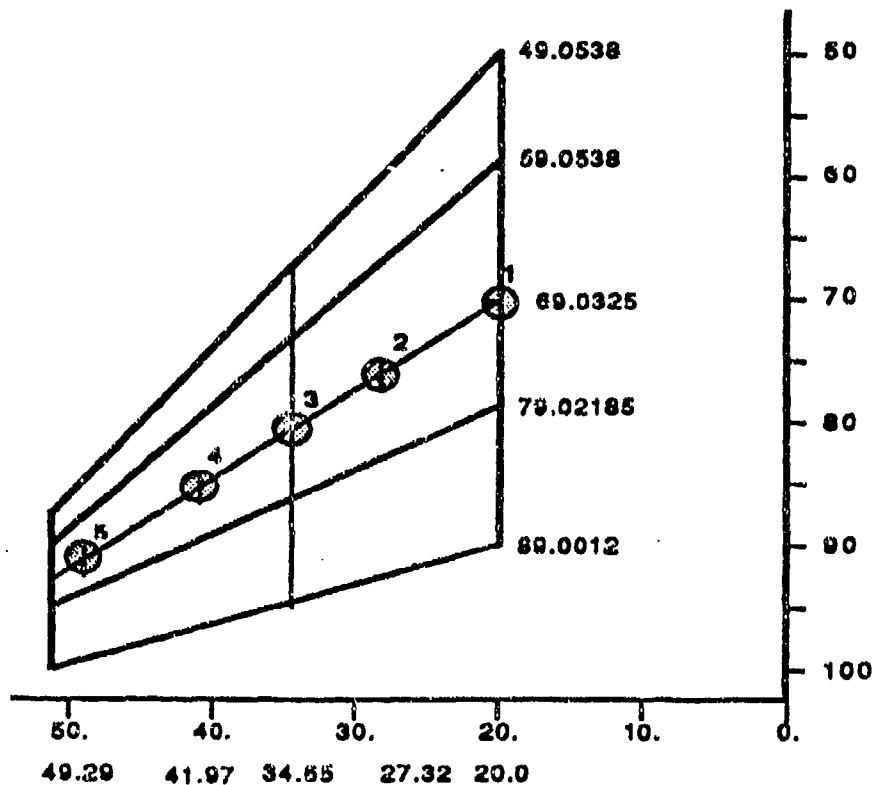


Figure 6-5. Wing Locations for Bending and Torsional Moment Data

Once the initial limits were defined in terms of the hinge, torsion and bending loads, time histories were run to evaluate the dynamic transient loads. Based on the time histories the surface maximum deflections were adjusted to prevent hinge, torsion or bending moment exceedance.

### 6.1.3 ROLL CONTROL SYSTEM TEST

The roll control system testing was segregated along two distinct lines, the time and frequency domains. These two domains served distinct functions in the evaluation of the model performance and in the validation of the analytic techniques used to develop and implement the control laws.

#### 6.1.3.1 Frequency Domain Results

Frequency domain testing was conducted for two distinct purposes. First and foremost, the purpose was to ensure control system stability and thus guarantee tunnel safety. Second, the tests allowed for the evaluation of the analytic techniques used in the synthesis and analysis of the control laws and the validation techniques employing real-time simulation with hardware in the loop. The results of the AFW wind tunnel frequency domain testing and correlation with predicted results from the design analytic tools and real-time simulation tests are presented in the following paragraphs.

Frequency domain testing was conducted in the classic open-loop manner. An analog signal generated by a frequency generator was input to the controller as though it were a roll stick command in an actual vehicle. The response was measured at the output of the roll gyro demodulator and the roll rate command to roll rate gyro output transfer function was determined. Figure 6-6 presents a block diagram of the functional components of the system. A hardware switch, installed in the computer cabinet, facilitated the breaking of the loop at the gyro demodulator output and allowed true open loop testing as well as closed loop testing. All frequency analyses were conducted using a Hewlett-Packard spectrum analyzer. Bode magnitude and phase techniques were the primary method of evaluation; however, Nyquist plots were also constructed at several flight conditions for future analysis and correlation.

The standard method of excitation was a logarithmic sweep ranging from 2 Hz to 20 Hz. Prior to the test, an analytic evaluation determined the proper level of excitation. The goal of this analysis was to optimize the signal to noise ratio of the system while remaining within the linear bounds of the system. The results of this analysis established initial signal generator voltage levels that produced the best quality transfer function results and predicted the behavior of the model when tested.

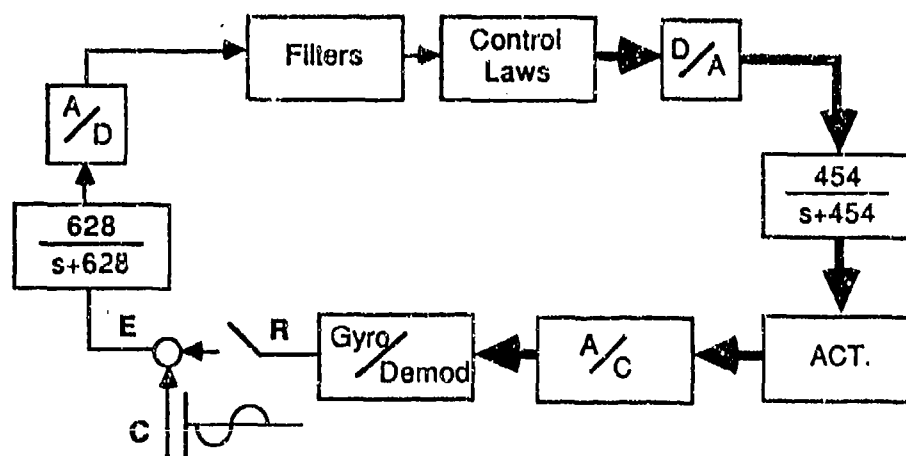


Figure 6-6. Test Setup for Frequency Domain Testing

Prior to the tunnel entry, the roll control laws were implemented in a real-time computer simulation and validated. The blocks labeled ACT., A/C and Gyro/Demod in Figure 6-6 were simulated with an Applied Dynamics AD-10 real-time computer which allowed frequency domain testing in a manner identical to that used in the tunnel. This effort gave additional credibility to the validity of the real-time implementation of the system and aided in refining the frequency testing techniques. These results were also used to corroborate results from frequency domain analysis which was conducted in the synthesis and analysis task used to develop the control laws.

Results of the wind tunnel tested gain and phase margins are presented in Table 6-2. At all flight conditions tested in the tunnel, the required gain and phase margins (6 db and 45 deg) were met and showed the system had ample robustness. All Bode plots exhibited near flat response up to five Hertz, at which point the response began to roll off. Figure 6-7 presents a typical wind tunnel open loop Bode plot with the analytic predictions superimposed on it.

Although the trends in the frequency response plots were accurately predicted, the actual wind tunnel tested gain and phase margins were slightly lower than the values predicted with the real-time hardware in the loop and the analytic prediction. This could be attributed primarily to the roll gyro and demodulator dynamics. All analysis and simulation was conducted using the manufacturers specifications. Before the tunnel test was initiated a series of air-off free falls (model released from a bank angle of 90 degrees and allowed to roll to straight and level by the center of gravity offset) were conducted in order to correlate the roll gyro output (roll rate) with the roll pot (bank angle) output. This effort showed that the steady state output of the roll gyro was reasonable; however, it is suspected that the gyro dynamics were inaccurately modeled.

Figure 6-8 presents a frequency response correlation plot between the analytic methods, real-time simulation and the tunnel test. Model effects can be seen between 10 and 20 Hertz which were not modeled analytically. These are caused by the first two flexible modes. These modal effects contributed slightly to the final gain and phase margins since the crossover frequencies are altered, but are not significant enough to cast doubt upon the validity of the design process.

Nearly constant gain and phase margins existed across the entire test envelope as presented in Table 6-3. Since roll control authority is distributed to the most effective surfaces at all flight conditions, roll control power for small surface deflections is nearly constant. Natural

Table 6-2

WIND TUNNEL GAIN AND PHASE MARGINS

Flight Cond.		Gain Margin	Phase Margin
Mach	q(psf)		
0.7	150.0	6.5 db	67°
0.9	150.0	7.0 db	64°
0.9	250.0	7.5 db	65°
1.05	340.0	7.0 db	64°
1.15	250.0	7.0 db	75°
1.15	340.0	7.0 db	67°

M = 1.15, q = 250.0

P/Pc OPEN LOOP

—— TUNNEL RESULT  
 - - - ANALYTIC PREDICTION

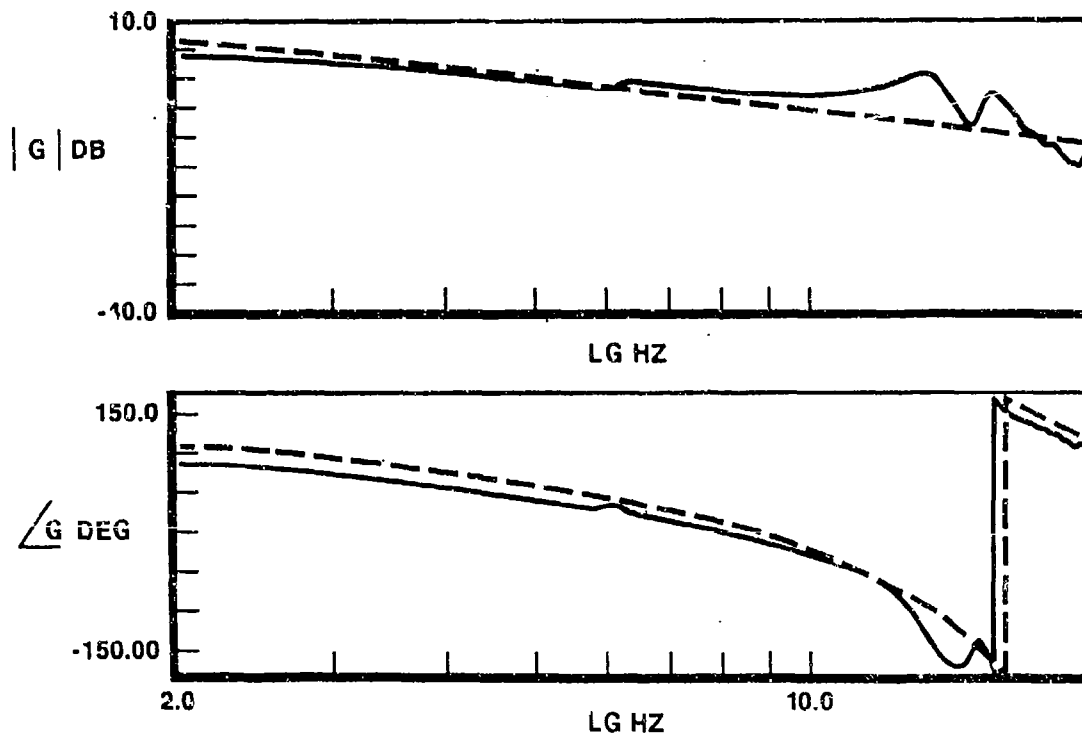


Figure 6-7. Bode Plot of the Roll Controller Comparing Test Results and Analytical Predictions

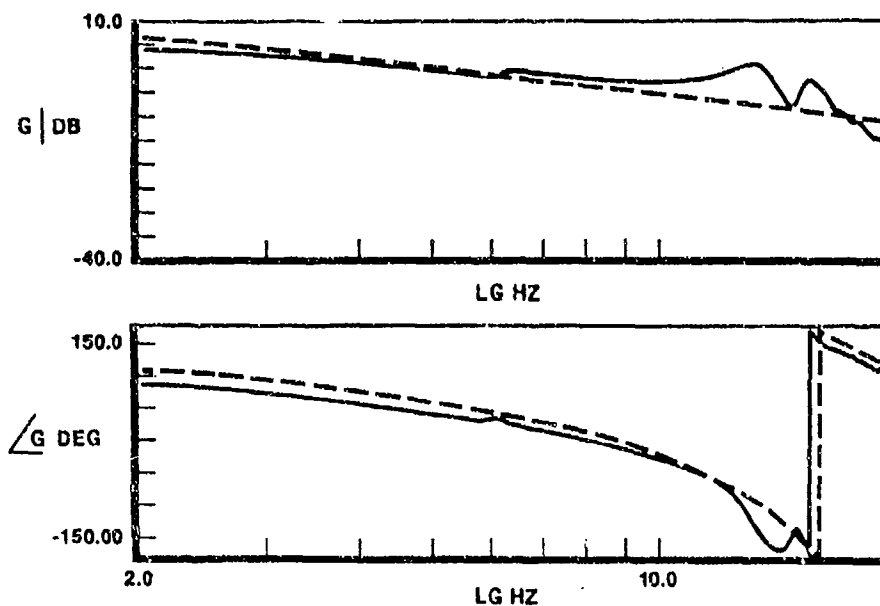


Figure 6-8. Correlation of Bode Plots for Three Test Methods

Table 6-3

GAIN AND PHASE MARGIN SUMMARY

Flight Cond.		Gain Margin			Phase Margin		
Mach	q(ps <sub>f</sub> )	Analytic	AD-10	Tunnel	Analytic	AD-10	Tunnel
0.7	150.0	10 db	8.5 db	6.5 db	78°	72°	67°
0.9	150.0	9 db	8.0 db	7.0 db	72°	69°	64°
0.9	250.0	11 db	9.0 db	7.5 db	82°	74°	65°
1.05	340.0	11 db	8.5 db	7.0 db	74°	67°	64°
1.15	250.0	12 db	10.0 db	7.0 db	82°	78°	75°
1.15	340.0	10 db	8.0 db	7.0 db	79°	72°	67°

roll damping on the vehicle varied little over the test range which results in a nearly constant plant for the frequency response testing. This effect also accounts for the similarity in the roll rate feedback gains.

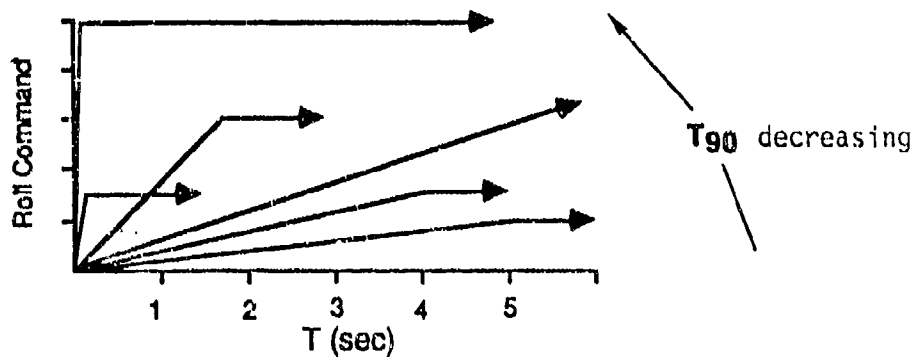
#### 6.1.3.2 Time Domain Results

The primary purpose of the roll time domain test was to obtain high roll rate performance at high subsonic speed to low supersonic speeds at the system design "hard points" (low Mach/dynamic pressure where leading edges were ineffective, near trailing edge outboard control surface roll reversal, and near trailing edge inboard control surface roll reversal). Time domain testing of the model consisted of a series of successively more demanding ramp inputs (roll command amplitude and ramp rate) with the final command consisting of a step of arbitrarily large magnitude. At each wind tunnel test condition this series of roll rate commands consisted of seven transients in addition to a no command free fall from a bank angle of  $-90$  degrees. The commands started at low amplitude and slow ramp rate and progressed to a high amplitude step input. Figure 6-9 presents the ramp commands used at each of the six test points.

Several air-off pre-test procedures were conducted to validate the controller implementation setup and calibration. Figure 6-10 presents the results of a simple procedure that was used to ensure that the roll gyro was properly calibrated before the tunnel was sealed. The sting mounted roll pot output, which served as the model bank angle ( $\theta$ ) signal, was known to be accurate; this signal could be integrated to produce a roll rate ( $p$ ) term which could be directly compared to the roll gyro output. The model was manually rotated in an oscillatory manner in order to produce the desirable sensor outputs. Figure 6-10 shows, that within the limit of accuracy of the strip chart recorders, the gyro calibration as set by the supplier was correct.

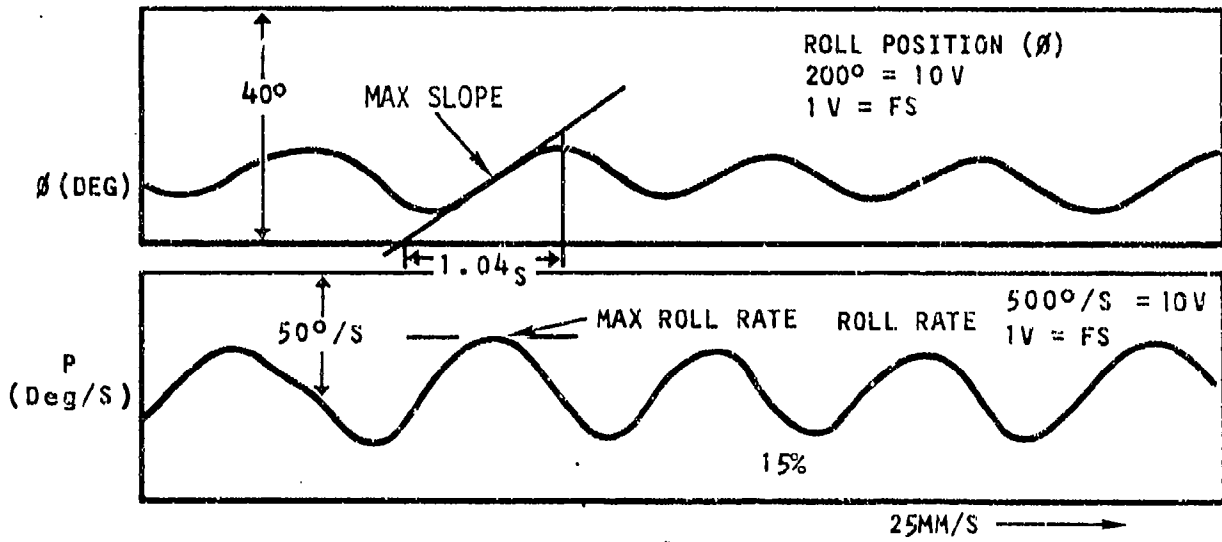
A similar air-off test was conducted to validate the proper implementation of the roll rate feedback system. The model was rotated to a bank angle of  $-90$  degrees and then the roll rate feedback system was turned on. Next, the brake was released and the center of gravity offset of the vehicle restored it to a straight and level. Since the roll rate feedback system was on and no roll rate was commanded, the surfaces attempted to maintain the model at zero roll rate. Since the model was in an air-off environment the surfaces had no effect on roll rate and were driven to their position limits. Examination of the strip chart output of the surfaces and vehicle motion indicated the polarity and magnitude of the surfaces were correct. This test duplicated a test conducted previous to model shipping for tunnel installation. (Similar tests were conducted on the trim system prior to the tunnel closure.)

The goal of the roll time domain testing was to achieve aggressive roll rates in transonic and supersonic flight regimes. Data gathered during the tests consisted of the vehicle roll angle ( $\phi$ ), roll rate



Roll Case	RAMP TIME (SEC)	RAMP AMPLITUDE (DEG/SEC)
1	10.0	20.0
2	4.0	20.0
3	0.05	20.0
4	7.0	60.0
5	1.5	60.0
6	4.0	100.0
7	.05	100.0

Figure 6-9. Progressive Pseudo-Stick Ramps Used Roll System Tests



FROM MAX SLOPE OF ROLL POT  $\frac{20^\circ}{1.04s} = 19.23^\circ/s$

AT MAX SLOPE OF ROLL POT ROLL GYRO =  $20^\circ/s$

Figure 6-10. Validation of Roll Gyro Output Using Manually Oscillated Wind-Off Model

(p), and surface deflection angles ( $\delta_x$ ). Data for vehicle loads consisting of surface hinge moments and torsion and bending moments at the wing root and mid-span locations were also collected. Hinge moments were derived by the delta-pressure method where the pressure differential across the actuator vane is related to the total force on the surface. Torsion and bending moments were derived from wing mounted strain gages. In addition to these basic signals which were of prime concern to the roll test procedures, all other vehicle parameters were recorded on FM tape and are available for future design efforts.

Figure 6-11 presents a typical tunnel test time history. In this case, the flight condition is Mach = 1.15,  $q = 250.0$  psf and the candidate effectors are the trailing edge inboard (TEI) and leading edge outboard (LEO). The time history begins at a trimmed bank angle of  $-90$  degrees and small surface deflections. The bottom transient represents the shaped pseudo-stick input to the roll control laws. Following pseudo-stick input, the model is seen to accelerate and reach a maximum roll rate of 265 deg/sec. When the model passes through zero bank angle, the pseudo-stick command is removed (set to zero) and the model decelerates to zero roll rate and is held at a non-zero bank angle by the roll trim system. This time history is typical of all maximum roll rate time histories.

Roll test flight conditions can be divided into three distinct groups: conventional roll, roll at aileron reversal, and roll beyond aileron reversal. These distinct regimes can be seen in Table 6-4 by the surfaces selected. Conventional roll is characterized by the use of the two wing trailing edge surfaces (TEO and TEI) and was demonstrated at a dynamic pressure of 150 psf at Mach 0.7 and 0.9. As dynamic pressure increases the trailing edge outboard surface approaches its reversal point and becomes ineffective. At this point in the regime leading edge outboard and trailing edge inboard surfaces are employed. The two flight conditions for this situation are at a dynamic pressure of 250 psf at Mach 0.9 and 1.15. During the final regime the trailing edge outboard surface is in full reversal and can again be used as an effector in conjunction with the leading edge outboard. The surface in reversal is represented by the negative signs in Table 6-4. Demonstration of roll beyond TEO reversal occurs at a dynamic pressure of 340 psf at Machs 1.05 and 1.15. The following paragraphs discuss the test results at these three distinct points in the test envelope. Figure 6-12 summarizes the tunnel test roll performance results.

Roll at the two conventional flight conditions ( $M = 0.7$  at 150 psf and  $M = 0.9$  at 150 psf) produced the required performance with no unexpected results. Further attempts to lower  $\bar{q}_0$  values were not pursued since the  $T_{90}$  performance requirements were achieved. These values could, however, be considerably lower by expansion of the control surface deflection envelopes since the maximum allowable torsion moments were well beyond those produced by the maneuvers.

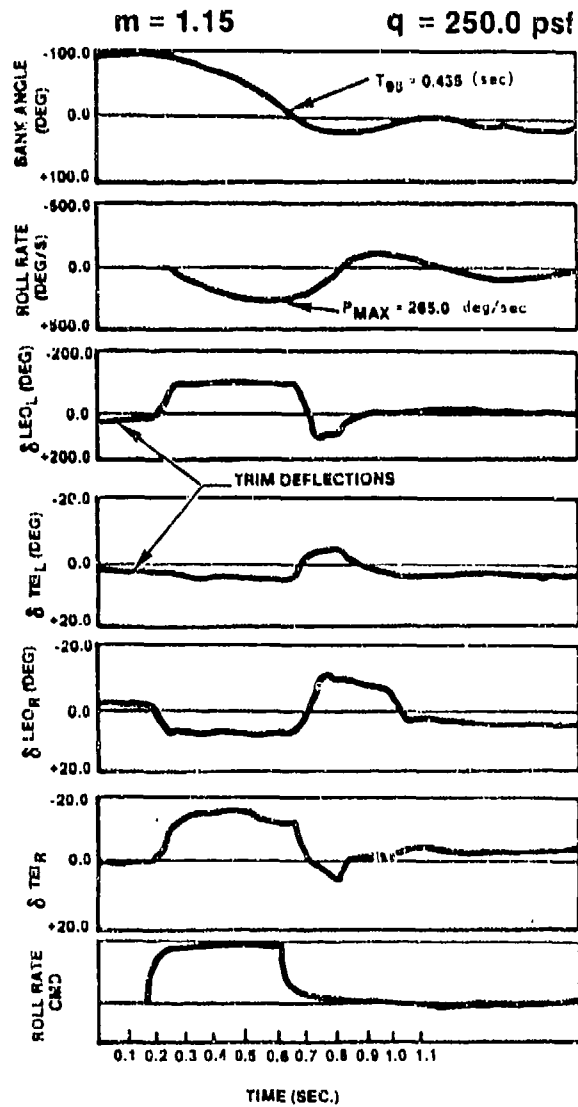


Figure 6-11. Typical Tunnel Time History for Maximum Roll Input

Table 6-4

ROLL CONTROL EFFECTOR SELECTION AND ROLL RATE FEEDBACK GAINS

Flight Cond.		Surfaces			k <sub>p</sub>
Mach	q(psf)	TEO	TEI	LEO	
0.7	150.0	X	X	—	0.21
0.9	150.0	X	X	—	0.22
0.9	250.0	—	X	X	0.19
1.05	340.0	-X	—	X	0.20
1.15	250.0	—	X	X	0.27
1.15	340.0	-X	—	X	0.23

Flight Cond.		Test Results (o/s)		
Mach	q(psf)	T <sub>90</sub> Req'd	T <sub>90</sub> Test	$\frac{\text{Test}}{\text{Req'd}}$
0.7	150.0	0.385	0.4	1.03
0.9	150.0	0.385	0.37	0.96
0.9	250.0	0.385	0.38	0.99
1.05	340.0	0.538	0.56*	1.04
1.15	250.0	0.538	0.45	0.86
1.15	340.0	0.538	0.53*	0.98

\*100°/sec leading edge rate limiter used at those points

Figure 6-12. Roll Performance Summary

Roll at or near TEO reversal was one of the critical tests since it is at this condition that the TEO surface passed through zero effectiveness, which it must do in order to be used in reversal at the higher dynamic pressures. At Mach 0.9 and 1.15 with a dynamic pressure of 250 psf, the LEO and TEI surfaces are used as illustrated in Figure 6-13. Design goals set forth by the scaled MIL-F-8785C requirements were met at both conditions with no unexpected results.

Roll beyond TEO reversal proved the most interesting of all tests conducted. At these two test conditions (Mach 1.05 and 1.15 at a dynamic pressure of 340 psf) the AFW concept was proven to work. Testing also provided valuable information pertaining to the feasibility of rolling maneuver load control. At these maximum dynamic pressure flight conditions, torsion and hinge moment loads were the most critical. Since hinge and torsion moment loads dominate parameters in achieving aggressive roll responses, the majority of the test effort focused on optimizing the roll system at the two maximum dynamic pressure test conditions.

During the maximum dynamic pressure tests, the leading edge outboard surface rates had to be lowered primarily due to the sampling frequency of the controller. The maximum surface position values were based on the analysis of bending, torsion and hinge moments (BM, TM, HM) obtained from the first tunnel entry. Since the control surface position limiters were implemented digitally with a 200 Hz input (the surface angles from rotary variable differential transducers [RVDT's]), the output value (surface command position) could only be controlled to the quantified value of the RVDT's.

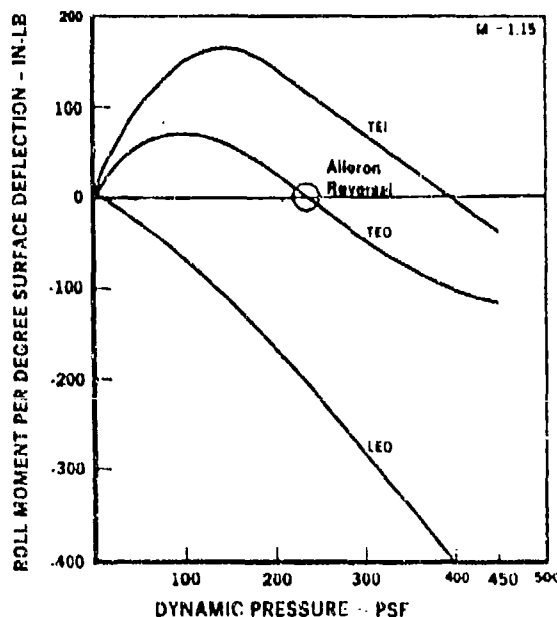


Figure 6-13. Rolling Moment vs Dynamic Pressure for Mach = 1.15

To initiate deceleration of the model following roll through zero bank angle, the right leading edge outboard surface moves from a positive (down) deflection, which is producing positive rolling moment, to a negative (up) deflection to decelerate the model. Two factors acting together caused the surface to move at very high rates. First the surface is unloading which causes it to move at rates that exceed the nominal 500 degrees/sec. no load rates. Second, the model is rolling at a high rate (over 250 degrees per second) causing a large roll rate component to the surface hinge moment ( $CHM_0$ ). The quantized steps through the controller were so large that by the time the limiters could act the surface had moved beyond its stall boundary and was departing. Lowering the maximum rate of the leading edge surface reduced the affect of the quantization of surface input signal to the limiter and allowed it to limit the surface to the desired value. Once the surface was rate limited to 100 degrees per second surface departure no longer occurred.

The control laws installed in the control computer contained analytically predetermined surface position limiters for both leading and trailing edge surfaces. These limits were based on a conservative design criteria that emphasized safety and simplicity over performance. They were set to prevent wing hinge and torsion moment tunnel trip level exceedance. The limiters did not reduce wing trim loads. During testing at several high dynamic pressure flight conditions, it became obvious that considerable reduction could be achieved by use of non-candidate effectors to reduce wing loads and thus allow more aggressive roll transients through expansion of the surface deflection envelopes.

One of the most successful demonstrations during the AFW roll test was the use of cambering for roll load redistribution. At Mach 1.15,  $q = 340.0$  psf, the primary non-candidate effector, the trailing edge inboard surface, was used as a camber device to unload the wing outboard hinge and torsion moments. These reductions were achieved by altering the local wing angle of attack through the application of an opposing torsion moment produced by the TEI surfaces. Figure 6-14 presents a composite time history of the effects of cambering. The most dramatic effect may be seen by observing the trim values of the outboard torsion moments (TMLD and TMRO). The trim moment is moved through the origin to a trim value with the opposite sign. The effect of this redistribution is a roll maneuver where the torsion loads are on average closer to the origin which ultimately results in the expansion of the surface deflection envelopes. Similar effects were produced on the LEO surface hinge moment since the twisting of the wing caused a positive (downward) change in the leading edge local angle-of-attack which resulted in decreasing the surface hinge moment.

Cambering was accomplished symmetrically and statically. Asymmetric camber was not attempted because of limitations in the controller mechanization, which did not permit the asymmetric camber deflections of non-candidate surfaces in the roll mode. If asymmetric camber were used it is most likely that a similar incremental effect would have been achieved on the opposite wing.

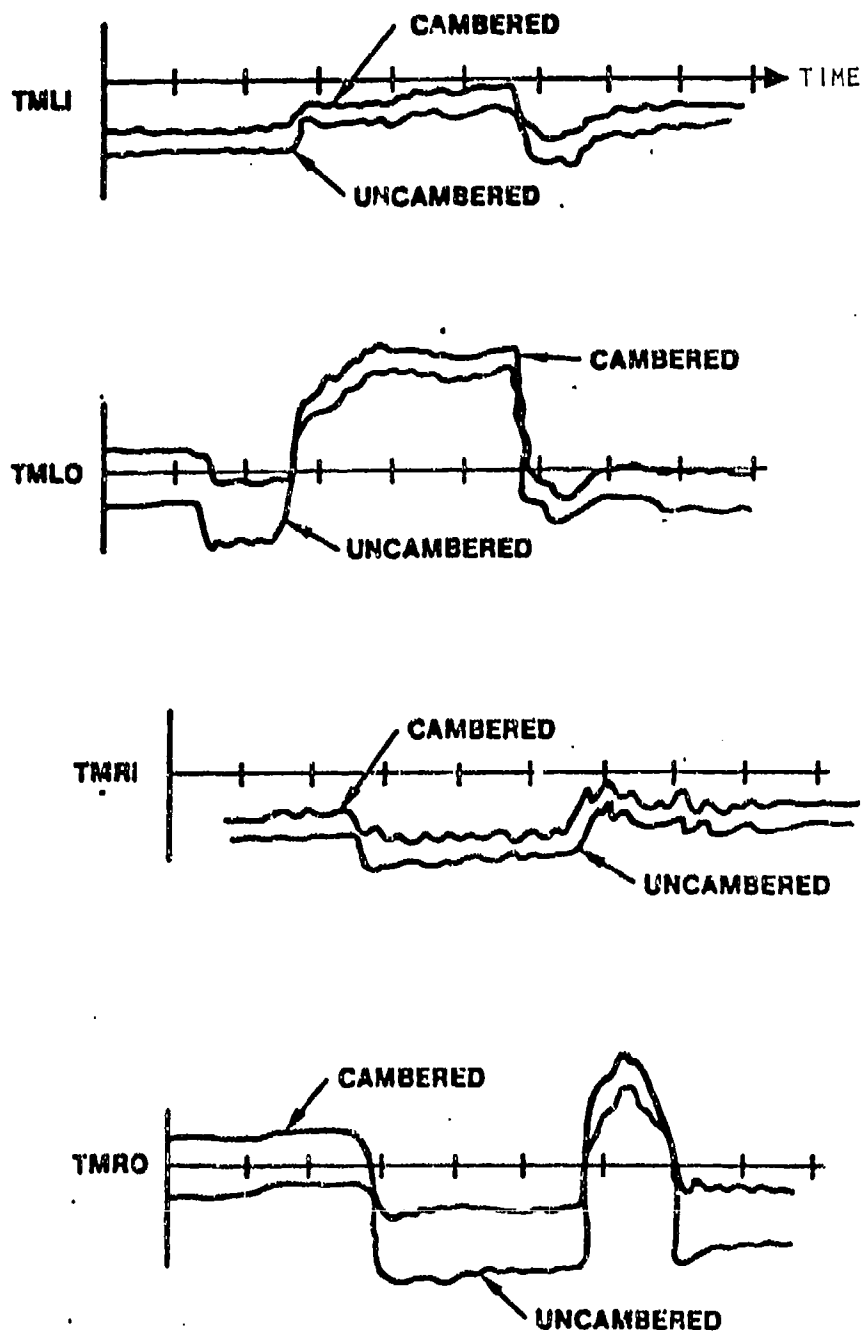


Figure 6-14. Effect of Camber on Wing Loads

Analytic results correlated very well with the tunnel results. The exceptions were where surface deflection envelopes were expanded during the tunnel test. Table 6-5 shows the final test results and the analytic predictions taken from non-real-time non-linear simulation. Results from the real-time simulation effort are not presented since the results are identical to those of the non-real-time simulation effort. The real-time simulation was validated with the non-real-time simulation which served as the "truth" model. In addition to the  $T_{90}$  values, roll time constants correlated very well across the test envelope, thereby indicating that low frequency dynamics were properly modeled.

#### 6.1.4 ROLL CONTROL DESIGN AND TEST CONCLUSION

The wind tunnel test of the AFW model validated, dynamically, the AFW roll concept at high subsonic through low supersonic flight regimes. System stability was achieved across the model frequency range. The flexibility of the wing had minimal effect on the observability, controllability and robustness of the roll mode. Although model dynamics exist within the frequency range of controllability, their effects upon the system were small. All time domain performance goals were met or exceeded, and the preliminary investigation of the effect of cambering proved that roll loads can be dramatically reduced or redistributed. The analytical methods used for

Table 6-5

#### CORRELATION OF ANALYTIC PREDICTIONS AND WIND TUNNEL FINAL TEST RESULTS

Flight Cond.				
Mach	q(psi)	$T_{90}$ Req. **	$T_{90}$ Test	$T_{90}$ Analytic
0.7	150.0	0.385	0.4	0.41
0.9	150.0	0.385	0.37	0.40
0.9	250.0	0.385	0.38	0.42
1.05	340.0	0.538	0.56 *	0.52
1.15	250.0	0.538	0.45	0.48
1.15	340.0	0.538	0.53 *	0.52

\*\*MIL SPEC REQUIREMENTS  
SCALED TO MODEL

\*LEADING EDGE OUTBOARD  
SURFACES RATE LIMITED  
TO 100 DEG/SEC

modeling and controls synthesis and analysis proved well founded. Linear aerodynamics proved to be adequate for control law synthesis in conjunction with model dynamics used for correlation. The porting of linear aerodynamics to a real-time simulator was easily accomplished and invaluable in the validation and verification efforts on the real-time digital controller and associated interface hardware. The fact that linear aerodynamics proved adequate for the development of roll control laws as long as modal dynamics models are available for correlation, can in a full scale development effort have significant positive economic impact. Finally, the control mechanization provided that a simple but flexible digital control system can be used to test a wind tunnel model at high frequencies with off-the-shelf microprocessor technology. This allowed extremely aggressive testing to occur early in a technology demonstration program.

## 6.2 MANEUVER LOAD CONTROL DESIGN AND TESTS

The goal for the maneuver load control (MLC) tests was to maintain the wing root bending moment (BM) within some design maximum. There were two methods that were tested and analyzed during the second wind tunnel test. The first method required the trailing edge (TE) surfaces to follow a predetermined camber schedule. The second method used the strain gages mounted on the wing to provide a feedback signal to the trailing edge outboard (TEO) surfaces. The camber schedules were tested at one flight condition, (Mach 0.9, dynamic pressure = 35 psf), and the strain gage feedback method was tested at two flight conditions (Mach 0.9, dynamic pressure 35 and 100 psf).

Wing root BM was measured and verified to have been maintained within design maximums with the strain gages mounted on the wing. Figure 6-15 presents the location on the wing of the strain gages. There were eight strain gages that measured bending moment at four different locations on each wing. There were inboard and outboard locations for both wings, with two sets of gages at each location for redundancy. The inboard strain gages were used for measurement and control during the MLC tests.

### 6.2.1 MLC USING CAMBER SCHEDULES

Nonlinear bending moment data, measured during the first wind tunnel test, were used to define modifications to the original minimum drag camber schedules that would limit the bending moment at the wing root. The original schedules commanded the four wing surfaces ( $\delta_{LEO}$ ,  $\delta_{LEI}$ ,  $\delta_{TEO}$ ,  $\delta_{TEI}$ ) as functions of angle-of-attack. The original schedules for the trailing edges were then modified to restrict the wing root bending moment.

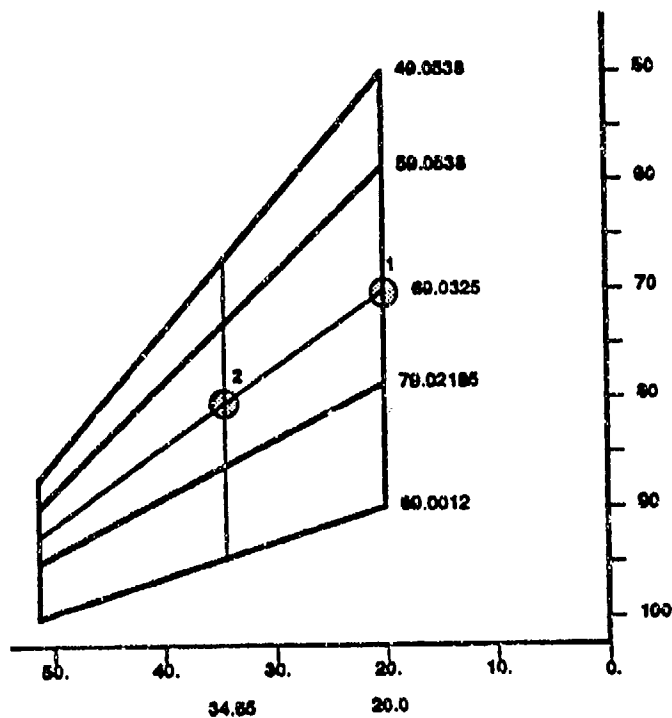


Figure 6-15. Location of Strain Gages, Left Wing Only Shown

Equations 1 and 2, which represent total lift coefficient and total bending moment coefficient

$$C_L = C_{L\alpha_0} + C_{L\alpha} \alpha + C_{LLEO} \delta_{LEO} + C_{LLEI} \delta_{LEI} + C_{LTEO} \delta_{TEO} + C_{LTEI} \delta_{TEI} \quad (1)$$

$$C_B = C_{B\alpha_0} + C_{B\alpha} \alpha + C_{BLEO} \delta_{LEO} + C_{BLEI} \delta_{LEI} + C_{BTEO} \delta_{TEO} + C_{BTEI} \delta_{TEI} \quad (2)$$

were utilized to make the necessary modifications to the existing camber schedules which were developed. ( $C_{L\alpha_0}$  and  $C_{B\alpha_0}$  were nonlinear with respect to angle of attack. The camber schedule modifications limited the wing root bending moment while maintaining the same lift curve slope as a function of angle of attack. Figure 6-16 presents a simple block diagram of this control system. Figure 6-17 shows the camber schedules, both before and after modification.

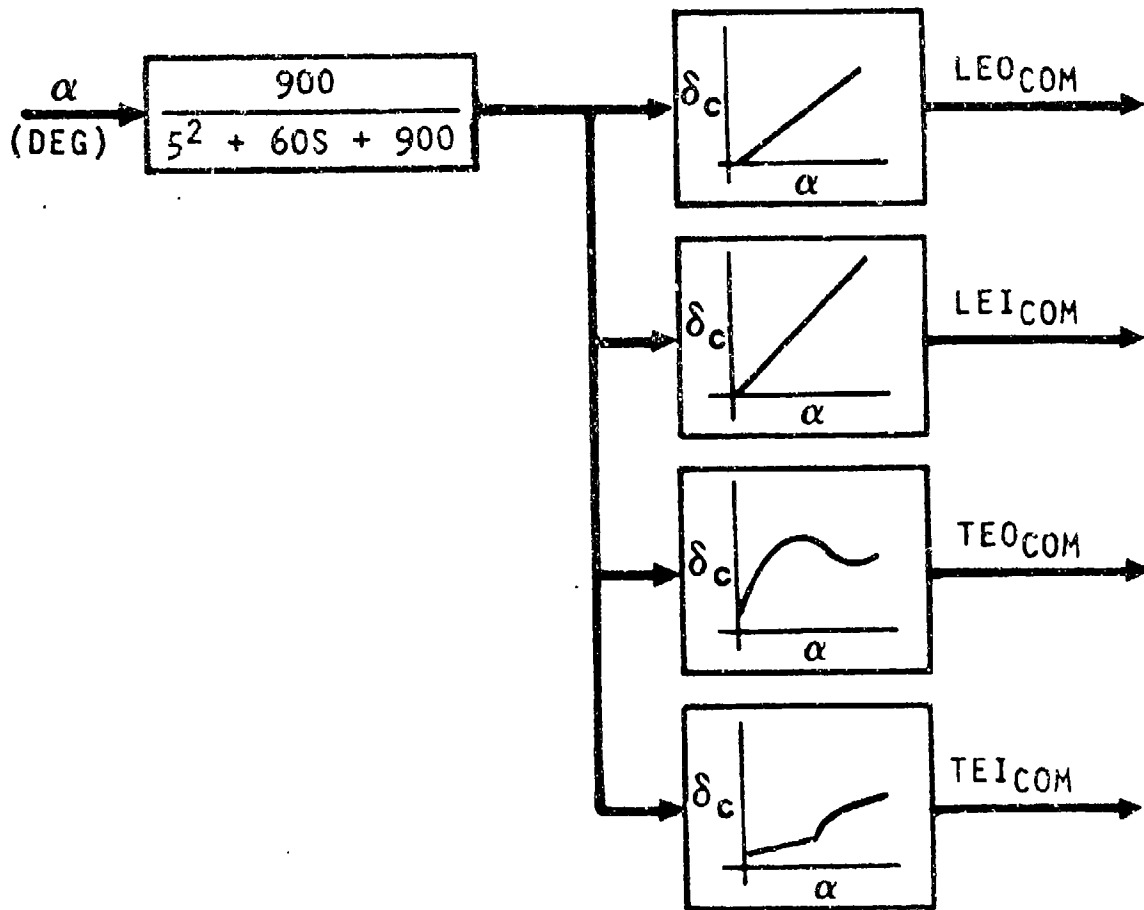


Figure 6-16. Simple Control System for MLC Utilizing Camber Schedules

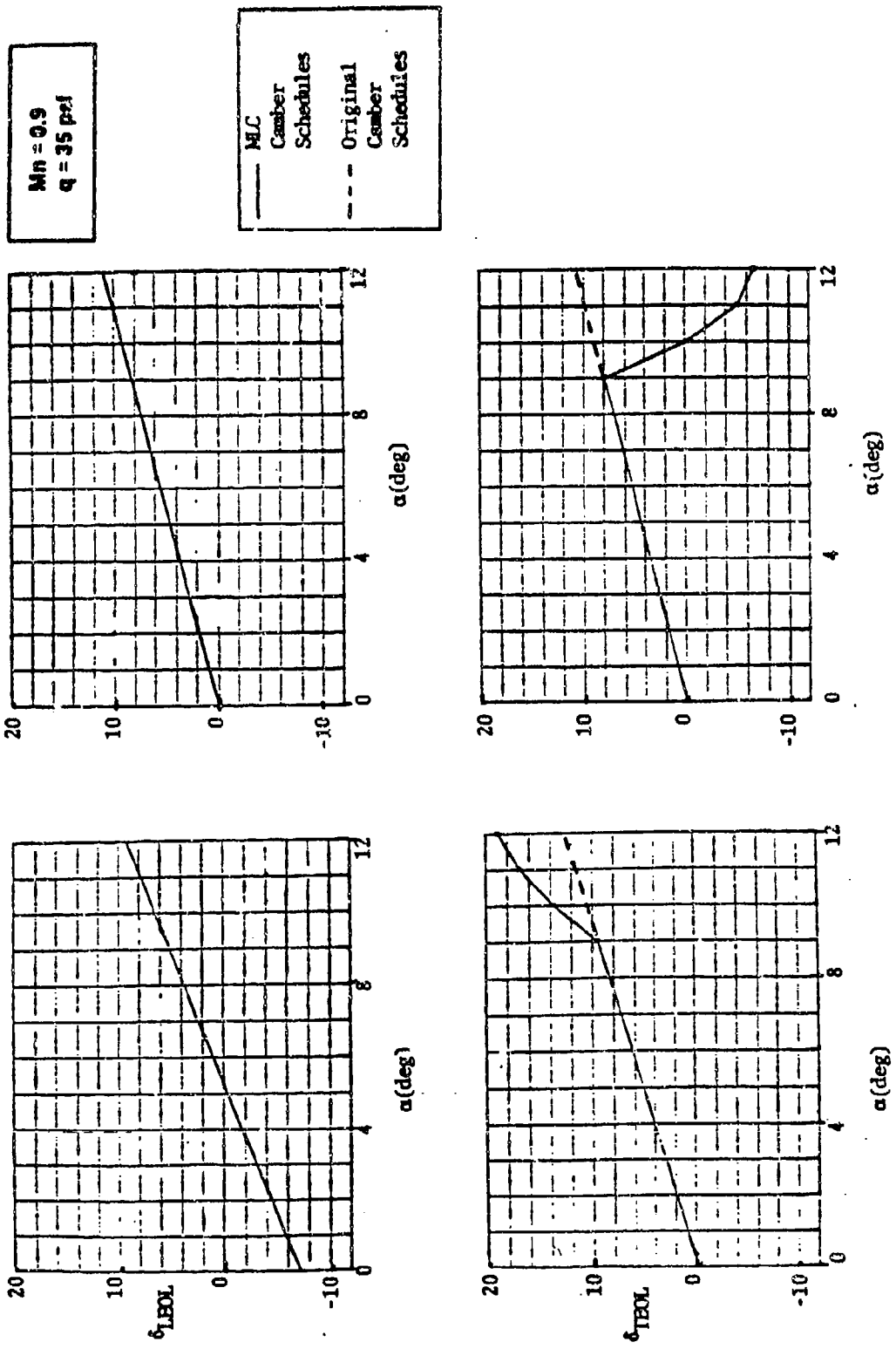


Figure 6-17. Original Camber Schedules Maneuver Load Control Camber Schedules to Limit Wing Root Bending Moment

### 6.2.2 TEST RESULTS OF MLC USING CAMBER SCHEDULES

Both the original minimum drag camber schedules and the MLC camber schedules were flown at Mach 0.9, dynamic pressure 35 psf and compared. Figure 6-18 shows the test results for a slow ramp to 12 degrees angle-of-attack and back to 0 degrees. Superimposed on this plot are results from analysis using Rockwell's Aircraft Dynamic Simulation program (ADS). Figure 6-19 presents a similar comparison, but with a response to an angle-of-attack step command to the model. The percentage reduction in wing root bending moment is tabulated in Table 6-6. The ramp response shows a slight overshoot of the design maximum bending moment. This overshoot is attributed to differences between the actual and modeled nonlinearities of bending moment with respect to angle-of-attack. Wind tunnel data from the first tunnel entry were taken at 0, 4, 8 and 12 degrees angle-of-attack. The camber schedules could have been better defined if the data were available at more points than the four measured. For steady state response, bending moment was reduced by 14.5 percent versus the 19 percent predicted using the time domain model which utilized the first wind tunnel entry's measured data.

### 6.2.3 MLC USING STRAIN GAGE FEEDBACK (SGF)

A controller was designed and then tested utilizing strain gage feedback (SGF) to alleviate wing root bending moment. Bending moment measured by the wing root strain gage was compensated and fed back as necessary to the trailing edge outboard surfaces, while the other wing surfaces followed the unmodified camber schedules presented in Figure 6-17. Tests using this method were performed at two flight conditions: Mach 0.9, dynamic pressure 35 and 100 psf.

Several requirements were established for the analytical design of the SGF MLC. These requirements, shown in Table 6-7, are grouped in three sets: one, requirements that should be met in the  $s$  and  $W'$  planes; two, requirements for the frequency domain ( $s$  and  $W'$  domain); and three, requirements in the time domain.

Linear analysis used the Digital Control and Analysis Program (DICAP) with models that were established from the aerodynamic data. After the linear analysis, the design was substantiated using the aerodynamic model established in Rockwell's Aircraft Dynamic Simulation (ADS) program. Finally, the design was verified using a structural modal model in ADS. This design process, using both DICAP and ADS, is illustrated in Figure 6-20.

During testing, requirements in the frequency domain and the time domain were verified. Open-loop frequency responses were used to verify that gain and phase margins were 6 db and 45 degrees, respectively, as required by MIL-F-9490D. Transient tests were performed to ensure that the MLC SGF controller maintained the bending moment to the design maximum with less than 20 percent overshoot.

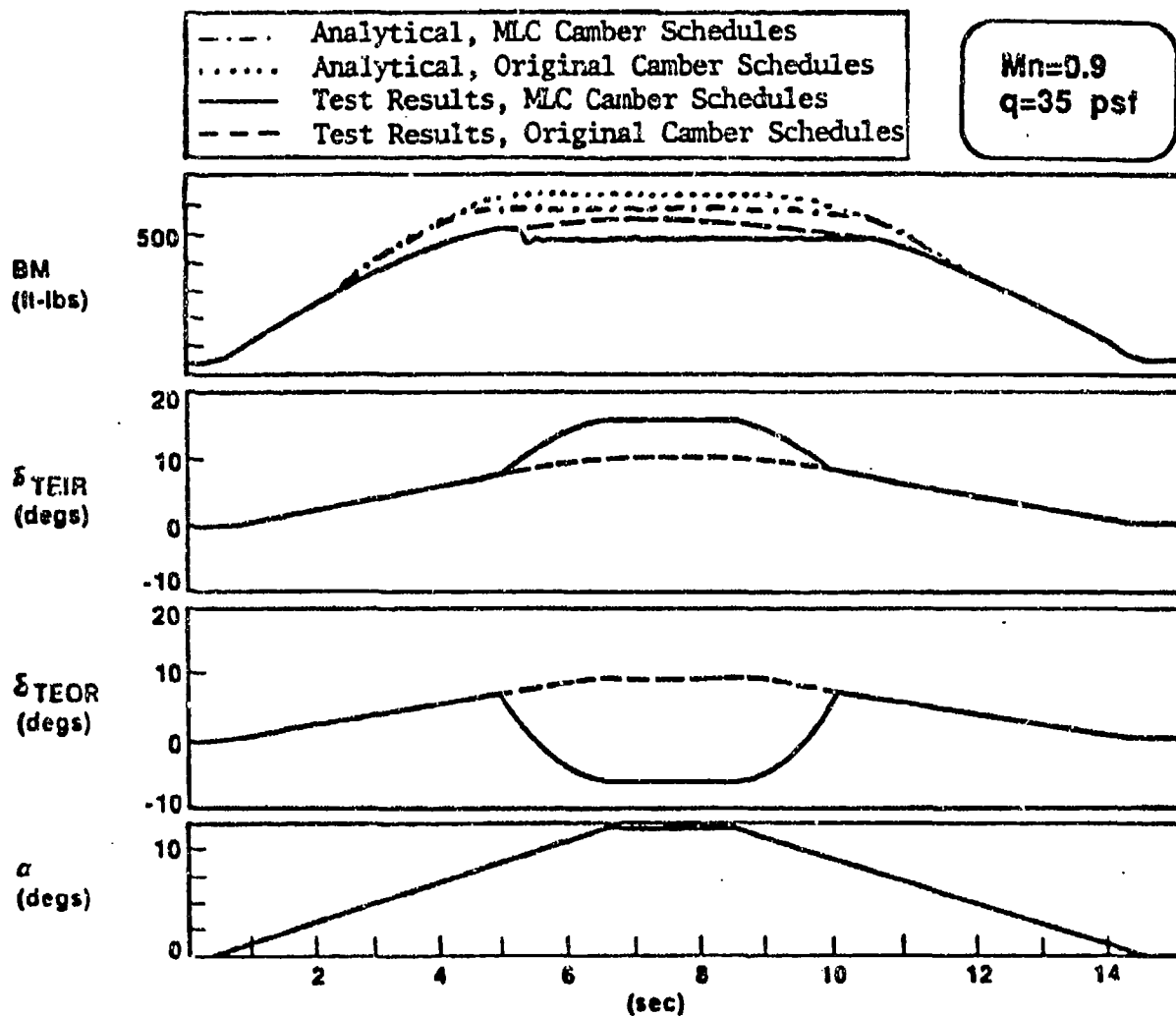


Figure 6-18. Utilizing Camber Schedules to Reduce the Wing Root Bending Moment, Analytical and Test Results

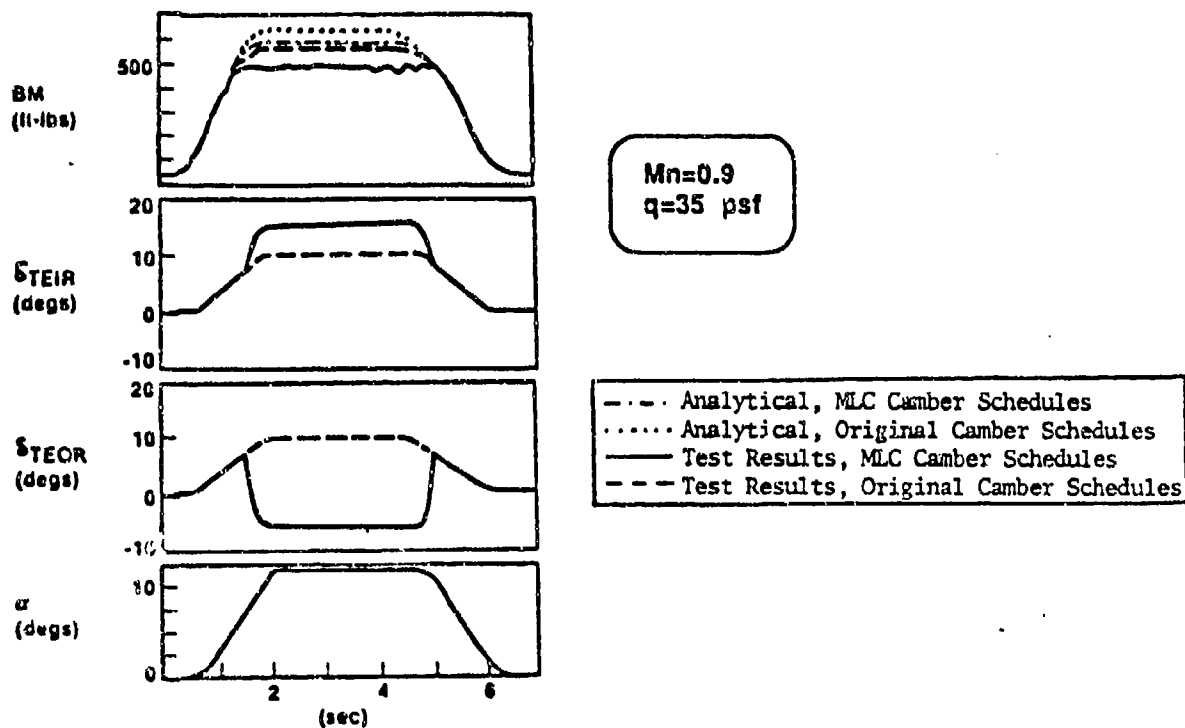


Figure 6-19. Test Results for a Step command Show a Significant Reduction in Bending Moment ( $M_n = 0.9$ ,  $q = 35$  psf)  
 Figure 6-19

Table 6-6

BOTH RAMP AND STEP RESPONSES SHOW A SIGNIFICATION REDUCTION IN BENDING MOMENT ( $M_n = 0.9$ ,  $q = 35$  psf)

	% Reduction in Bending Moment	
	Aero Analytical	Test Results
Ramp Response	19.5	6 (14 SS) *
Step Response	19.5	14

\*SS = Steady State

Table 6-7

MLC ANALYTICAL DESIGN REQUIREMENTS

- **S and W' plane**
    - $0.35 \leq \zeta \leq 0.7$  for the dominant 2nd order root
  
  - **S and W' bode plots**
    - 20 dB/decade crossover above 1 rad/sec
    - 40 dB/decade rolloff rate above 10 rad/sec
    - Gain margin  $\geq 6$  dB
    - Phase margin  $\geq 45^\circ$
- } MIL-F-9490D
- 
- **Transients**
    - Overshoot  $\leq 20\%$
    - Zero steady-state error

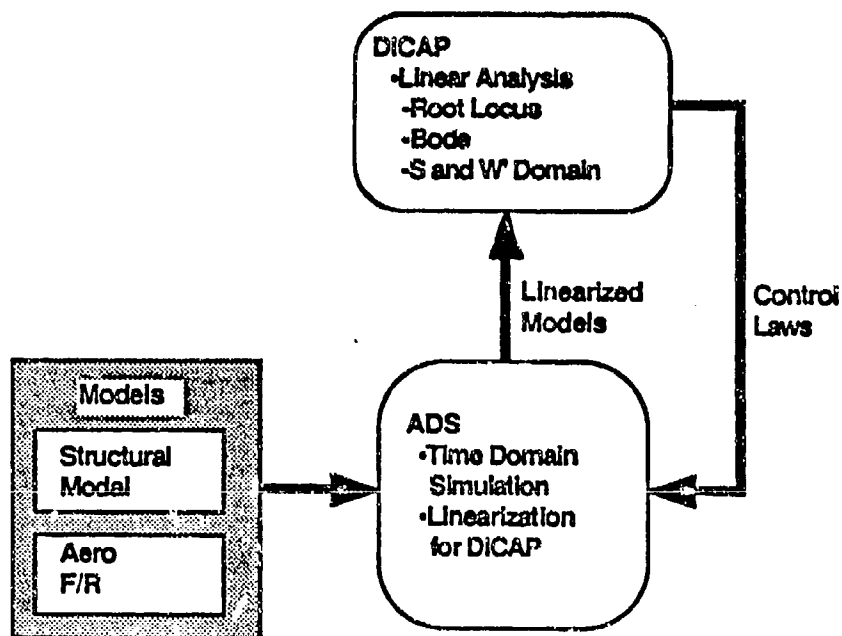


Figure 6-20. Rockwell's Design Process for Developing the SGF Maneuver Load Controller

The MLC SGF system is presented in Figure 6-21. Notice that this figure also shows the camber schedules in block diagram form, which demonstrates the relationship between the camber schedules and SGF MLC. Since the original camber schedules are linear relative to angle-of-attack, the camber schedules are represented by an intercept at zero alpha and a gain that corresponds to the slope. With this control system, the trailing edge outboard surfaces are used for controlling bending moment and are only used when the wing root bending moment approaches bending moment maximum.

#### 6.2.4 TEST RESULTS OF MLC STRAIN GAGE FEEDBACK

Frequency domain tests were performed at both flight conditions. Three methods for measuring the open loop frequency response were tested at Mach 0.9, dynamic pressure 35 psf. These three different approaches are illustrated in Figure 6-22. First, open loop frequency response was measured where the controller loop open (switch open) and the command and reference signals were MLCC and MLCR, respectively. The second method measured open loop frequency response with the controller loop closed (switch closed). The frequency sweep inserted at MLCC; the command and reference signals were MLCE and MLCR, respectively. Third, measurements were obtained with the switch closed where the frequency sweep was input into the digital controller at MLCDC; and the command and reference signals were MLCDE and MLCDR, respectively.

Figure 6-23 presents a comparison of the three open-loop frequency responses obtained using the three approaches for the flight condition Mach 0.9, dynamic pressure 35 psf. This comparison was at an angle-of-attack equal to 0. With the controller loop closed, the system experiences a DC gain offset because the bending moment feedback (MLCR) is non-zero. This anomaly is aggravated when the angle-of-attack is raised, resulting in higher bending moment feedback.

A comparison between the test and analytical open-loop frequency response is presented in Figure 6-24. The analytical model, based on the second tunnel entry's measured data, correlates well with the actual test data. This excellent correlation is due to the limited bandwidth designed into the MLC controller to prevent structural mode coupling. This design limited the controller to a region where modeling characteristics were very good. Table 6-8 lists the gain and phase margins, and shows that the design goals of 6 db gain margin and 45 degrees phase margin were met by both the analytical and test results.

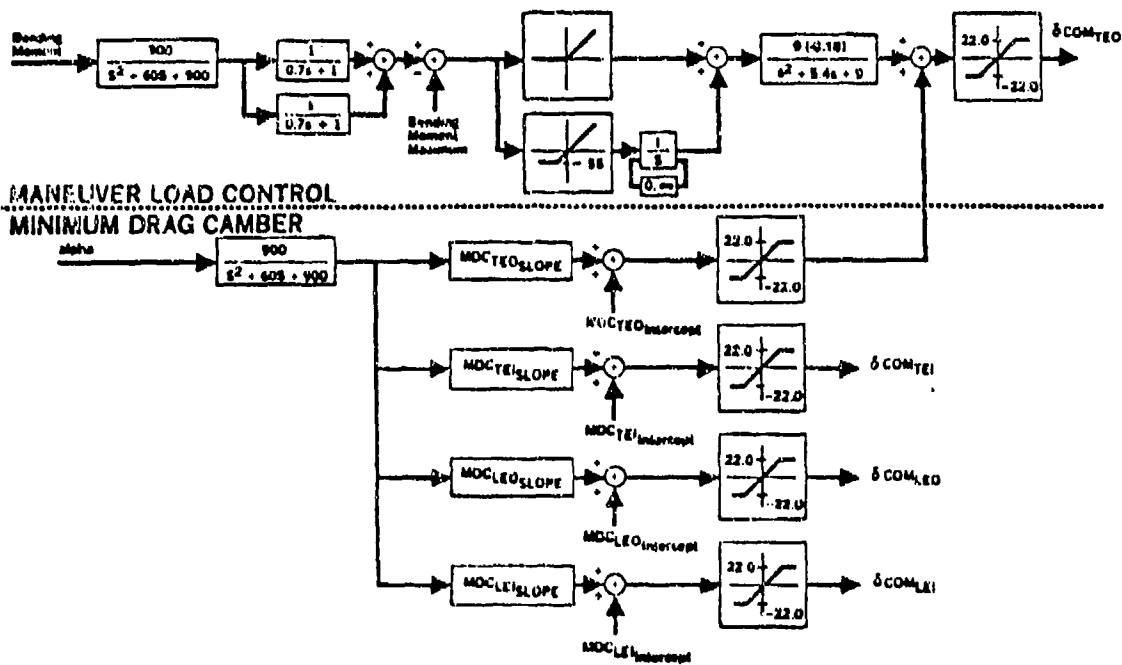


Figure 6-21. Maneuver Load Control System Utilizing Strain Gage Feedback

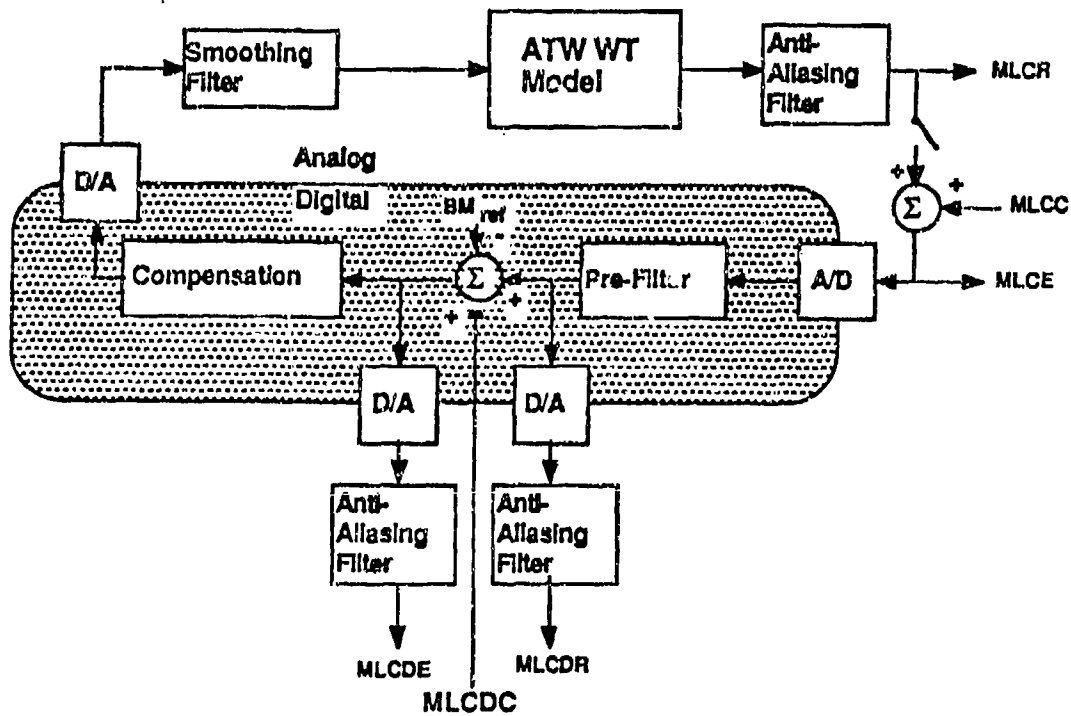


Figure 6-22. Multiple Methods Used to Measure Open Loop Frequency Response

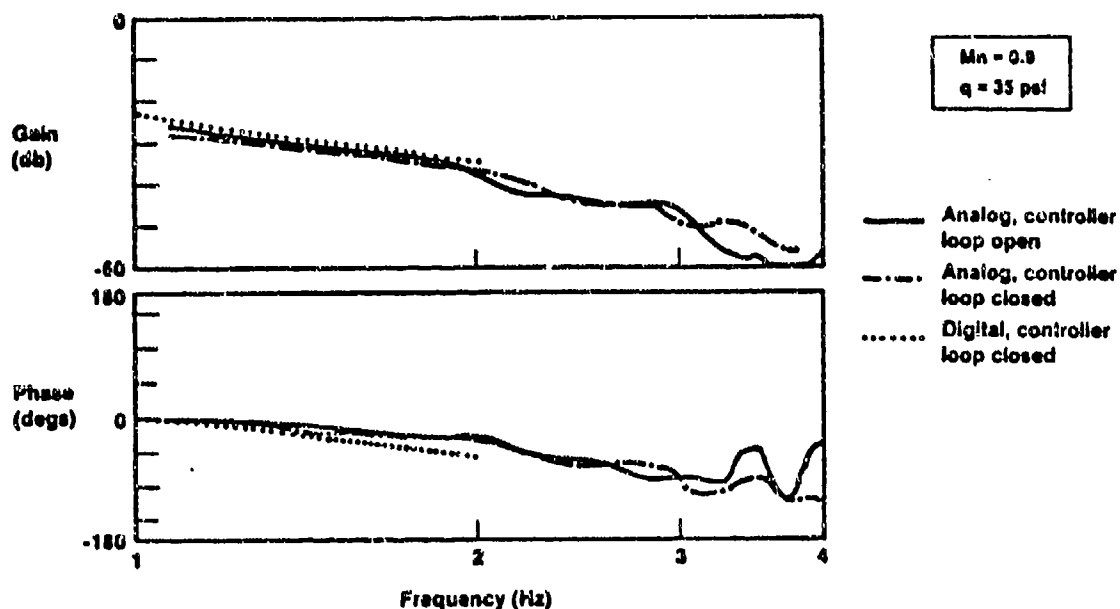


Figure 6-23. Comparison Between Three Methods of Obtaining the Open Loop Frequency Response

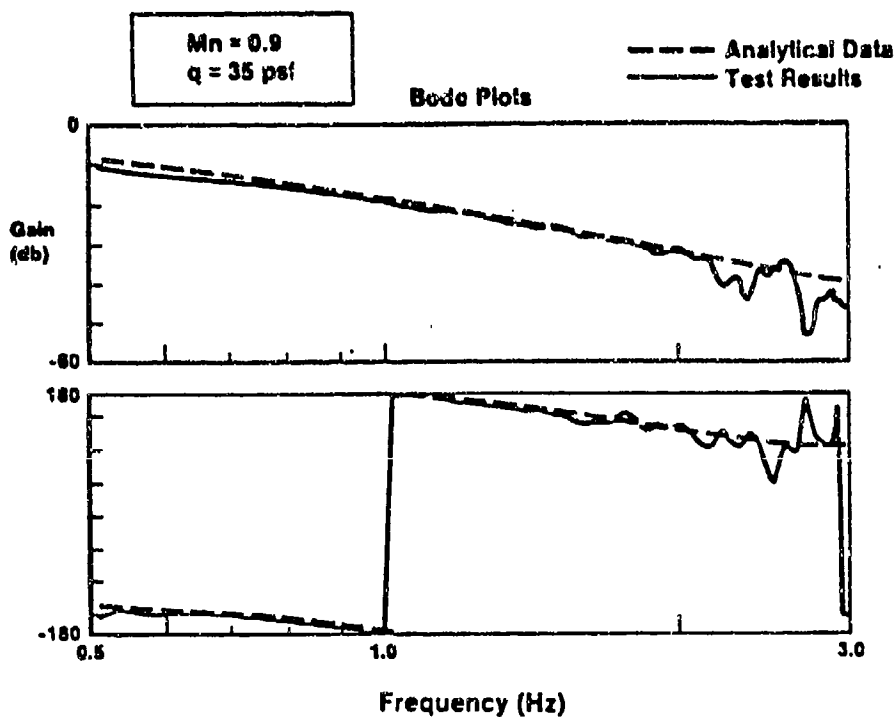


Figure 6-24. Comparison Between Analytical Modeling and Test Results

Table 6-8

COMPARISON OF ANALYTICAL AND TEST GAIN AND PHASE MARGINS  
FOR THE SGF MLC SYSTEM

	Gain Margin		Phase Margin	
	Aero Analytical	Test Results	Aero Analytical	Test Results
Mn=0.9 q=35 psf	17.5 db	19.2 db	100 deg	100 deg
Mn=0.9 q=100 psf	12.5 db	12.0 db	60 deg	42.5 deg

Transient results for the two flight conditions are presented in Figures 6-25 and 6-26. Each figure illustrates both the response during the slowest ramp command and then the response due to the fastest ramp command. Figures 6-27 and 6-28 present similar results, that were generated using ADS. This simulation was based on the nonlinear aerodynamic data measured during the first wind tunnel entry. Figures 6-29 and 6-30 present the same transients, but these were generated with ADS utilizing structural modal data. Figures 6-28 and 6-30 show simulation results for dynamic pressure 100 psf cases. The model was pitched to a maximum of 8 degrees angle-of-attack, two degrees higher than actually tested. During testing the bending moment maximum was lowered to account for the lower angle-of-attack. All other system gains and compensation remained the same, just as they did for varying flight conditions.

Figure 6-31 presents the percent overshoot and the percent reduction in bending moment for all the simulation and test results. Generally, a 20-percent reduction in bending moment was achieved, and all test results exhibited less than a 20-percent overshoot.

#### 6.2.5 MLC DESIGN AND TEST CONCLUSION

Two methods were designed to reduce the wing root bending moment by approximately 20 percent and then verified during the second wind tunnel entry of the AFW wind tunnel model. MLC by following camber schedules was successful, but shown to be particularly sensitive to modeling errors, as originally expected. The second method, MLC by using strain gage feedback, was shown to be less sensitive to these modeling errors, again as originally expected.

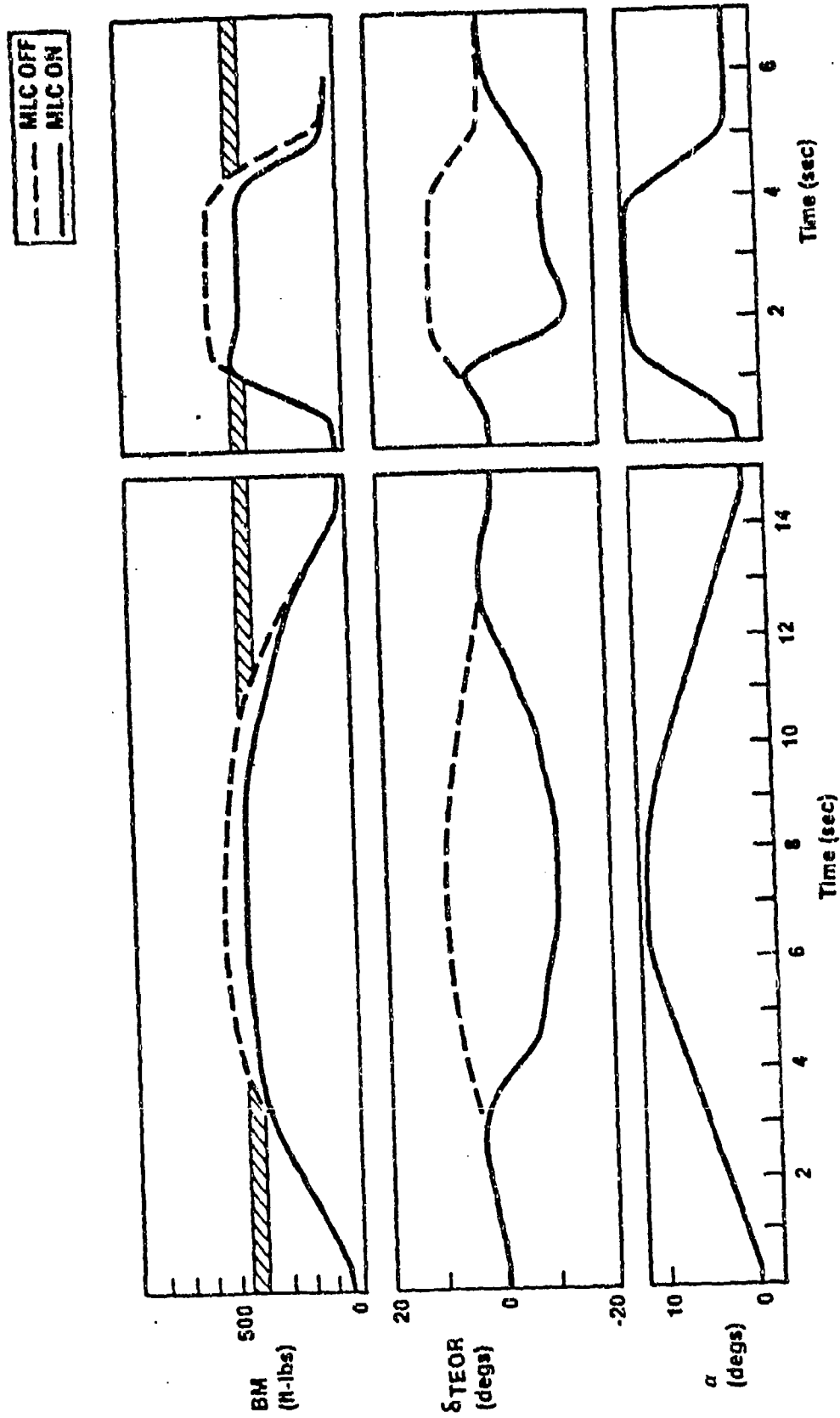


Figure 6-25. Reduction of Maximum Bending Moment During Ramp and Step Response ( $M = 0.9$ ,  $q = 35$  psf)

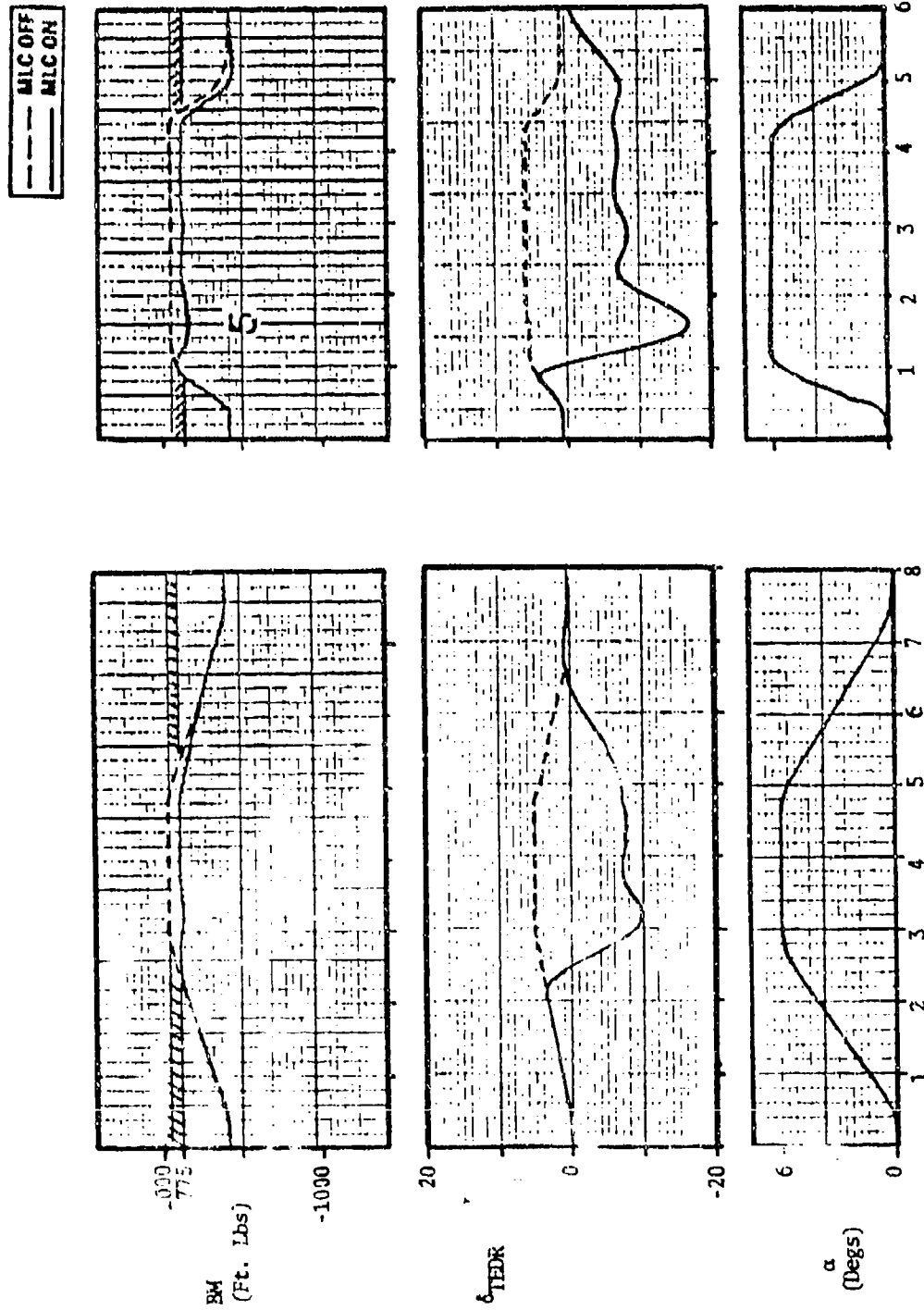


Figure 6-26. Reduction of Maximum Bending Moment During Ramp and Step Response ( $M = 0.9$ ,  $q = 100$  psf)

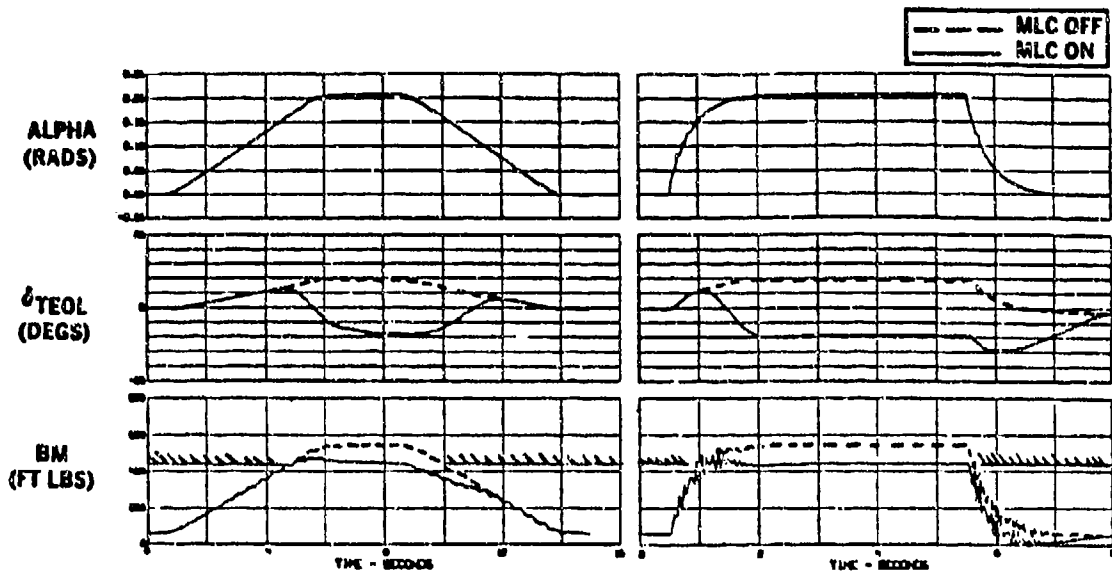


Figure 6-29. Structural Modal Model Showing Reduction of Maximum Bending Moment During Ramp and Step Responses ( $M = 0.9$ ,  $q = 35$  psf)

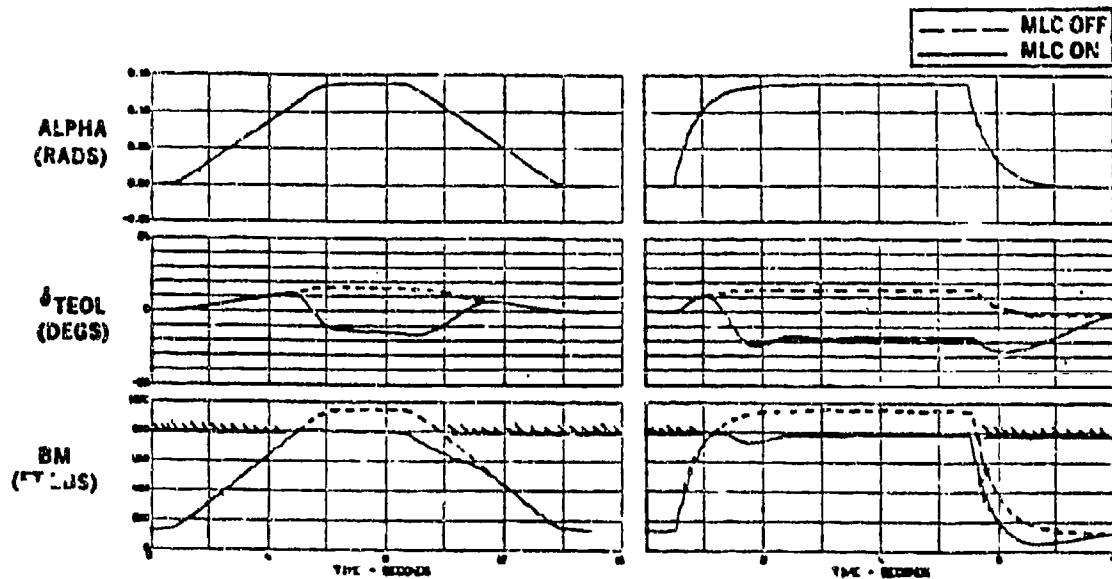


Figure 6-30. Structural Modal Model Showing Reduction of Maximum Bending Moment During Ramp and Step Responses ( $M = 0.9$ ,  $q = 100$  psf)

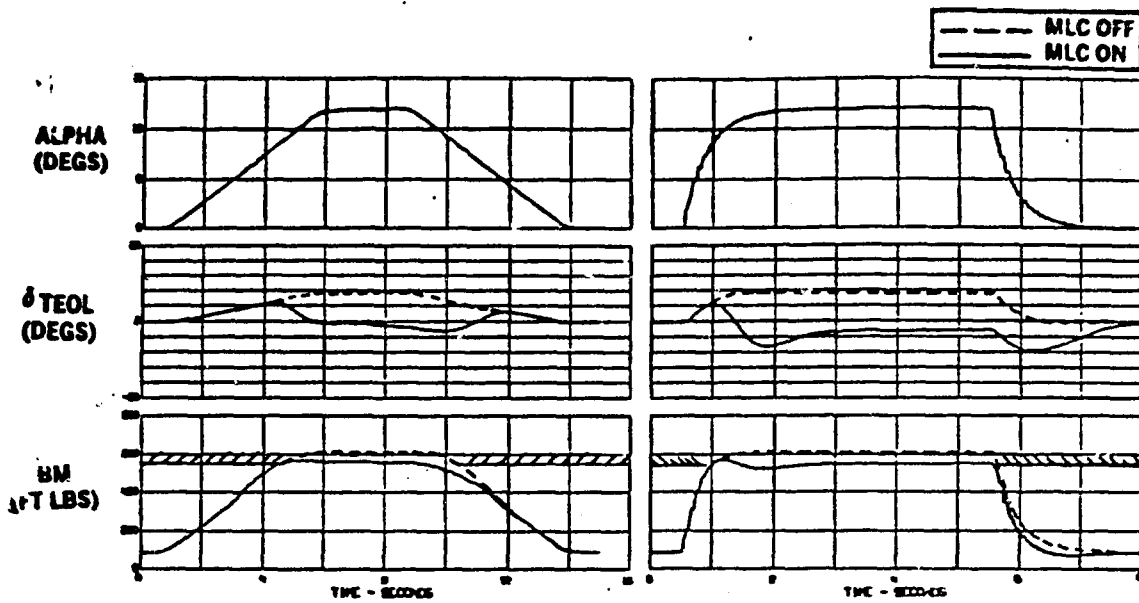


Figure 6-27. Nonlinear Aerodynamic Model Showing Reduction of Maximum Bending Moment During Ramp and Step Responses ( $M = 0.9$ ,  $q = 35$  psf)

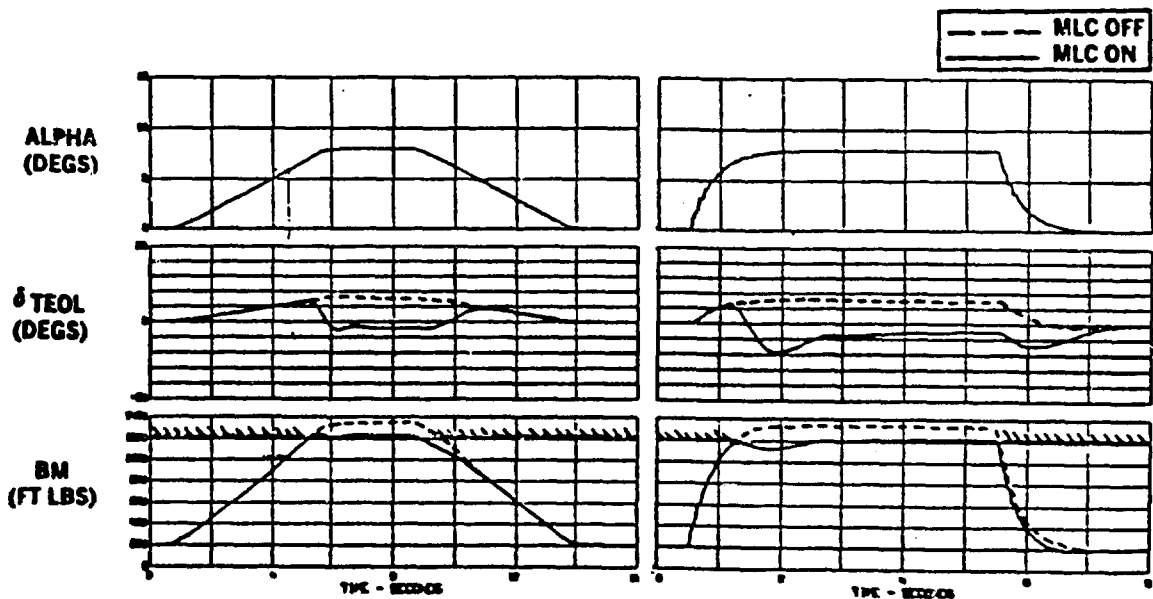


Figure 6-28. Nonlinear Aerodynamic Model Showing Reduction of Maximum Bending Moment During Ramp and Step Responses ( $M = 0.9$ ,  $q = 100$  psf)

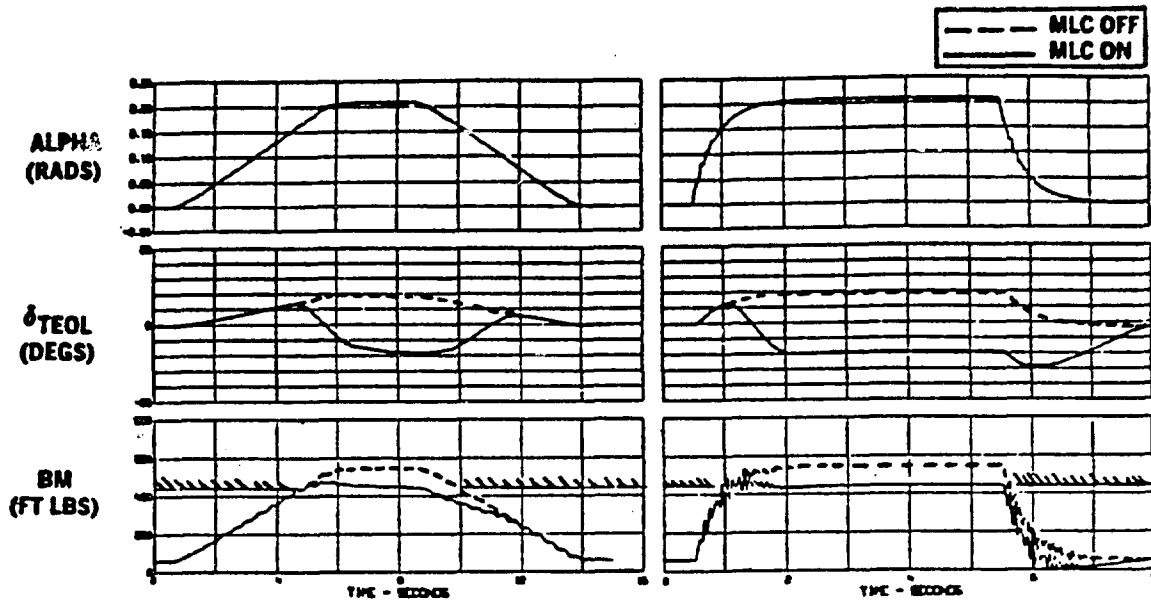


Figure 6-29. Structural Modal Model Showing Reduction of Maximum Bending Moment During Ramp and Step Responses ( $M = 0.9$ ,  $q = 35$  psf)

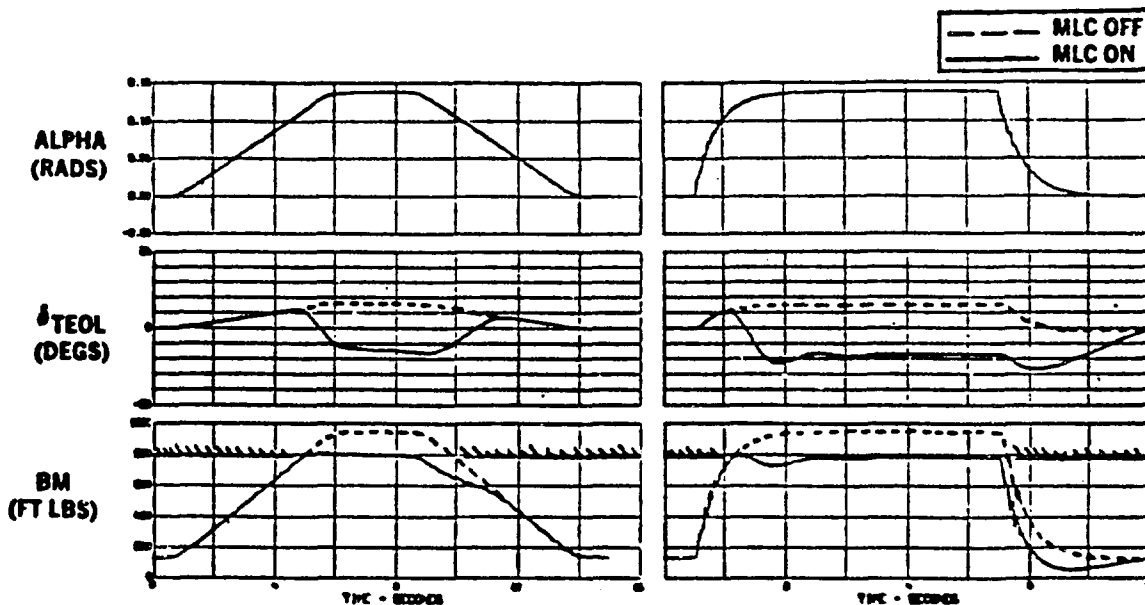
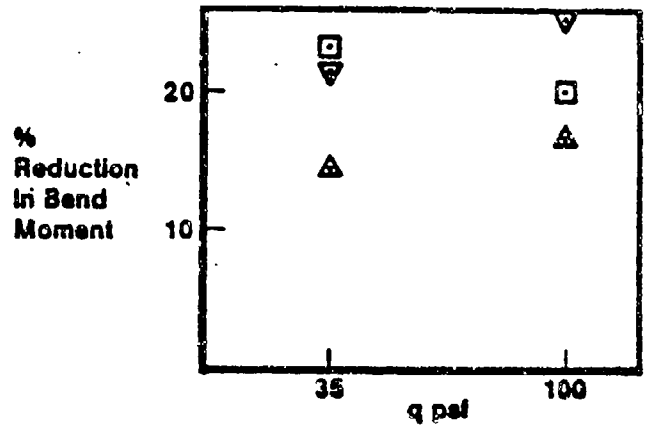
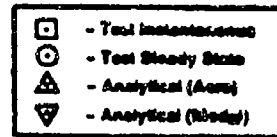
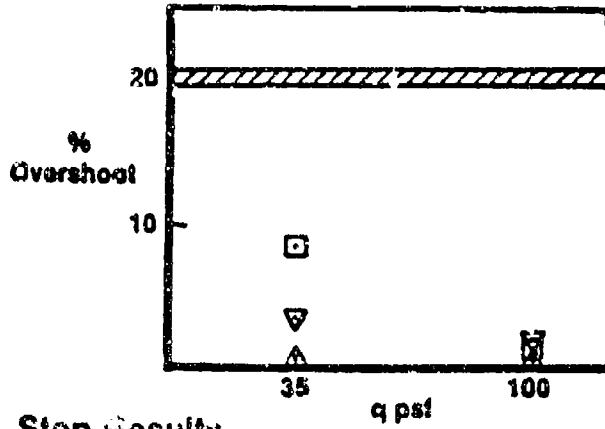


Figure 6-30. Structural Modal Model Showing Reduction of Maximum Bending Moment During Ramp and Step Responses ( $M = 0.9$ ,  $q = 100$  psf)

### Ramp Results



### Step Results

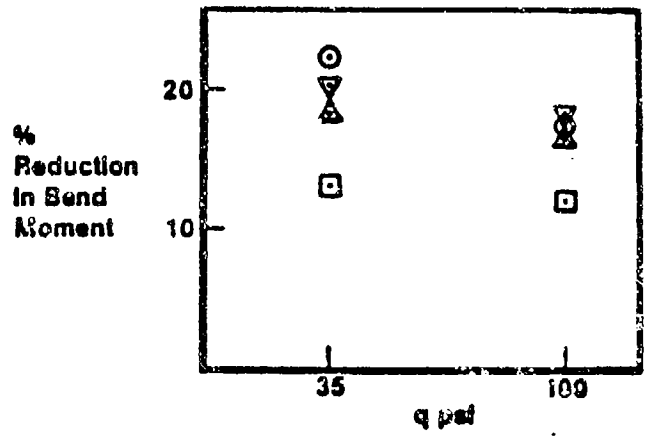
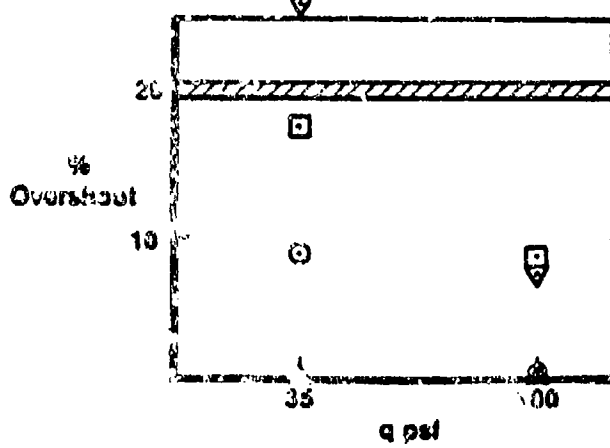


Figure 6-31. Static and Dynamic Reductions of Wing Root Bending Moment Achieved Using the SGF MLC System for Test and Analyses

### 6.3 STRUCTURAL MODE CONTROL (SMC) SYSTEM DESIGN AND TESTS

The SMC system was designed to reduce wing structural dynamic response caused by turbulence and/or control surface excitations. The system design could be implemented as a gust load alleviation system or ride quality system on an air vehicle. The system design procedures and analytical modeling tools are the same that would be required for a flutter suppression system.

Wind tunnel tests of the closed loop SMC system were not successfully conducted. Attempts at conducting these tests at the wind tunnel indicated an improper digital implementation of the control laws. This was not discovered before testing because a real time simulation validating the control laws and software against the simulator was not conducted before wind tunnel tests. (Simulations were conducted for both the roll and MLC systems which were successfully tested.)

Due to the implementation problem, no closed loop SMC test data could be obtained. Open loop test data were obtained. This data was used to validate the analytical modeling techniques which provide confidence that the SMC system could meet its objectives when properly implemented.

#### 6.3.1 SMC CONTROL LAW DEVELOPMENT

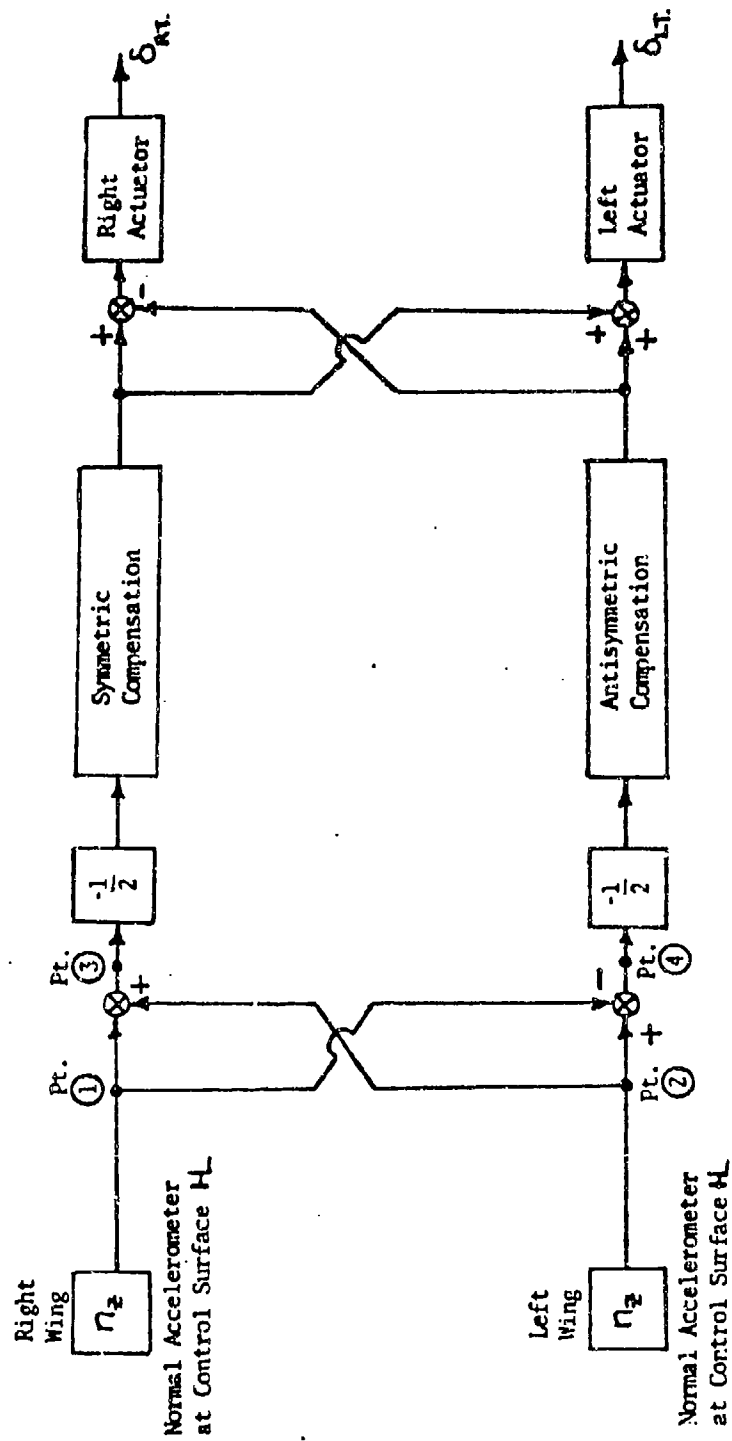
The objective of the system is to reduce the response of structural dynamic modes due to oscillating inputs such as turbulence. To meet this objective, wing accelerometer information is processed through a closed loop feedback system which moves the control surfaces to add aerodynamic damping to the structure. The system is designed as a single-input-single-output (SISO) system. Only one control surface pair is used along with one accelerometer pair. However, both symmetric and antisymmetric systems are designed to operate simultaneously. This is accomplished by separating the right and left accelerometer signals into symmetric and antisymmetric wing signals, designing separate SMC control laws for symmetric and antisymmetric systems, and then recombining the control surface commanded output. Figure 6-32 shows a schematic of the SMC system. Figure 6-33 shows how accelerometer-load factor calculations are analytically developed for the points indicated in Figure 6-32.

The compensation chosen for both the symmetric and antisymmetric loops have a generalized form shown below:

$$\text{comp} = K \left( \frac{as}{s+a} \right) \left( \frac{b}{s+b} \right) \left( \frac{c}{s+c} \right) \left( \frac{d}{s+d} \right) \quad (\text{act})$$

where: K      gain factor

- a - break frequency of high frequency rolloff filter
- b - break frequency of compensator
- c - break frequency of smoothing filter
- d - break frequency of antialiasing electronic prefilter
- act - actuator dynamics



The indicated processing of wing mounted normal accelerometer signals separates symmetric motion signals from antisymmetric motion signals. See equations on following page.

Figure 6-32. Generalized Schematic of Structural Mode Control Systems for AFW Model 1

Pt. ①

$$(\eta_z)_R = - \sum_{i=1}^n \frac{\phi_i^R \ddot{\eta}_i}{g} - \sum_{j=1}^m \frac{\phi_j^R \ddot{\eta}_j}{g}$$

ANTISYM

Pt. ②

$$(\eta_z)_L = - \sum_{i=1}^n \frac{\phi_i^L \ddot{\eta}_i}{g} - \sum_{j=1}^m \frac{\phi_j^L \ddot{\eta}_j}{g}$$

ANTISYM

6-43

Pt. ③

$$(\eta_z)_R + (\eta_z)_L = - \sum_{i=1}^n \frac{(\phi_i^R + \phi_i^L) \ddot{\eta}_i}{g} - \sum_{j=1}^m \frac{(\phi_j^R + \phi_j^L) \ddot{\eta}_j}{g}$$

ZERO

[Pure Symmetric Motion]

Pt. ④

$$(\eta_z)_L - (\eta_z)_R = - \sum_{i=1}^n \frac{(\phi_i^R - \phi_i^L) \ddot{\eta}_i}{g} - \sum_{j=1}^m \frac{(\phi_j^R - \phi_j^L) \ddot{\eta}_j}{g}$$

ANTISYM

[Pure Antisymmetric Motion]

Nomenclature

$\eta_z$  Normal load factor. Subscript L for left and subscript R for right

$g$  acceleration of gravity

$\phi_i$  Normalized mode shape for mode i and j respectively. Superscript L for left and superscript R for right

$\ddot{\eta}_i$  Generalized coordinate acceleration for mode i and j respectively

SYM Symmetric

ANTISYM Antisymmetric

Figure 6-33. Analytical Accelerometer Load Factor Calculations

The frequency for the smoothing filter which was predesigned electronic hardware, was 454 rad/sec. The high frequency rolloff filter

break frequency was chosen to be 60 rad/sec to prevent instabilities in the higher modes outside of the range of interest (0 to 360 rad/sec). The limit for the compensator break frequency was set at 200 rad/sec. This satisfied the requirement that the filter frequency must be no greater than approximately 1/6 of the sampling rate so that it could be detected during a frequency sweep.

Substitution of the designated break frequencies back into the equation yields the following form

$$\text{comp} = K \left( \frac{60s}{s+60} \right) \left( \frac{b}{s+b} \right)^2 \left( \frac{454}{s+454} \right) \left( \frac{628}{s+628} \right) \quad (\text{act})$$

where K = gain factor  
b = break frequency of compensator  
act = actuator dynamics

The two remaining variables used to optimize the performance of the control system were the gain factor and the compensator break frequency.

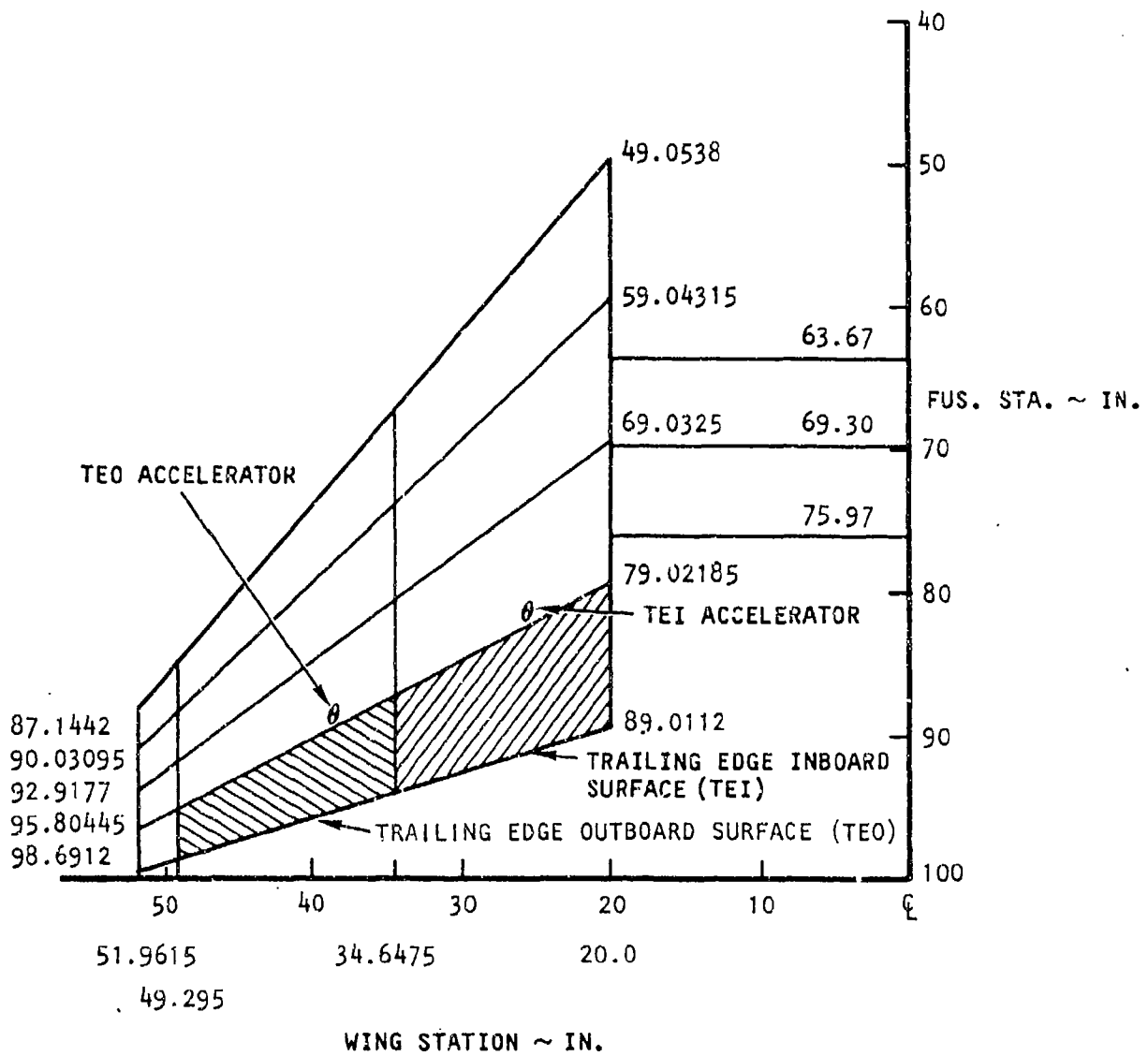
In addition to the performance goals of the system, stability requirements were specified. These requirements are system gain margin of 6 dB and a phase margin of  $\pm 60$  degrees.

Four SMC control laws were designed to use different control surfaces and wing response inputs. They were:

- 1) Trailing edge outboard surface and accelerometer symmetric
- 2) Trailing edge outboard surface and accelerometer antisymmetric
- 3) Trailing edge inboard surface and accelerometer symmetric
- 4) Trailing edge inboard surface and accelerometer antisymmetric

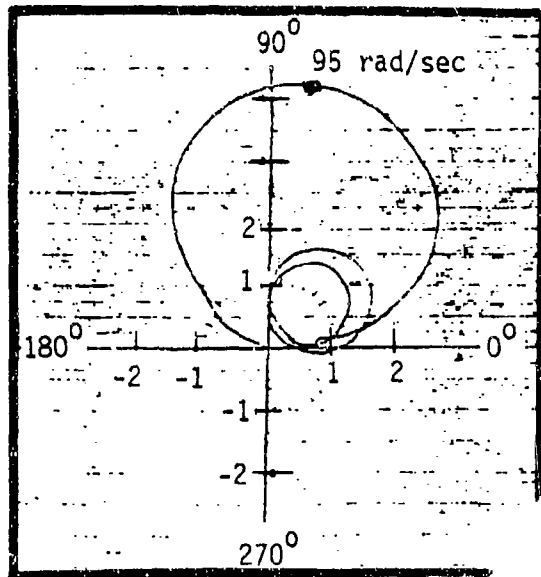
Figure 6-34 shows the control surfaces and accelerometer locations.

The symmetric trailing edge outboard structural mode control system synthesis is illustrated by the Nyquist plots in Figure 6-35. The basic plant or the frequency response of the aircraft without controls is shown in Figure 6-35a, the plant plus the fixed or preassigned filters with the actuator included is shown in Figure 6-35b, and Figure 6-35c represents the complete system. In order to calculate a gain factor which met the stability criteria, a series of Bode plots were constructed to show the process. Figure 6-36 shows a Bode plot for the basic plant, Figure 6-37 shows a Bode plot for the basic plant plus the preassigned filters and actuator, and Figure 6-38 shows a Bode plot of the basic plant with full compensation. The goal was to calculate a gain which would drop the magnitude down to -6 db on the Bode plot of the complete system where the phase passes through 180°. The phase passes through 180° at three locations on Figure 6-38. The point selected had a frequency of 193 rad/sec. This frequency is where the magnitude was largest in comparison with the other two transition points.

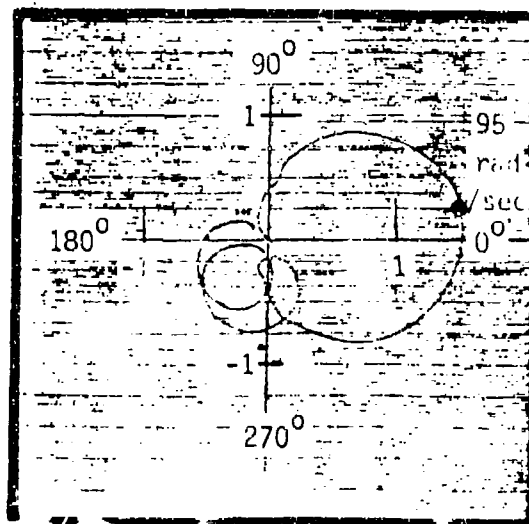


LEFT WING PANEL SHOWN, RIGHT WING PANEL HAS SAME DETAILS

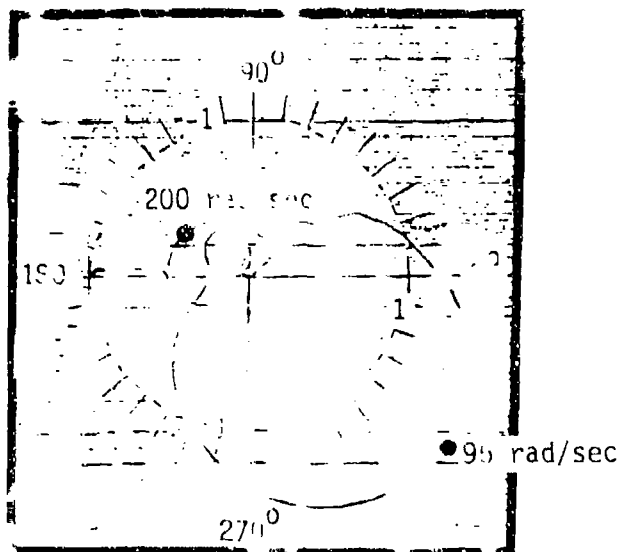
Figure 6-34. AFW Model Control Surfaces and Companion Accelerometer Locations



(a) Basic



(b) Basic + Act.

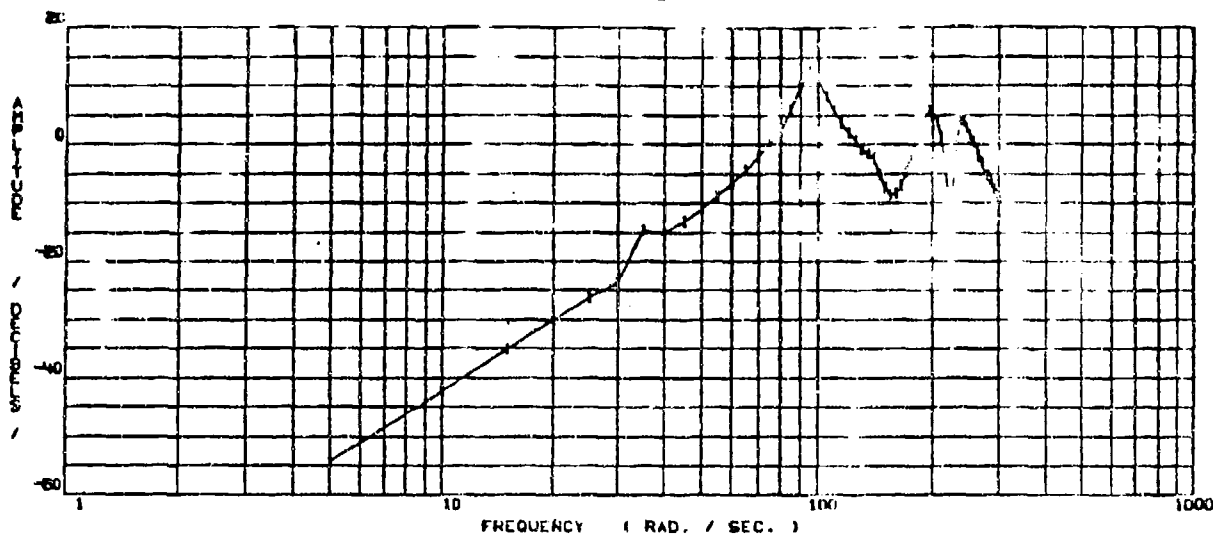


(c) Basic + Actuator + Compensator

Trailing Edge Outboard Symmetric

$$Law = - (0.01149) \left( \frac{60s}{s+60} \right) \left( \frac{200}{s+200} \right)^2 \left( \frac{454}{s+454} \right) \left( \frac{628}{s+628} \right) \quad (act)$$

Figure 6-35. Normal Load Factor at Trailing Edge Outboard Control Surface Due to TEO Deflections



FREQUENCY VS. PHASE ANGLE \* BASIC

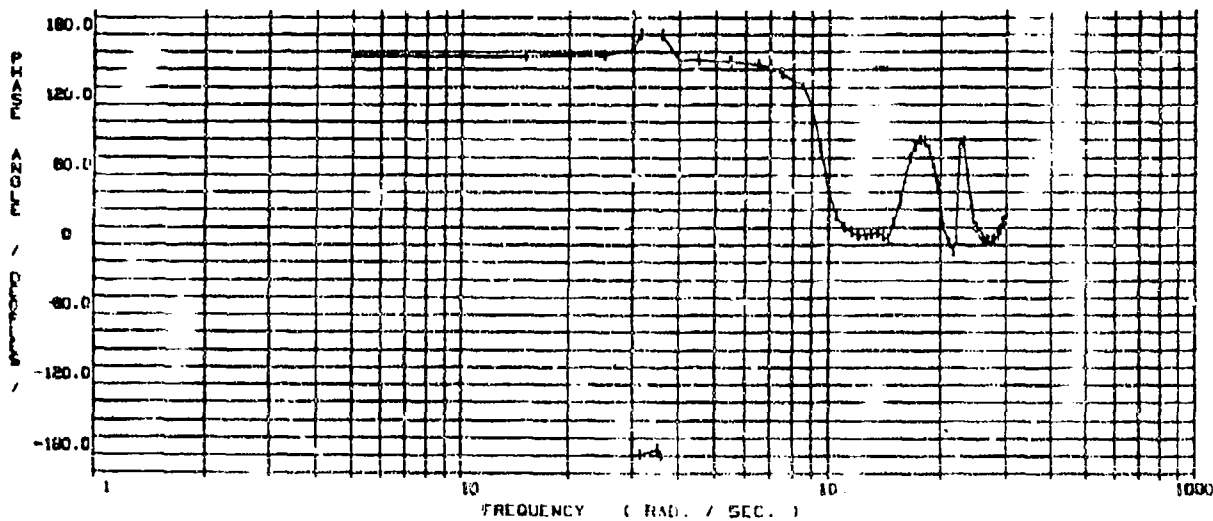
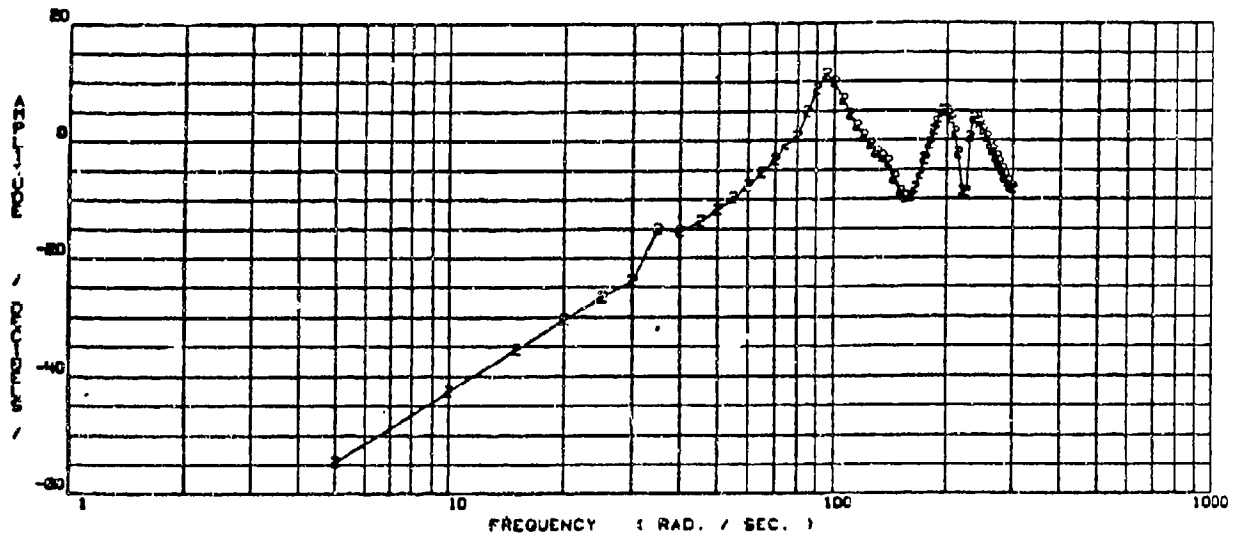


Figure 6-36. Bode Plot of Basic Plant for Symmetric TE0  
 AFW Model Structural Mode Control System,  
 $M = 1.15$ ,  $q = 225$  psf

ATM 1/6 MODEL, SYM.  $M = 1.15$  ( T.E.O. ACCEL. / DELTA T.E.O. )  
 FREQUENCY VS. MAGNITUDE \*\* BASIC + ACTUATOR

87/07/11 3  
 COMPOD



FREQUENCY VS. PHASE ANGLE \*\* BASIC + ACTUATOR

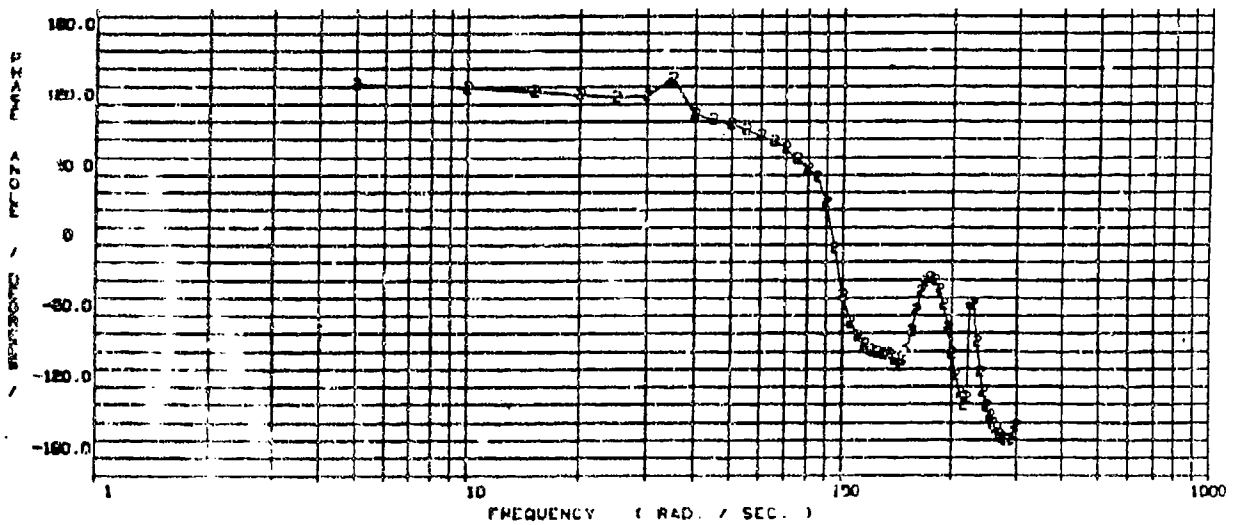
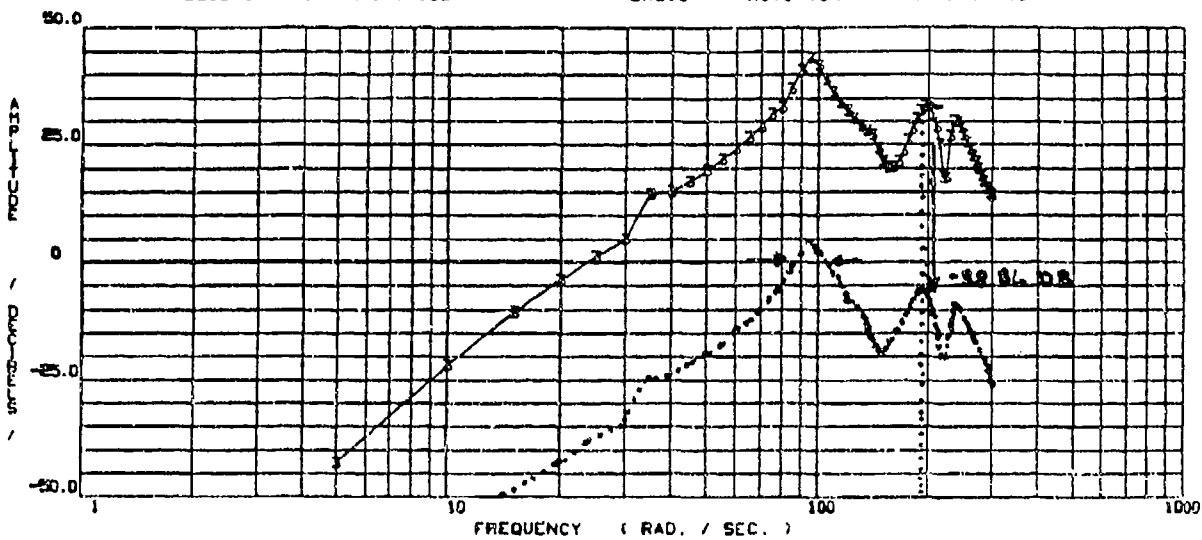


Figure 6-3 . Bode Plot of Basic Plant plus Actuator with Preassigned Filters for Symmetric TEO AFW Model Structural Mode Control System,  $M = 1.15$ ,  $q = 225$  psf

ATW 1/6 MODEL, SYM, M = 1.15 ( T.E.O. ACCEL. / DELTA T.E.O. )  
 FREQUENCY VS. MAGNITUDE \*\*\* BASIC + ACTUATOR + COMPENSATION

87/07/11  
 00P000 4



FREQUENCY VS. PHASE ANGLE \*\*\* BASIC + ACTUATOR + COMPENSATION

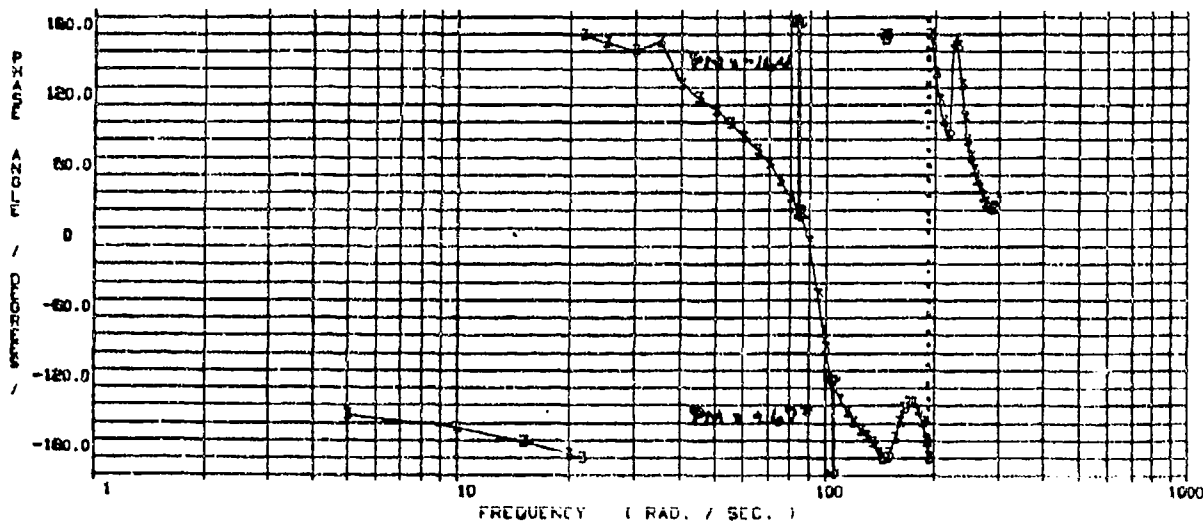


Figure 6-38. Bode Plot of Basic Plant with Total compensation  
 Included for Symmetric TEO AFW Model Structural Mode Control System,  
 $M = 1.15$ ,  $q = 225$  psf

The magnitude of the response at 193 rad/sec had to be reduced 38.86 dB to obtain a gain margin of 6 dB. The gain factor is -38.86 dB or 0.0114. The reduced response is approximately 0.4 at -60° phase margin and 0.9 at +60°. Since the response is less than 1.0 at both 120° and 240°, the phase margin is greater than  $\pm 60^\circ$  and the gain margin is 6 dB.

Figure 6-39 illustrates a significant reduction in the response between the open loop power spectral density plot (PSD) of the symmetric TEO load factor due to TEO deflection as compared with the closed loop structural mode control PSD. The RMS value (or the square root of the area under each of the curves shown) is shown as a measure of the overall reduction in response.

Table 6-9 summarizes the control laws and their corresponding RMS values. The symmetric and antisymmetric SMC systems demonstrated good performance while satisfying the stability constraints.

### 6.3.2 SMC ANALYSIS AND COMPARISON WITH TEST RESULTS

A structural dynamic, analytical model was developed for the SMC system development. Natural vibration modes were used to model the structural dynamic response of the wind tunnel model. Those were obtained from the analytical vibration model tuned to match model ground vibration test data. Actuator dynamics, curve fit from measured test data were used to model the control surface actuators. Unsteady aerodynamics for the basic model and control surfaces were calculated using a Rockwell developed Unsteady Aerodynamic Woodward code. The aerodynamics were calculated at the Mach numbers of 0.9 and 1.15 at several reduced frequencies and curve-fit into the Laplace domain for frequency response analyses.

The SMC data, along with desired control laws, were used in frequency response calculations to determine system performance (due to control surface excitation) and stability.

Open loop test data from the wind tunnel test was recorded in the form of Nyquist plots for symmetric and antisymmetric cases. The Nyquist plots for the analytical model are compared with the test results in Figure 6-40 for the antisymmetric motion and Figure 6-41 for symmetric motion. The similarity is apparent by comparing the location of the major loop or peak of each pair. The test data used to compare with the analytical model were recorded from the left wing accelerometers. A comparison of the test data for the left and right wing is shown in Figure 6-42 for the antisymmetric case and in Figure 6-43 for the symmetric case.

The test data recorded in the wind tunnel were later reduced to obtain a frequency response spectrum. These data were compared directly with analytical data in Figures 6-44 through 6-47 in the form of Bode plots. The response due to a trailing edge inboard deflection for either the symmetric or antisymmetric cases reveals a marked phase difference over the range from 100 to 200 rad/sec. This phase difference is also revealed in the cross response

ATM 1/8 MODEL, SYM, M = 1.15 T E O ACCEL / T E O 100, 43  
 PHI \* /NZ/ RESPONSE STATION \* \* \*

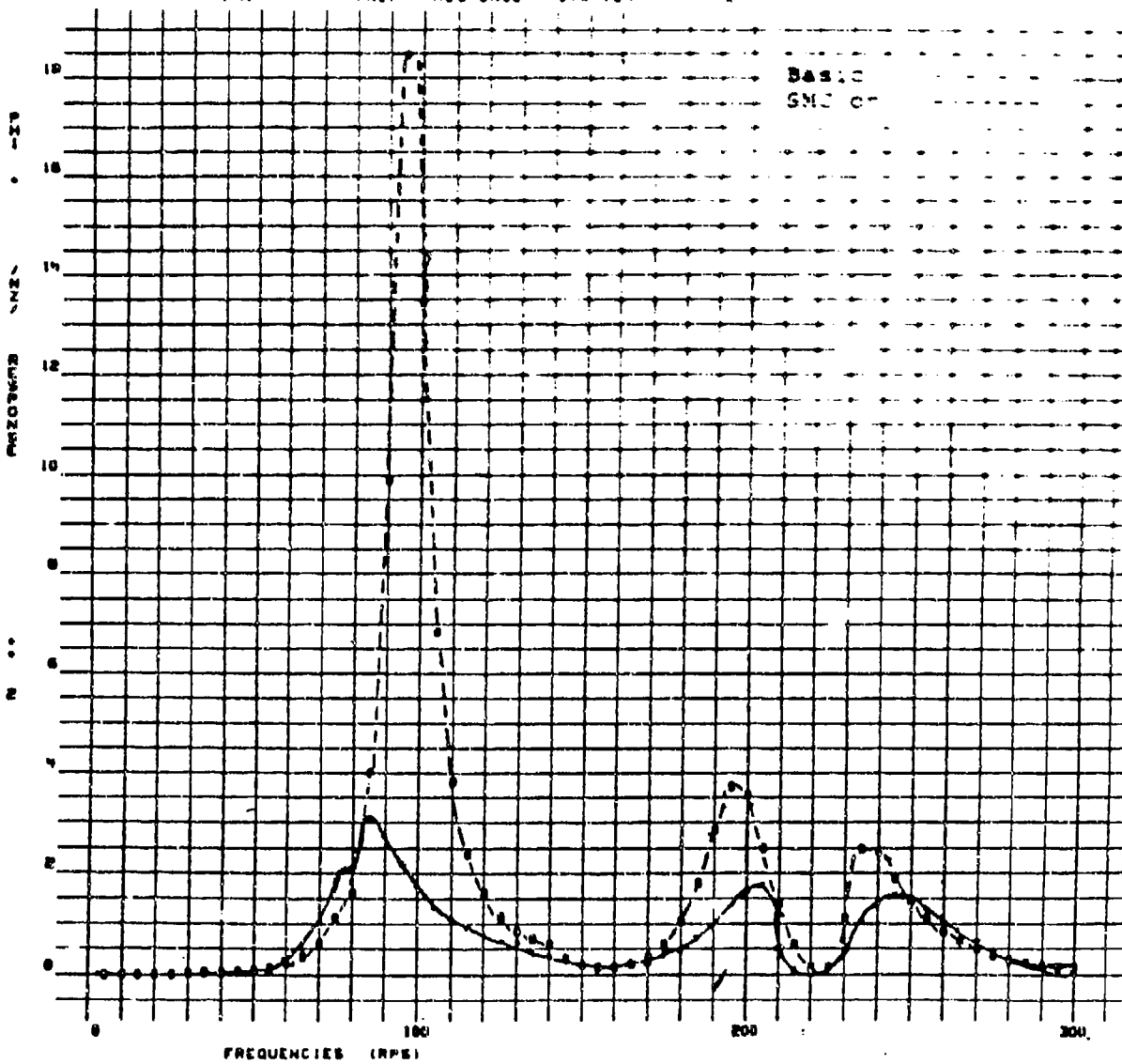


Figure 6-39. AFW Model Power Spectral Density Plot of Symmetric TEO  
 Basic and Closed Loop SMC System,  $M = 1.15$ ,  $q = 225$  psf  
 Basic RMS = 22.388, SMC on RMS = 14.388

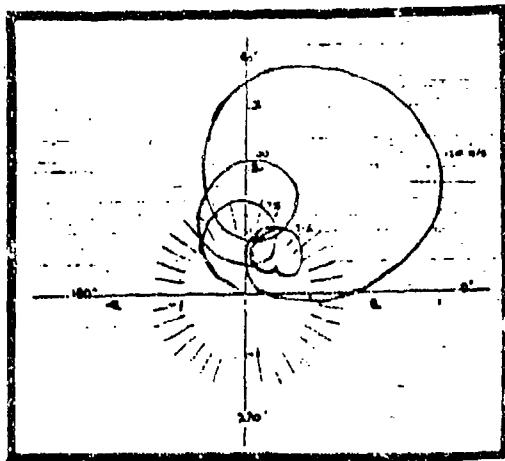
Table 6-9  
STRUCTURAL MODE CONTROL LAW SUMMARY

Control Surface	Gain Factor (K)	Gain Margin (db)	Phase Margin (deg)	Performance RMS (g's)
Symm. T.E.O.				
Basic	-	-	-	22.388
SMC on	- 0.0114	6.00	+67°, -164°	14.388
Symm. T.E.I.				
Basic	-	-	-	10.946
SMC on	- 0.0185	6.00	+141°, -191°	5.858
A/S T.E.O.				
Basic	-	-	-	19.303
SMC on	- 0.0076	8.87	∞	14.192
A/S T.E.I.				
Basic	-	-	-	15.121
SMC on	- 0.0103	6.00	∞	13.111

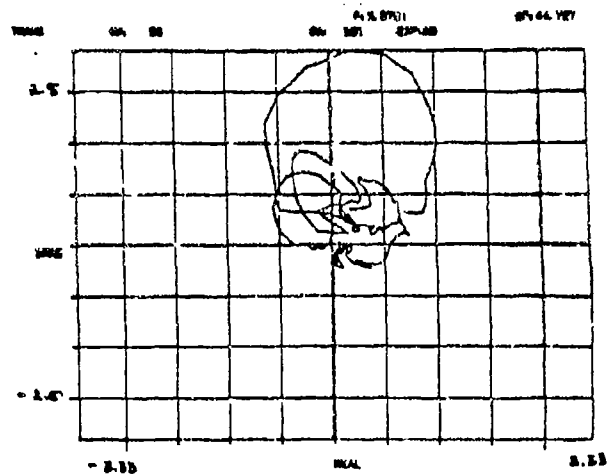
\* All control laws are modeled as the following:

$$C.S. \text{ Law} = K \left( \frac{60s}{s+60} \right) \left( \frac{200}{s+200} \right)^2 \left( \frac{454}{s+454} \right) \left( \frac{628}{s+628} \right) (\text{act})$$

where: K - gain factor  
act - actuator dynamics

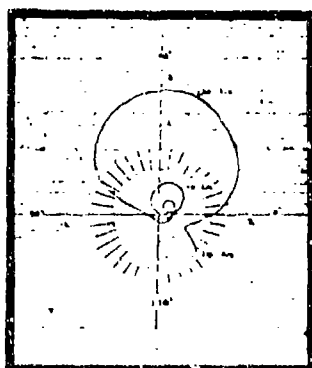


(a)  
Analytical TE0

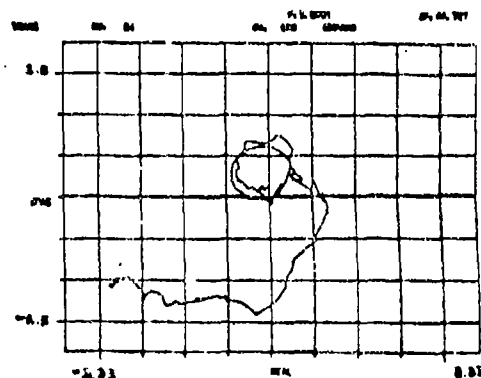


(b)  
Test TE0

Normal Load Factor at TEI Control Surface Due to  
TEI Deflection



(c)  
Analytical TEI

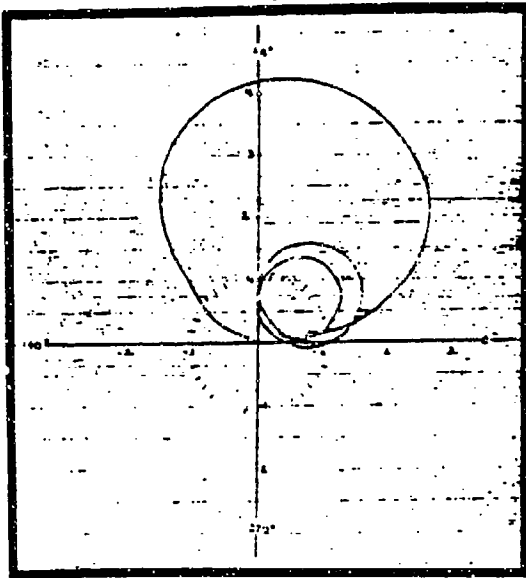


(d)  
Test TEI

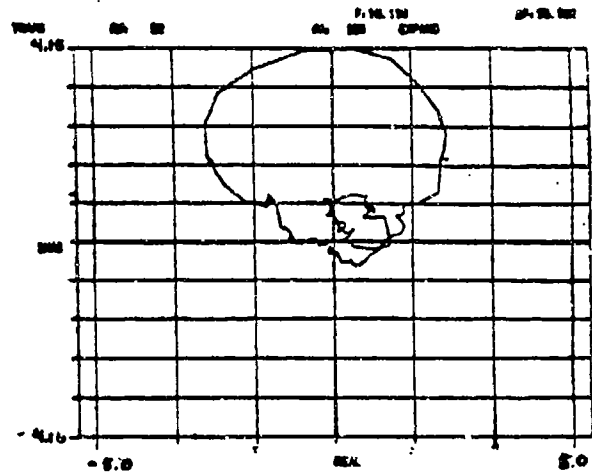
Note:

Nyquist Plots of AFW Model - Comparison of Analytical and Test Data -  
Basic Antisymmetric, Brake On,  $M = 1.15$ ,  $q = 225$  psf.

Figure 6-40. Normal Load Factor at Control Surface Due  
to Deflection

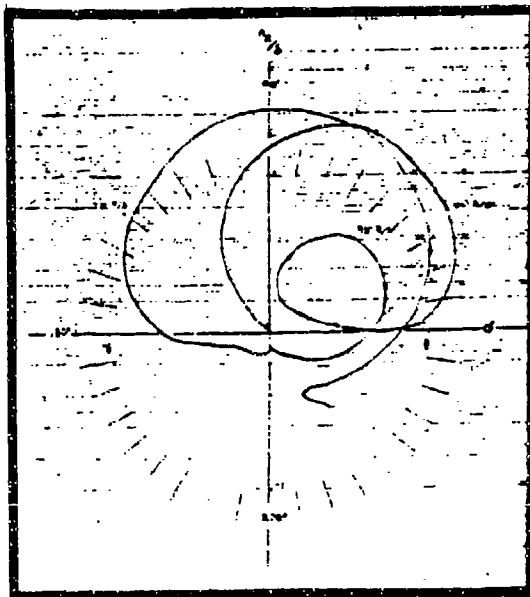


(a)  
Analytical TE0

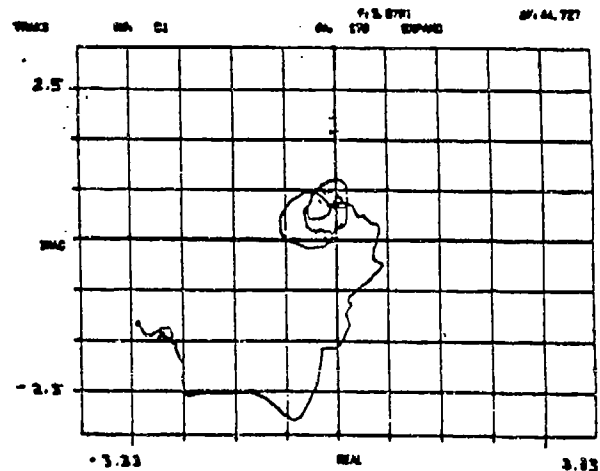


(b)  
Test TE0

Normal Load Factor at TEI Control Surface Due to TEI Deflection



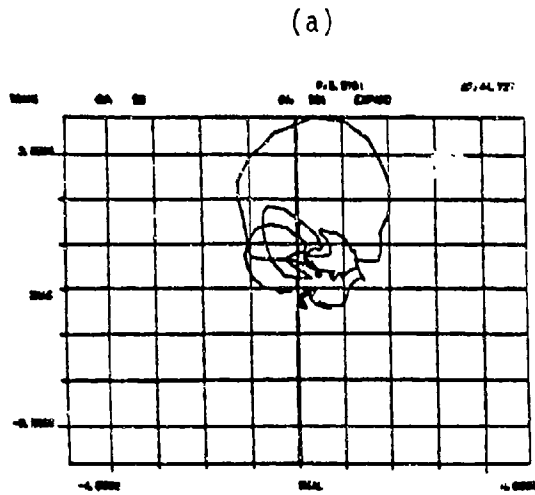
(c)  
Analytical TEI



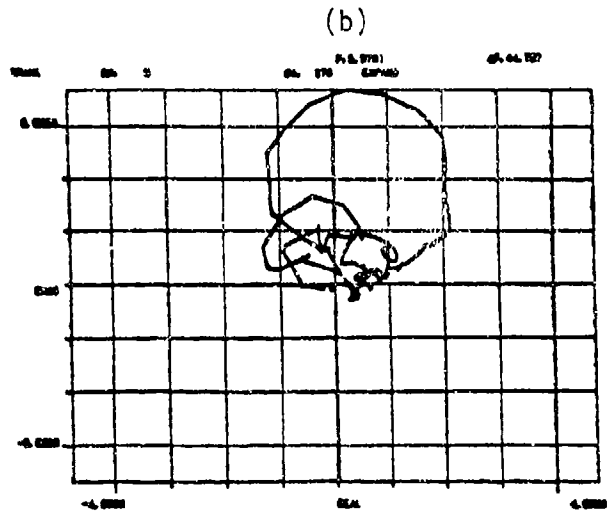
(d)  
Test TEI

Note: Nyquist Plots of AFW Model - Comparison of Analytical and Test Data  
Basic Symmetric,  $M = 1.15$ ,  $q = 225$  psf.

Figure 6-41. Normal Load Factor at Control Surface Due to Deflection

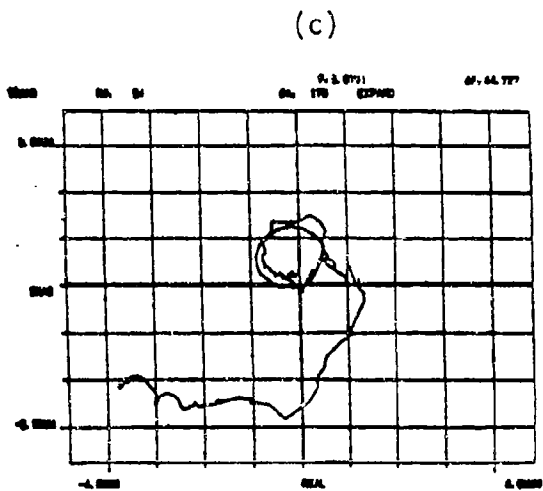


Left Wing

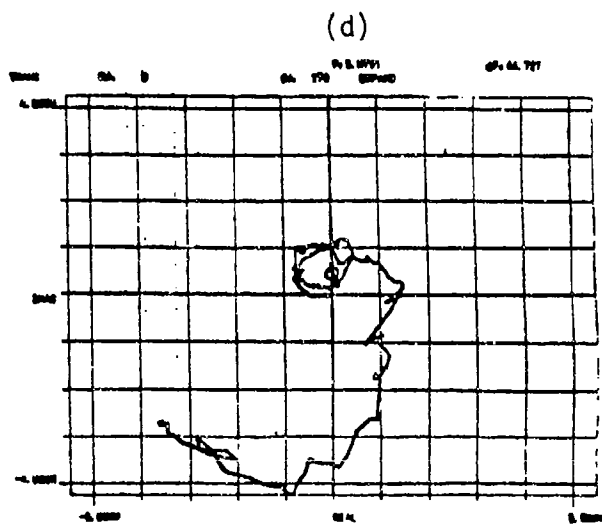


Right Wing

Normal Load Factor at TEI Control Surface Due to TEI Deflection - Basic Open Loop



Left Wing

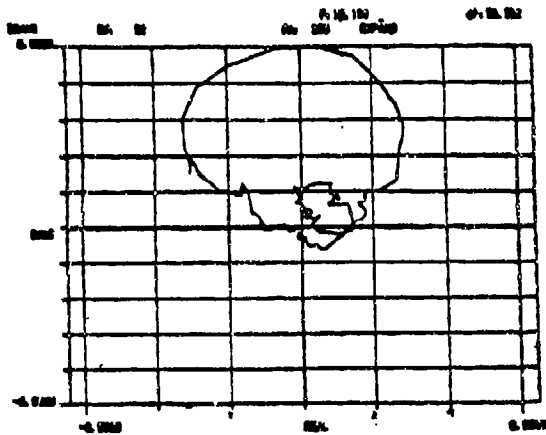


Right Wing

Note:

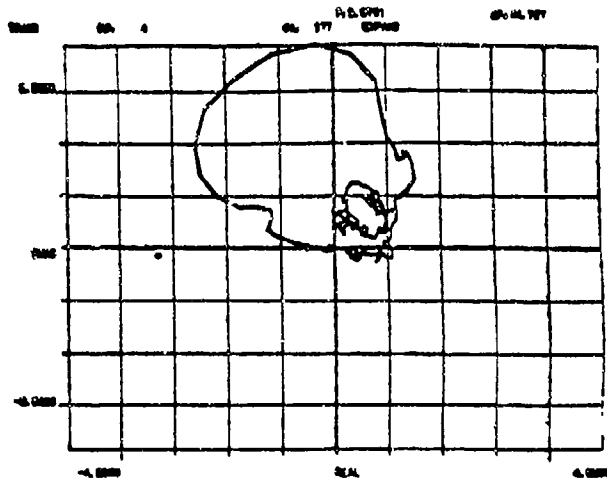
Nyquist Plots of AFW Model - Comparison of Test Data Right and Left Wing - Antisymmetric, Brake On,  $M = 1.15$ ,  $q = 225$  psf.

Figure 6-42. Normal Load Factor at Control Surface Due to Deflection - Basic Open Loop



(a)

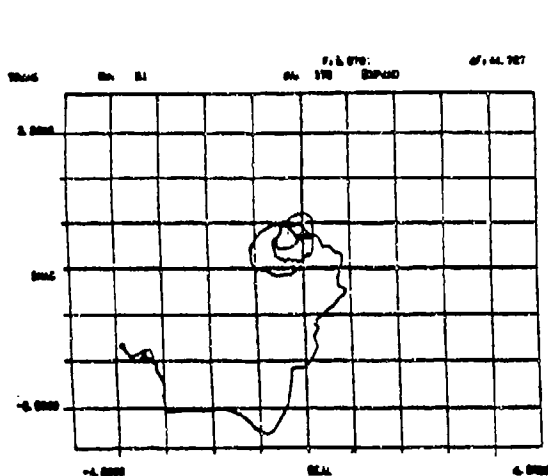
Left Wing



(b)

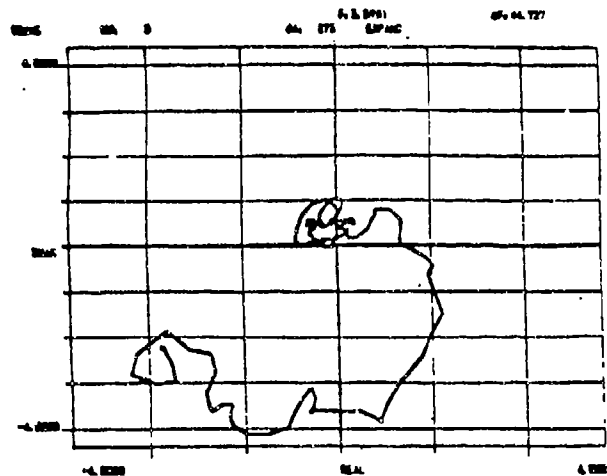
Right Wing

Normal Load Factor at TEI Control Surface Due to  
TEI Deflection - Basic Open Loop



(c)

Left Wing



(d)

Right Wing

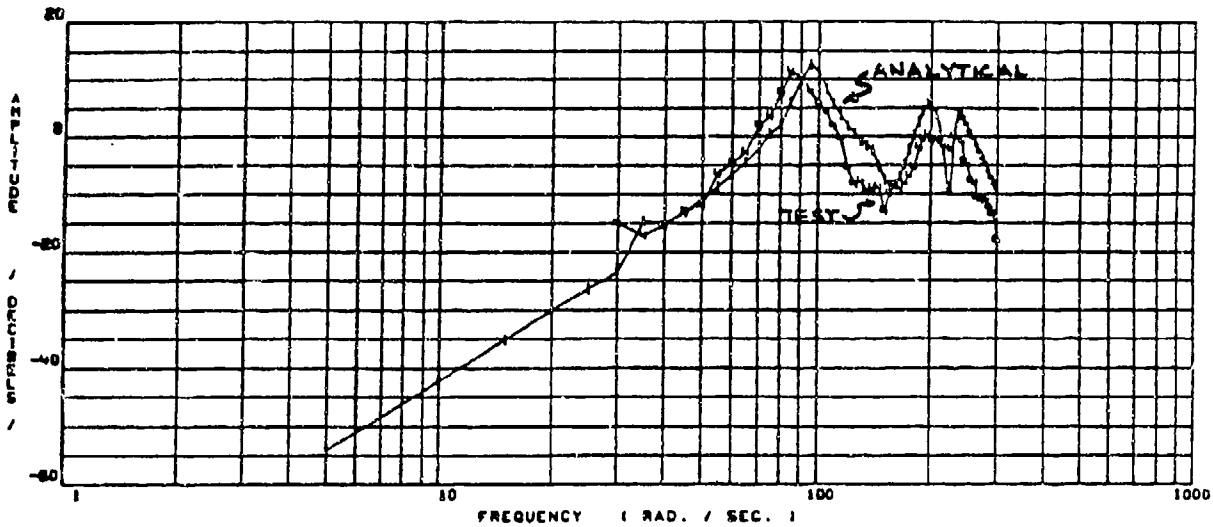
Note:

Nyquist Plots of AFW Model - Comparison of Test Data - Right and Left  
Wing - Symmetric, Brake On,  $M = 1.15$ ,  $q = 225$  psf.

Figure 6-43. Normal Load Factor at Control Surface Due to Deflection - Basic Open Loop

FREQUENCY VS. MAGNITUDE

\*\*\* BASIC ANALYTICAL VS. TEST DATA



FREQUENCY VS. PHASE ANGLE

\*\*\* BASIC ANALYTICAL VS. TEST DATA

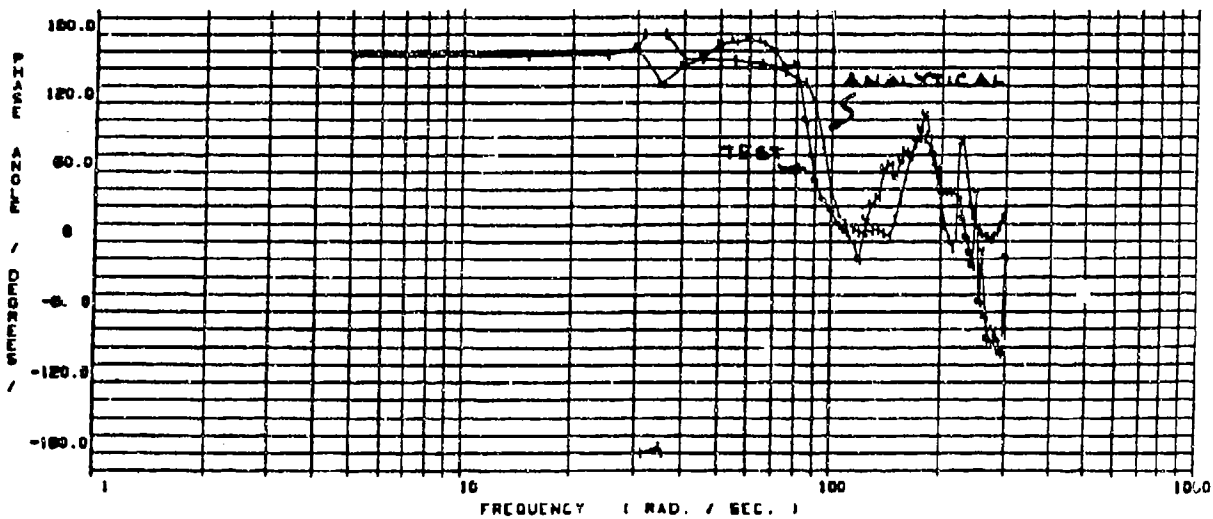
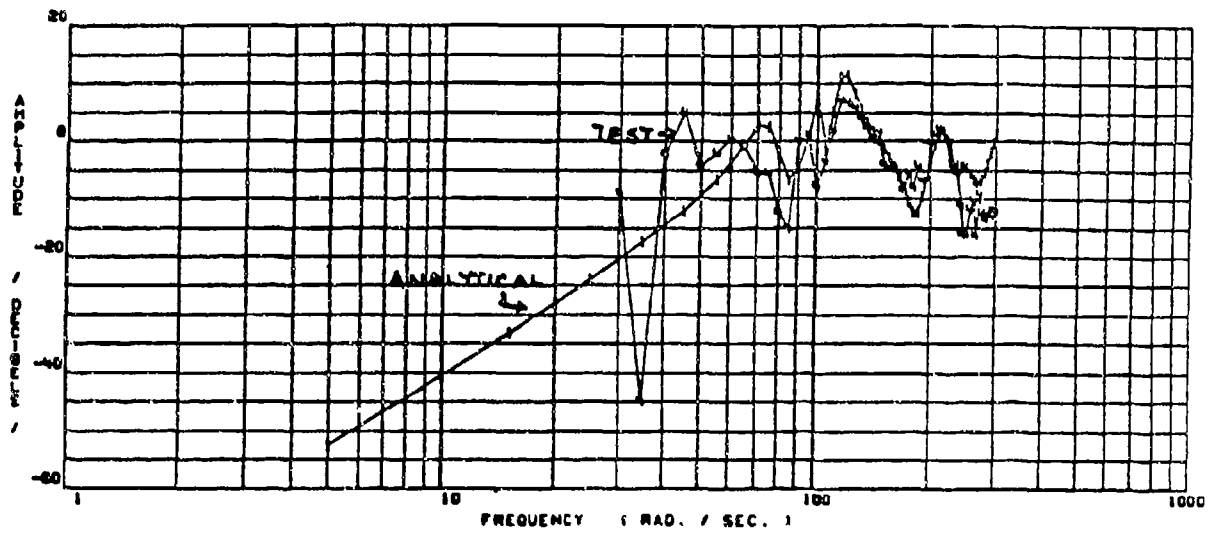


Figure 6-44. Bode Plot of Basic Plant for Symmetric TEO Structural Mode Control System, Analytical Results vs Test, M = 1.15, q = 225 psf

FREQUENCY VS. MAGNITUDE

\*\*\* BASIC ANALYTICAL VS. TEST DATA



FREQUENCY VS. PHASE ANGLE

\*\*\* BASIC ANALYTICAL VS. TEST DATA

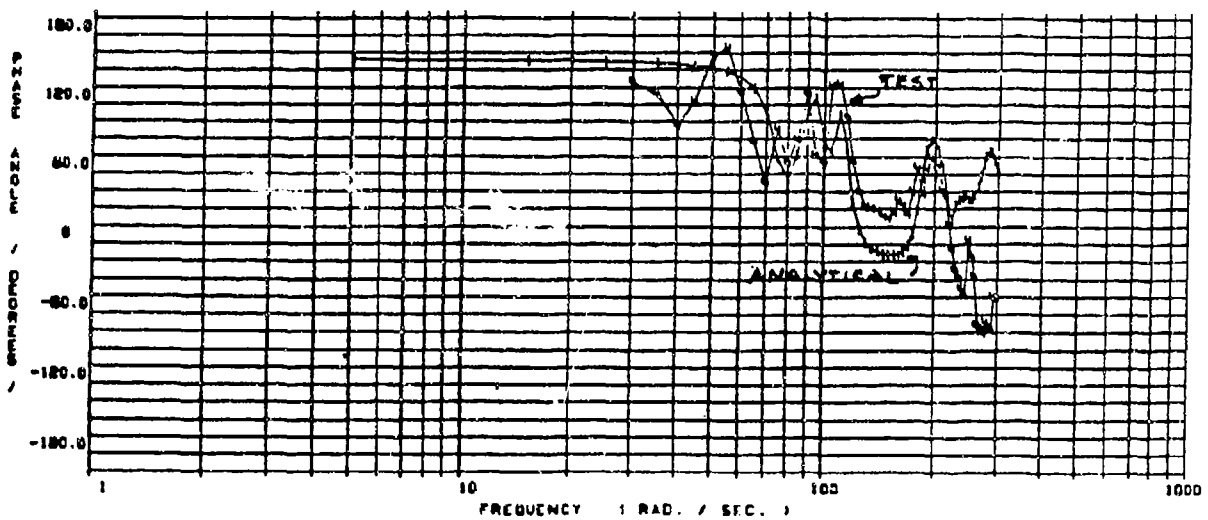


Figure 6-45. Bode Plot of Basic Plant for Antisymmetric TEO Structural Mode Control System, Analytical Results vs Test,  $M = 1.15$ ,  $q = 225$  psf

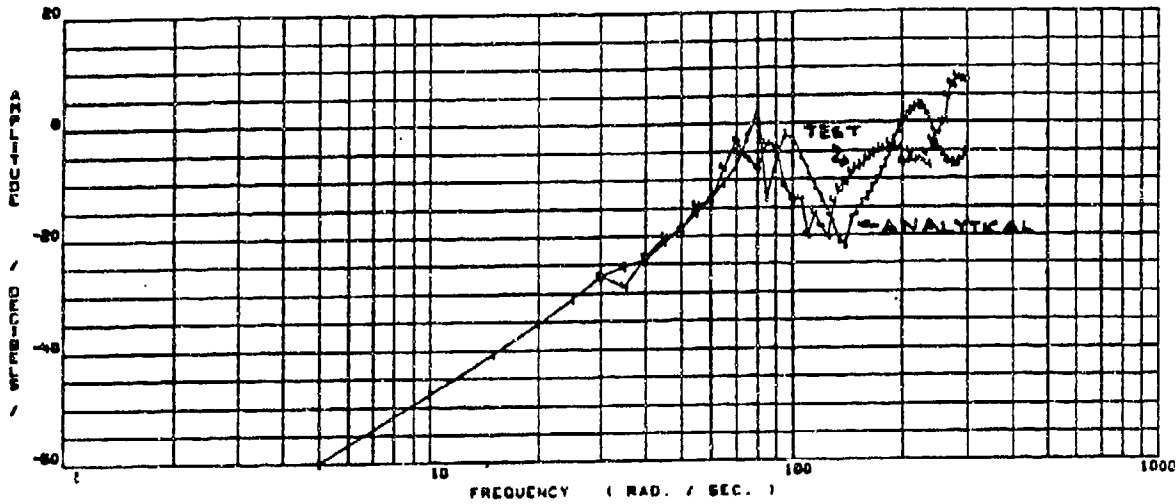
SYM 1.15 MODEL, SYM, M=1.15 ( T.E.I. ACCEL. / T.E.I. DELTA )

07/07/13  
COMP000

6

FREQUENCY VS. MAGNITUDE

\*\*\* BASIC ANALYTICAL VS. TEST DATA



FREQUENCY VS. PHASE ANGLE

\*\*\* BASIC ANALYTICAL VS. TEST DATA

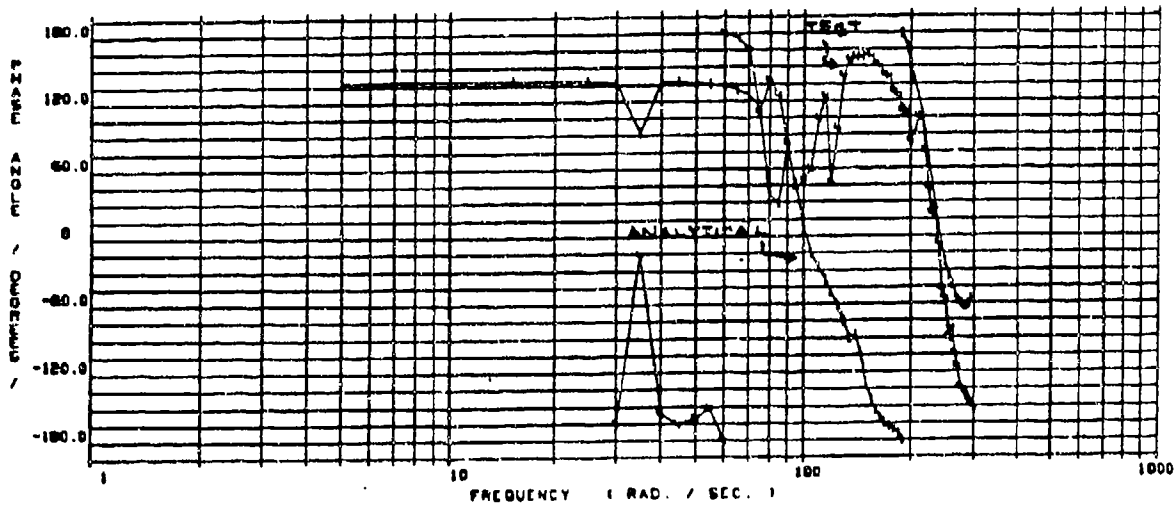
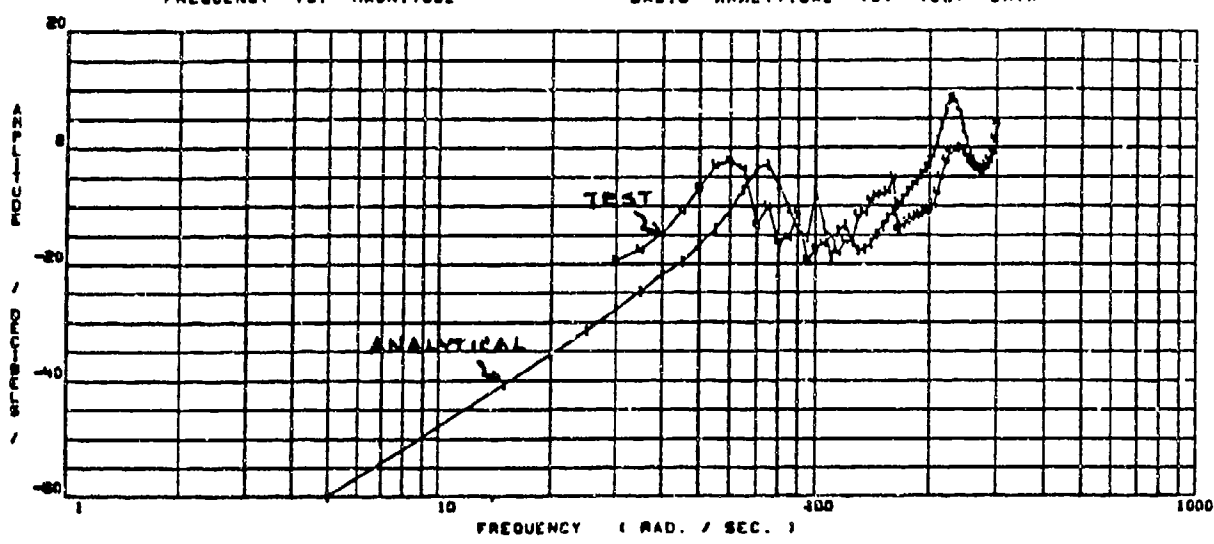


Figure 6-46. Bode Plot of Basic Plant for Symmetric TEI Structural Mode Control System, Analytical Results vs Test,  $M = 1.15$ ,  $q = 225$  psf

FREQUENCY VS. MAGNITUDE \*\*\* BASIC ANALYTICAL VS. TEST DATA



FREQUENCY VS. PHASE ANGLE \*\*\* BASIC ANALYTICAL VS. TEST DATA

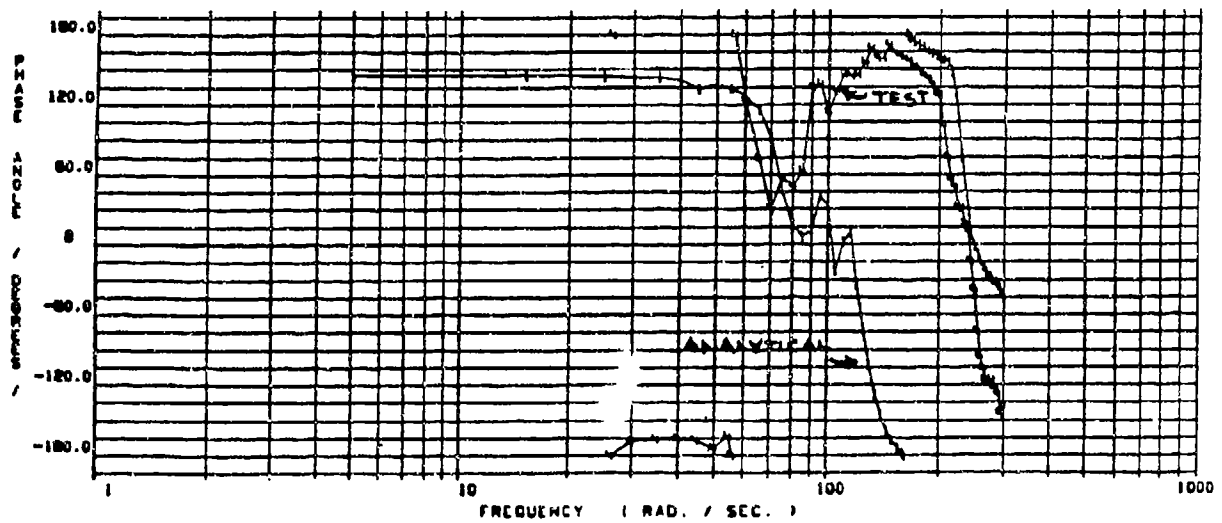


Figure 6-47. Bode Plot of Basic Plant for Antisymmetric TEI Structural Mode Control System, Analytical Results vs Test, M = 1.15, q = 225 psf

plots of the TEO load factor due to TEI surface deflection and TEI load factor due to TEO surface deflection, Figures 6-48 and 6-49. The reduction in the phase error for the cross plots point to a possible localized error.

A comparison of the test and analytical data for the trailing edge inboard load factor due to surface deflection at Mach 0.9 (Figure 6-50) shows that analyses matched the test for both surfaces and that phase difference was not apparent for the trailing edge inboard. The difference in results obtained for the Mach 1.15 data can be attributed to the linear codes limited capability to predict the aerodynamics in this Mach region accurately.

### 6.3.3 SMC SYSTEM CONCLUSIONS

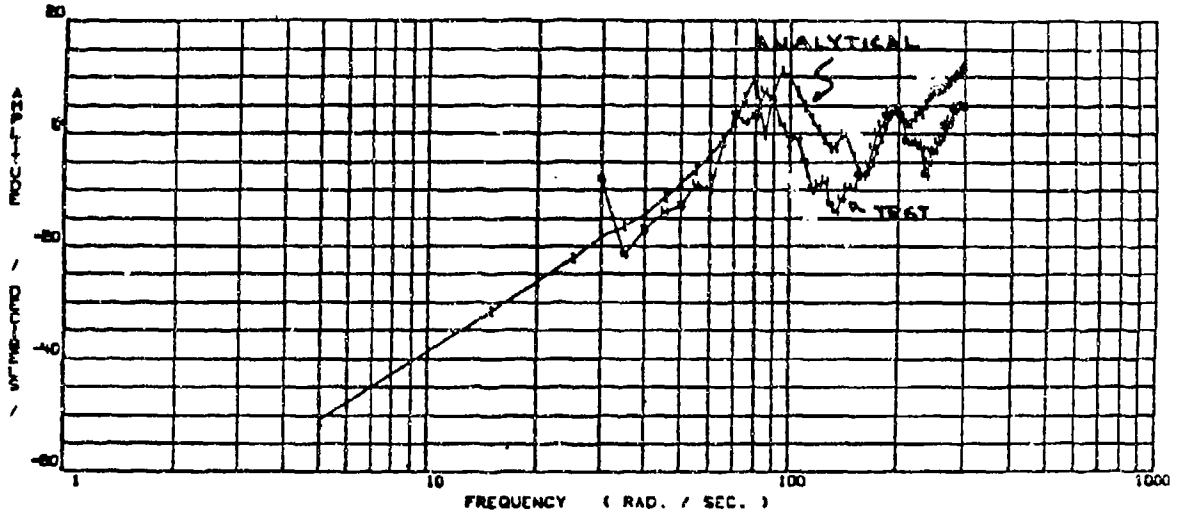
Although the SMC system was not successfully tested in the wind tunnel, open loop frequency response data were obtained. These data correlated quite well with analytical data in most cases. This correlation provides confidence that the predicted closed loop performance would have been obtained if the system were properly implemented.

To ensure successful testing of the SMC system, the use of real-time simulation to aid development and to verify proper implementation of control systems is necessary. Future developments of SMC type systems will include the use of real-time simulations.

ATM 1/6 MODEL, SYM. M = 1.15.  
FREQUENCY VS. MAGNITUDE

( T.E.O. ACCEL. / DELTA T.E.I )  
\*\*\* BASIC ANALYTICAL VS. TEST DATA

87/05/20 6  
00 P000



FREQUENCY VS. PHASE ANGLE \*\*\* BASIC ANALYTICAL VS. TEST DATA

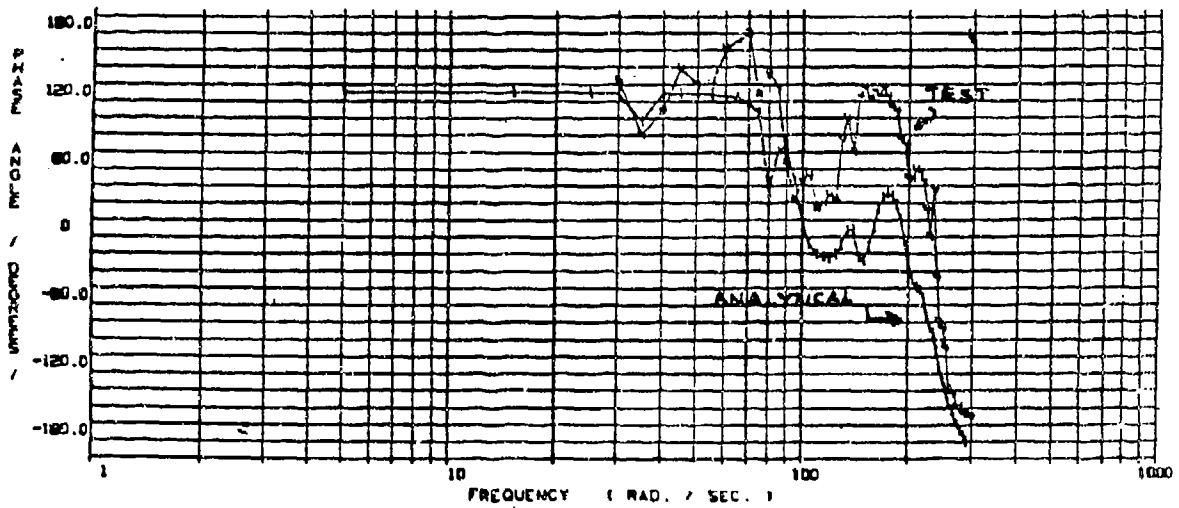


Figure 6-18. Bode Plot of Symmetric Normal Load Factor at TE0  
Due to TEI Deflection, M = 1.15, q = 225 psf

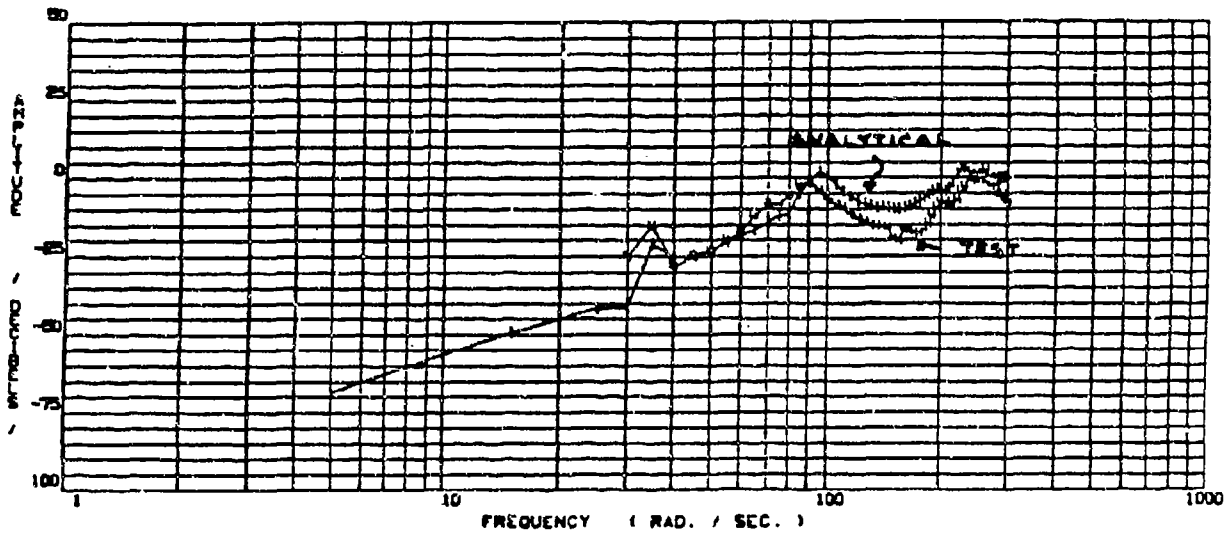
ATM 1/8 MODEL. SYN. M = 1.15.  
FREQUENCY VS. MAGNITUDE

( T.E.E. ACCEL. / DELTA T.E.O. )

07/05/20  
COMP000

6

\*\*\* BASIC ANALYTICAL VS. TEST DATA



FREQUENCY VS. PHASE ANGLE

\*\*\* BASIC ANALYTICAL VS. TEST DATA

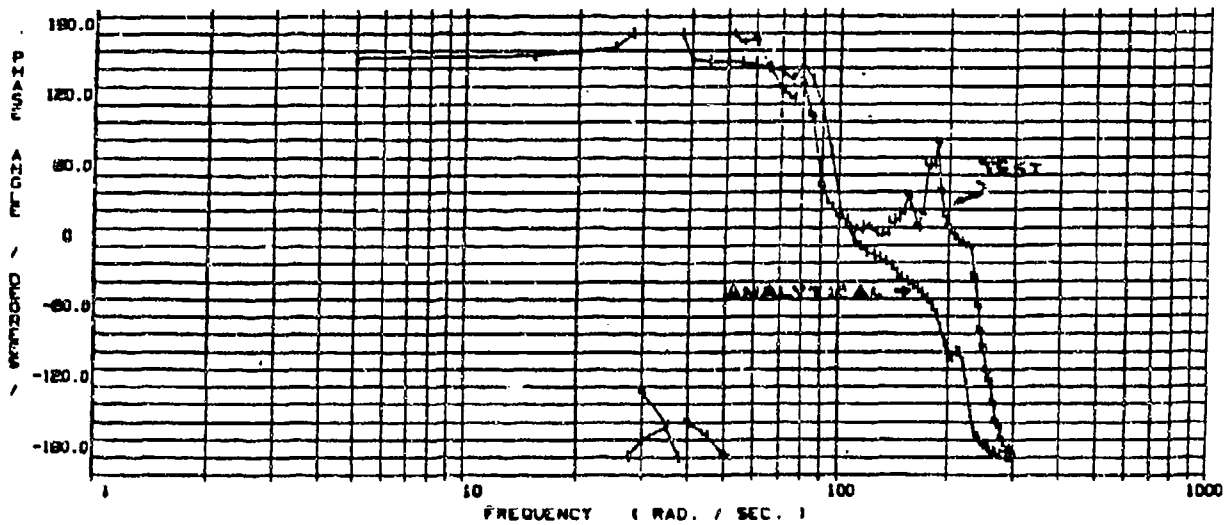


Figure 6-49. Bode Plot of Symmetric Normal Load Factor at TEI  
Due to TEO Deflection, M = 1.15, q = 225 psf

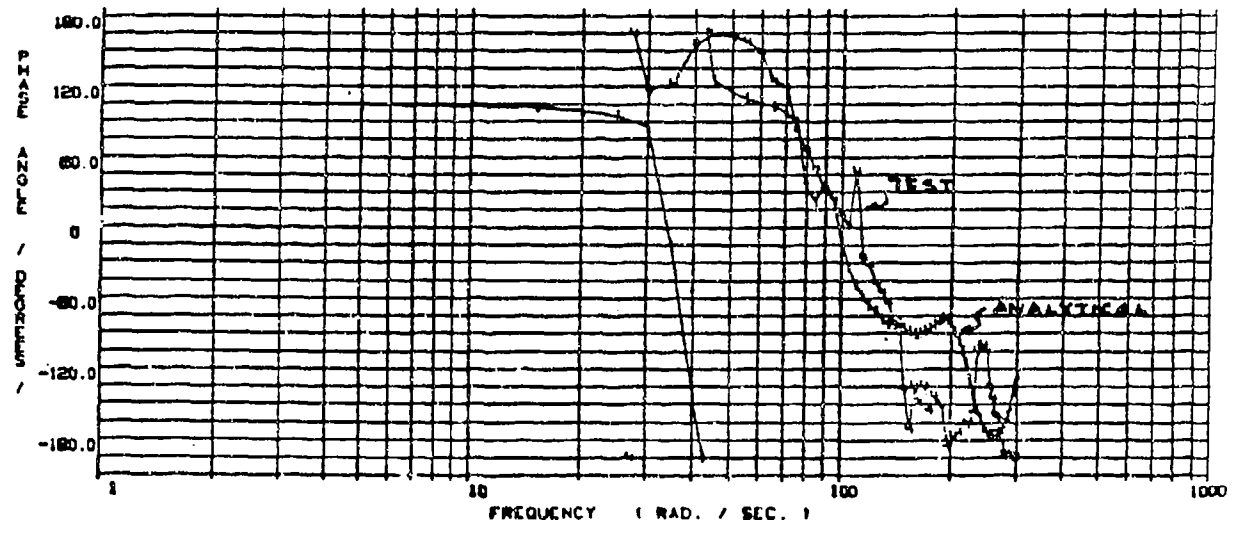
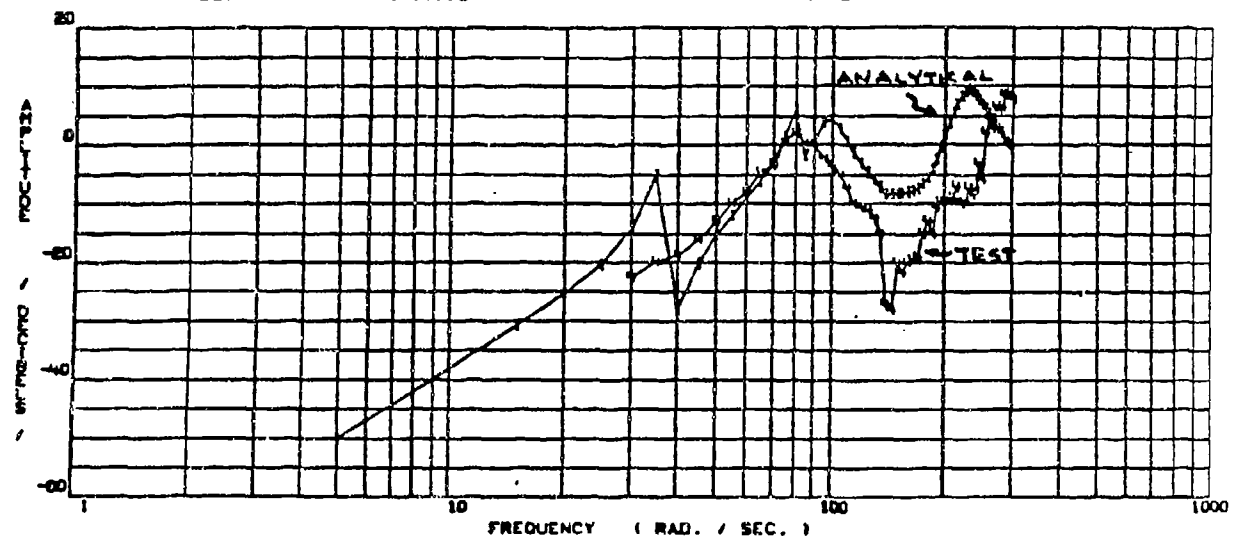


Figure 6-50. Bode Plot of Basic Plan for Symmetric TEI Structural Mode Control System, Analytical Results vs Test, M = 0.9, q = 250 psf

## 7.0 EVALUATION OF AFW TECHNOLOGY AND CONCLUSIONS

The transonic, active control wind tunnel test program provided test verification of the AFW concept. The test results also validated the analytical tools used in the design and analysis process. The static tests conducted during the first tunnel entry verified the transonic, flexible control power predicted by the analytical tools. The dynamic, active control tests conducted during the second tunnel entry verified the high roll rate performance across the flight envelope which was predicted by the control systems design and analyses tools.

The full-scale AFW aircraft design, from which the wind tunnel model was scaled, was thereby validated because the same analytical tools validated by the wind tunnel test program were used in the aircraft design process.

### 7.1 MODEL SCALING TO FULL-SCALE

Although the AFW wind tunnel model was scaled both statically and dynamically to match a full-scale vehicle, care must be taken with the interpretation of the results. There are many factors which manifest themselves in a full-scale vehicle which were not simulated with this wind tunnel model. This, however, does not mean that the results cannot be meaningful relative to predictions of full-scale results.

Aeroelastically, the AFW model scaled well to the full scale aircraft design. The only significant differences were the model roll inertia scaling and the control surface actuator rate and hinge moment scaling. The model's total roll inertia was approximately 15 percent larger than the scaled aircraft roll inertia, due to inertia of the rolling portion of the sting. This effect resulted in the model roll acceleration being lower than the scaled aircraft's. The model actuators were miniature rotary vane actuators, which scale from full scale to yield higher rates and lower hinge moments than the scaled aircraft's rates and hinge moments. The increase in actuator rates effectively increases model roll acceleration, but the reduction in hinge moment reduces the steady state roll rate and roll acceleration. All these combined aeroelastic scaling differences basically negate each other, resulting in a model roll response that would closely match that of the scaled aircraft. Figure 7-1 presents a tabulated summary of scaling effects on model roll response.

In roll, several aspects of a full-scale vehicle cannot be simulated in a model. The most prominent of these is off-axis coupling terms which effects the ultimate roll performance of the vehicle. Although this coupling can be minimized by a well designed control system, the action of that system will ultimately impact the final performance. In many current aircraft these coupling terms are so severe that roll rate limiters must be used to prevent unanticipated departures. Studies using the full scale vehicle from which the

MODEL	SCALED TO A/C	TYPICAL A/C	EFFECT ON MODEL
Actuators:	Rates $\approx 400.0$ o/s	$\approx 150.0$ o/s'	100 o/s'
Hit:	TE typical of full scale A/C LE 50% low of full scale A/C		Decrease T90
Model actuators have faster rates but were capable of much smaller loads			Decrease T90
Plant - Roll Inertia: model was larger than F.S.			No Effect
- Structural Dynamics - model simulated A/C			Increase T90
- Static			Increase T90
- Dynamic			Increase T90
- 1 DOF vs 6 DOF			Increase T90
Flight Control Computer	200 Hz (model) $\approx 77$ Hz (scaled model)	64 Hz (A/C)	No Effect

Figure 7-1. Model - Full Scale A/C Correlation

AFW model was designed indicated it could be controlled at the extremely aggressive roll rates achieved in the wind tunnel without departure problems through the proper application of stability augmentation systems. This is achieved through the proper design of the off roll axis control effectors.

Since results from the wind tunnel model had excellent correlation with analytic predictions, it can be inferred that a full-scale vehicle will be well predicted. This is because the same analytical tools used for the wind tunnel model design are used for full-scale aircraft design.

## 7.2 RECOMMENDATIONS FOR FUTURE RESEARCH

Rockwell's independent research program and the transonic active control wind tunnel program have developed a broad data base which validate the AFW concept. However, these programs have demonstrated only part of the technologies and design methodologies that could be applied within the AFW concept definition.

Additional aircraft benefits could also be obtained from control concepts that have not been verified under this wind tunnel program. They are:

- Antisymmetric maneuver load control to reduce loads in rolling maneuver.
- Flutter suppression for both clean wings and stores which would allow further reduction in weight and an increase in flexible control power.
- The use of multiple control modes operating together; eg; AFW roll with maneuver load control and flutter suppression.

In addition to these technologies, methods for integrated aircraft design using AFW technology need to be developed. AFW technology requires a high degree of interaction between aerodynamic, controls and structures disciplines. Its potential benefits will only be achieved when truly multidisciplinary methods are developed and used. These methods will be required to simultaneously optimize structural control and aerodynamic system designs on a given geometric configuration, and also have the capability to perturb the geometry for a truly optimum design.

## 7.3 CONCLUSIONS

The Rockwell AFW concept of using wing flexibility for enhanced control power has been verified in the transonic flight regime by this wind tunnel program. The ability to design and control an aircraft using a flexible wing provides increased ability to obtain multipoint aerodynamic performance through the use of aeroelastic tailoring.

Additionally, flexible wing structures have lower weight than stiff structures. This synergistic effect combines to allow an aircraft design that either has a significantly reduced size for a fixed level of performance or increased performance for a fixed size.

Finally, the wind tunnel test program verified that the analytical tools used in the AFW design process were adequate to develop a successful advanced aircraft design.

APPENDIX  
MEASURED PRESSURE DATA  
COMPARISON

Measured Pressure data are compared with CFD calculations from the Rockwell Full-potential, Aeroelastic, and CFD codes.

# PRESSURE PROFILE

MACH NO- 0.900  
REF. ALPHA- 0.048  
DYN. PRES 0- 1.740  
STATION- 0.436

CLEAN

— FULL POTENTIAL

○ UPPER DATA  
● LOWER DATA

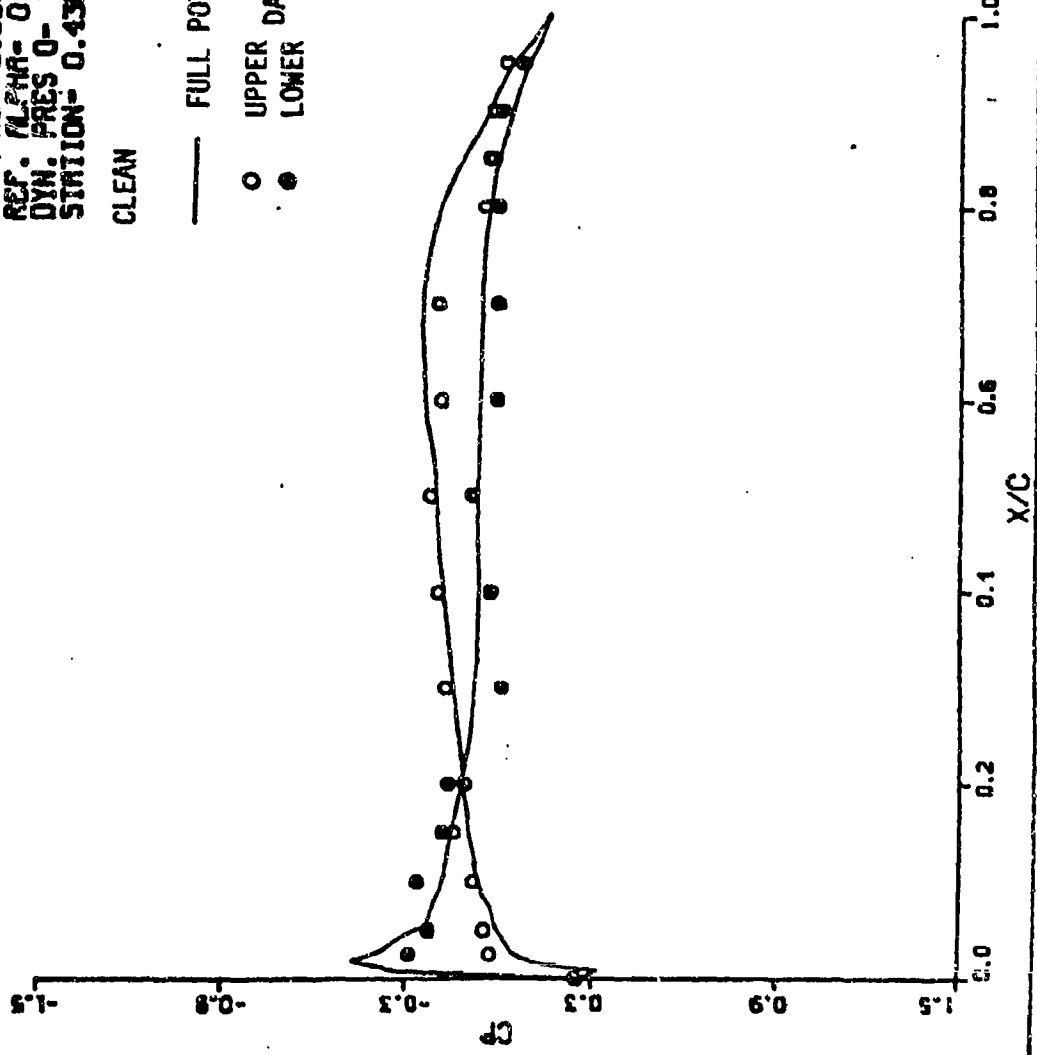


Figure A-1. Pressure Distributions of Flexible AFW Wind Tunnel Model Wing.

# PRESSURE PROFILE

MACH NO- 0.900  
REF. ALPHA- 0.046  
DYN. PRES 0- 1.740  
STATION- 0.587

CLEAN

— FULL POTENTIAL

○ UPPER DATA

● LOWER DATA

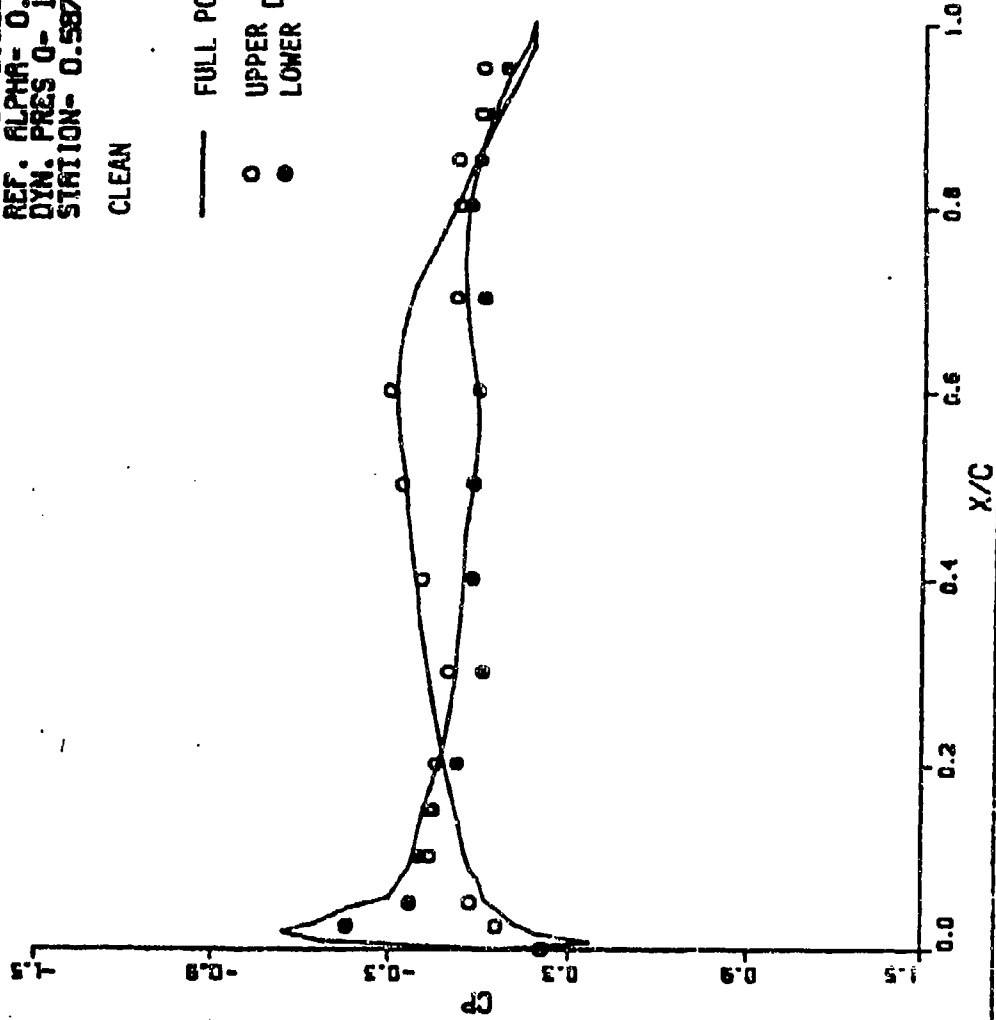


Figure A-2. Pressure Distributions of Flexible AFW Wind Tunnel Model Wing.

# PRESSURE PROFILE

MACH NO- 0.900  
REF. ALPHA- 0.048  
DYN. PRES 0- 1.740  
STATION- 0.699

CLEAN

— FULL POTENTIAL

○ UPPER DATA  
● LOWER

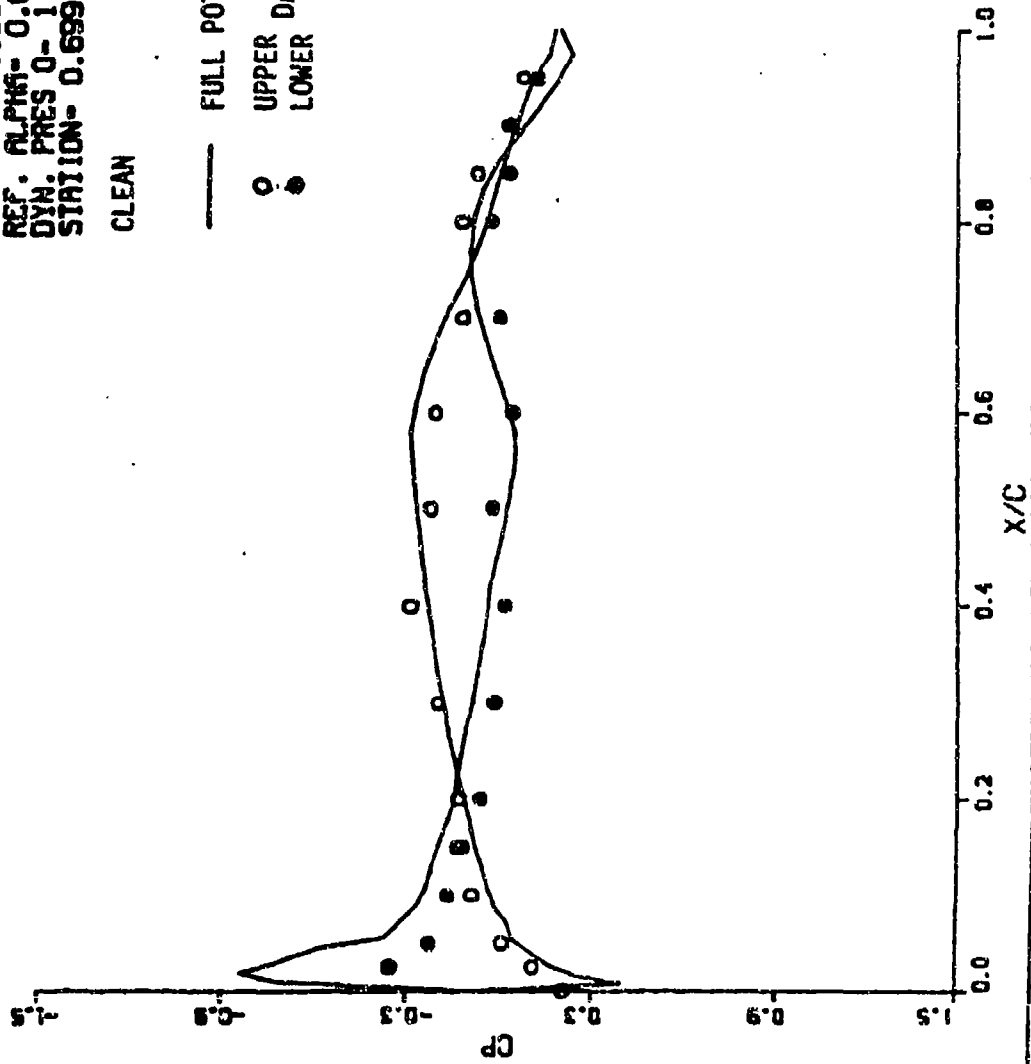


Figure A-3. Pressure Distributions of Flexible AFW Wind Tunnel Model Wing.

# PRESSURE PROFILE

MACH NO- 0.900  
REF. ALPHA- 0.048  
DYN. PRES 0- 1.740  
STATION- 0.811  
CLEAN

— FULL POTENTIAL

○ UPPER DATA  
● LOWER DATA

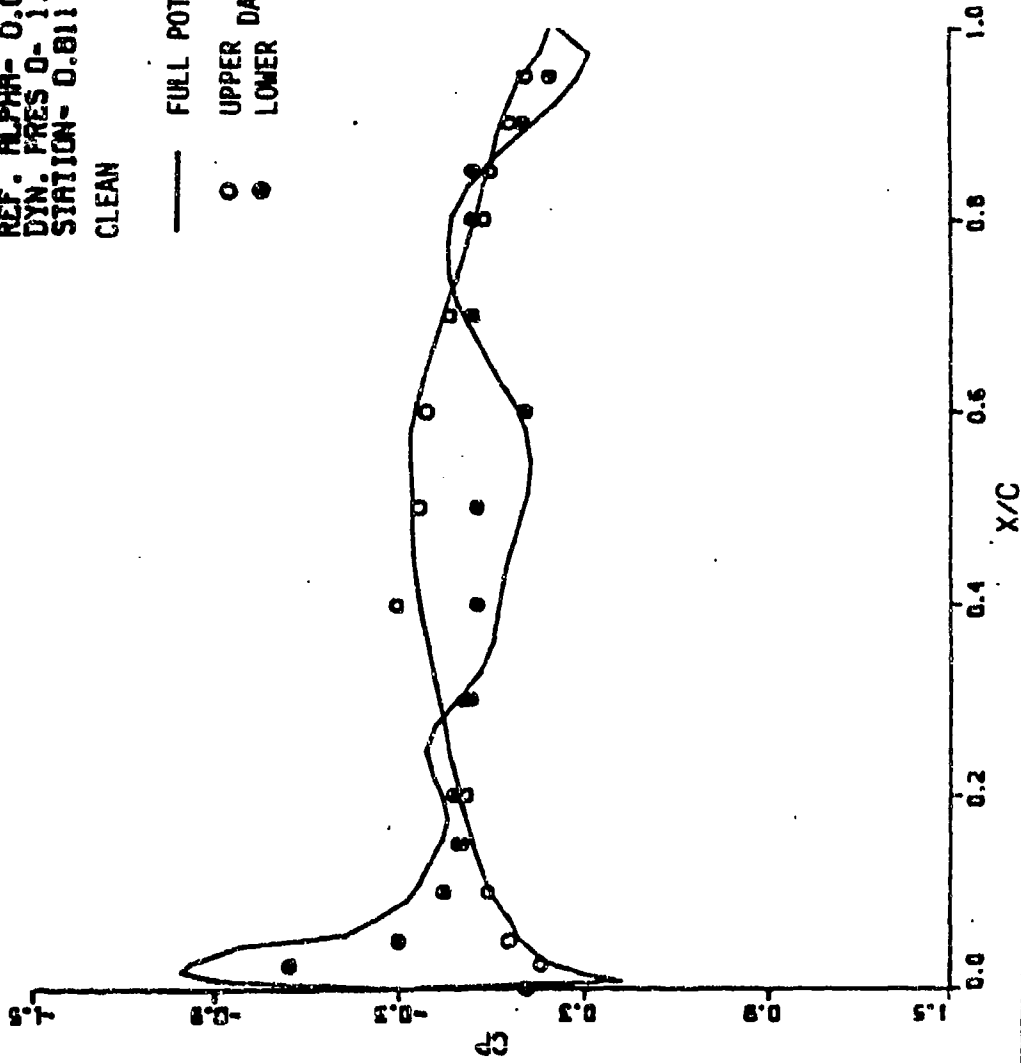


Figure A-4. Pressure Distributions of Flexible AFW Wind Tunnel Model Wing.

# PRESSURE PROFILE

MACH NO- 0.900  
REF. ALPHA- 0.048  
DYN. PRES 0- 1.740  
STATION- 0.924  
CLEAN

— FULL POTENTIAL  
○ UPPER DATA  
● LOWER DATA

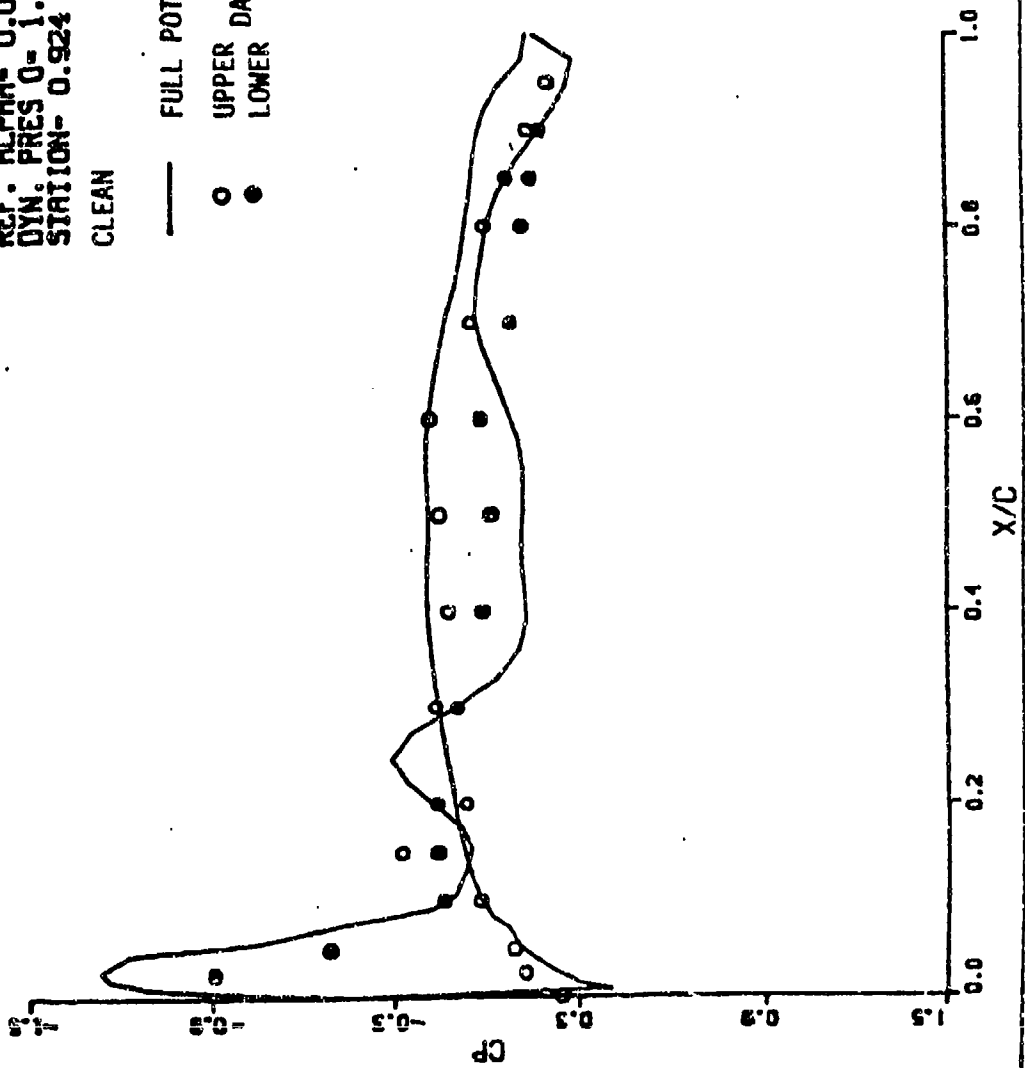


Figure A-5. Pressure Distributions of Flexible AFW Wind Tunnel Model Wing.

# PRESSURE PROFILE

MACH NO- 0.900  
REF. ALPHA- 0.048  
DYN. PRES 0- 1.054  
STATION- 0.436  
 $\delta_{TEO} = 5.0$

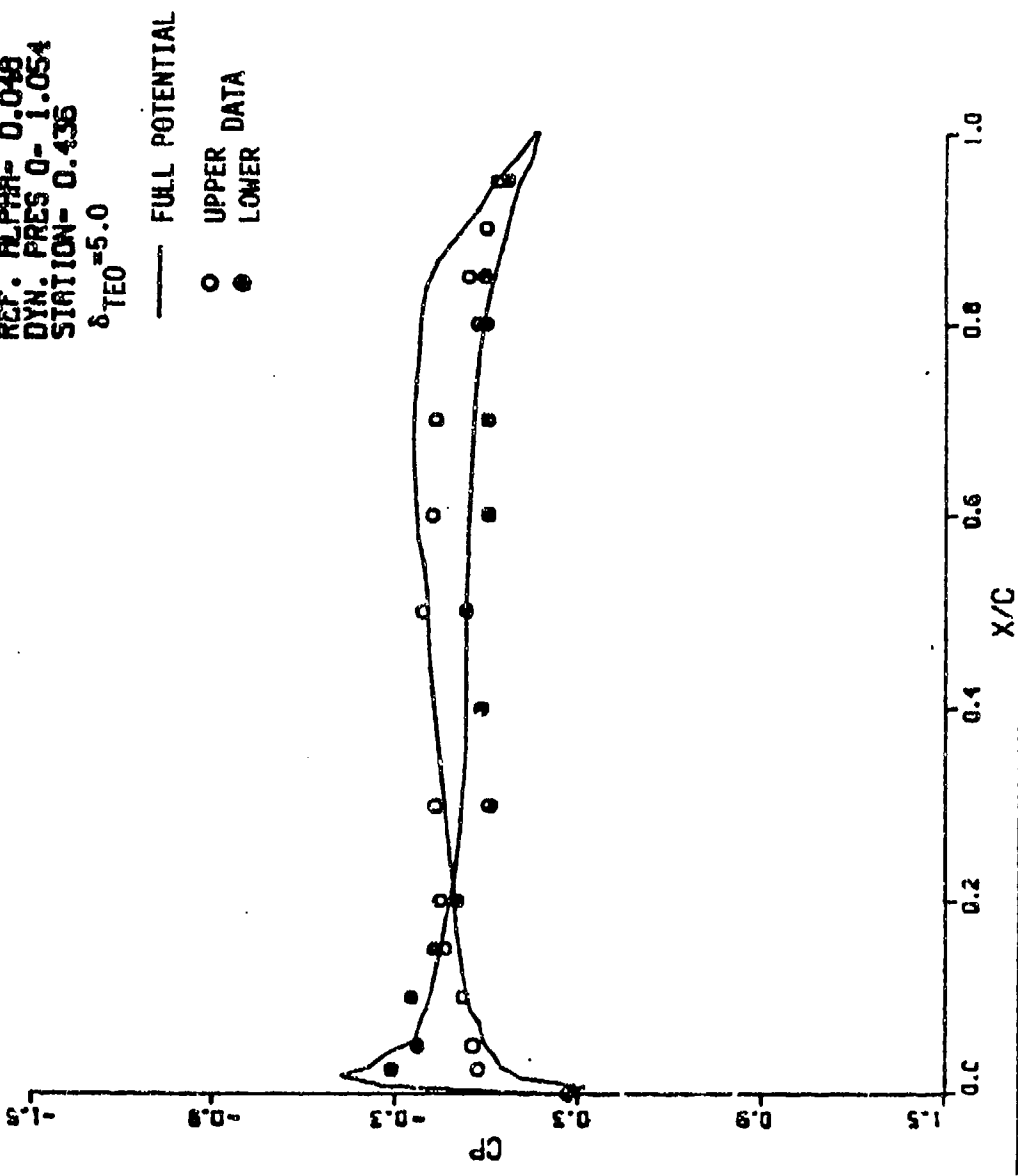


Figure A-6. Pressure Distributions of Flexible AFW Wind Tunnel Model Wing.

# PRESSURE PROFILE

MACH NO- 0.900  
REF. ALPHA- 0.048  
DYN. PRES 0- 1.054  
STATION- 0.587

$\delta_{TE0} = 5.0$

— FULL POTENTIAL  
○ UPPER DATA  
● LOWER DATA

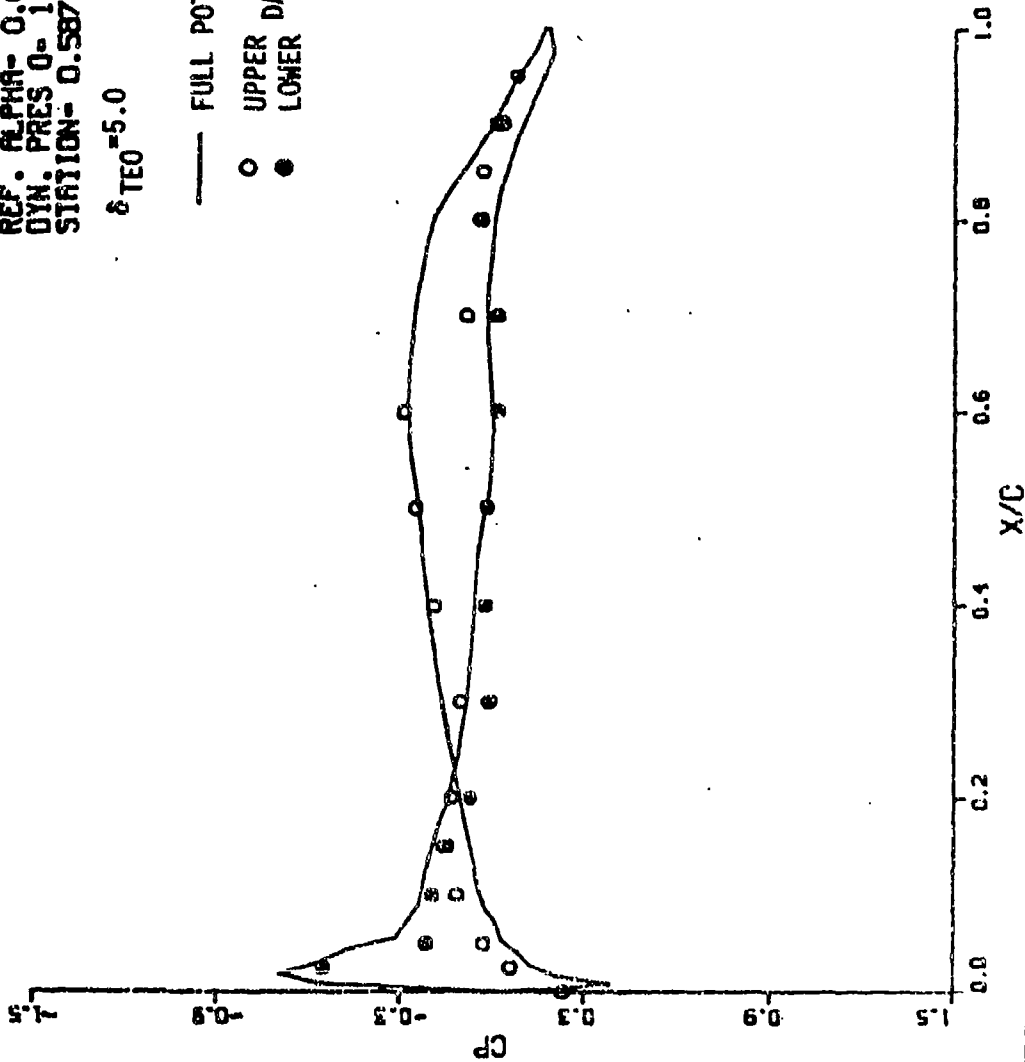


Figure A-7. Pressure Distributions of Flexible AFW Wind Tunnel Model Wing.

# PRESSURE PROFILE

MACH NO- 0.900  
REF. ALPHA- 0.048  
DYN. PRES 0- 1.054  
STATION- 0.699

$\delta_{TEO} = 5.0$

— FULL POTENTIAL

○ UPPER DATA  
● LOWER

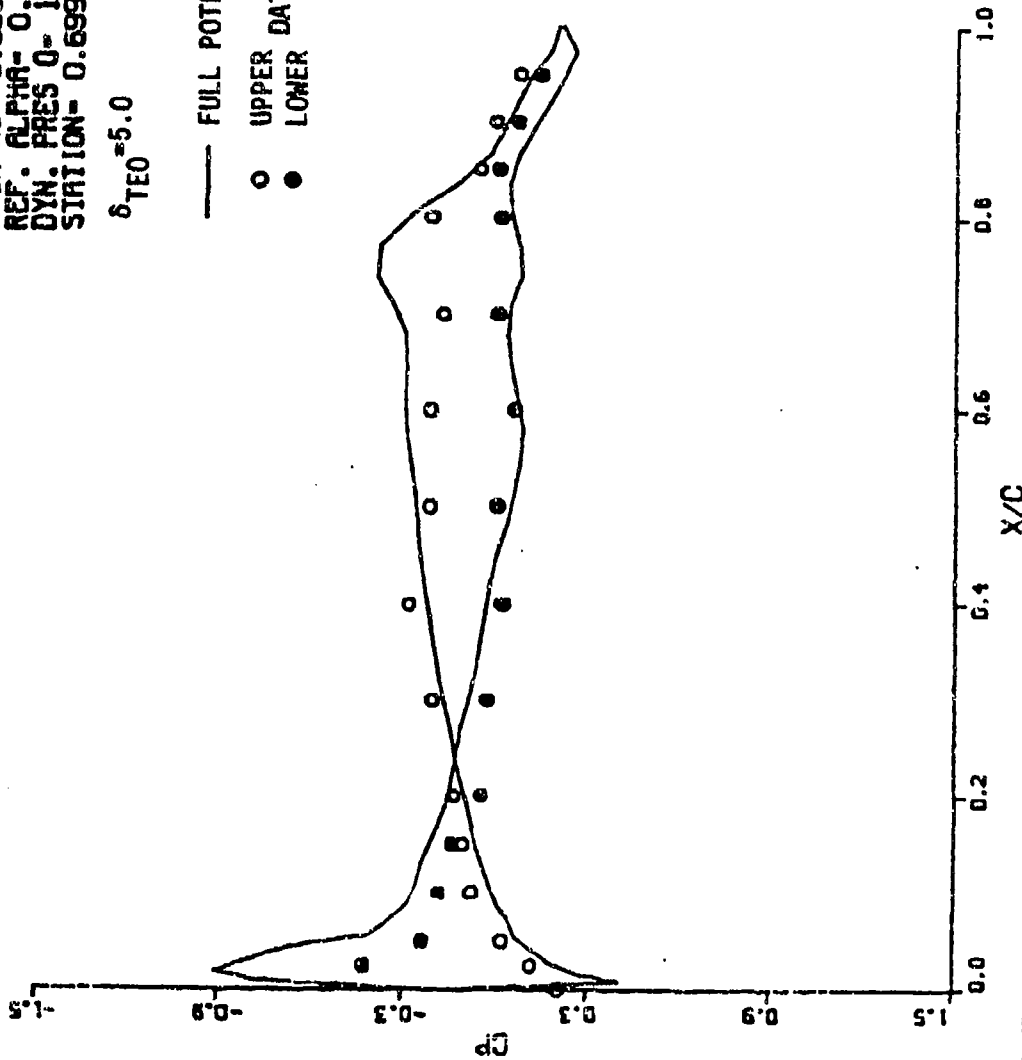


Figure A-8. Pressure Distributions of Flexible AFW Wind Tunnel Model Wing.

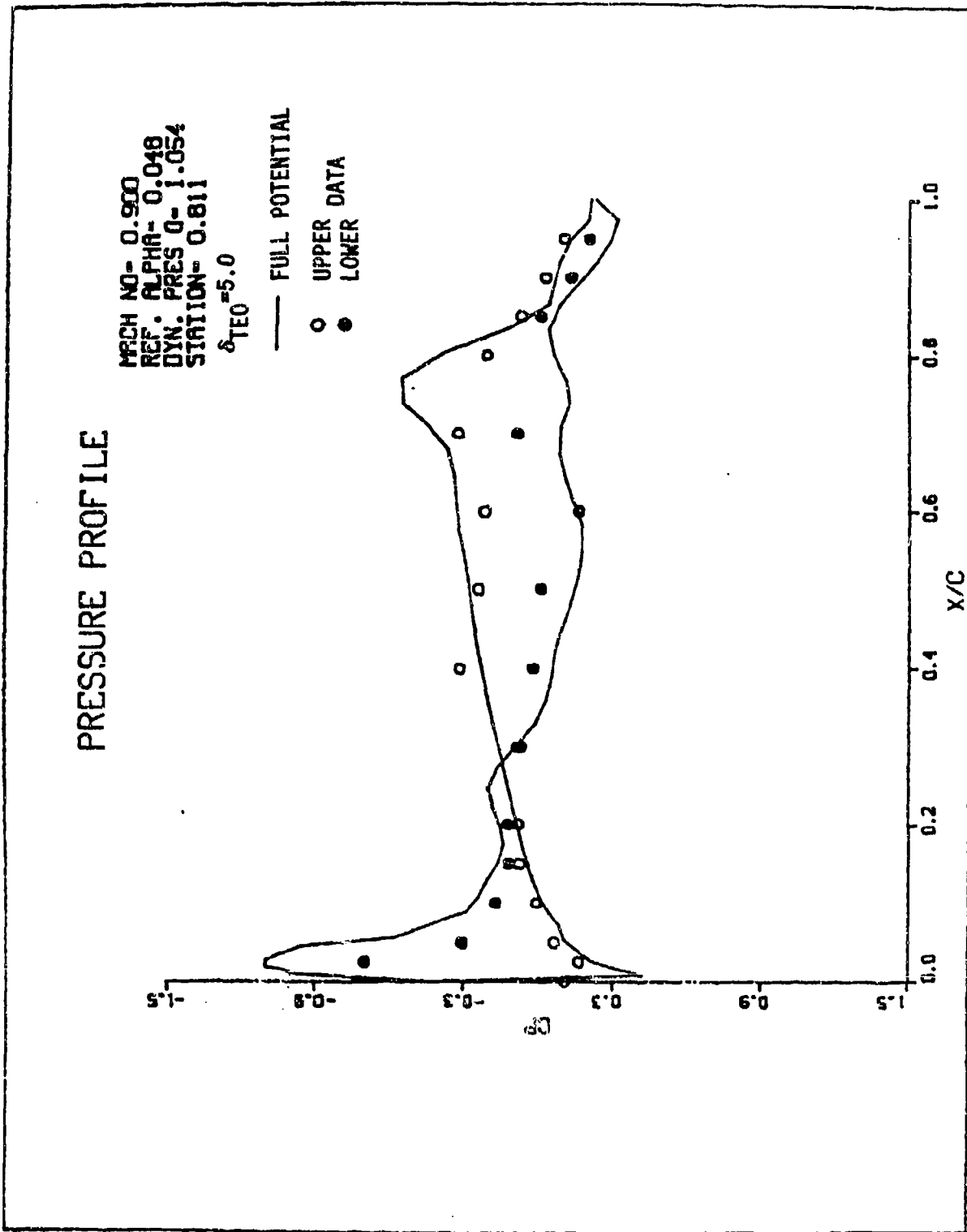


Figure A-9. Pressure Distributions of Flexible AFW Wind Tunnel Model Wing.

# PRESSURE PROFILE

MACH NO- 0.900  
REF. ALPHA- 0.048  
DYN. PRES 0- 1.054  
STATION- 0.924

$\delta_{TEO} = 5.0$

— FULL POTENTIAL

○ UPPER DATA

● LOWER DATA

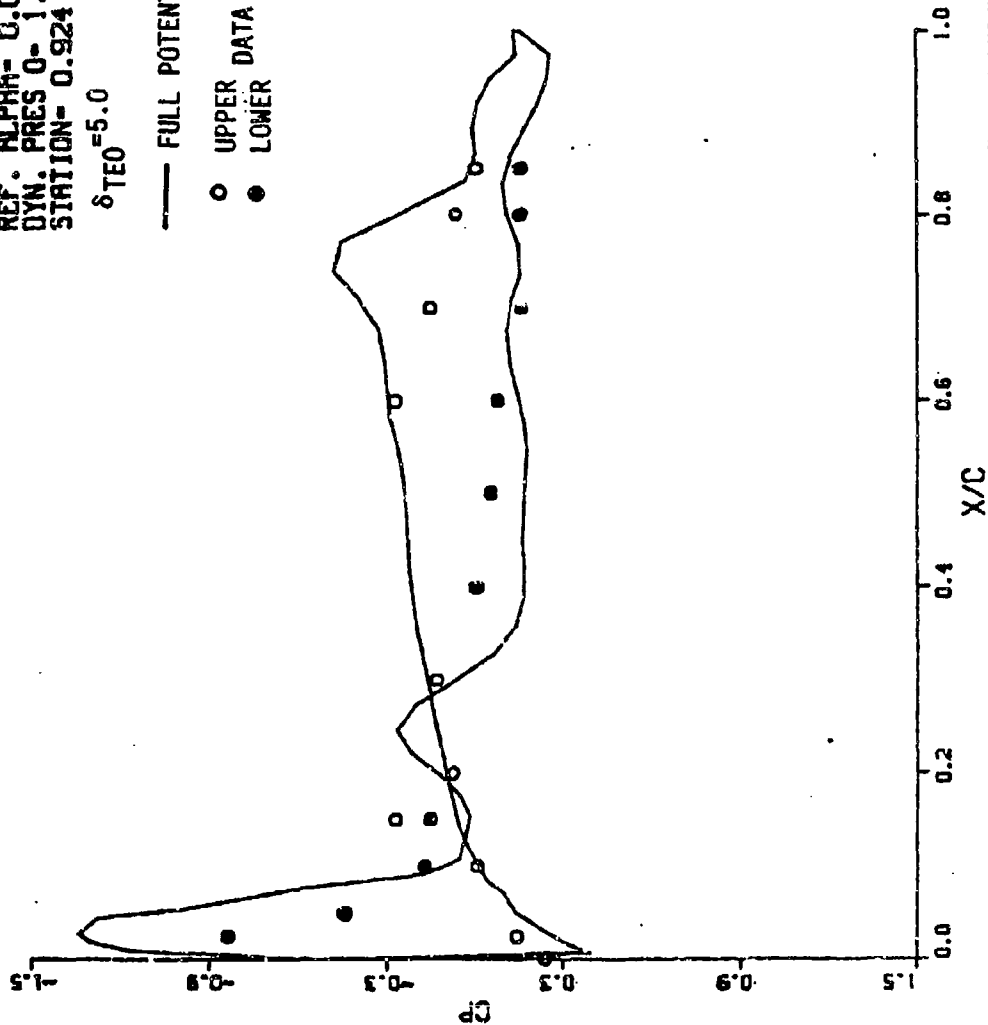


Figure A-10. Pressure Distributions of Flexible AFW Wind Tunnel Model Wing.

# PRESSURE PROFILE

MACH NO- 0.900  
 REF. ALPHA- 0.048  
 DYN. PRES 0- 1.054  
 STATION- 0.436  
 $\delta_{TEO}^* = -5.0$

— FULL POTENTIAL

○ UPPER DATA  
● LOWER DATA

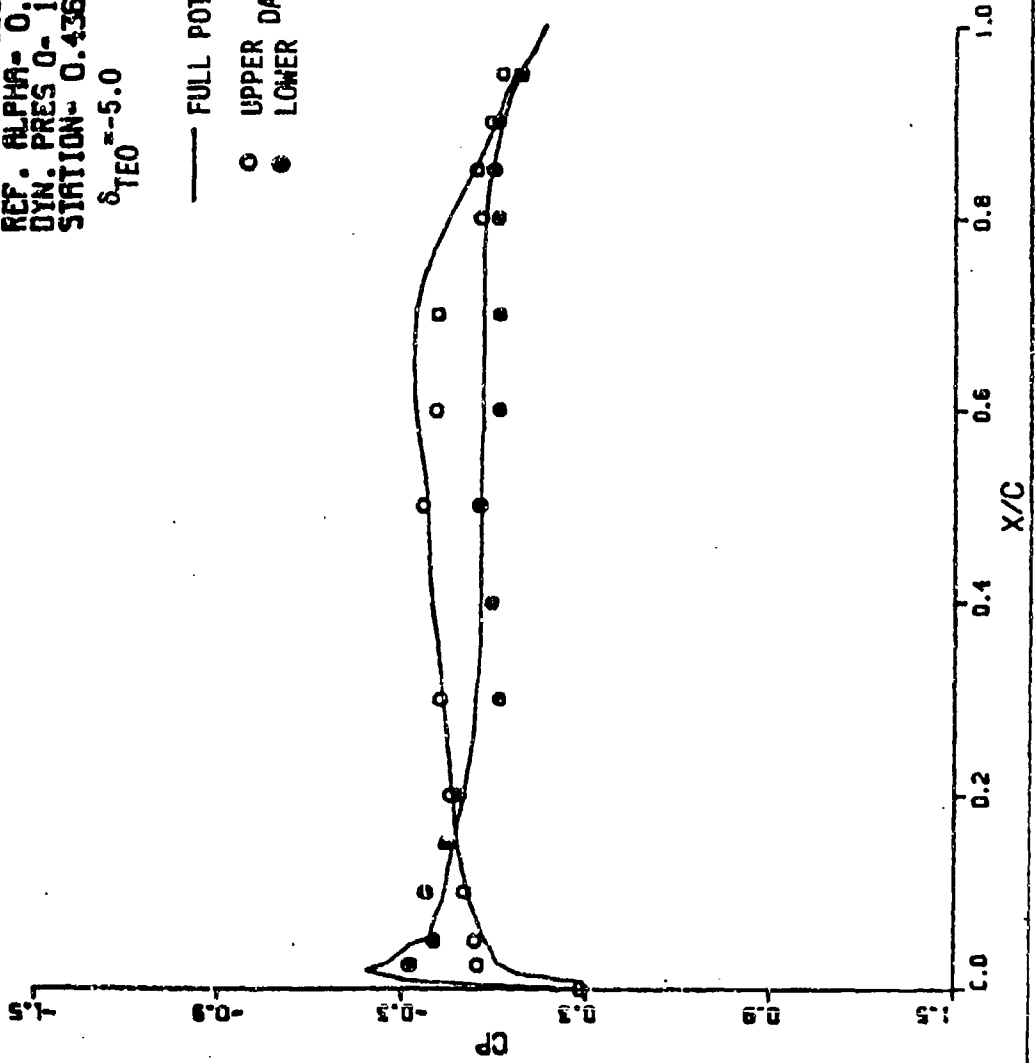


Figure A-11. Pressure Distributions of Flexil e AFW Wind Tunnel Model Wing

# PRESSURE PROFILE

MACH NO- 0.900  
REF. ALPHA- 0.048  
CYN. PRES Q- 1.054  
STATION- 0.587

$\delta_{TEO} = -5.0$

— FULL POTENTIAL

○ UPPER DATA  
● LOWER DATA

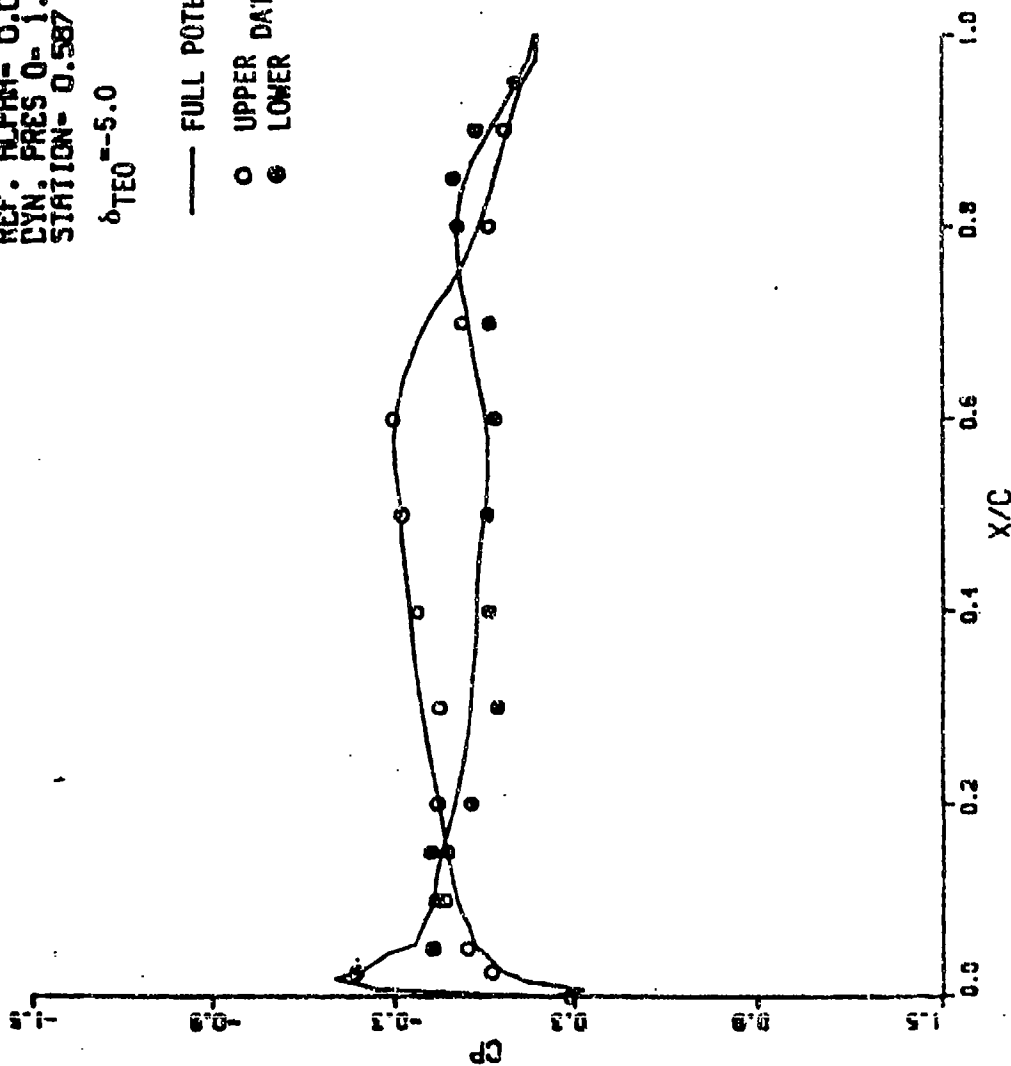


Figure A-12. Pressure Distributions of Flexible AFW Wind Tunnel Model Wing.

# PRESSURE PROFILE

MOCH NO- 0.900  
REF. ALPHA- 0.048  
DYN. PRES Q- 1.054  
STATION- 0.698

$\delta_{TEO} = -5.0$

— FULL POTENTIAL

○ UPPER DATA

● LOWER DATA

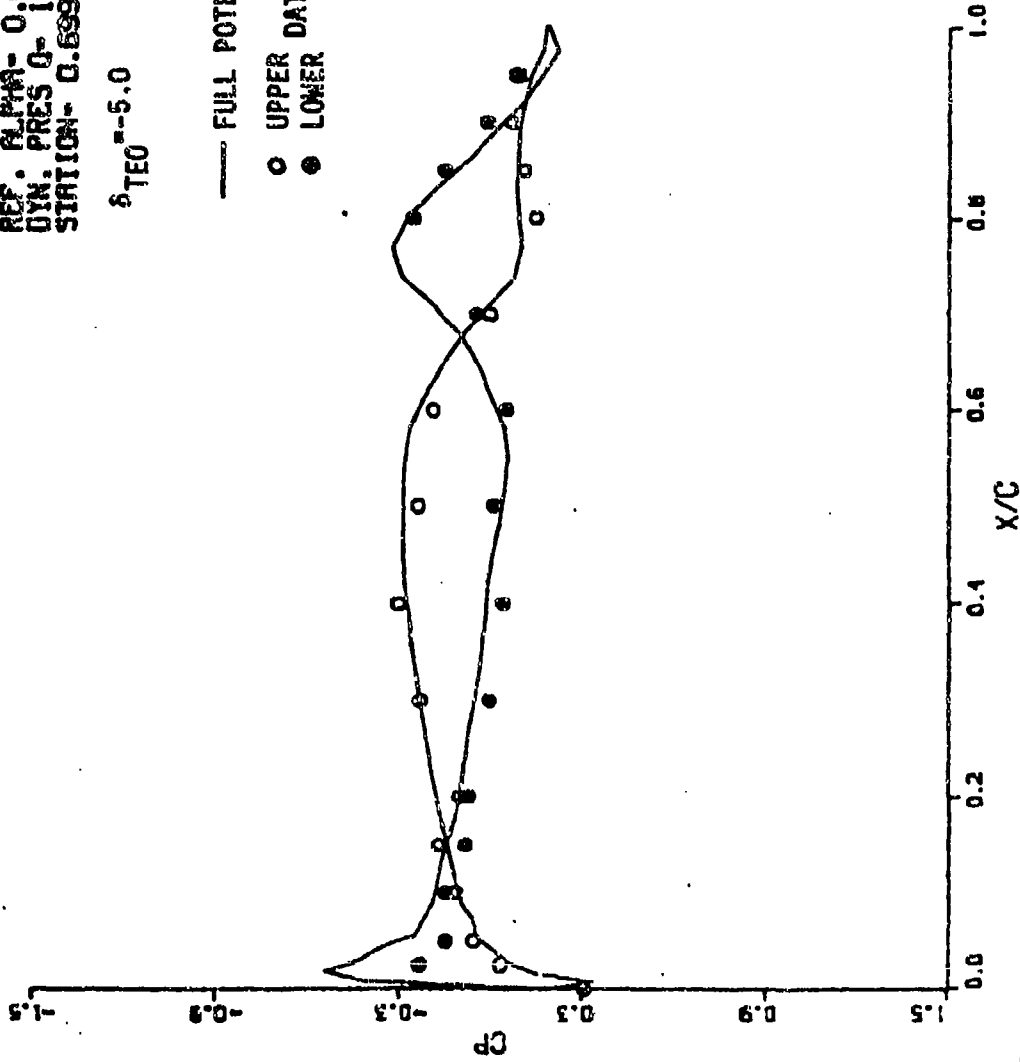


Figure A-13. Pressure Distributions of Flexible AFW Wind Tunnel Model Wing.

# PRESSURE PROFILE

MACH NO- 0.900  
REF. ALPHA- 0.048  
DYN. PRES 0- 1.054  
STATION- 0.811  
 $\delta_{TEO} = -5.0$

— FULL POTENTIAL

○ UPPER DATA  
● LOWER DATA

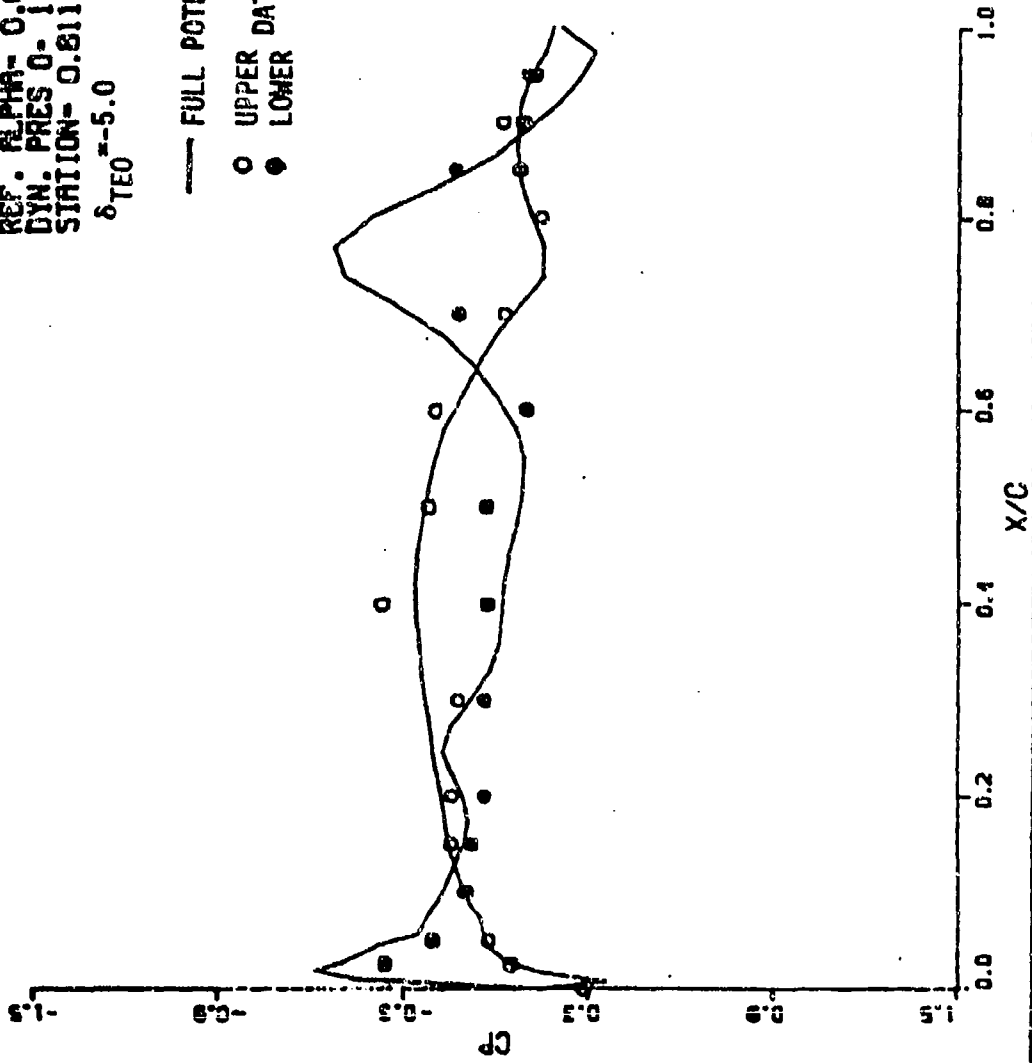


Figure A-14. Pressure Distributions of Flexible AFW Wind Tunnel Model Wing.

# PRESSURE PROFILE

MACH NO- 0.900  
REF. ALPHA- 0.048  
DYN. PRES 0- 1.054  
STATION- 0.924

$\delta_{TEO} = -5.0$

— FULL POTENTIAL  
○ UPPER DATA  
● LOWER DATA

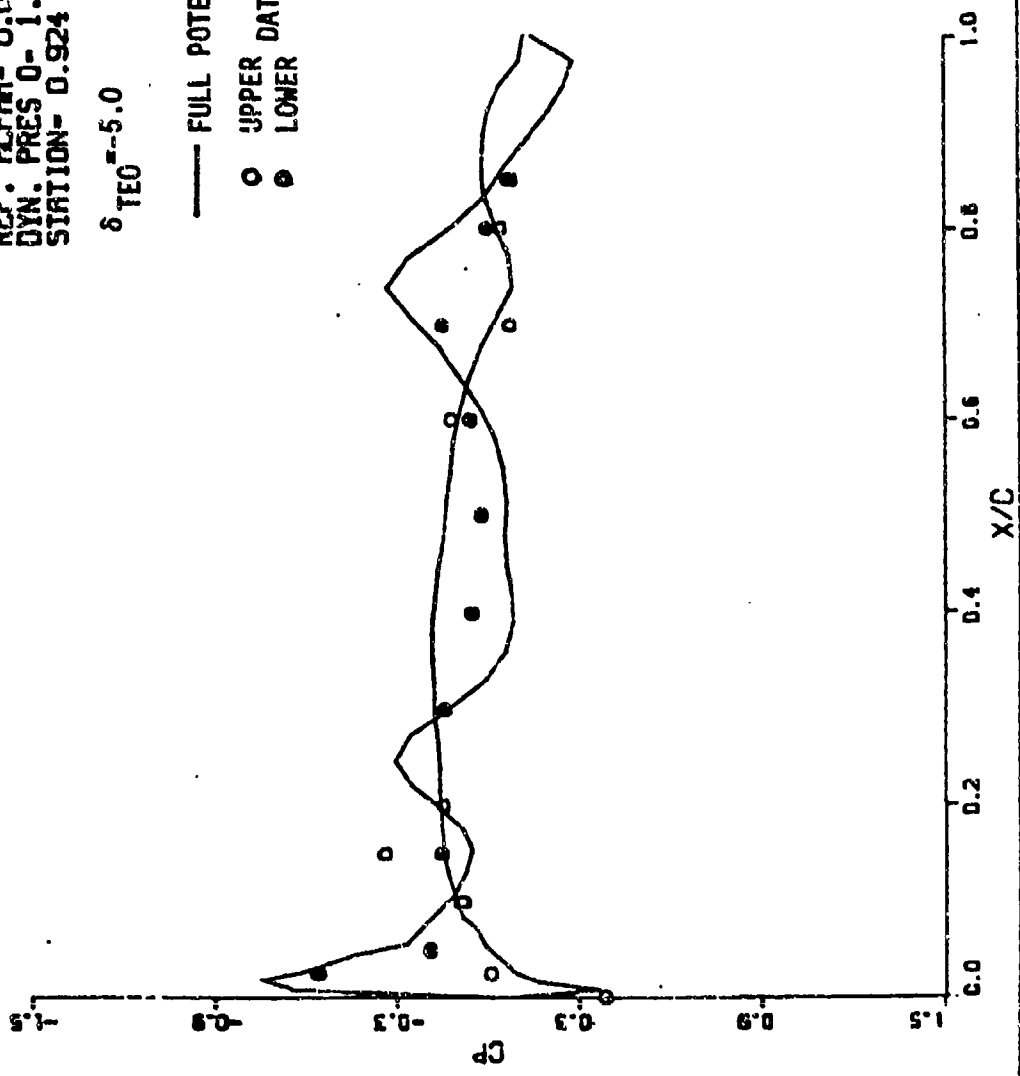


Figure A-15. Pressure Distributions of Flexible AFW Wind Tunnel Model Wing.

# PRESSURE PROFILE

MACH NO- 1.150  
REF. ALPHA- 1.660  
DYN. PRES 0- 2.350  
STATION- 0.436

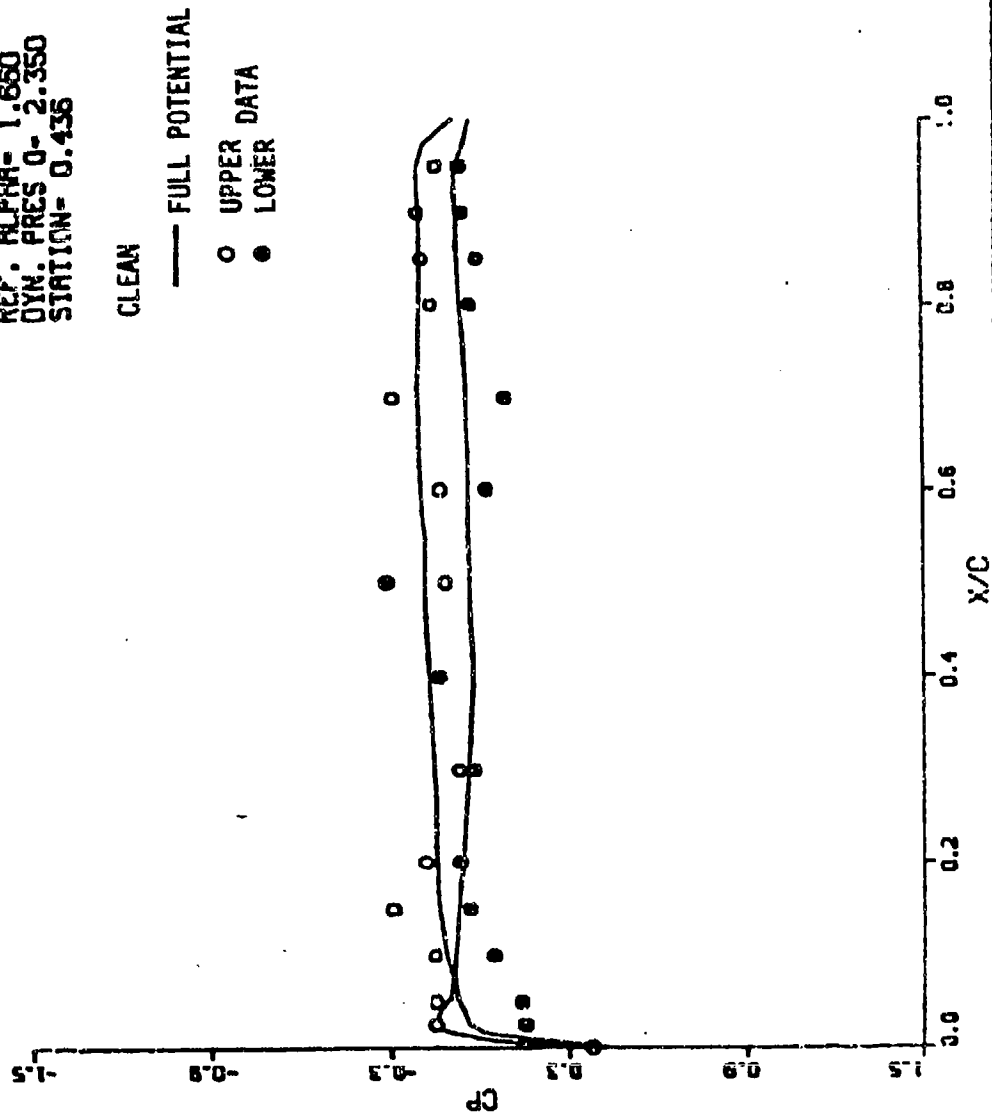


Figure A-16. Pressure Distributions of Flexible AFW Wind Tunnel Model Wing.

# PRESSURE PROFILE

MACH NO- 1.150  
REF. ALPHA- 1.680  
DYN. PRES 0- 2.350  
STATION- 0.587

CLEAN

— FULL POTENTIAL

○ UPPER DATA

● LOWER DATA

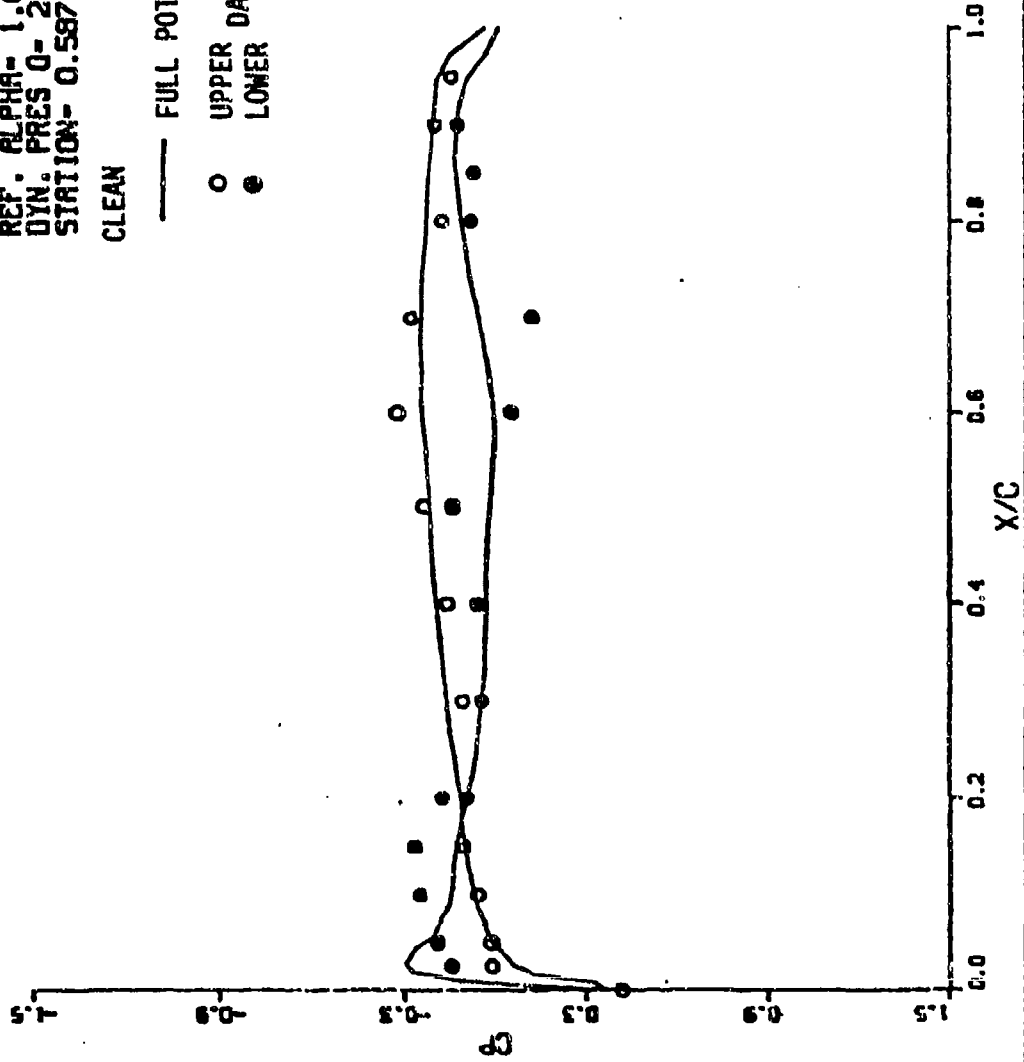


Figure A-17. Pressure Distributions of Flexible AFM Wind Tunnel Model Wing.

# PRESSURE PROFILE

MACH NO- 1.150  
REF. ALPHA- 1.660  
DYN. PRES Q- 2.350  
STATION- G.689

CLEAN

— FULL POTENTIAL

○ UPPER DATA  
● LOWER DATA

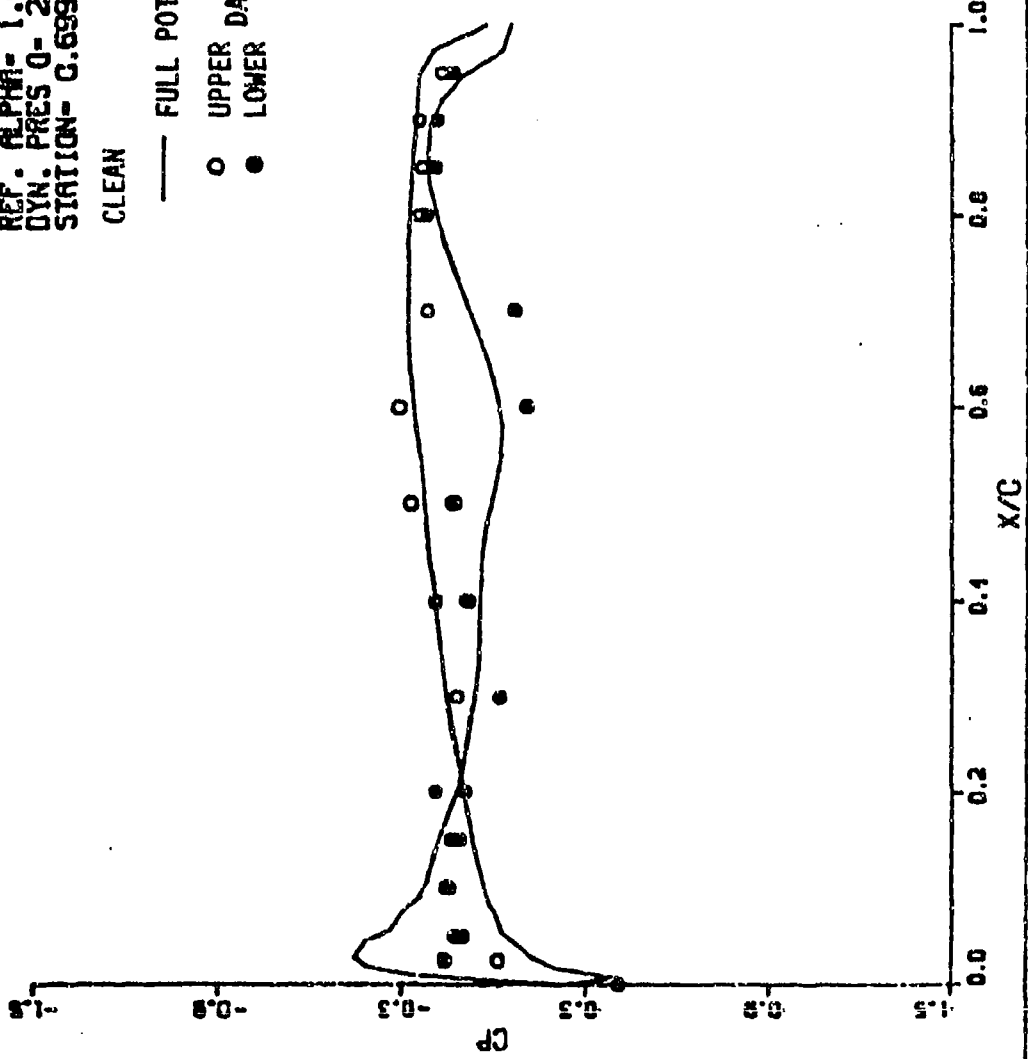


Figure A-18. Pressure Distributions of Flexible AFN Wind Tunnel Model Wing.

# PRESSURE PROFILE

MACH NO- 1.150  
REF. ALPHA- 1.680  
DYN. PRES Q- 2.350  
STATION- 0.811

CLEAN

— FULL POTENTIAL

○ UPPER DATA

● LOWER DATA

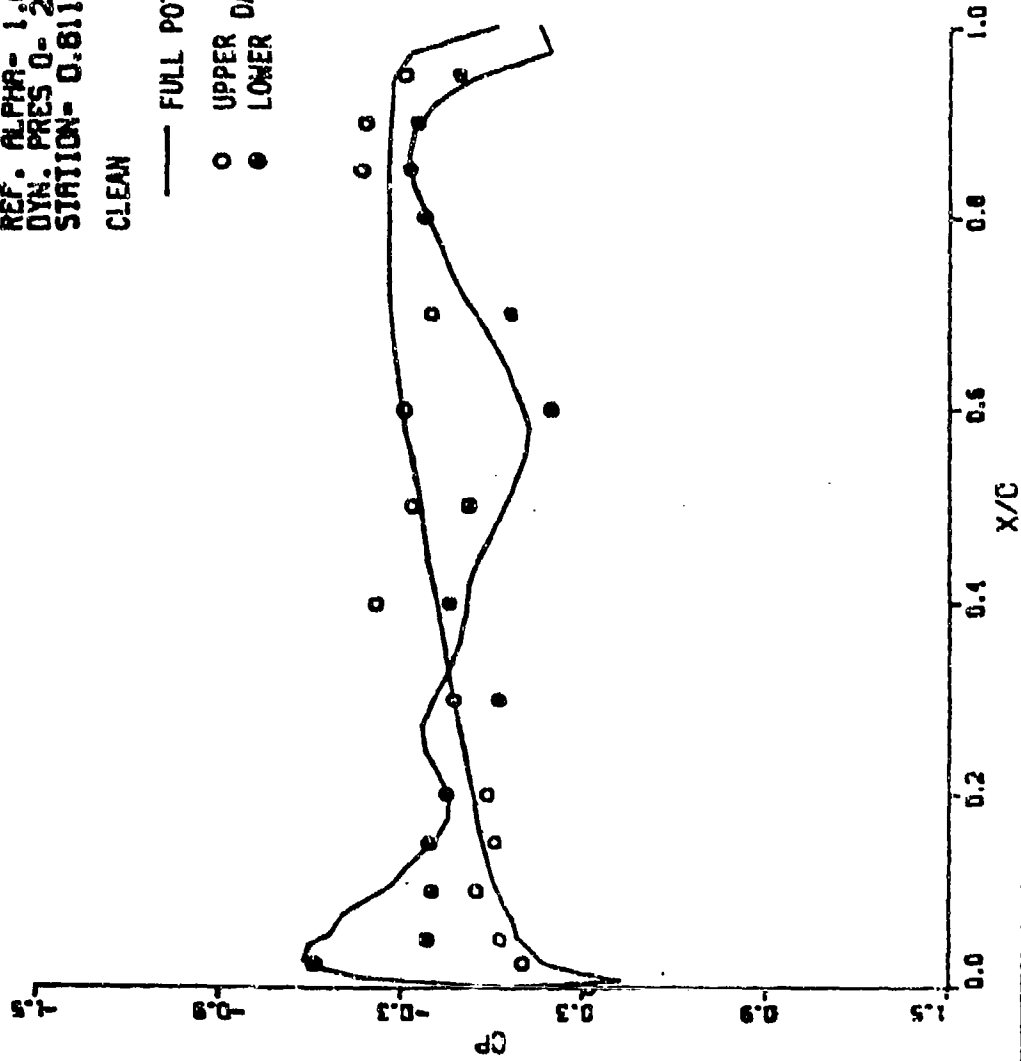


Figure A-19. Pressure Distributions of Flexible AFW Wind Tunnel Model Wing.

# PRESSURE PROFILE

MACH NO- 1.150  
 REF. ALPHA- 1.650  
 DYN. PRES Q- 2.350  
 STATION- 0.924

CLEAN

— FULL POTENTIAL

○ UPPER DATA

● LOWER DATA

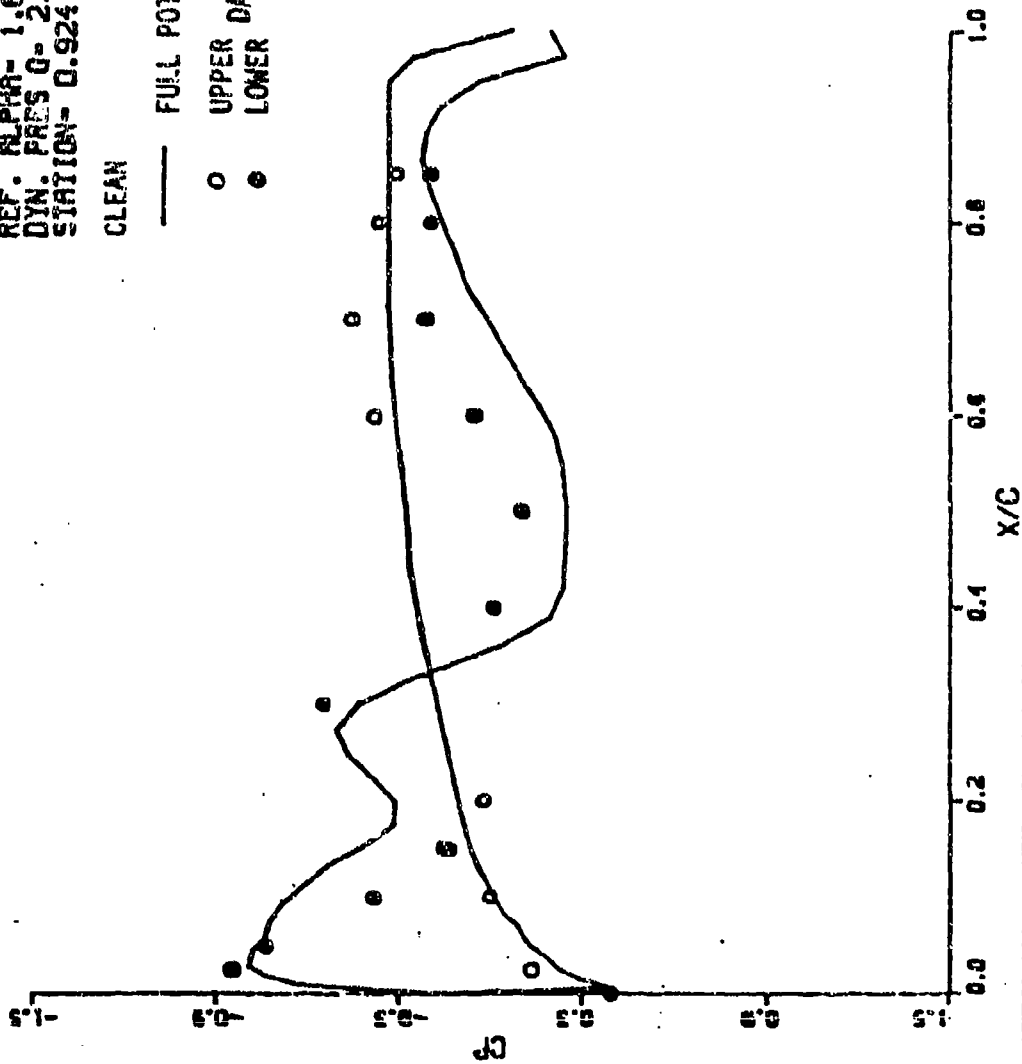


Figure A-20. Pressure Distributions of Flexible AFW Wind Tunnel Model Wing.

# PRESSURE PROFILE

MACH NO- 1.150  
REF. ALPHA- 1.660  
DYN. PRES 0- 2.350  
STATION- 0.436

$\delta_{TEO} = 2.0$

— FULL POTENTIAL

○ UPPER DATA  
● LOWER DATA

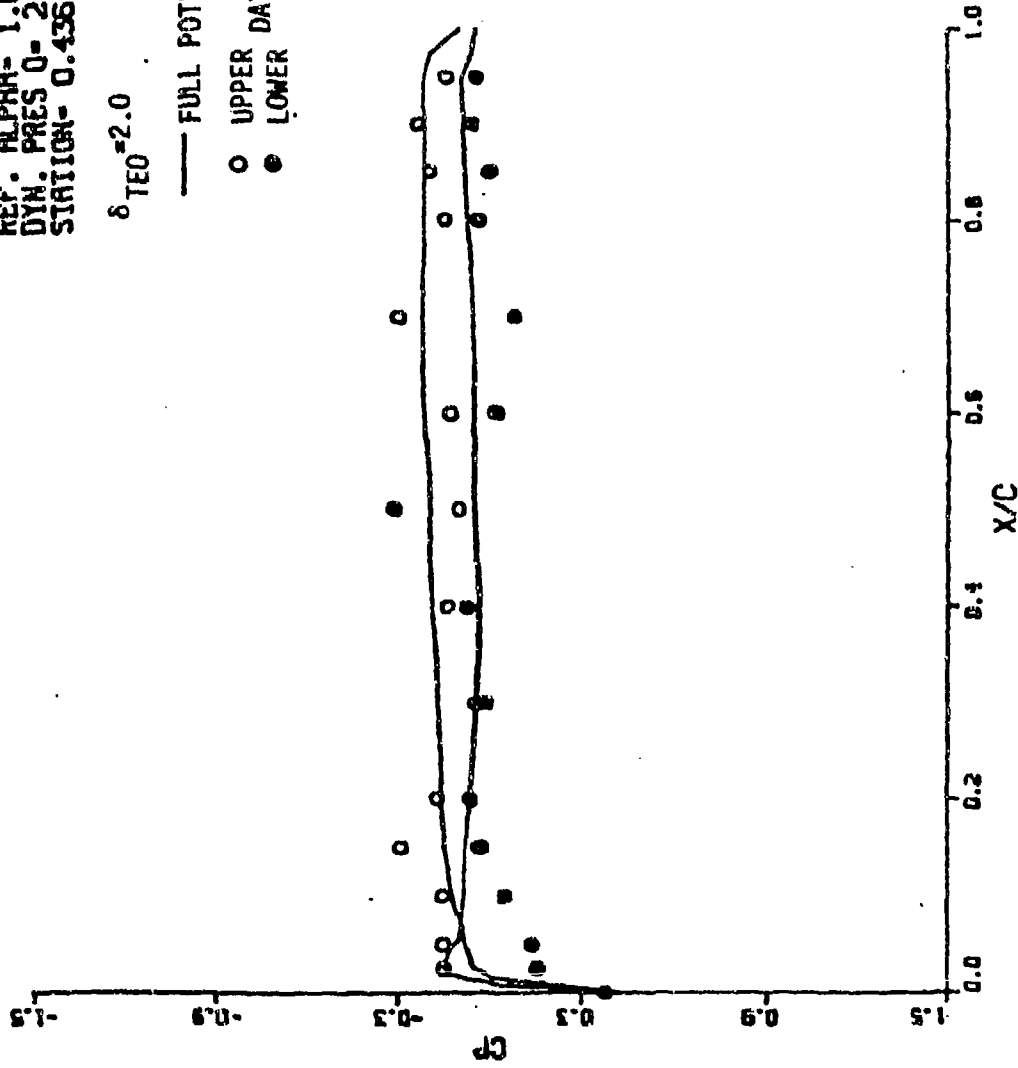


Figure A-21. Pressure Distributions of Flexible AFM Wind Tunnel Model Wing.

# PRESSURE PROFILE

MACH NO- 1.150  
REF. ALPHA- 1.660  
DYN. PRES 0- 2.350  
STATION- 0.587

$\delta_{TEO} = -2.0$

— FULL POTENTIAL

○ UPPER DATA  
● LOWER DATA

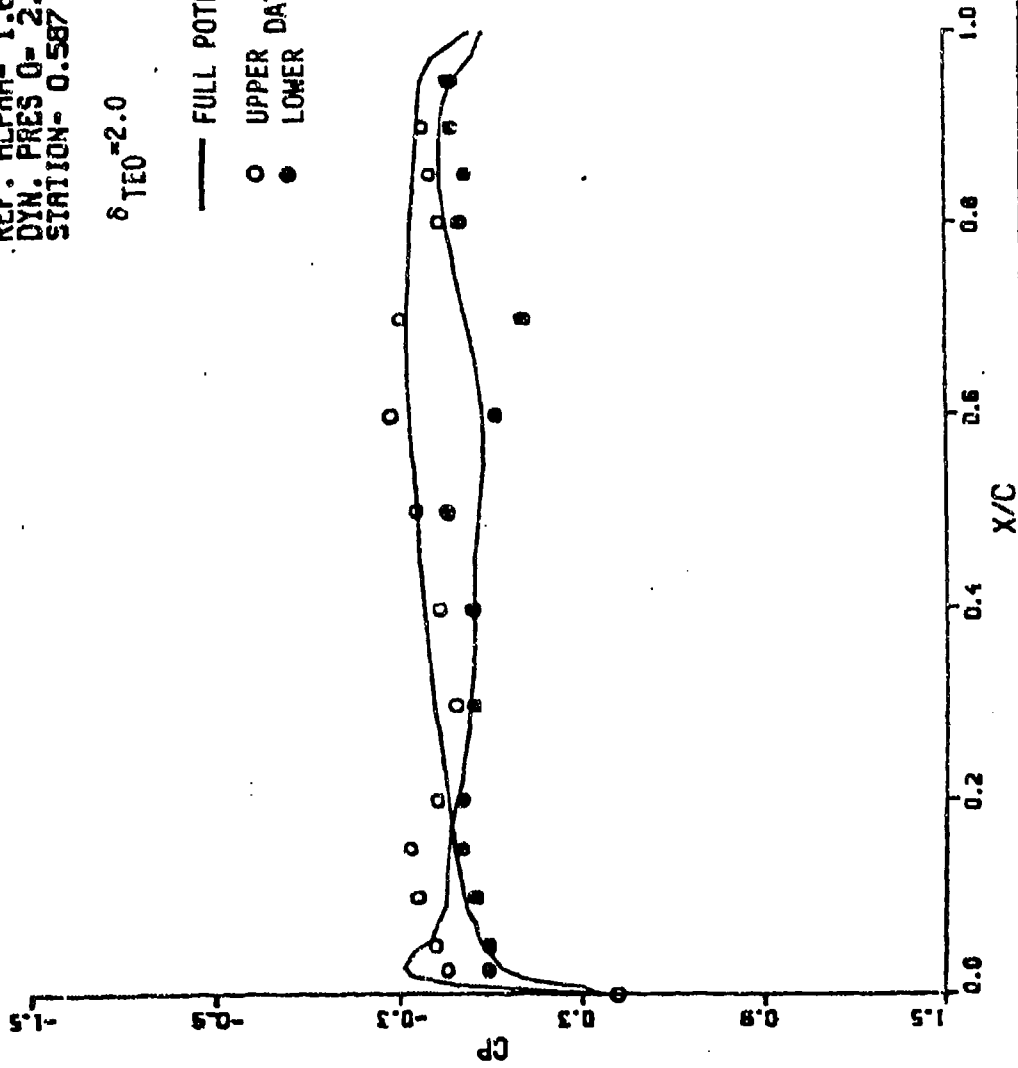


Figure A-22. Pressure Distributions of Flexible AFW Wind Tunnel Model Wing.

# PRESSURE PROFILE

MACH NO- 1.150  
REF. ALPHA- 1.660  
DYN. PRES 0- 2.350  
STATION- 0.699  
 $\delta_{TEO} = 2.0$

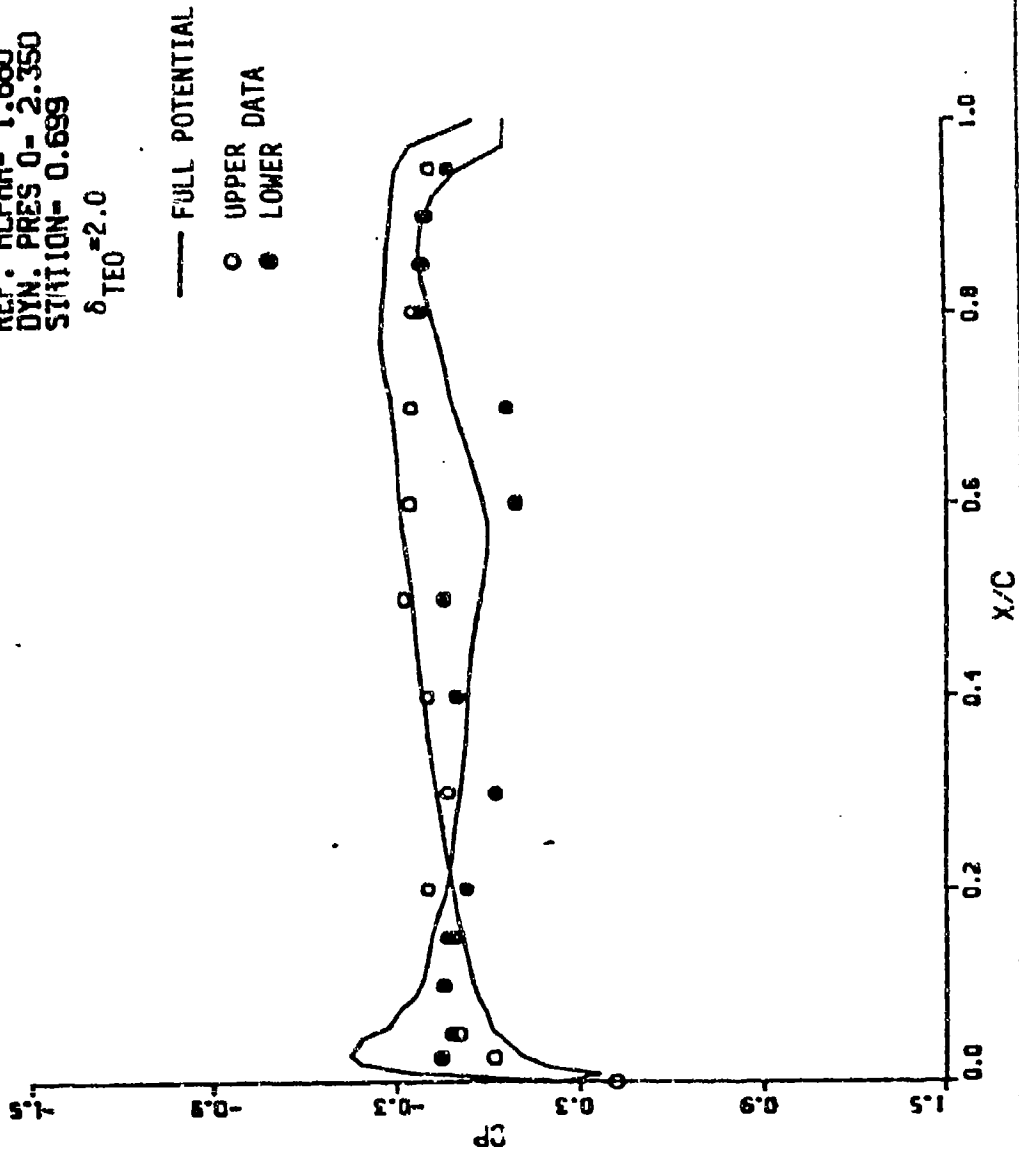


Figure A-23. Pressure Distributions of Flexible AFW Wind Tunnel Model Wing.

# PRESSURE PROFILE

MACH NO- 1.150  
REF. ALPHA- 1.660  
DYN. PRES 0- 2.350  
STATION- 0.811

$\delta_{TEO} = 2.0$

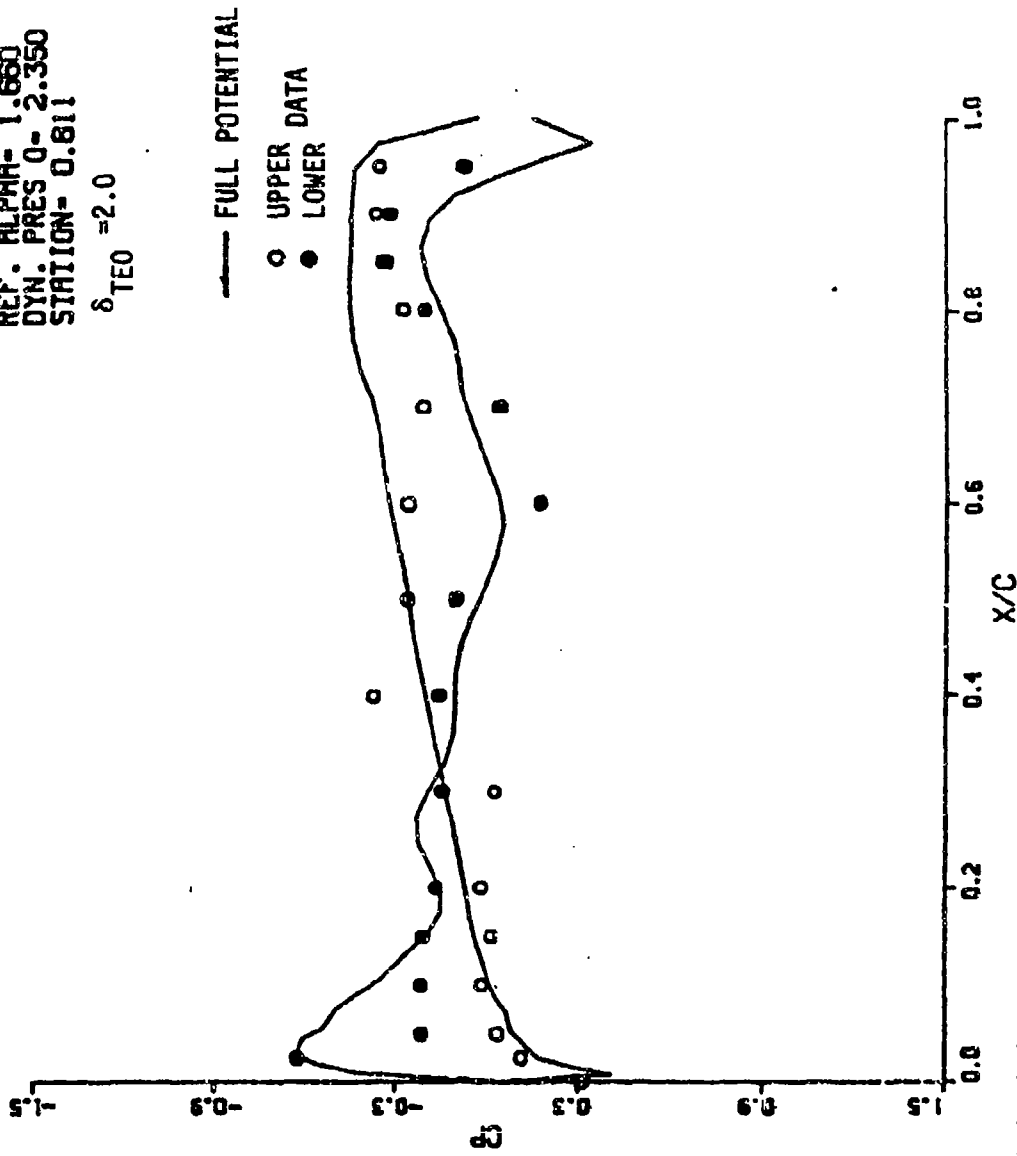


Figure A-24. Pressure Distributions of Flexible AFW Wind Tunnel Model Wing.

# PRESSURE PROFILE

MACH NO- 1.150  
REF. ALPHA- 1.880  
DYN. PRES Q- 2.350  
STATION- 0.924  
 $\delta_{TEO} = 2.0$

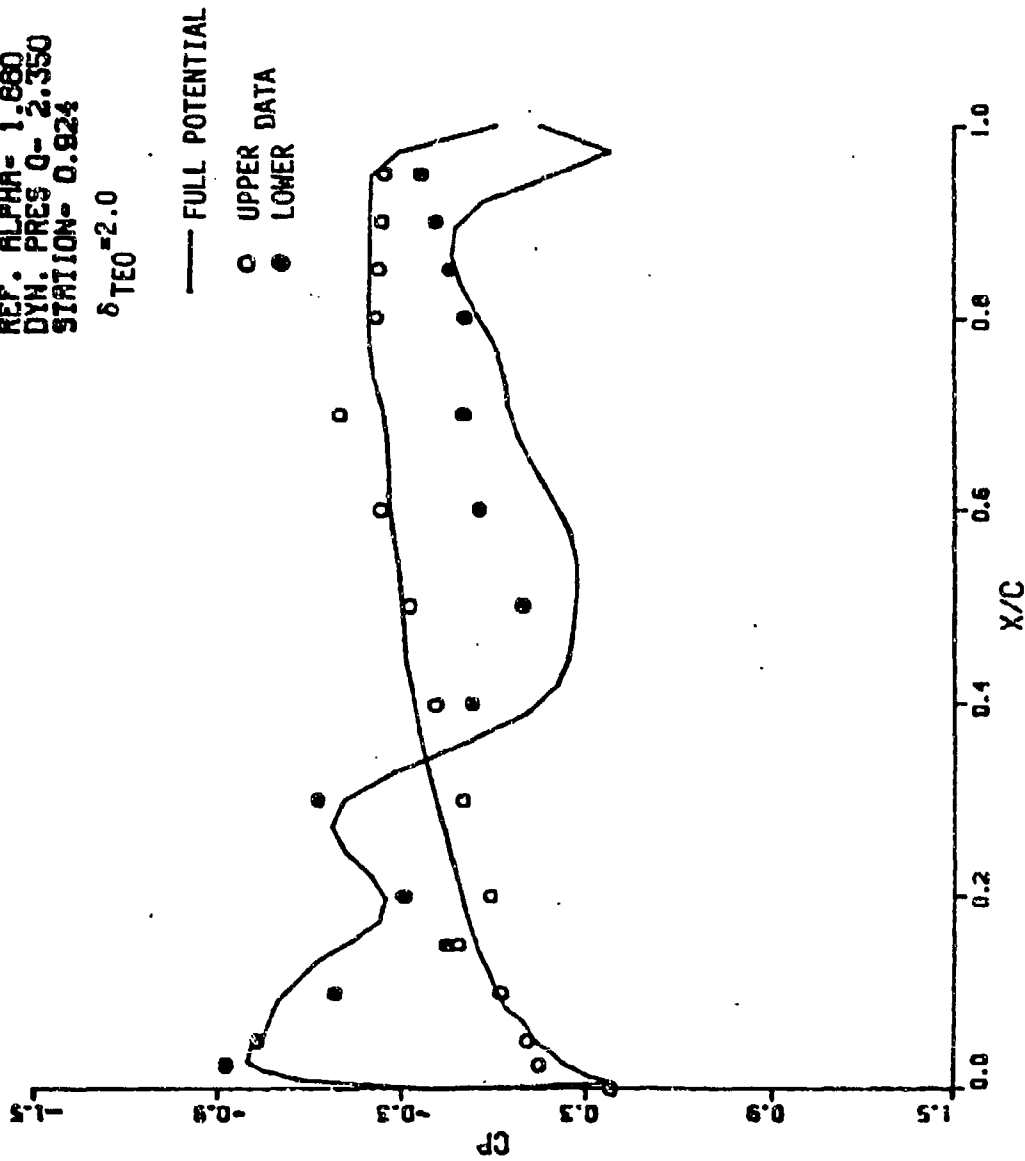


Figure A-25. Pressure Distributions of Flexible AFW Wind Tunnel Model Wing.

# PRESSURE PROFILE

MACH NO- 1.150  
REF. ALPHA- 1.680  
DYN. PRES Q- 2.350  
STATION- 0.436

$\delta_{TEO} = -2.0$

— FULL POTENTIAL

○ UPPER DATA  
● LOWER DATA

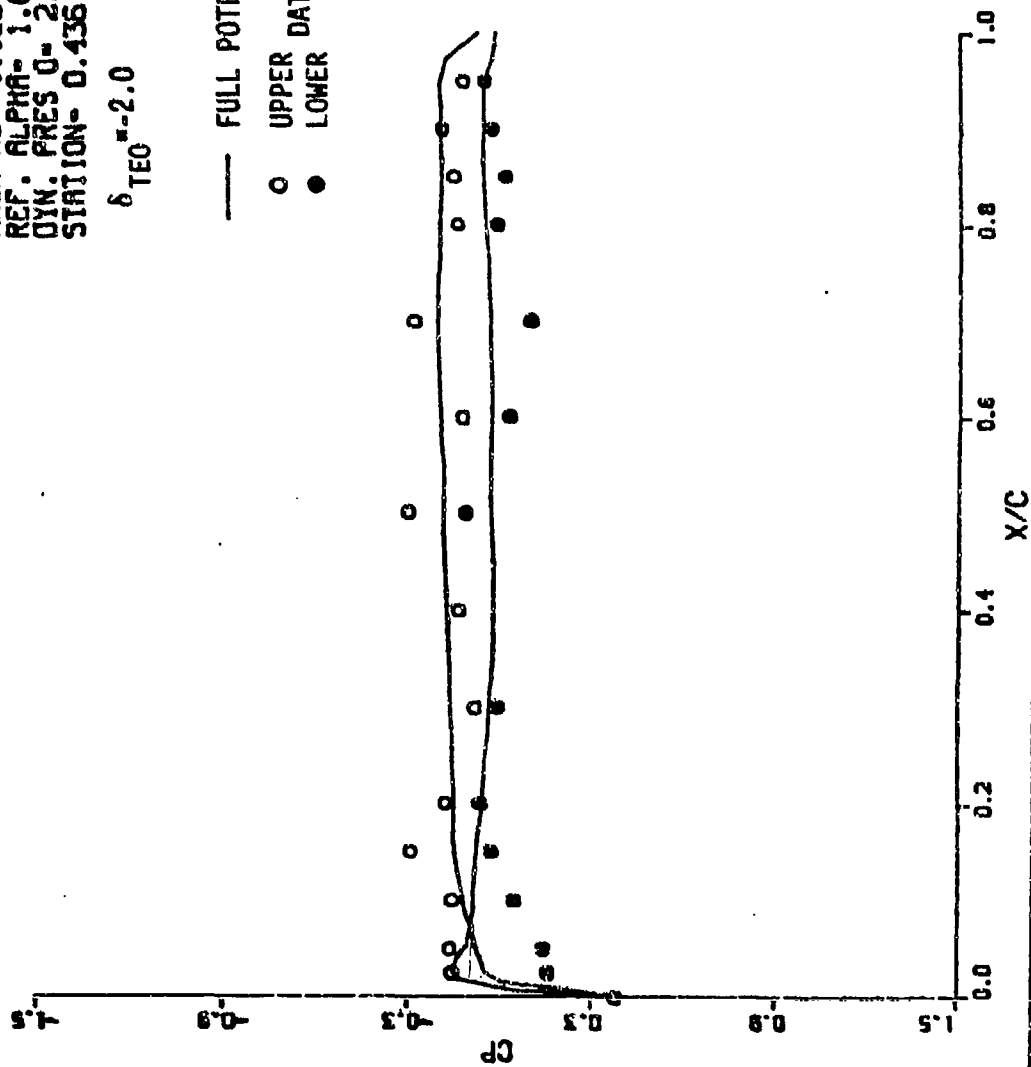


Figure A-26. Pressure Distributions of Flexible AFW Wind Tunnel Model Wing.

# PRESSURE PROFILE

MACH NO- 1.150  
REF. ALPHA- 1.660  
DYN. PRES 0- 2.350  
STATION- 0.587

$\delta_{TED} = -2.0$

— FULL POTENTIAL

○ UPPER DATA  
● LOWER DATA

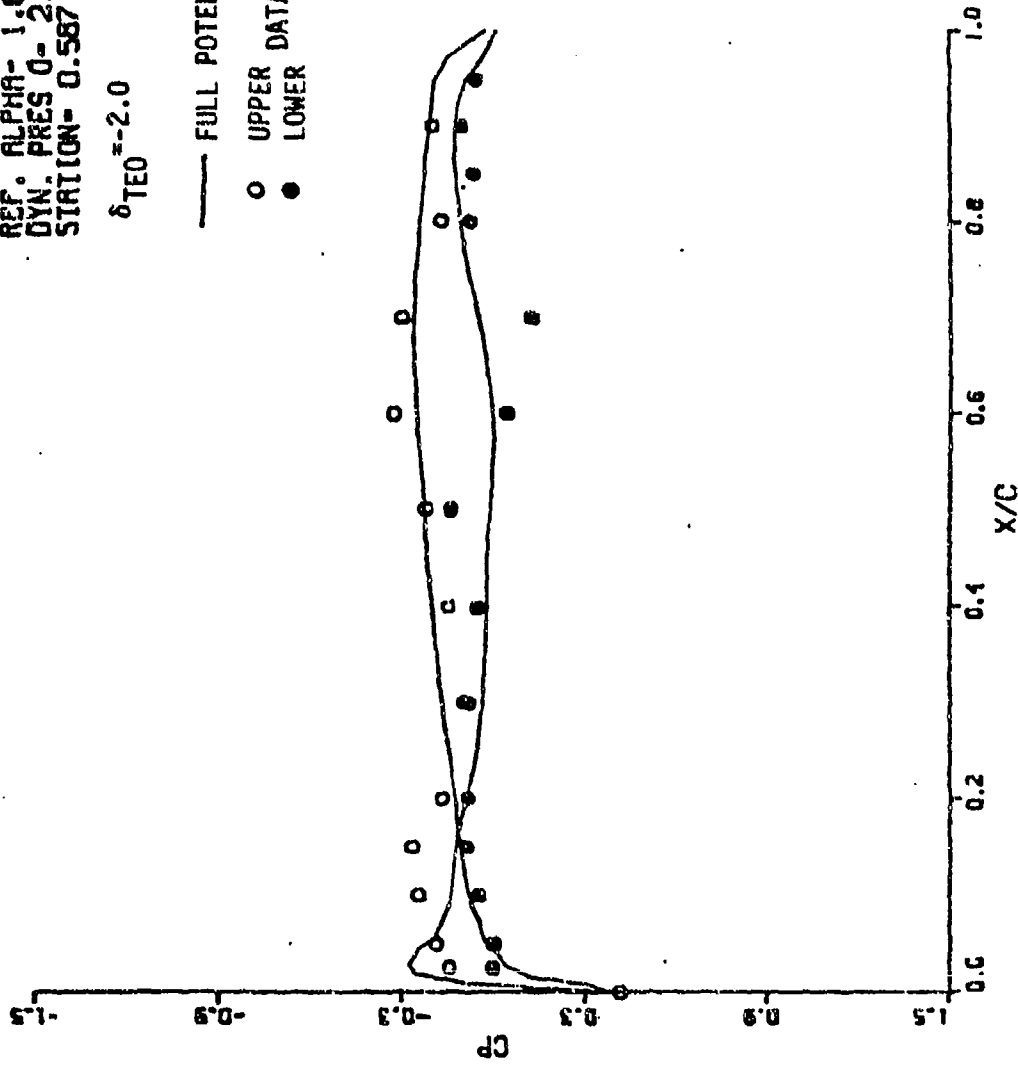


Figure A-27. Pressure Distributions of Flexible AFW Wind Tunnel Model Wing.

# PRESSURE PROFILE

MACH NO- 1.150  
 REF. ALPHA- 1.660  
 DYN. PRES 0- 2.350  
 STATION- 0.699

$\delta_{TEO} = -2.0$

— FULL POTENTIAL

○ UPPER DATA

● LOWER DATA

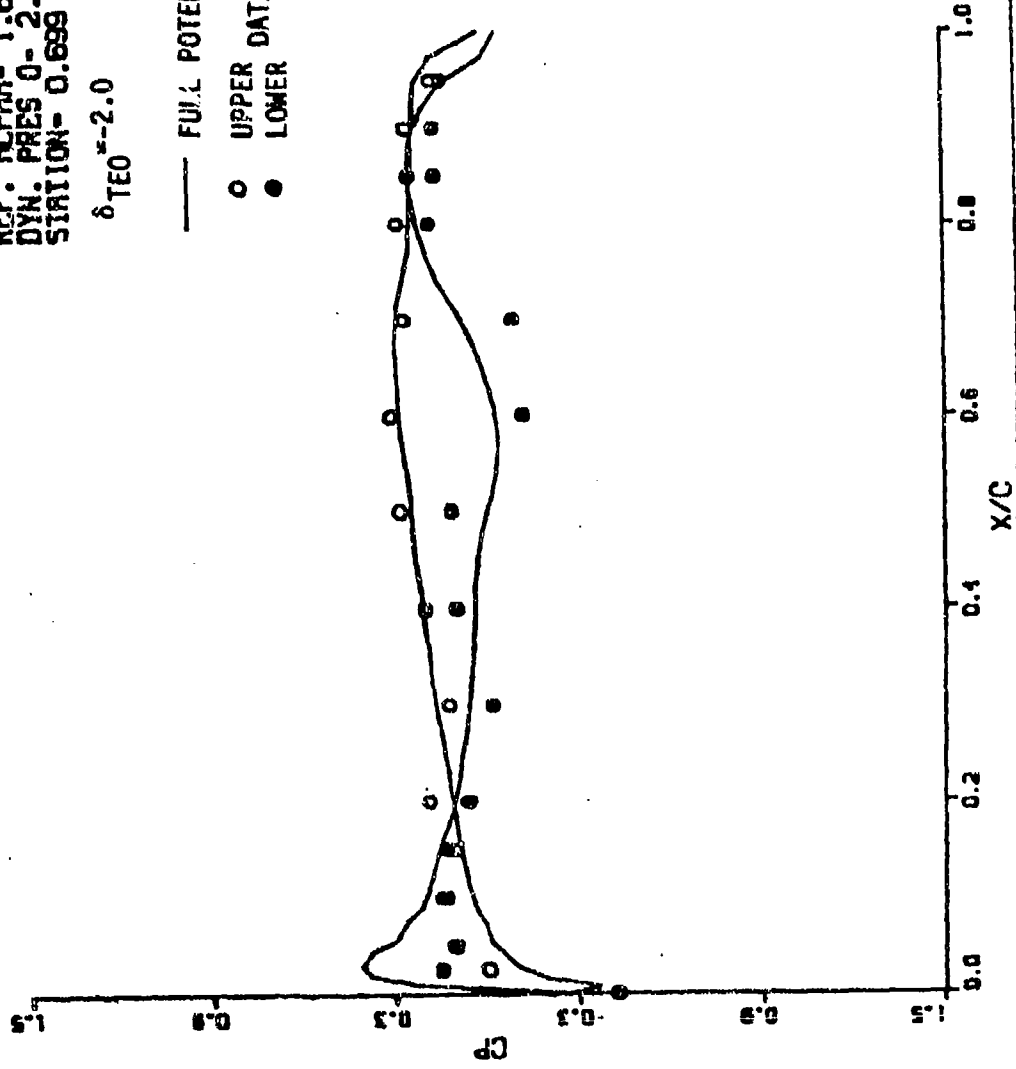


Figure A-28. Pressure Distributions of Flexible AFW Wind Tunnel Model Wing.

# PRESSURE PROFILE

MACH NO- 1.150  
 REF. ALPHA- 1.680  
 DYN. PRES Q- 2.350  
 STATION- 0.811

$\delta_{TEO} = -2.0$

— FULL POTENTIAL

○ UPPER DATA

● LOWER DATA

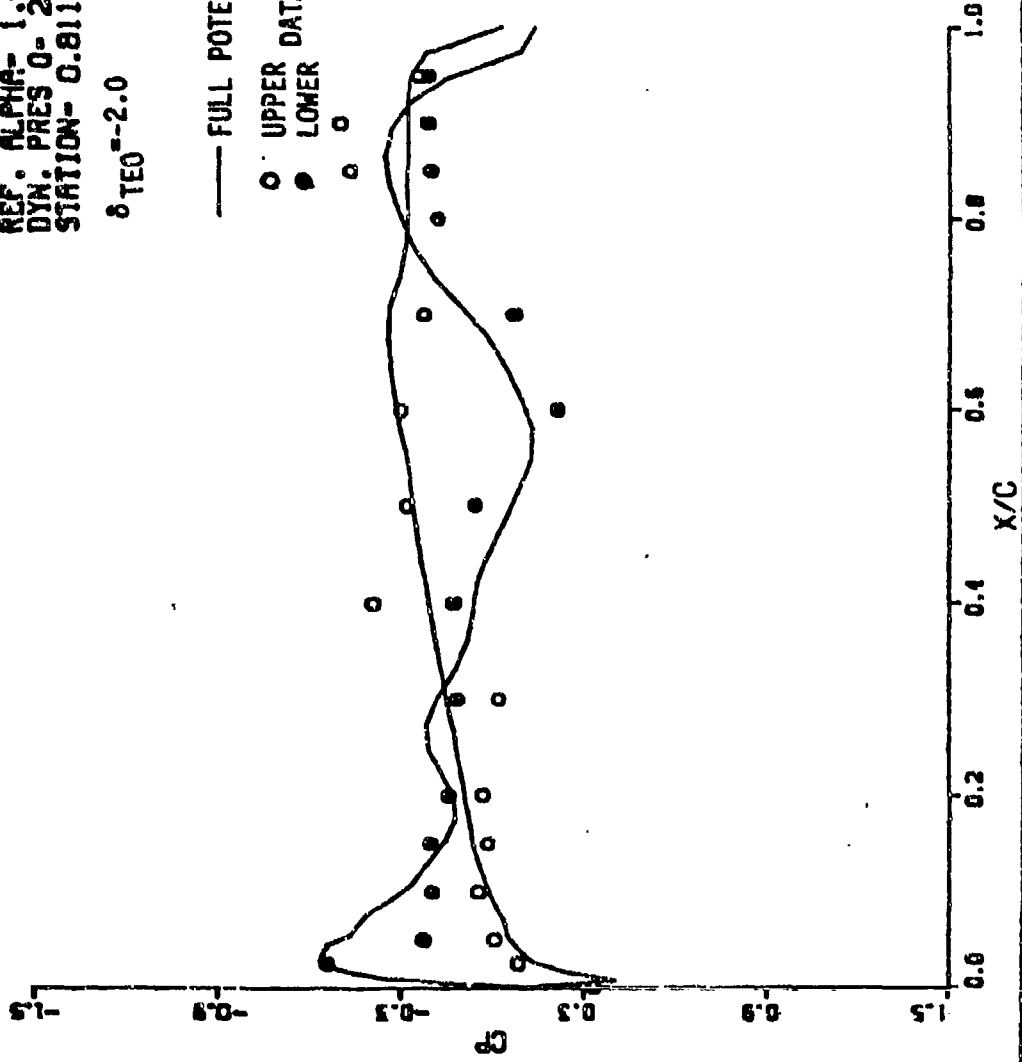


Figure A-29. Pressure Distributions of Flexible AFW Wind Tunnel Model Wing.

# PRESSURE PROFILE

MACH NO- 1.150  
REF. ALPHA- 1.660  
DYN. PRES 0- 2.350  
STATION- 0.924  
 $\delta_{TEO} = -2.0$

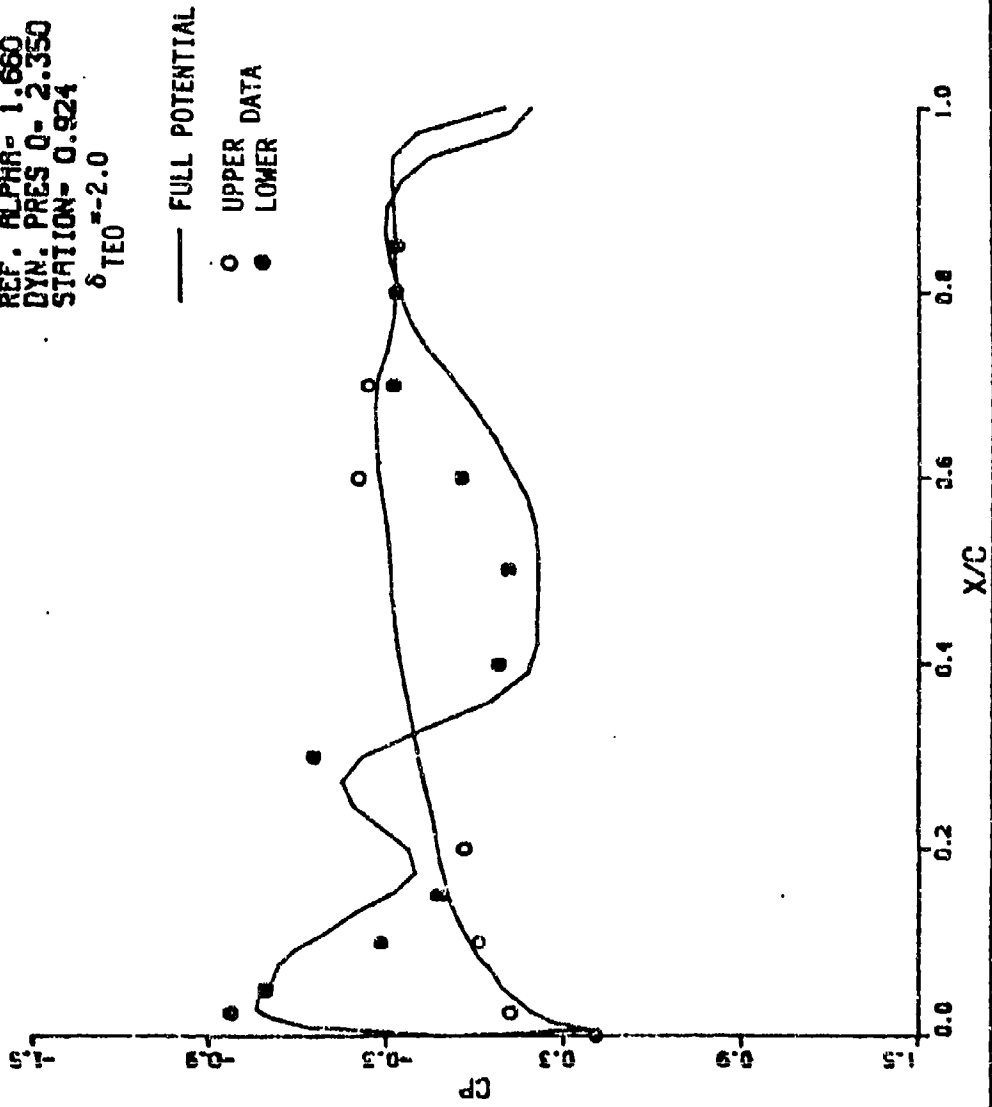


Figure A-30. Pressure Distributions of Flexible AFW Wind Tunnel Model Wing.

# PRESSURE PROFILE

MACH NO= 0.900  
 REF. ALPHA= 0.060  
 DYN. PRES Q= 1.032  
 STATION= 0.436  
 $\delta_{TEI}$  = 2.75  
 $\delta_{TEO}$  = 3.50

— FULL POTENTIAL  
 ○ UPPER DATA  
 ● LOWER DATA

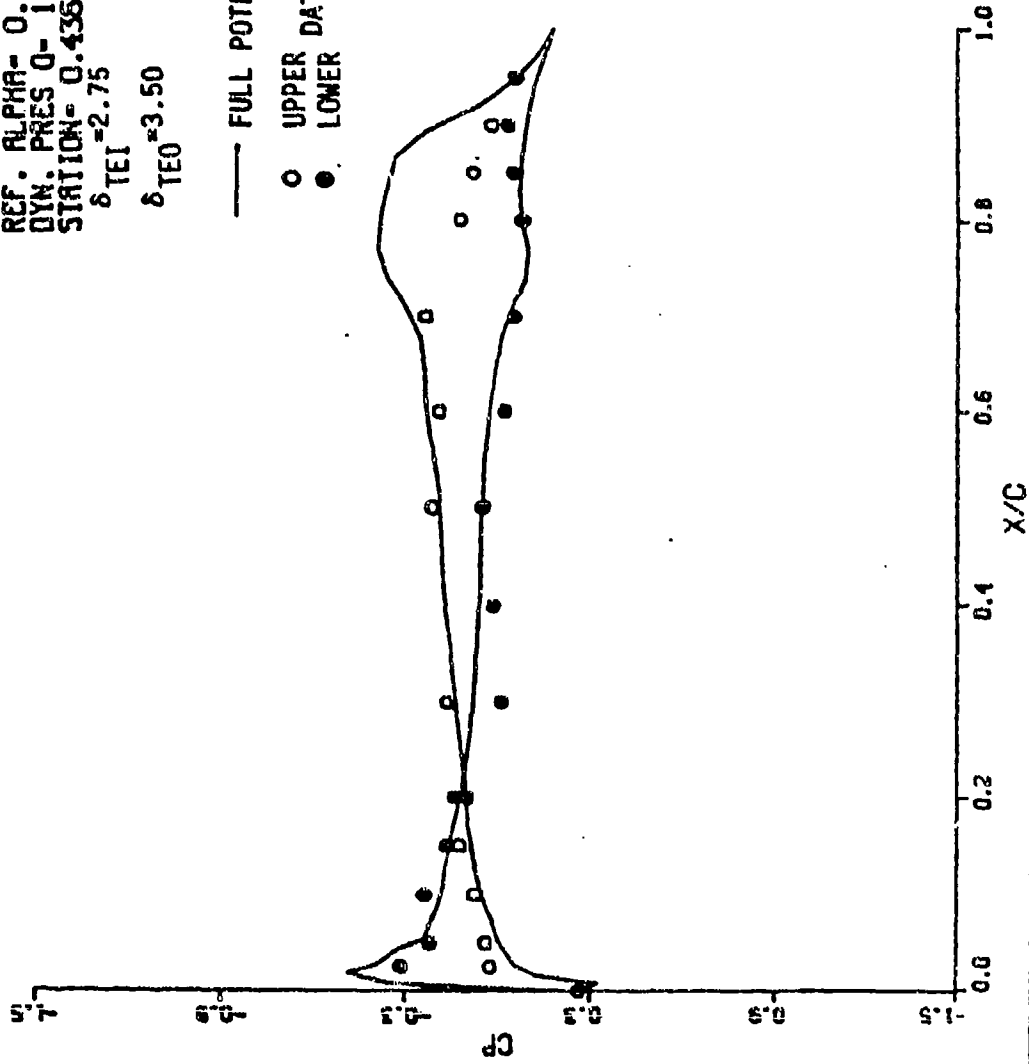


Figure A-31. Pressure Distributions of AFW Wing With Control Surfaces Deflected

# PRESSURE PROFILE

MACH NO- 0.900  
REF. ALPHA- 0.060  
DYN. PRES G- 1.032  
STATION- 0.587  
 $\delta_{TEI}$  -2.75  
 $\delta_{TEO}$  -3.50

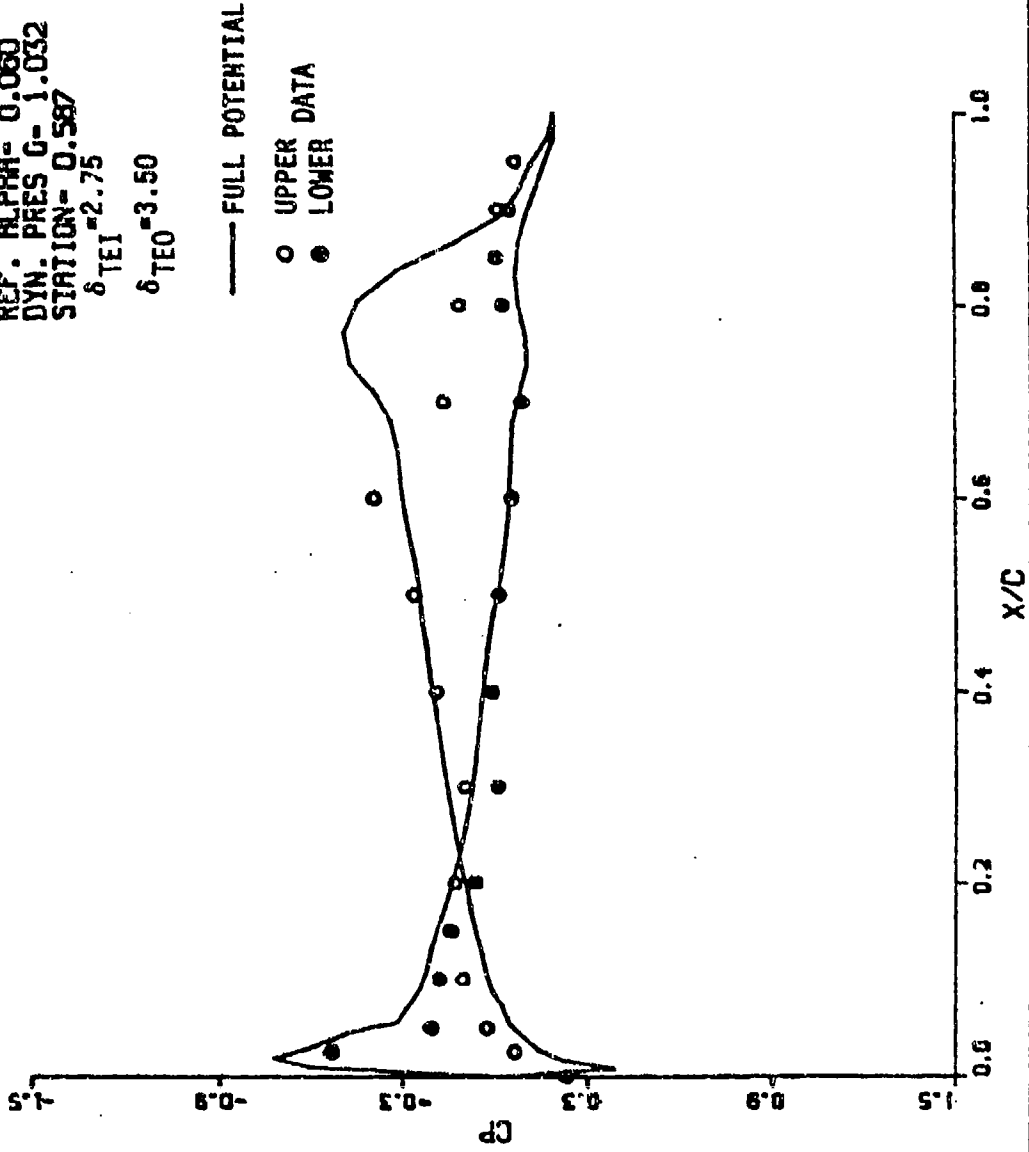


Figure A-32. Pressure Distributions of AFW Wing With Control Surfaces Deflected

# PRESSURE PROFILE

MACH NO- 0.900  
REF. ALPHA- 0.060  
DYN. PRES Q- 1.032  
STATION- 0.699  
 $\delta_{TEI}$ -2.75  
 $\delta_{TEO}$ -3.50

— FULL POTENTIAL

○ UPPER DATA

● LOWER DATA

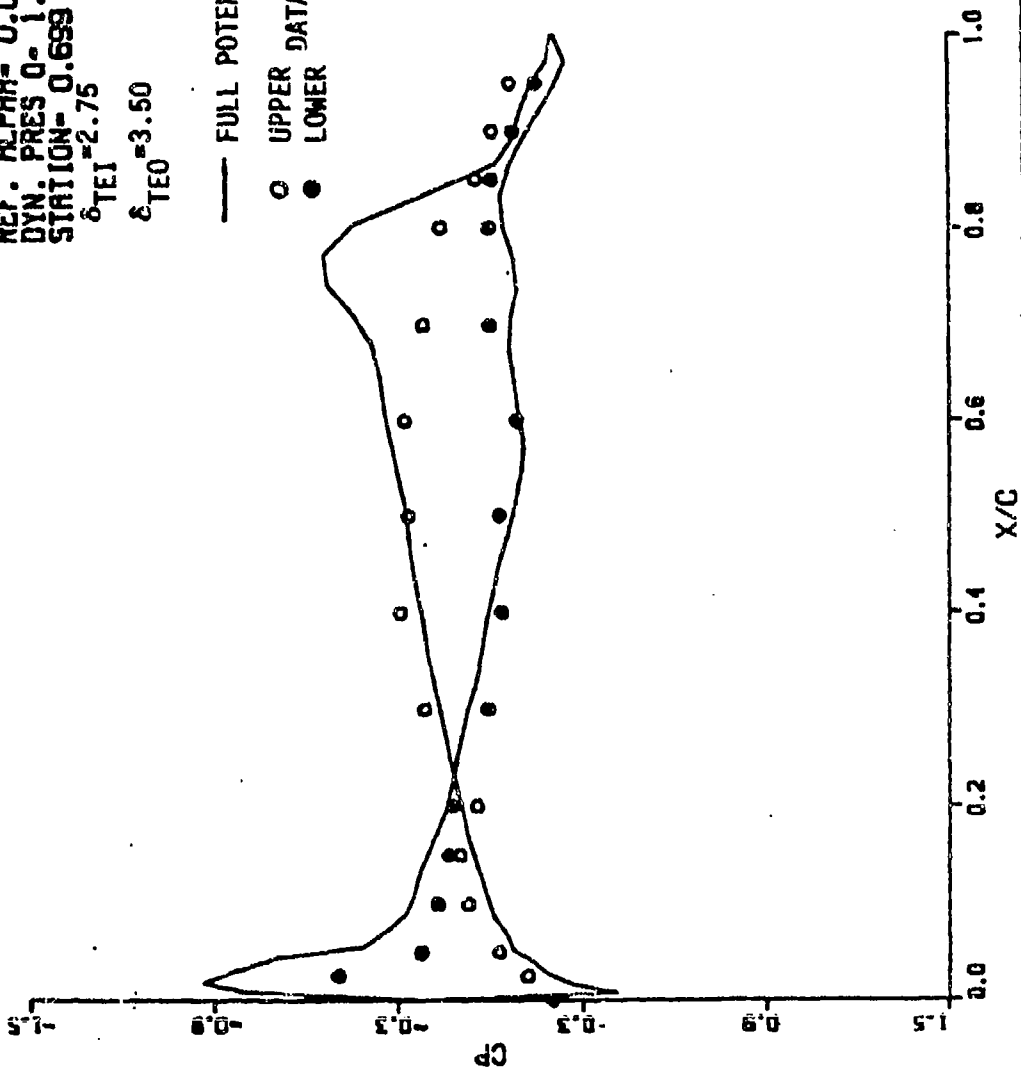


Figure A-33. Pressure Distributions of AFW Wing With Control Surfaces Deflected

# PRESSURE PROFILE

MACH NO- 0.900  
 REF. ALPHA- 0.060  
 DYN. PRES Q- 1.032  
 STATION- 0.811  
 $\delta_{TEI} = 2.75$

$\delta_{TEO} = 3.50$

— FULL POTENTIAL

○ UPPER DATA  
 ● LOWER DATA

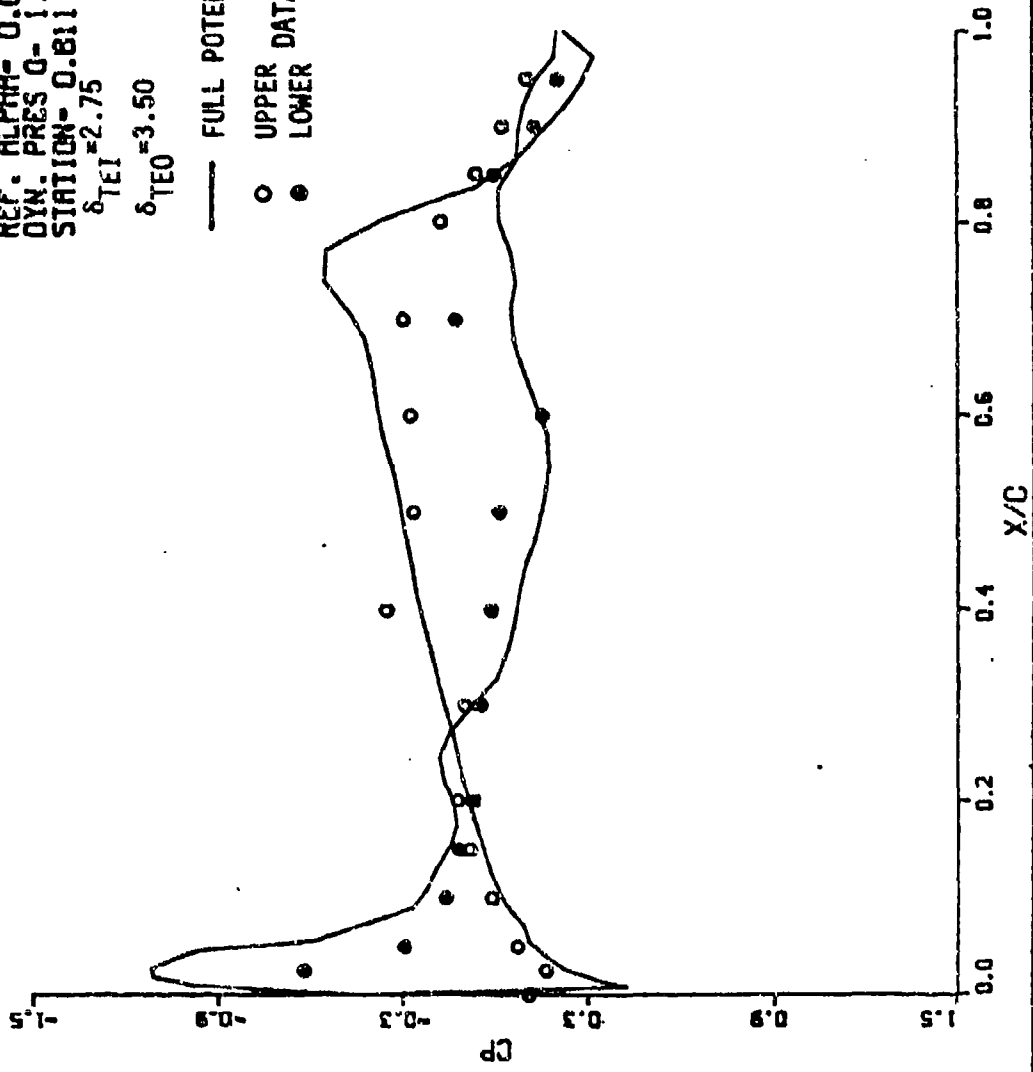


Figure A-34. Pressure Distributions of AFM Wing With Control Surfaces Deflected

# PRESSURE PROFILE

MACH NO- 0.900  
 REF. ALPHA- 0.060  
 DYN. PRES 0- 1.032  
 STATION- 0.924  
 $\delta_{TEI} = 2.75$   
 $\delta_{TEO} = 3.50$

— FULL POTENTIAL

○ UPPER DATA

● LOWER DATA

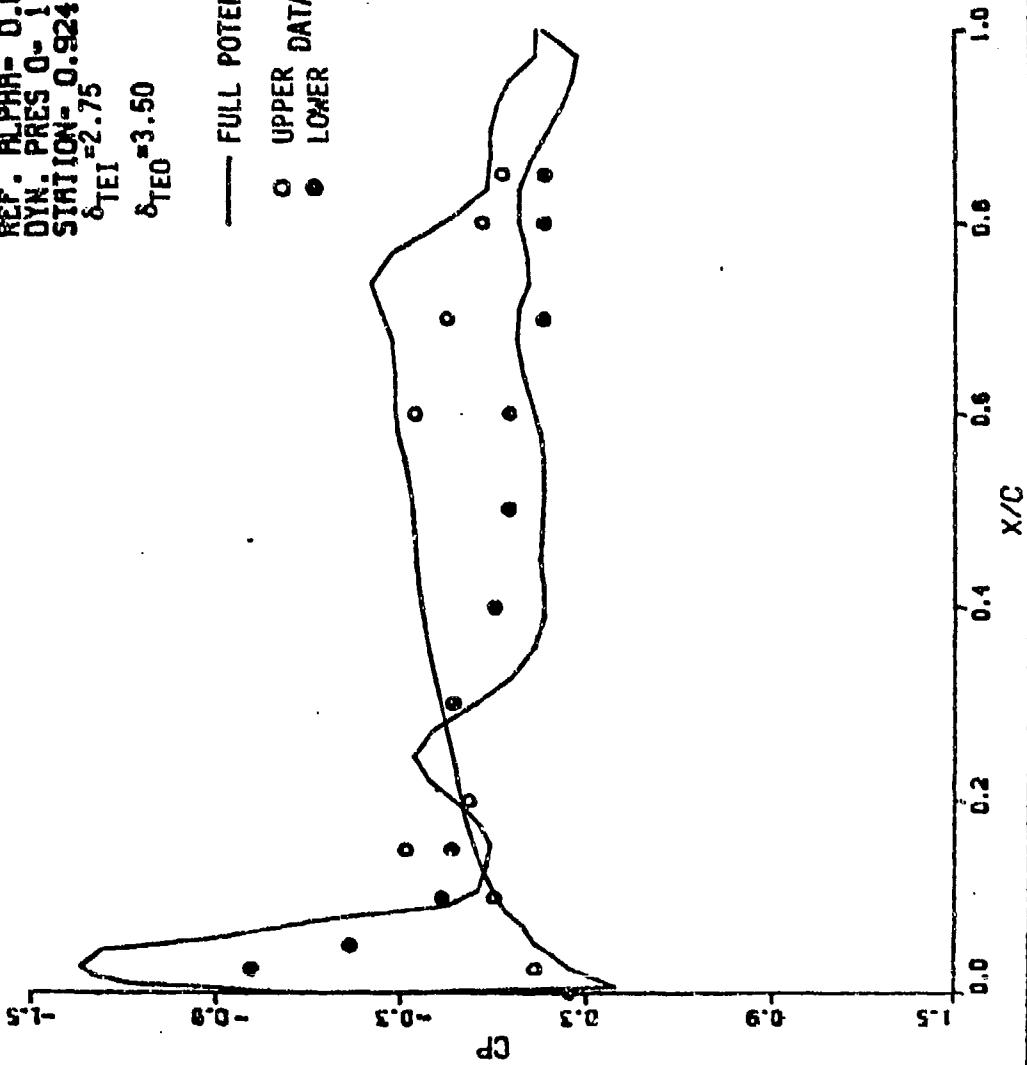


Figure A-35. Pressure Distributions of AFW Wing With Control Surfaces Deflected

# PRESSURE PROFILE

MACH NO- 0.900  
REF. ALPHA- 1.000  
DYN. PRES Q- 1.729  
STATION- 0.435  
 $\delta_{LEO} = -2.5$   
 $\delta_{TEI} = 1.25$

— FULL POTENTIAL

○ UPPER DATA  
● LOWER DATA

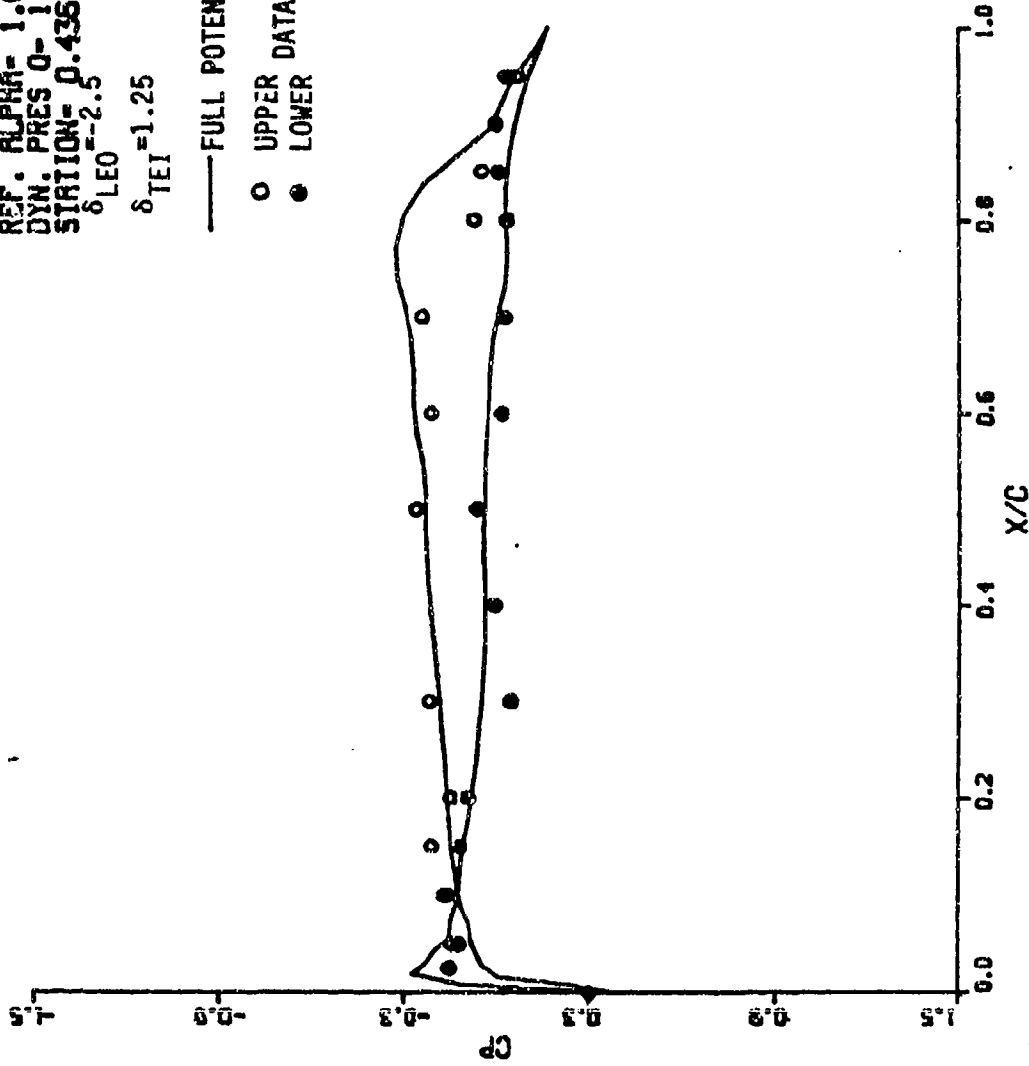


Figure A-36. Pressure Distributions of AFW Wing With Control Surfaces Deflected

# PRESSURE PROFILE

MACH NO- 0.900  
 REF. ALPHA- 1.000  
 DYN. PRES 0- 1.728  
 STATION- 0.587  
 $\delta_{LEO} = -2.9$   
 $\delta_{TEI} = 1.25$

— FULL POTENTIAL  
 ○ UPPER DATA  
 ● LOWER DATA

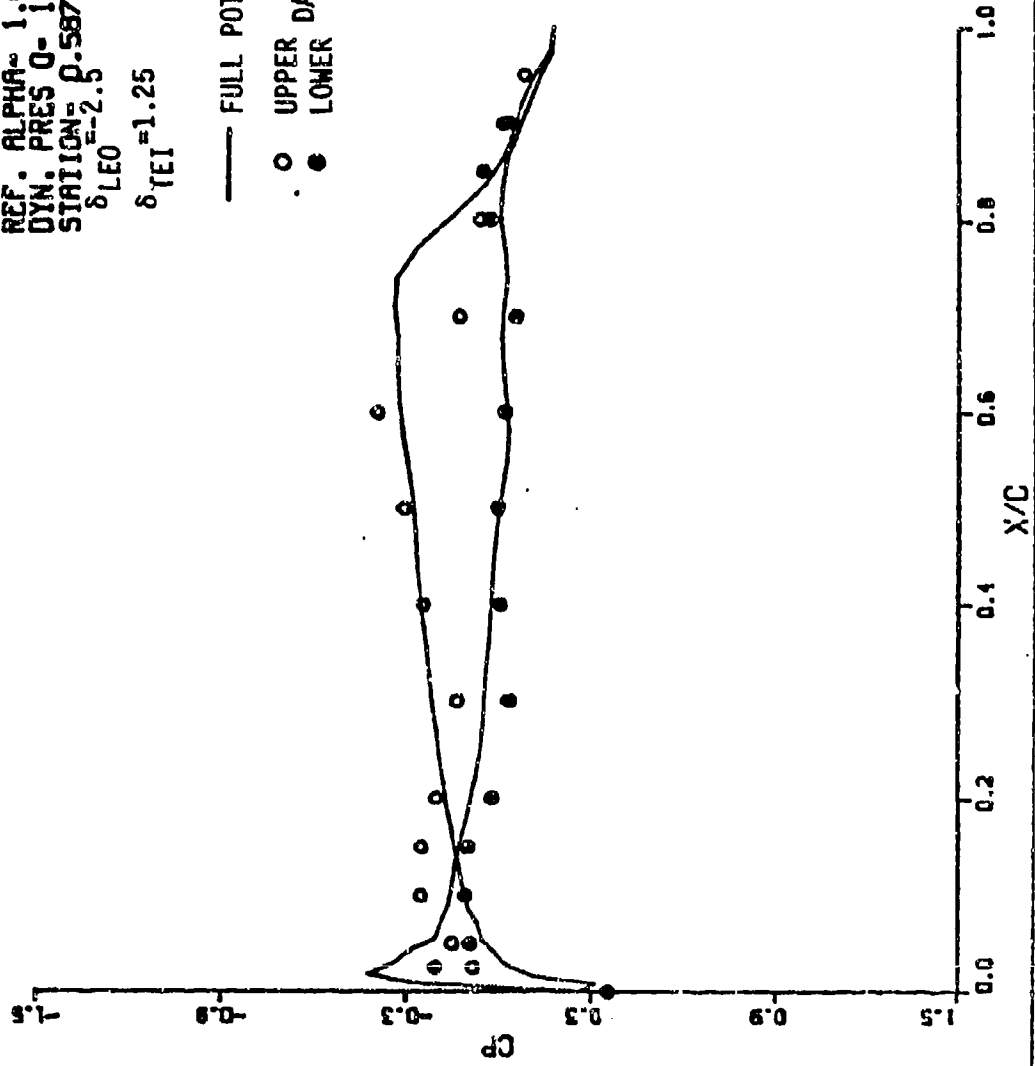


Figure A-37. Pressure Distributions of AFW Wing With Control Surfaces Deflected

# PRESSURE PROFILE

MACH NO= 0.900  
REF. ALPHA= 1.000  
DYN. PRES Q= 1.729  
STATION= 0.699

$\delta_{LEO} = -2.5$

$\delta_{TEI} = 1.25$

— FULL POTENTIAL

○ UPPER DATA

● LOWER DATA

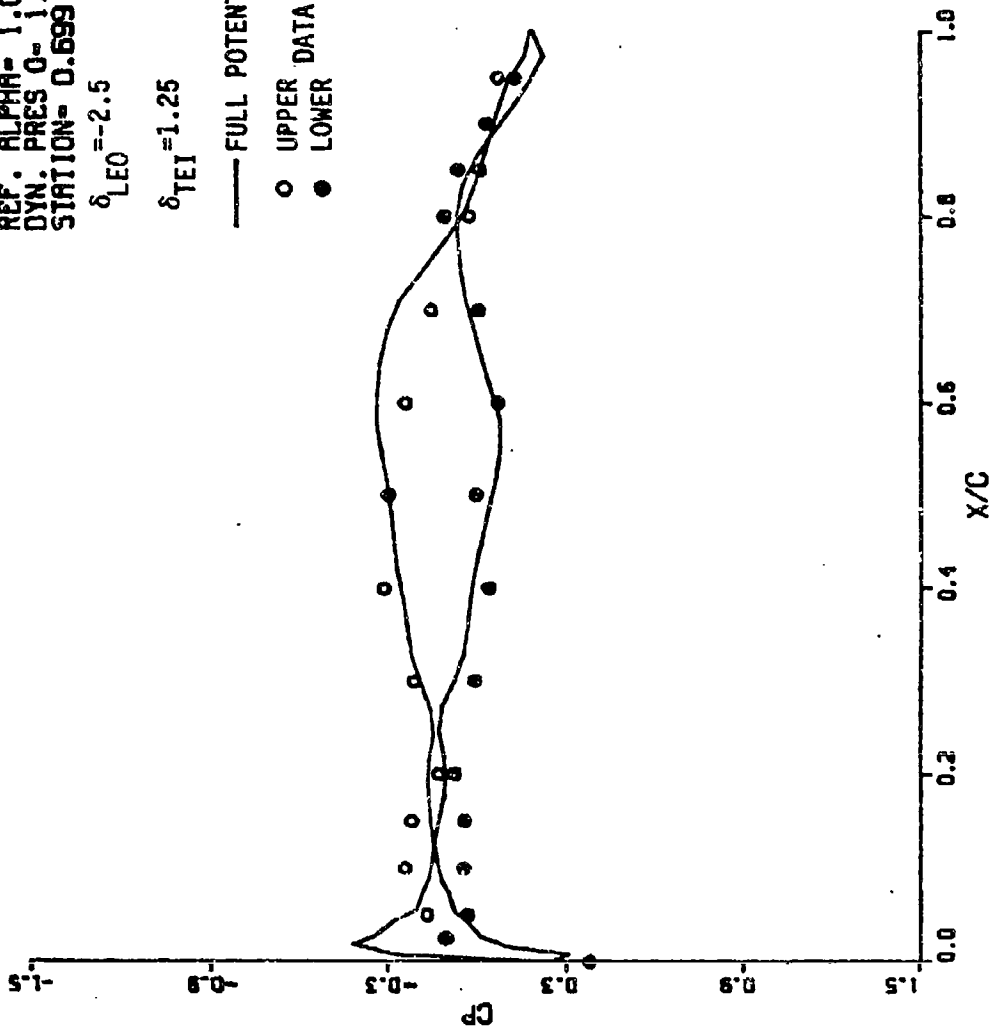


Figure A-38. Pressure Distributions of AFW Wing With Control Surfaces Deflected

# PRESSURE PROFILE

MACH NO- 0.900  
REF. ALPHA- 1.000  
DYN. PRES 0- 1.729  
STATION- 0.811

$\delta_{LEO} = -2.5$

$\delta_{TEI} = 1.25$

— FULL POTENTIAL

○ UPPER DATA

● LOWER DATA

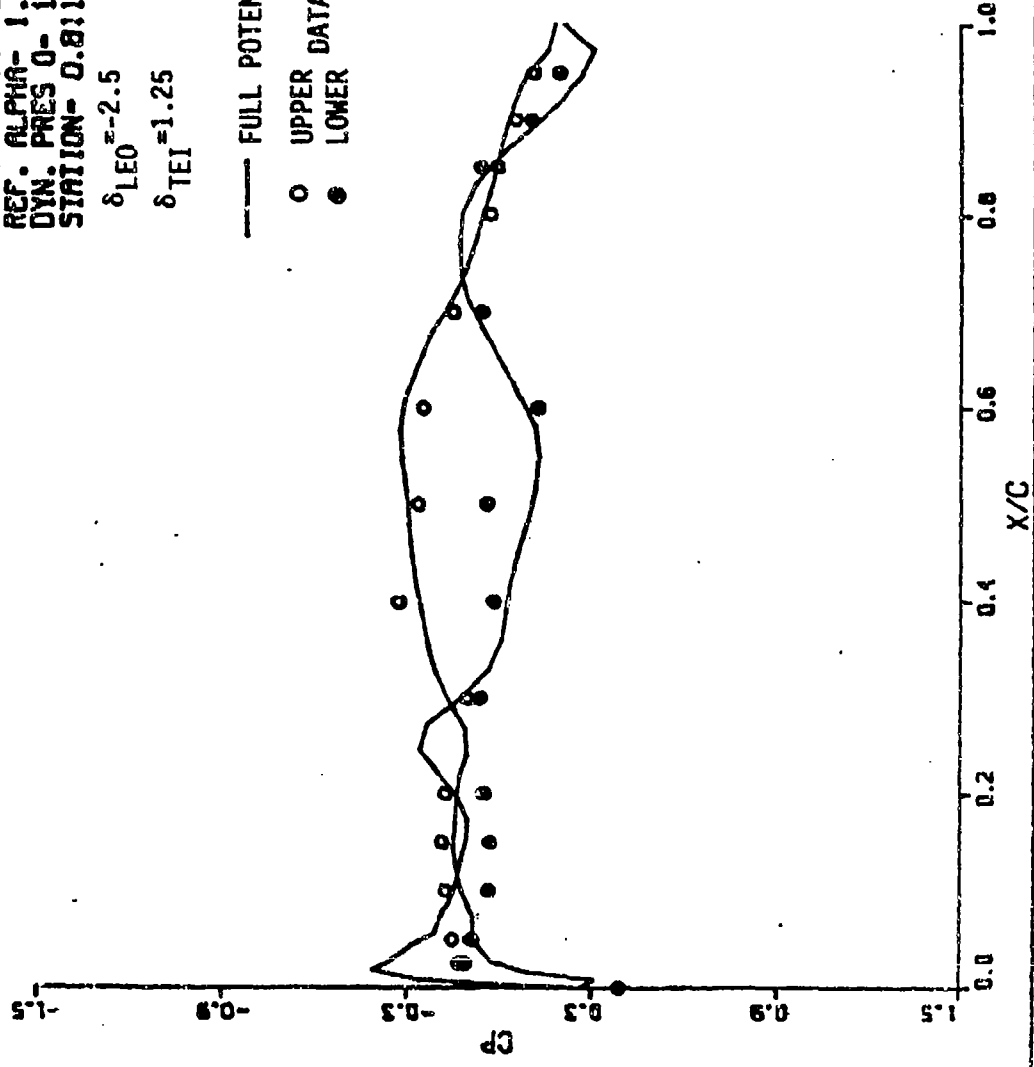


Figure A-39. Pressure Distributions of AFW Wing With Control Surfaces Deflected

# PRESSURE PROFILE

MACH NO- 0.800  
 REF. ALPHA- 1.000  
 DYN. PRES 0- 1.729  
 STATION- 0.924

$\delta_{LEO} = -2.5$

$\delta_{TEI} = 1.25$

— FULL POTENTIAL

○ UPPER DATA

● LOWER DATA

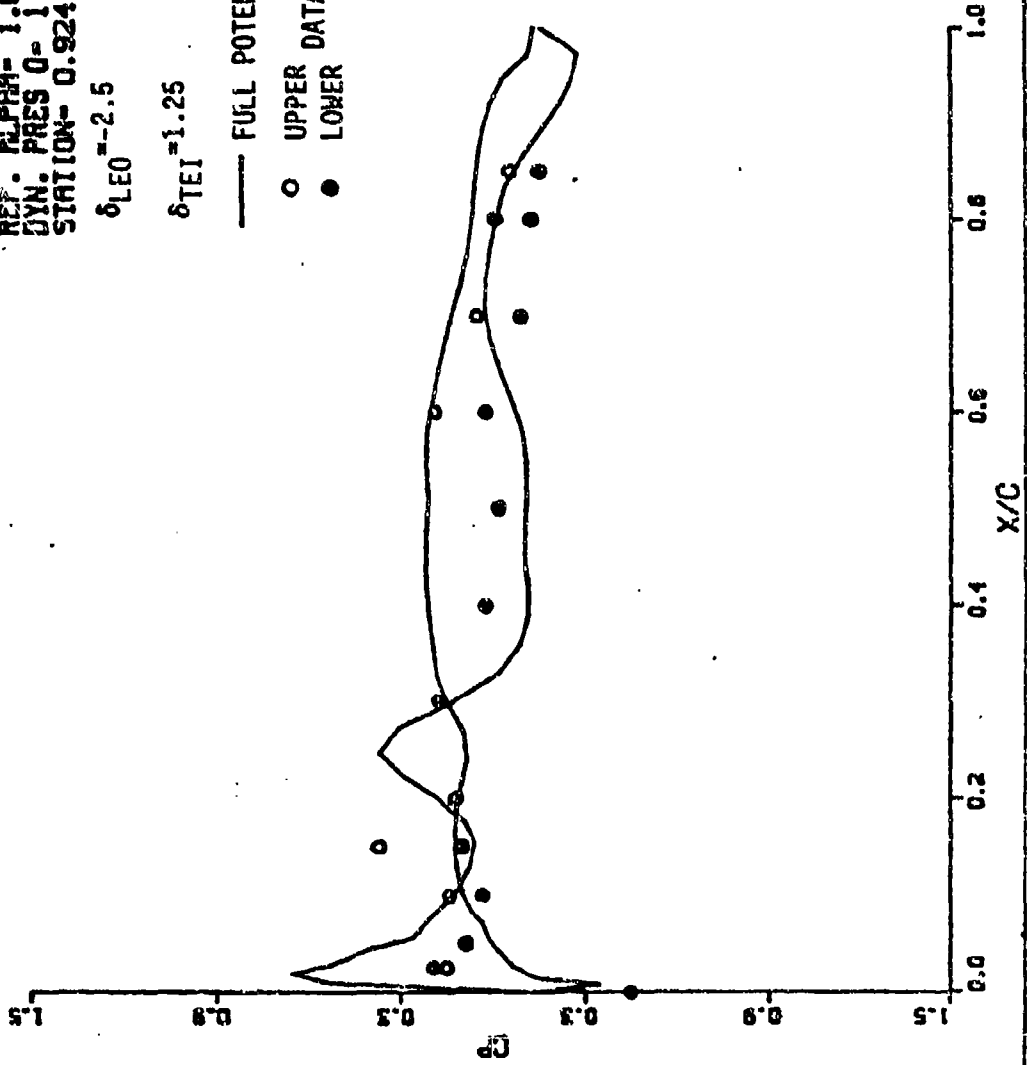


Figure A-40. Pressure Distributions of AFM Wing With Control Surfaces Deflected.

# PRESSURE PROFILE

MACH NO- 1.150  
 REF. ALPHA- 1.650  
 DYN. PRES Q- 2.361  
 STATION- 0.436

$\delta_{LEO} = -2.5$

$\delta_{TEI} = -1.25$

$\delta_{TEO} = -3.0$

— FULL POTENTIAL

○ UPPER DATA  
 ● LOWER DATA

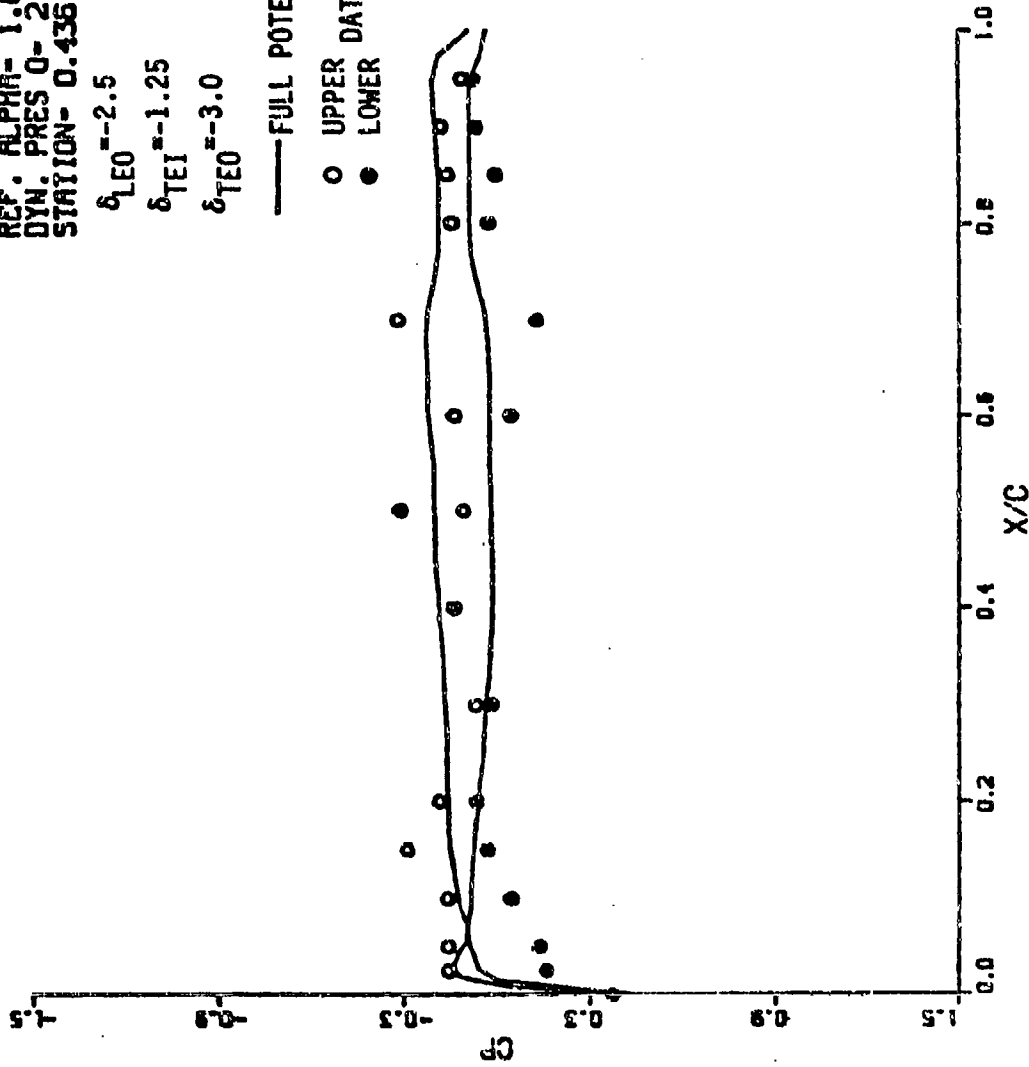


Figure A-41. Pressure Distributions of AFW Wing With Control Surfaces Deflected

# PRESSURE PROFILE

MACH NO= 1.150  
 REF. ALPHA= 1.650  
 DYN. PRES Q= 2.361  
 STATION= 0.587

$\delta_{LEO} = -2.50$   
 $\delta_{TEI} = -1.25$   
 $\delta_{TEO} = -3.00$

— FULL POTENTIAL

○ UPPER DATA  
 ● LOWER DATA

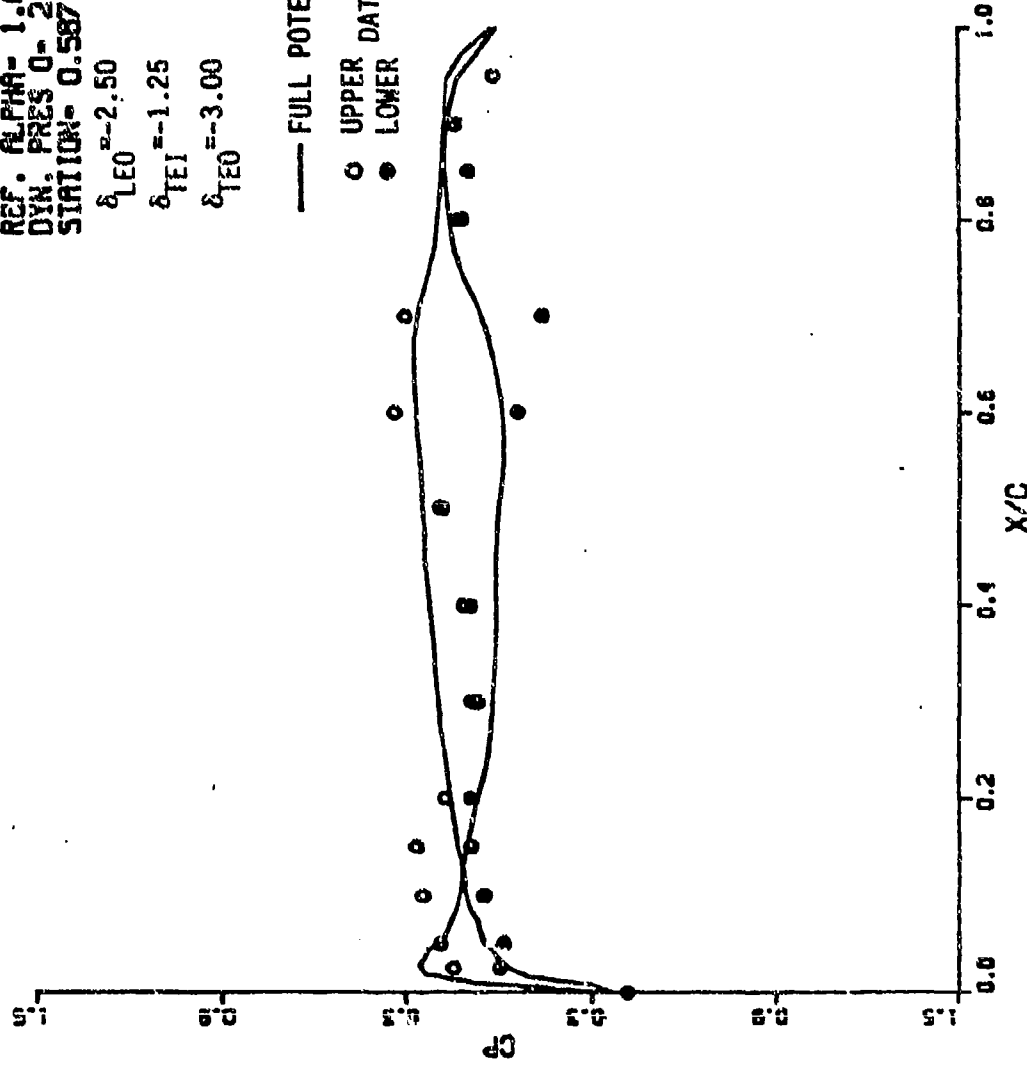


Figure A-42. Pressure Distributions of AFW Wing With Control Surfaces Deflected

# PRESSURE PROFILE

MACH NO- 1.150  
 REF. ALPHA- 1.650  
 DYN. PRES Q- 2.361  
 STATION- 0.688

$\delta_{LEO}$  -2.50  
 $\delta_{TEI}$  -1.25  
 $\delta_{TEO}$  -3.00

— FULL POTENTIAL

○ UPPER DATA  
 ● LOWER DATA

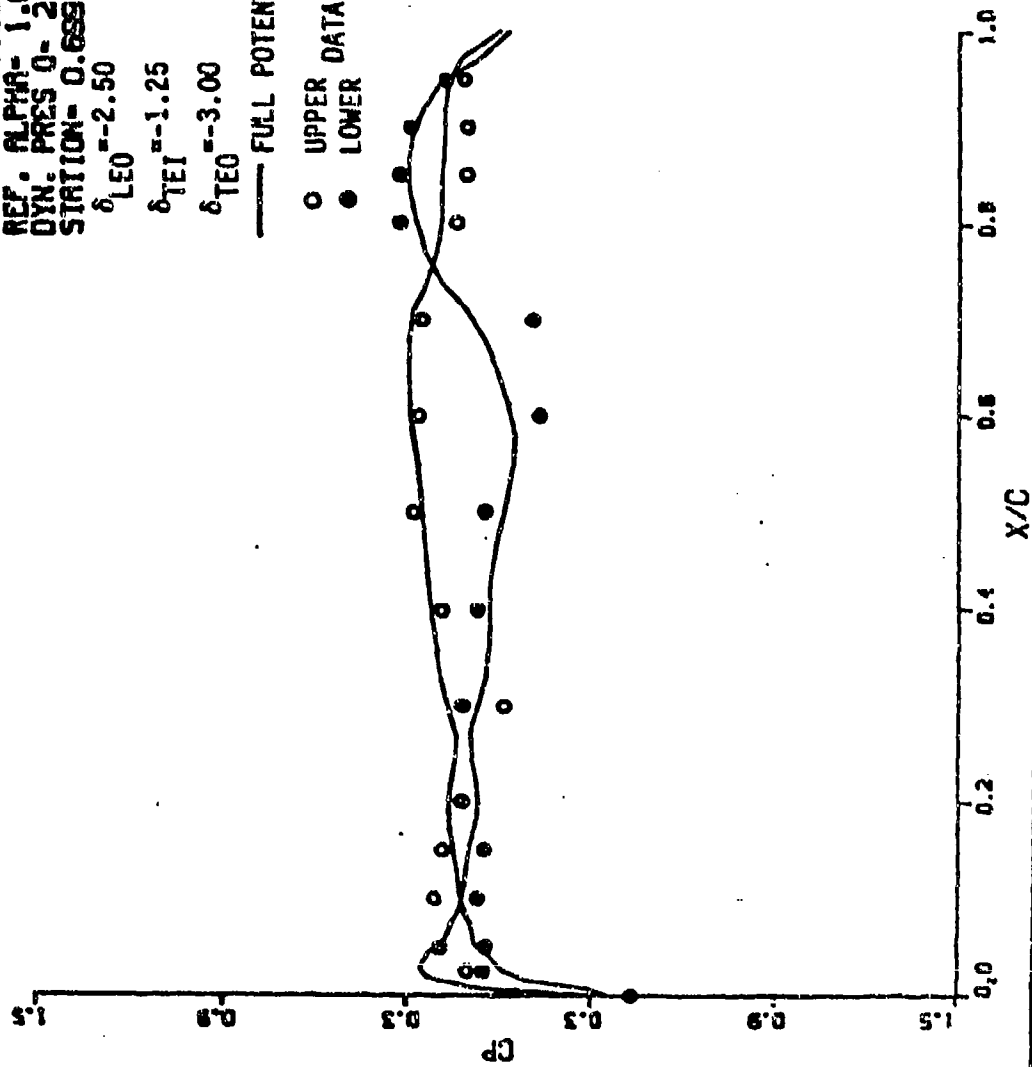


Figure A-43. Pressure Distributions of AFW Wing With Control Surfaces Deflected

# PRESSURE PROFILE

MACH NO- 1.150  
 REF. ALPHA- 1.650  
 DYN. PRES Q- 2.361  
 STRIATION- 0.811  
 $\delta_{LEO}$  -2.50  
 $\delta_{TEI}$  -1.25  
 $\delta_{TEO}$  -3.00

— FULL POTENTIAL

○ UPPER DATA

● LOWER DATA

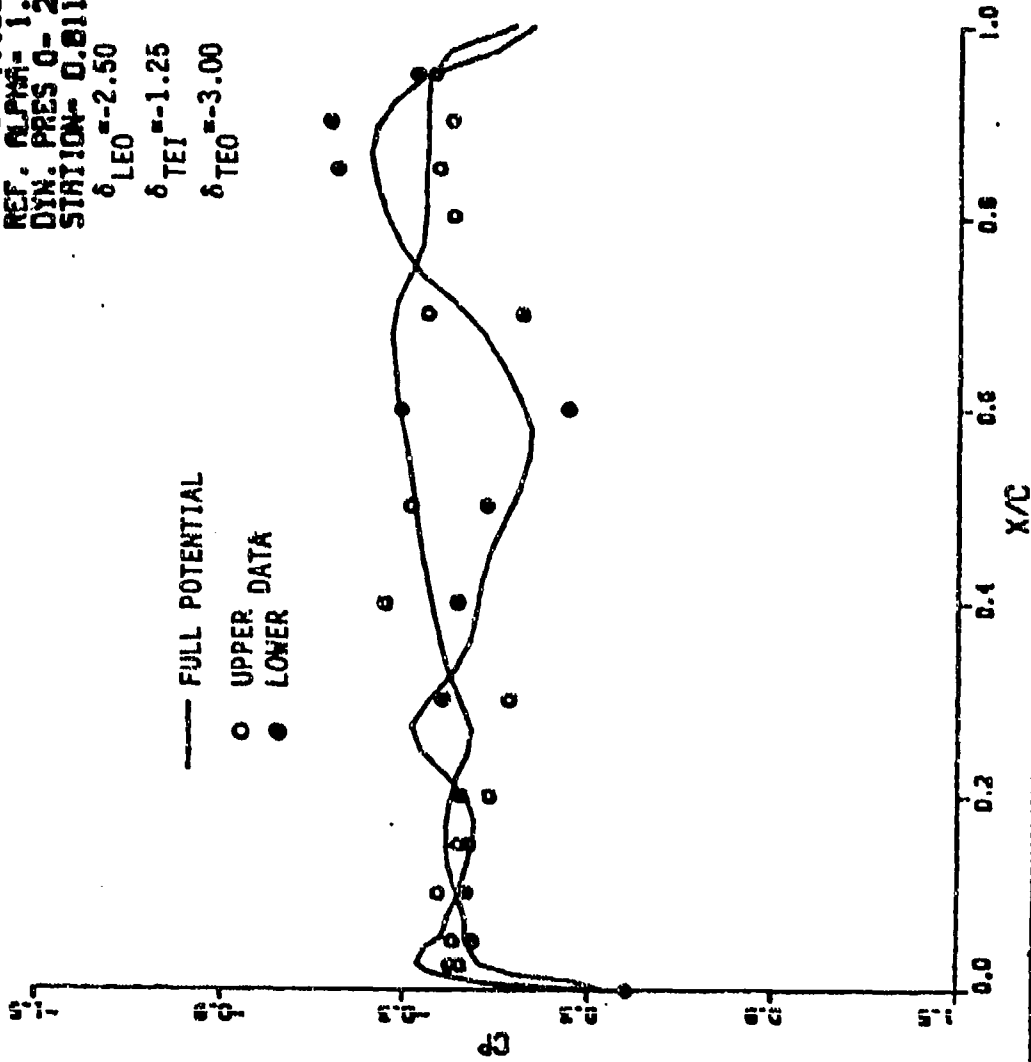


Figure A-44. Pressure Distributions of AFV Wing With Control Surfaces Deflected

# PRESSURE PROFILE

MACH NO- 1.150  
 REF. ALPHA- 1.650  
 DYN. PRES Q- 2.361  
 STATION- 0.924

$\delta_{LEO} = -2.50$   
 $\delta_{TEI} = -1.25$   
 $\delta_{TEO} = -3.00$

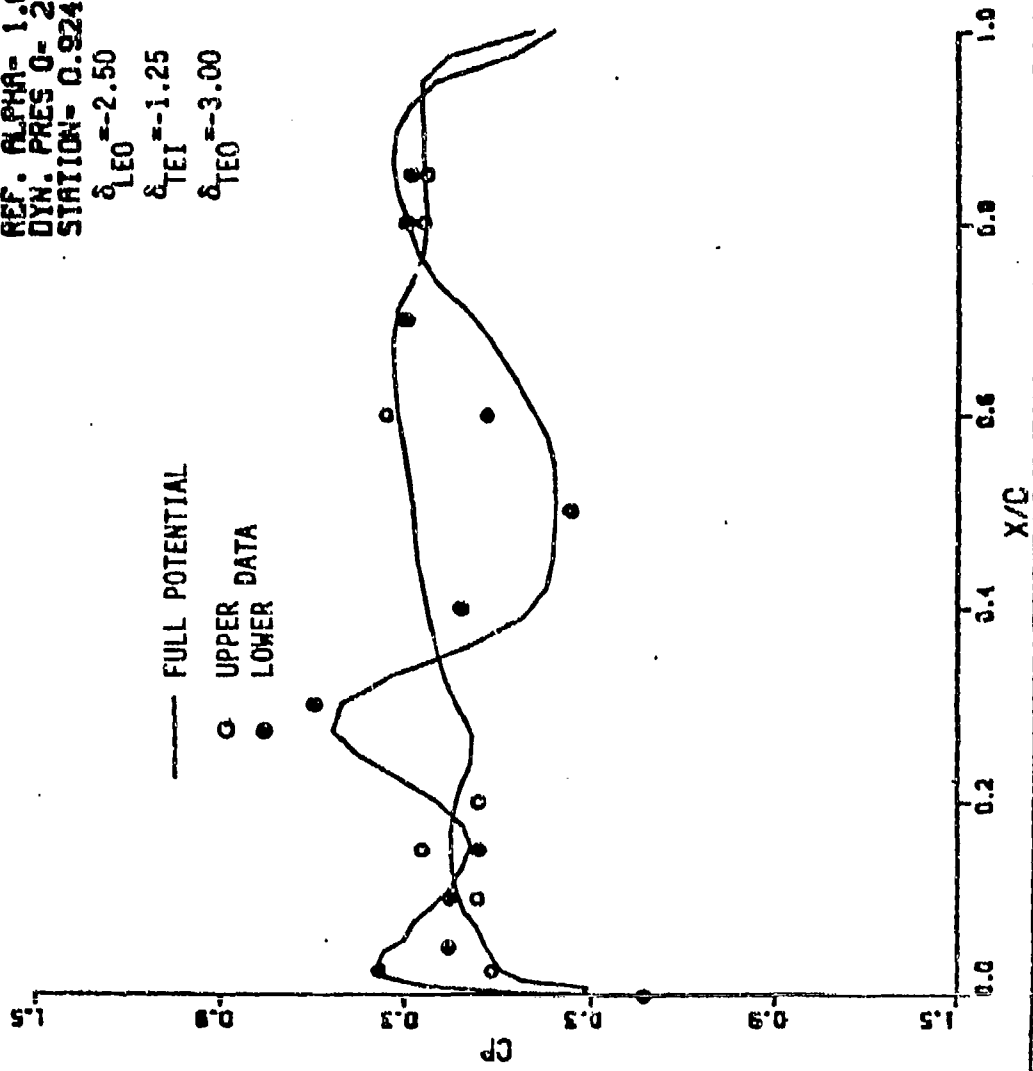


Figure A-45. Pressure Distributions of AFV Wing With Control Surfaces Deflected



# DEPARTMENT of DEFENSE

Directorate for Freedom of Information and  
Security Review, Room 2C757  
1155 Defense Pentagon  
Washington, DC 20301-1155

---

## Facsimile Transmittal

30 November 2001

**To:** Mr. Larry Downing

Organization: DTIC  
Office Phone:  
FAX Number: (703) 767-9244

**From:** Sharon Reinke, Navy Division,  
DFOISR/WHS/DOD

Phone: (703) 697-2716  
FAX: (703) 693-7341

Total Pages Transmitted (including cover sheet): 04

Comments: I am forwarding the FOIA request DTIC received, the DTIC forwarding letter, and a list of documents. The documents in the attached list have been released to a FOIA requester [under our case number 01-F-2458] and are, therefore, cleared for public release. If you have questions, give me a call.

# AMERICAN LAWYER MEDIA

105 MADISON AVENUE, NEW YORK, NY 10016  
212-779-9200

April 11, 2001

*01-F-2458*

Defense Technical Information Center  
Attn: Kelly Akers, FOIA Manager  
8725 John J. Kingman Road Suite 0944  
Fort Belvoir, VA 22060-6218

## FOIA REQUEST

Dear Ms. Akers:

American Lawyer Media respectfully requests, under the Freedom of Information Act, a copy of each of the following records:

- AD B253477, XV-8A Flexible Wing Aerial Utility Vehicle, by H. Kredit, January 1964, 144 pages
- AD B252433, Pilot's Handbook for the Flexible Wing Aerial Utility Vehicle XV-8A, March 1964, 52 pp
- AD B200629, Flex Wing Fabrication and Static Pressure Testing, by Larry D. Lucas, June 1995, 80 pages
- AD B198352, Materials Analysis of Foreign Produced Flex Wings, by Albert Ingram, march 1995, 16 pp.
- AD B131204, Active Flexible Wing Technology, by Gerald D. Miller, Feb. 1988, 256 pages
- AD B130217, Producibility Analysis of the Alternative Antitank Airframe Configuration Flex Wing, June 1988, 112 pages
- AD B126450, From Deha Glider to Airplane, June 1988, 5 pages
- AD ~~B~~803668, Sailwing Wind Tunnel Test Program, September 1966, 125 pages
- AD 477 482, An Evaluation of Flex-Wing Aircraft in Support of Indigenous Forces Involved in Counterinsurgency Operations by R.A. Wise, Feb 1965, 74 pages
- AD 461202, XV-8A Flexible Wing Aerial Utility Vehicle, H. Kredit, Feb. 1965, 100 pages
- AD 460405, XV-8A Flexible Wing Aerial Utility Vehicle, Final Report, Feb. 1965, 113 pages
- AD 431128, Operational Demonstration and Evaluation of the Flexible Wing Precision Drop Glider in Thailand, by William R. Quinn, November 1963, 22 pages.
- AD 430150, Comparative Evaluation of Republic Bikini Drone System, Final Report, 1943?

We agree to pay up to \$200 for costs associated with this request. We are grateful for your kind assistance in this matter. Please contact me at 212-313-9067 if you have any questions relating to our request.

Sincerely,



Michael Ravnitzky  
Editor

*Encl*